



**DEPARTMENT OF MATERIALS
LOUGHBOROUGH UNIVERSITY**

Impact of ion irradiation damage on SiC and ZrN mechanical properties

By Stuart Robertson

A Doctoral Thesis Submitted in Partial Fulfilment of the
Requirements for the Award of Doctor of Philosophy of
Loughborough University

Supervisor: Dr Houzheng Wu

September 2019

Abstract

Key to the safe operation of nuclear reactors is the understanding of materials degradation due to neutron damage. Ion implantation is often used as a surrogate for neutron damage when screening nuclear candidate materials. Ion implantation results in a thin damage layer, the mechanical properties of which are often difficult to determine. In this study a micromechanical test regime is developed in a model material, 6H single crystal silicon carbide (SiC). This test technique is then applied to gold ion irradiated zirconium nitride (ZrN).

Micromechanical test samples are often prepared using a focused ion beam. However, ion beam milling has the potential to damage the crystal structure of a material and introduce residual stress. Therefore, a range of cutting strategies were used to assess the effects of focused ion beam cutting on the modulus and strength of SiC cantilevers. The effects of sample size were also explored. Gallium ion milling resulted in amorphisation of the surface of the SiC crystal micro cantilevers. The thickness of the amorphous zone was then reduced using low voltage cleaning. Low voltage cleaning did not, however, result in increased mechanical performance as other unintended consequences such as cantilever edge rounding occurred. SiC exhibited a plastic deformation threshold of around $0.3 \times 0.3 \mu\text{m}$ but did not exhibit a significant size effect. Nanoindentation was used as a benchmark test to compare to the mechanical properties gathered during micro bend testing. Under indentation conditions, a size effect was identified in hardness and modulus but not in fracture toughness. Modulus results from indentation, and micro bend testing was comparable when ion damage was accounted for.

Hot pressed ZrN samples were ion implanted with gold ions. Microstructural characterisation, nanoindentation and micromechanical tests were performed in the ion implanted zone. Microstructural characterisation identified a dual phase microstructure consisting of ZrN and Zr_2ON_2 . The implanted layer consisted of implanted gold ions followed by a network of dislocations centred around a depth of $1.20 \mu\text{m}$. High-resolution electron backscatter diffraction (HR-EBSD) identified that tensile surface stresses and compressive subsurface stress had been introduced. Nanoindentation linked ion implantation to increased hardness and no modification in modulus. Micromechanical testing indicated a reduction in modulus and strength.

This work highlighted the need to understand sample size effect and ion damage on micro mechanical tests if they are to be used for screening nuclear materials.

Keywords: SiC; ZrN; micromechanical testing; micro bending; nanoindentation; HR-EBSD.

Acknowledgements

First I would like to thank Dr Houzheng Wu, not just for his supervision but for his continued enthusiasm and support for my work. Having the opportunity to learn new techniques and to conduct so many interesting and exciting experiments has been a real pleasure. Working together has been brilliant, and I look forward to our continued collaboration.

Having been an unremarkable school student making it through university and on to a PhD has been a pleasant surprise. I think this has been in no small part due to the love, support and encouragement of my parents: for this I can only thank them!

I would also like to thank my partner Wayne for not just enduring our engineering chats but showing interest in my work and reminding me to lighten up sometimes.

The member of the LMCC have been very accommodating in allowing me to try new techniques. Scott Doak, in particular, was crucial to developing the micro bend testing technique. Scott has unbelievable sticking power and persistence to complete experiments which are not going to plan. I must also thank Zhaoxia Zhao for teaching me about TEM; her enthusiasm for TEM operation and physics is infectious. Further to Scott and Zhaoxia, I would like to thank Sabrina Yan, Keith Yendall, Ryan MacLachlan and Sam Davis for their willingness to share their expertise.

Many thanks to Guo-Jun Zhang and Bao Weichao who provided the ZrN samples and collaborated on some of the HR-TEM and nanoindentation work.

My fellow PhDs have been superb fun to knock about with on this strange endeavour. James Wade and Arthur Swarbrick both helped show me the ropes when I started out. In later years Charles Jackson, Rob Crookes, Ollie Scafe and Dan Bradshaw all weathered a fair amount of discussion about results, complaining about mistakes and inane chat, which all made the PhD process very enjoyable.

Publication list

- Structural integrity and characteristics at lattice and nanometre levels of ZrN polycrystalline irradiated by 4 MeV Au ions. June 2018, Journal of the European Ceramic Society. W. Bao, S. Robertson, H. Wu, *et al.*
- In-situ micro bend testing of SiC and the effects of Ga + ion damage. September 2017. Journal of physics conference series. S. Robertson, S. Doak, Z. Zhou, H. Wu.
- Characterisation of Al/SiC MMCs fabricated using siliconised carbon fibres. July 2017. Proceedings of the 5th Decennial International Conference on Solidification Processing. S. Hogg, H. Li, O. Stephenson, S. Robertson, Z. Zhou, H. Wu.
- Surface engineering alumina armour ceramics with laser shock peening to enhance the hardness, fracture toughness, microstructure and compressive residual stress. Sep 2017, Materials & design. P. Shukla, S. Robertson, H. Wu *et al.*
- Plastic Deformation of Polycrystalline Alumina Introduced by Scaled-Down Drop-Weight Impacts. July 2016, Materials Letters, vol. 175. J. Wade, S. Robertson, Y. Zhu, H. Wu.

Contents

Abstract.....	I
Acknowledgements.....	III
Publication list	IV
Contents	V
List of key abbreviations.....	VIII
1. Introduction.....	1
1.1. Nuclear ceramics background.....	1
1.2. Aims and objectives.....	10
2. Literature review.....	11
2.1. Radiation damage in materials.....	11
2.2. Ion damage.....	14
2.2.1. Ion beam simulation.....	21
2.2.2. Ion damage as a surrogate for nuclear damage.....	23
2.2.3. Summary.....	24
2.3. Micromechanical testing.....	25
2.3.1. Introduction.....	25
2.3.2. Sample preparation	27
2.3.3. Size effect and plasticity	38
2.3.4. Summary.....	41
2.4. Sharp indenter indentation.....	42
2.4.1. Micro-indentation.....	42
2.4.2. Size effect of hardness measurement.....	43
2.4.3. Strength estimation from indentation.....	46
2.4.4. Fracture toughness	47
2.4.5. Nanoindentation.....	47
2.4.6. Continuous stiffness measurement (CSM) nanoindentation.....	50
2.4.7. Indenter design and geometry.....	53
2.4.8. Indentation / nanoindentation of ion and neutron damaged materials.....	56
2.4.9. Comparative analysis of indentation and micromechanical testing.....	58
2.5. Measuring strain at the microscale.....	61
2.5.1. Introduction.....	61
2.5.2. HR-EBSD	62
2.5.3. Transmission electron microscopy (TEM).....	66
2.5.4. Summary.....	67
2.6. Silicon carbide (SiC).....	68

2.6.1.	Introduction.....	68
2.6.2.	Manufacture of SiC.....	69
2.6.3.	Mechanical properties of SiC.....	73
2.6.4.	Crystallography and damage in SiC.....	74
2.6.5.	Effects of ion damage on SiC.....	76
2.6.6.	Micromechanical testing of SiC.....	78
2.6.7.	Nanoindentation and indentation of SiC.....	81
2.7.	Zirconium nitride (ZrN).....	84
2.7.1.	Introduction.....	84
2.7.2.	Manufacture of ZrN.....	84
2.7.3.	Mechanical properties ZrN.....	86
2.7.4.	Crystallography of ZrN.....	86
2.7.5.	Effects of ion damage on ZrN.....	87
2.7.6.	Micromechanical testing of ZrN.....	89
2.7.7.	Nano-Indentation of ZrN.....	89
2.8.	Concluding remarks.....	91
3.	Experimental procedures.....	92
3.1.	Raw materials.....	92
3.2.	Sample preparation.....	94
3.3.	Characterisation.....	96
3.3.1.	Scanning electron microscopy (SEM).....	99
3.3.2.	X-ray diffraction (XRD).....	108
3.4.	Transmission electron microscopy (TEM) Analysis.....	108
3.4.1.	TEM Sample preparation.....	108
3.4.2.	Conventional transmission electron microscopy.....	110
3.4.3.	High-resolution electron microscopy (HRTEM).....	111
3.4.4.	Scanning transmission electron microscopy and Energy-dispersive X-ray spectroscopy (STEM-EDS).....	111
3.5.	Microbeam testing.....	112
3.5.1.	Focused ion beam microscopy.....	112
3.5.2.	Microbeam preparation.....	113
3.5.3.	Microbeam testing.....	115
3.5.4.	Data analysis and mechanics of microcantilevers.....	117
3.6.	Nanoindentation.....	120
3.6.1.	Nanoindentation of single crystal 6H silicon carbide.....	120
3.6.2.	ZrN nanoindentation.....	122
4.	Results and discussion.....	124
4.1.	Micromechanical characterisation of 6H single crystal silicon carbide.....	124

4.1.1.	Surface inspection	124
4.1.2.	6H single crystal silicon carbide bulk chemistry	125
4.1.3.	Nanoindentation of 6H single crystal silicon carbide	126
4.1.4.	Gallium Ion milling effects on SiC micro bend testing	137
4.1.5.	Micro bend size effect in single crystal 6H SiC.....	150
4.1.6.	Single crystal 6H silicon carbide micro mechanical characterisation conclusions	158
4.2.	Characterisation of zirconium nitride (ZrN) and ion implanted ZrN.....	160
4.2.1.	Introduction.....	160
4.2.2.	SEM analysis of ZrN and ion implanted ZrN	160
4.2.3.	High-resolution electron backscatter diffraction (HR-EBSD) of ZrN and ion implanted ZrN	170
4.2.4.	X-ray diffraction (XRD) of ZrN and ion implanted ZrN.....	179
4.2.5.	TEM analysis of ZrN and ion implanted ZrN.....	181
4.2.6.	Nanoindentation of ZrN.....	195
4.2.7.	Micro mechanical testing ZrN and ion implanted ZrN	203
4.2.8.	Micro bend testing of ZrN and ion implanted ZrN	206
5.	Conclusions.....	212
5.1.	Silicon carbide	213
5.2.	Zirconium nitride resistance to gold ion irradiation.....	214
5.3.	Recommendations for future work	215
5.3.1.	Recommendations for future SiC analysis.....	215
5.3.2.	Recommendations for future testing of ZrN	216
	References.....	217
7.	Appendix.....	229
7.1	X-ray photoelectric spectroscopy (XPS) of SiC experimental.....	229
7.2	SiC surface chemistry XPS.....	229
5.3.3.	Raman and fluorescence microscopy.....	232
7.3	Raman analysis of SiC.....	233
7.4	TKD HR-EBSD of ZrN	235

List of key abbreviations

BED	Backscatter electron detector
BC	Band contrast (measure of electron back scatter pattern quality)
BS	Band slope (measure of electron back scatter pattern quality)
BSE	Backscatter/ backscatter imaging
EBSD	Electron backscatter diffraction
EBSP	Electron backscatter pattern
EDS	Energy dispersive spectroscopy
ECCI	Electron channelling contrast imaging
GXRD	Grazing incident angle X-ray diffraction
HR-EBSD	High-resolution electron backscatter diffraction
HR-TEM	High-resolution transmission electron microscopy
I ZrN	Gold ion irradiated zirconium nitride
LED	Lower electron detector
MAD	Mean angular deviation (measure of electron back scatter pattern quality)
MD	Molecular dynamic modelling
RS	Raman spectroscopy
SE	Secondary electron / secondary electron imaging
SEM	Scanning electron microscope
SiC	Silicon carbide
STEM	Scanning transmission electron microscopy
TEM	Transmission electron microscope
USD	Upper secondary electron detector
V ZrN	Virgin / un irradiated zirconium nitride
WD	Working distance
XPS	X-ray photo electric spectroscopy
XRD	X-ray diffraction
ZrN	Zirconium nitride
Zr ₂ ON ₂	Zirconium oxynitride
ZrO ₂	Zirconium oxide (zirconia)

1. Introduction

1.1. Nuclear ceramics background

Nuclear fission has been commercially used as a source of energy since 1954. Fission relies on an unstable atom absorbing a neutron resulting in a fission event; during this fission event, two new atoms of a slightly lighter atomic mass than the parent atom (fission fragments) are produced along with neutrons and binding energy. The binding energy includes radiation and heat which are converted to electricity typically by steam turbines. The new neutrons, if moderated correctly, have the potential to fission further atoms, creating a chain reaction and thus producing more energy and more neutrons, resulting in a self-sustaining reaction.

The first self-sustaining nuclear reactor “Pile 1” was built at the University of Chicago by a group of scientists including Enrico Fermi in 1942. Pile 1 was constructed from graphite and wooden blocks with no radiation shielding and no cooling system. This remarkably crude design produced a mere 0.5 watts. However, this prototype demonstrated that criticality could be reached, thus confirming the potential of nuclear energy.

At the present-day, world power demand is increasing, in particular, demand for power is rising rapidly in growing economies such as China and India. Countries typically balance their energy portfolio to be able to respond to energy demands over the day, with nuclear, coal and wind making up the base load of energy production, while gas and hydroelectric deal with peak demand. Despite recent changes in America's stance, the global consensus is that greenhouse gases should be reduced. Nuclear energy produces very low greenhouse emissions and consistent power, making it an ideal baseload power source. For this reason, nuclear power is of interest to the growing energy markets of China and India. Below is a summary of nuclear reactors in operation (Table 1):

Table 1 Operational nuclear power plants a global summary [1].

Reactor type	Main countries	Number	GWe	Fuel	Coolant	moderator
Pressurised water reactor (PWR)	US, France, Japan, Russia, China	282	264	enriched UO ₂	water	water
Boiling water reactor (BWR)	US, Japan, Sweden	78	75	enriched UO ₂	water	water
Pressurised heavy water reactor (PHWR)	Canada, India	49	25	natural UO ₂	heavy water	heavy water
Advanced gas-cooled reactor (AGR & Magnox)	UK	14	8	natural U (metal), enriched UO ₂	CO ₂	graphite
Light water graphite reactor (RBMK & EGP)	Russia	11+4	10.2	enriched UO ₂	water	graphite
Fast neutron reactor (FBR)	Russia	3	1.4	PuO ₂ and UO ₂	liquid sodium	None
Totals		441	384			

Improvements in uranium enrichment technologies by the 1970s, and the high cost of gas-cooled fast reactors, resulted in the proliferation of light water reactors (282 PWR/LWR) globally as seen in (Table 1). LWRs make up 85% of the world's nuclear energy production, with pressurised water reactors running at 300°C being most prevalent. A typical schematic for an LWR is shown in Figure 1 below. Many of the reactors operational today are running beyond their design life cycle. It is in these circumstances that a deep understanding of nuclear degradation of material is required. First, we must consider the operational condition to which nuclear materials are exposed.

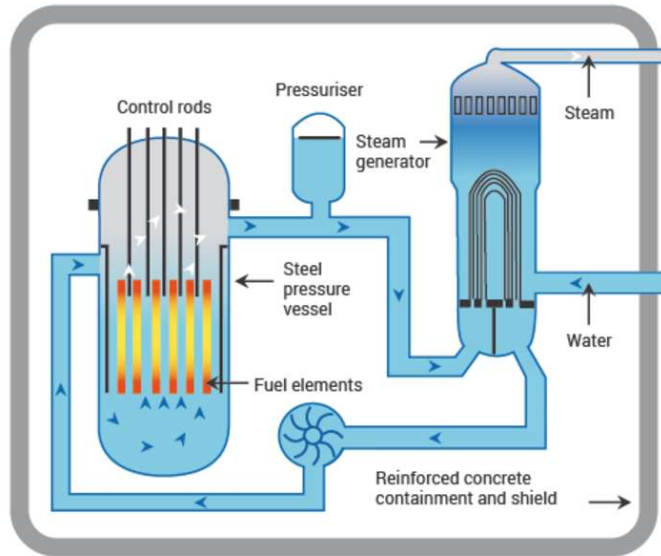


Figure 1 Schematic diagram of a pressurised water reactor (PWR)[2].

The basic operation of nuclear reactors consists of the critical reactor heating a cooling medium; this medium is used to produce steam which in turn rotates a turbine to produce electricity. The amount of heat produced is controlled using control rods which mediate the nuclear reaction.

Most reactor designs use fuel supplied in the form of uranium oxide (UO_2) pellets. The fuel pellets (usually about 1 cm diameter and 1.5 cm long) have a high melting point of 2800°C and are typically arranged in a long zirconium alloy (Zircaloy) tube to form a fuel rod. Zircaloy is hard, corrosion-resistant, transparent to neutrons, weldable and formable, making it an ideal material for fuel rods. The pellets are placed in 4 m long zirconium alloy tubes. These are backfilled with helium, sprung loaded and welded in place. Numerous rods make up each fuel assembly; typical reactors contain around 200-300 rod assemblies comprising of around 80-100 tons of uranium. The fuel assemblies can be placed in and out of the reactor core for refuelling. The main issues surrounding the failure of rods is the fretting wear, caused by the pellets vibrating in the tubes coupled with the effects of radiation damage. Further to this Zircaloy poses issues in the case of reactor overheating as the alloy can react with water, producing hydrogen and resulting in explosions in the core, as was observed in the Fukushima Daiichi incident of 2011. In the case of advanced gas-cooled reactors (AGRs), stainless steel is used as the operating temperatures are considerably higher (650°C compared to 300°C in LWR). Fuels are expected to reach temperatures of 700°C during

operation and 1600 °C under accidental conditions. The radiation levels experienced by the pellets are typically higher than 60 dpa-siC [3]. Figure 2 shows the hierarchical structure of a nuclear fuel rod assembly:

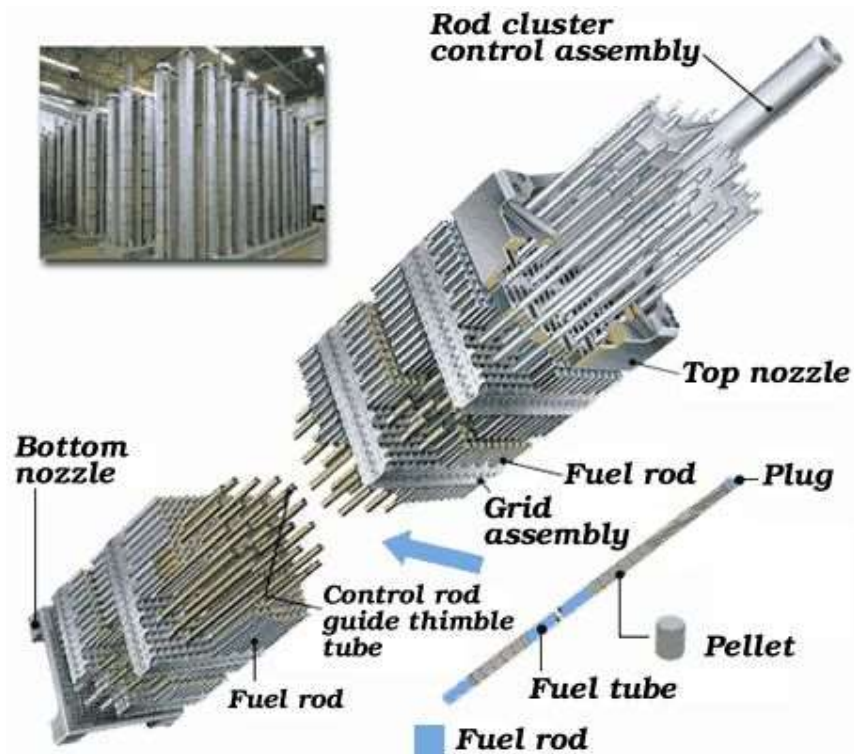


Figure 2 Nuclear fuel rod assembly showing the fuel hierarchy from pellets, rods to assemblies [4].

In LWR reactors sintered uranium oxide fuel pellets are typically used. The pellets are manufactured by pressing conditioned uranium dioxide powder into dies to form a green body pellet. The green body is then sintered, producing a fuel pellet. These fuel pellets are then “canned” in zirconium tubes as previously discussed.

The fuel particles used in pebble bed and gas-cooled reactor designs are TRISO (Tri-structural-isotropic) fuel [5], [6]. TRISO fuels were developed as part of the UK Dragon reactor project [5]. These fuel types use encapsulated uranium particles bound into a larger graphite matrix. Fuel particles are comprised of a tri-layer structure, referred to as TRISO fuel (as shown in **Figure 3**) [7]. TRISO fuel particles are manufactured by coating a uranium dioxide kernel with porous pyrolytic carbon (PyC) to act as a buffer layer and accommodate swelling of the fuel element [7]. This layer is followed by a dense, isotropic PyC layer and then a tough silicon carbide (SiC) layer which serves as the pressure vessel [7], [8]. The SiC layer is coated with another PyC layer to provide a bonding surface with the carbon matrix

used to fabricate fuel compacts. These coatings provide numerous functions: primarily the layers act as a pressure vessel to contain the fission products and stop contamination of the cooling system. Further to this, burnable poisons are often used in the fuel to even out the performance of the reactor over time. Both gadolinium and zirconium diboride are integral fuel burnable absorbers (IFBA) and are used as thin coatings on fuel pellets. These materials are neutron absorbers which decay under neutron exposure, compensating for the progressive build-up of neutron absorbers in the fuel as it is burned.

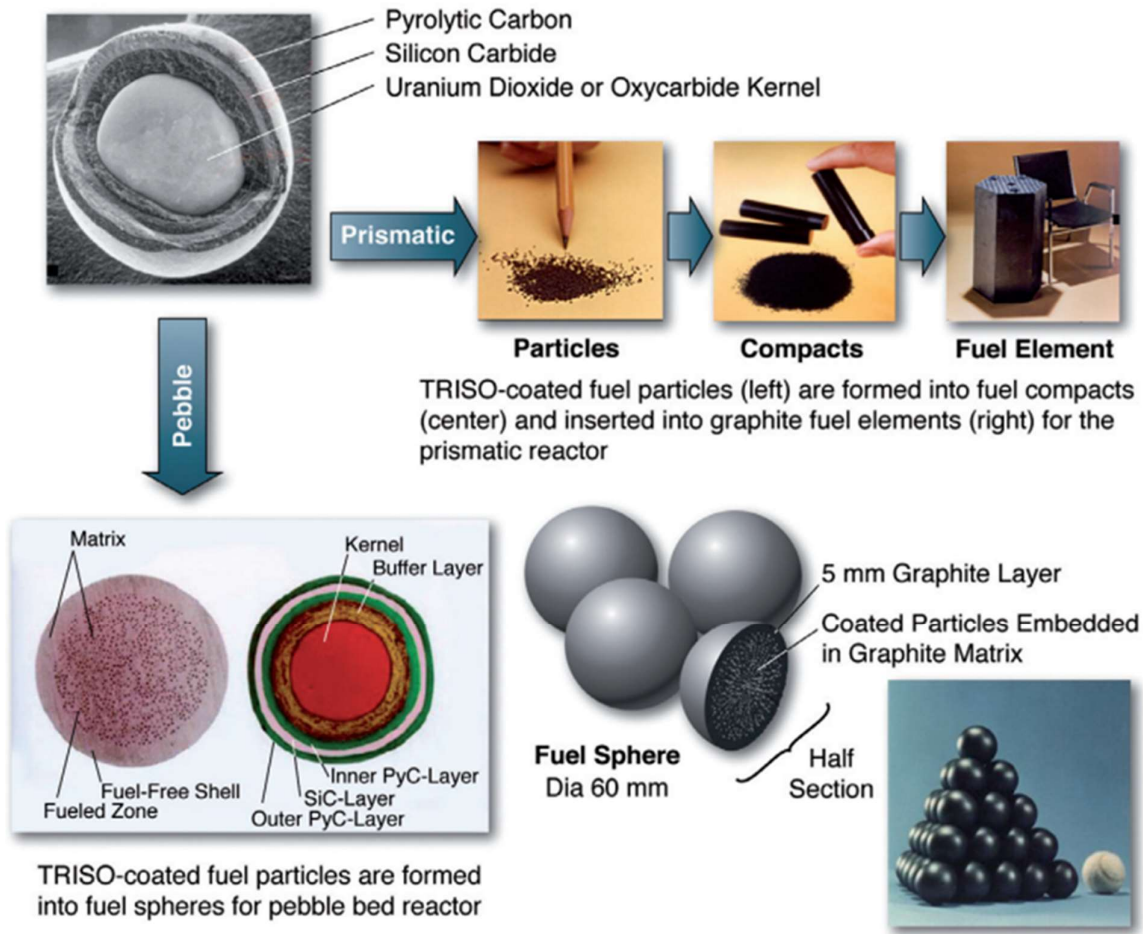


Figure 3 Example cross section of TRISO fuel pellets, along with prismatic and pebble fuel designs [9].

For TRISO fuels to operate safely, a detailed understanding of the mechanical properties of the SiC layer is crucial to achieving a reliable design for high-performance fuels. There are numerous challenges involved with materials degradation in present-day reactor designs and with extending the lifetime of current reactors. A step change in materials properties will be required for the safe operation of the next generation of nuclear reactor designs.

Generation IV nuclear reactors development began around 2001. Seven generation IV reactor designs have been proposed see (Table 2/Figure 4). It is clear that the operational temperatures, energy densities and neutron fluence are much higher in the new designs.

Table 2 Generation 4 reactor designs summarised [10].

	Neutron spectrum (fast/thermal)	Coolant	Temperature (°C)	Pressure	Fuel	Fuel cycle	Size (Mw)	Uses
Gas cooled fast reactors	fast	helium	850	high	U-238 +	closed, on site	1200	electricity & hydrogen
Lead cooled fast reactors	fast	lead or Pb-Bi	480-570	low	U-238 +	closed, regional	20-180** 300-1200 600-1000	electricity & hydrogen
Molten salt fast reactors	fast	fluoride salts	700-800	low	UF in salt	Closed	1000	electricity & hydrogen
Molten salt reactor - Advanced High-temperature reactors	thermal	fluoride salts	750-1000		UO ₂ particles in prism	Open	1000-1500	hydrogen
Schniodium cooled fast reactors	fast	sodium	500-550	low	U-238 & MOX	Closed	50-150 600-1500	electricity
Supercritical water cooled reactors	thermal or fast	water	510-625	very high	UO ₂	open (thermal)) closed (fast)	300-700 1000-1500	electricity
Very high-temperature gas reactors	thermal	helium	900-1000	high	UO ₂ prism or pebbles	Open	250-300	hydrogen and electricity

(High pressure = 7-15 MPa)(+ = with some U-235 or Pu-239), ** 'battery' model with long cassette core life (15-20 yr) or replaceable reactor module.

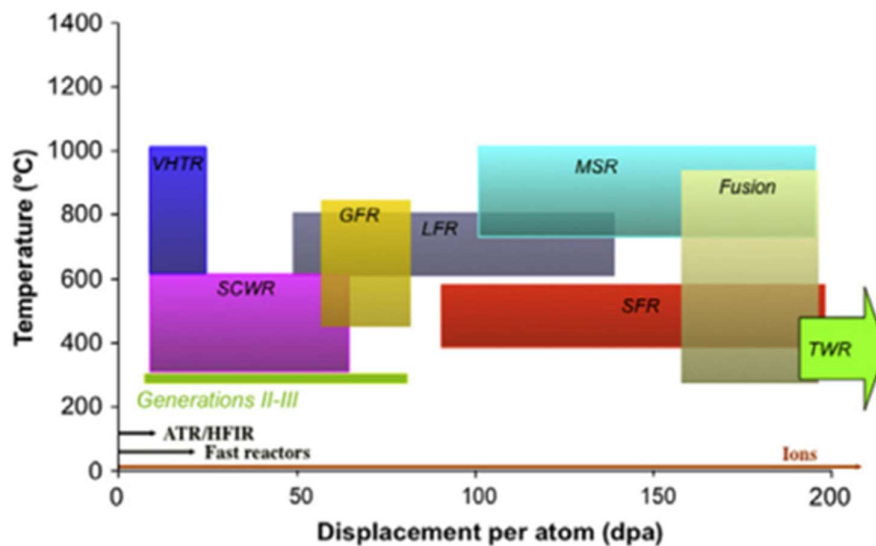


Figure 4 Plot of the temperature-dpa requirements for various reactor concepts and the achievable annual damage rates in different test reactors and with ion irradiation. Acronym codes VHTR = very high temperature reactor, SCWR = supercritical water reactor, GFR = gas fast reactor, LFR= lead fast reactor, MSR = molten salt reactor, SFR = sodium fast reactor, TWR=traveling wave reactor, Generations II-III=present daylight water reactors, ATR/HFIR=advanced test reactor, high flux isotope reactor [11].

The design intent is that locally or regionally, countries will move to closed loop fuel cycles, limiting the amount of nuclear waste by using a mix of reactor types. This mix of systems will limit waste and reduce the risks and costs of storing waste, making nuclear energy a more appealing option. Fundamentally, the aim is that more of the fuel rod be burned up during use, and this trend is already evident in the use of LWRs. Burning up more of the fuel rod requires higher enrichment levels. Reactors will be run at significantly higher temperatures and pressures, yielding higher efficiency. However, this will result in much higher demands on the materials used. These higher operating fluences will result in an increased build-up of gaseous radiation by-products, resulting in a need for higher strength materials. SiC is used at present for fuel coatings while chemical vapour deposited layers and fibre composite components are under investigation [3], [8]. ZrC is being investigated as a potential higher temperature and radiation resistance fuel coating, tube cladding and as a surrogate material to understand the degradation of actinides [12].

A factor in developing closed fuel cycles is the requirement to use surplus plutonium (Pu). Plutonium is a by-product of reprocessing nuclear fuels and decommissioning nuclear warheads [13]. Many nuclear waste products are vitrified in glass and stored; however, Pu

produces minor actinides which are expected to deteriorate the glass used for vitrification [13]. An alternative to vitrification is immobilisation in a ceramic matrix, but this solution still leaves the Pu stockpiled [13]. A more economically attractive option is to utilise Pu in “inert matrix fuel” (IMF) [13]. Using pure Pu fuel pellets would generate excessive heat for LWR Zircaloy fuel assemblies, resulting in premature failure of the fuel rods. Therefore, Pu fuel requires dilution in an inert matrix (hence the name “inert matrix fuel”). Materials selection for this inert matrix requires a material which will not alloy with the fuel tubes, have a high melting temperature, low vapour pressure, high radiation damage tolerance and low interaction with cooling. Specific requirements for each reactor type are detailed in (Table 3). Screening of candidate materials shows that carbides such as SiC, ZrC and B₄C react with Zr and Fe around 700 °C, making them an inappropriate choice [14]. ZrN and AlN are both promising candidate materials for IMF matrices [13], [14].

Table 3 nuclear material requirements for each reactor generation leading to fusion reactors [15].

Component	Fission (Gen 1)	Fission (Gen 4)	Fusion
Structural alloy maximum Temperature	<300°C	500-1000°C	550-1000°C
Max dose for core internal structures (total dpa)	~1 dpa	~30-150 dpa	~200 dpa
Max transmutation helium Concentration	~0.1 appm appm ~	~3-15	2000 appm (~10000 appm for SiC)
Coolants	water	He, H 2O, Pb-Bi, Na	O, He, Pb-Li, Li
Structural materials	Zircaloy, stainless steel	ferritic steel, SS, superalloys, composite	ODS & Ferritic/ martensitic steel, V alloy, SiC composite

Despite the potential advantages of nuclear energy, there are very real risks which have been realised on a number of occasions, most recently the Fukushima Daiichi nuclear disaster (2011), and in the past the Chernobyl disaster (1986) and Windscale/Sellafield (1957). In the case of each of these events, radioactive materials were released in sufficient quantity to result in widespread health and environmental effects. Operator error and safety system

design played a large part in each of these events. Materials selection and the understanding of the effects of radiation damage is a crucial part of safety system and reactor design, and an essential part of validating materials for use in nuclear reactors is developing a deep understanding of their damage tolerance to radiation and the effects of irradiation on mechanical properties.

In summary, a brief history of nuclear reactors has been presented from Fermi's first experiments to the present day and beyond to generation IV reactor designs. The materials problems involved in the next generation reactors and the issues with present-day material systems have also been touched upon. Of these properties, the key factors are resistance to thermal degradation at temperatures up to 1000 °C and resistance to 150 dpa neutron irradiation while maintaining structural integrity as a fuel container.

1.2. Aims and objectives

Aim: To understand and characterise the mechanical and microstructural changes which ZrN undergo during gold ion irradiation.

Objectives:

- a) Establish a microcantilever test technique in a model material, single crystal 6H SiC, to determine Young's modulus and fracture strength at the microscale.
- b) Use micro bend testing to evaluate mechanical property changes of ZrN following irradiation.
- c) Characterise the microstructural changes in ZrN before and after irradiation at a range of length scales.

2. Literature review

This review is intended to present the mechanisms that contribute to radiation damage and how these mechanisms present microstructurally and physically. Ion damage is often used as a surrogate for radiation damage. In this review the ion implantation process is detailed along with microstructural and mechanical property changes information. The suitability of ion damage as a surrogate for nuclear damage is also examined. Due to the shallow irradiation depths caused by ion damage, micromechanical testing is becoming a common test technique for the analysis of ion damaged surfaces.

As a complementary test technique, indentation is reviewed in the context of ion beam damage, size effect and ceramic characterisation. Both nanoindentation and micromechanical testing will then be critically compared for the characterisation of ion damaged ceramics. Following this, strain measurement is introduced at a range of length scales for the determination of residual stress in ion-implanted ceramics. Finally, both SiC and ZrN materials systems are reviewed in detail regarding micromechanical testing, indentation and ion beam damage.

2.1. Radiation damage in materials

Understanding nuclear damage of materials is vital for nuclear reactor operational life estimation. Materials lifetime analysis is critical for the development of new reactor materials which will be required to withstand higher temperatures and higher flux. First we must understand the operation of nuclear fission. For reactor criticality to be reached, fission material is required along with neutrons travelling sufficiently slowly to interact with the nucleus of the fuel atoms. Neutron fuel interaction can be split into six stages:

1. An energetic incident neutron interacts with the lattice of an atom.
2. Kinetic energy is imparted to the lattice atom.
3. Displacement of the atom from its lattice site produces a primary knock-on atom (PKA).
4. The movement of the displaced atom through the lattice creates further knock-on atoms.

5. The production of a collision cascade occurs (collection of point defects created by the PKA).
6. The termination occurs of the primary knock-on atom as an interstitial.

The removal of the atom from the lattice site and subsequent re-association in the lattice results in “self-interstitials” where atoms are redeposited back into the lattice (see Figure 5). This addition of atoms in the lattice results in self-interstitial vacancy pairs which are called Frenkel defects. Both the interstitials and vacancies are mobile in the lattice and can coalesce to form dislocation loops. These loops can also join to form voids. As these voids are the addition of defects they are not contributory to material swelling.

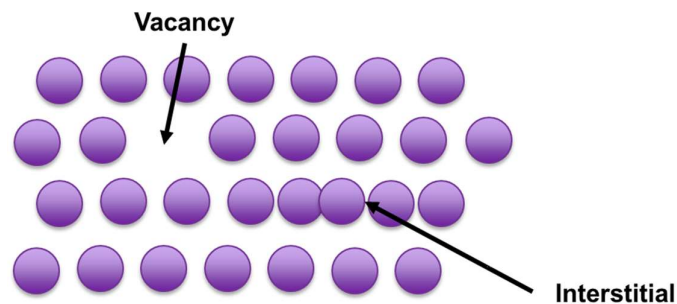


Figure 5 Schematic representation of lattice vacancy and self-interstitials [16].

There are a range of outcomes from this collision cascade; the incident neutron may be absorbed by the nucleus resulting in instability and subsequent decay, releasing an alpha particle in the process. Alpha particles consist of two protons and neutrons these particles are 2+ charge and highly ionising. Therefore, they pick up electrons from the surrounding lattice forming elemental helium. The addition of helium to the target lattice causes embrittlement and can act as a nucleation point for voids, which can lead to swelling. Further to these effects, some materials experience amorphisation, contributed to by both vacancies/interstitials, and He bubbles.

Zinkle *et al.* and Rodriguez *et al.* classified these damage modes dependent on radiation dose, and temperature relative to materials melt temperature (T_m) as seen in Table 4 [17], [18]. This Figure shows how both temperature and dose affect the damage accrued in materials. As such, testing must be designed to mimic operational exposure to elicit the correct forms of damage.

Table 4 Effects of radiation on structural materials based on temperature relative to melt and dose. Adapted from [17], [18].

Temperature (T/T _m)	Dose (dpa)	Defect and effect	Size
0 -0.4	0.1	Point defects: Vacancies and interstitials → hardening	One atomic diameter
0.1		Multiple point defects, clusters of point defects complexes of vacancies and interstitials with solutes → hardening and phase instability	A few atomic diameters
	10	Vacancy clusters and loops → Creep	Diameter < 7 nm
0.3	10	Interstitial loops	Diameter > 7 nm
	10	Rafts (agglomerates cluster and small loops)	6-10 nm thick, 100-200 nm in length and width
0.3-0.6	10	Voids → volumetric swelling	10-60 nm
0.5	10	Helium bubbles → embrittlement	3-30 nm
		Transmutation atoms (produced at all temperature but agglomerates at T/T _m >0.5)	

Testing resistance to representative levels of radiation damage is challenging as reactor lifetimes are in the order of 50 years. This makes placing samples in the reactor and waiting to analyse the material impractical. Specialist reactors for testing are available globally: in the USA two such reactors are operational. 8 dpa per year is achievable in these US-based reactors, while globally reactors reaching 20 dpa are available [11]. To gain a 200 dpa dose at 400 °C, which is a typical dose in a fast reactor, would take 10 years after which a cooling period would be required. Therefore, research reactors at present cannot get sufficiently ahead of the operational reactors. Following cooling, neutron damaged materials are still radioactive requiring analysis in a “hot cell” making analysis even more challenging. For these reasons, several surrogate damage techniques have been developed, namely: thermal ageing, heavy ion irradiation/implantation and proton irradiation. The combination of beam-induced heating and sample heating is often used to mimic reactor-like conditions when ageing samples. However, a factor which is often overlooked is the combined effects of

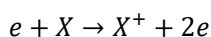
cyclic heating upon ion damaged microstructures; reactor-based materials damage is not incurred at a single time temperature and dose.

As described, neutron damaged materials are challenging to work with and infrequently produced. Neutron damage arises from impacting neutrons removing electrons from the shells of the target atom. The damage incurred from these interactions is often simulated by ion damage experiments; despite this, nuclear testing is the only option for materials validation.

2.2. Ion damage

Ion implantation has a wide range of applications for research and industry. Ion implanters are commonly used for focus ion beam microscopy, doping silicon wafers for electronics, specialist tool hardening techniques and the simulation of nuclear damage [19]. Grove is attributed with some of the first work on sputtering of surfaces [20]. Grove's work concerned "the electrolysis of gases" and showed that a thin silver layer (and other metals) exposed to ions would undergo "molecular disintegration", what today we refer to as sputtering [20]. His work and that of others led to ion implantation being researched more widely: notably in the early 1960s, Harwell laboratory, ran an important project focused on ion metal interactions [19], [21]. The driving force behind ion implantation research was primarily as an alternative to diffusion based doping techniques required for the development of silicon chips [21]. Despite this primary focus of implanter research on semiconductors, quickly it was identified by the Harwell researchers that ions could also be used to modify the properties of metals, and even improve corrosion or wear characteristics [21].

Ion accelerators have a wide range of scales, from focused ion beam microscopes which are the size of an SEM, to particle accelerators capable of producing hundreds of MeV. The production of positive ions can be created in a range of ways; most systems use photons, electrons or surface contact ionisation [22]. The basic process can be characterised by the Equation (1)[22]:



(1)[22]

Where X is the ionised element and e is an electron. For small ion sources, such as focused ion beam systems, gallium liquid metal ion sources are common; gallium has a low melting temperature thus it can be melted on a wire coil and accelerated from the coil in a tip using a

bias. For bigger ion sources and sources with a higher melting temperature or gaseous sources, this technique is not viable. To produce heavy ion beams a cathode filament technique/plasma source is commonly used, a schematic for a high current ion source is shown in Figure 6:

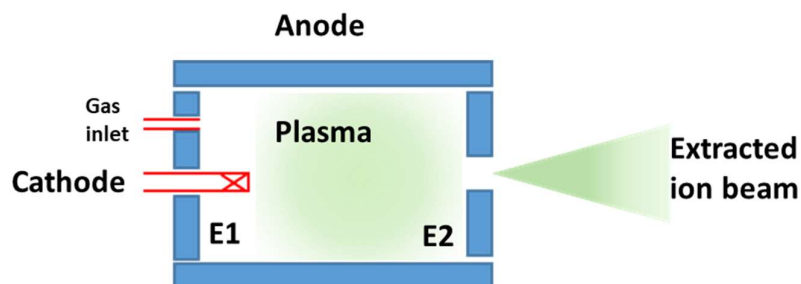


Figure 6 Schematic of a high current ion source of the cathode type [22].

In this source, a high current cathode is placed in an anode cylinder or cube. An extraction plate is placed opposite the cathode and used to extract the ions [22]. A plasma is struck in the cavity at a gas pressure of 10^{-10} to 10^{-3} torr [22]. Magnets are used to control the ions and limit them from colliding with the chamber sides thus limiting contamination. Rather than using high electrical current, microwaves and radio waves can also be utilised to excite the gas [22].

Once struck, plasma sources are directed through a slit or aperture at which point they are guided through optics of a similar type to those used in electron guns [22]. The plasma or beam of ions are accelerated, typically using 3-4 electrodes. In both 3 and 4 electrode systems the principle is the same; one beam forming electrode defines the potential of the plasma boundary while a suppressor electrode stops electrons from backstreaming into the plasma [22]. Once the ion plasma is produced, electromagnetic or electrostatic lenses are used to focus the beam of ions. In the case of MeV energy beams, electrostatic lenses are too weak to focus the beam, therefore, apertures are used to control the beam current [23]. In ion implanters decontamination of the beam is required to ensure that only the intended elemental species is implanted. Impurities can be included in the ion beam from the ion source chamber, sputtered material from the beamline interior and differing charge states of the ion of interest. Removal of contamination is often conducted with the use of a large 90° separation magnet. Following this, the beam can be accelerated further.

When an ion beam is incident on the sample, dependent on the beam energy ion size and sample properties, a range of interactions occur as shown in **Figure 7**. These interactions can

be divided into elastic and inelastic interactions. For ion implantation it is the implanted ion, its depth and distribution which is of interest. A succinct description of the ion implantation process is “the energy transfer from the incident particle to an atom resulting in mass or energy transfer back to the surface” [24]. The energy transferred back to the surface is used in the focused ion beam (FIB) where secondary electron yield can be used to form images and sputtering can be used for material removal. In secondary ion mass spectroscopy (SIMS), ion yield is used to determine the chemical composition of materials.

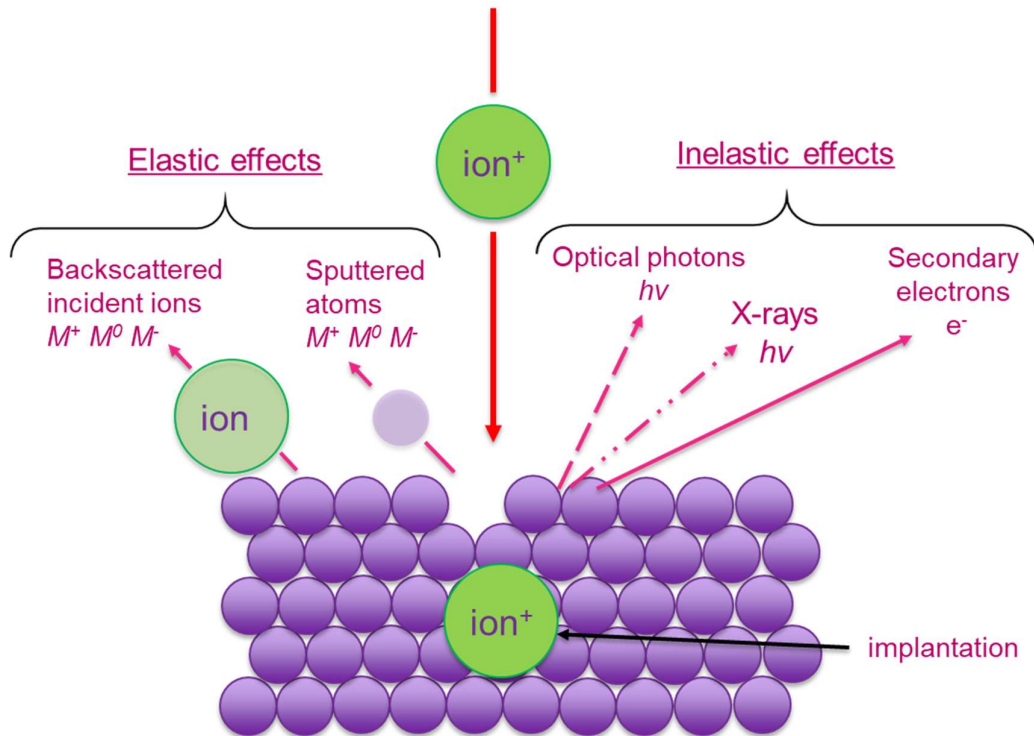


Figure 7 Schematic diagram of Ion-surface interactions showing both elastic and inelastic interactions, adapted from [24].

These interactions between the ion and surface have numerous effects on the microstructure of the ion implanted zone. An example microstructure following ion implantation is shown in Figure 8:

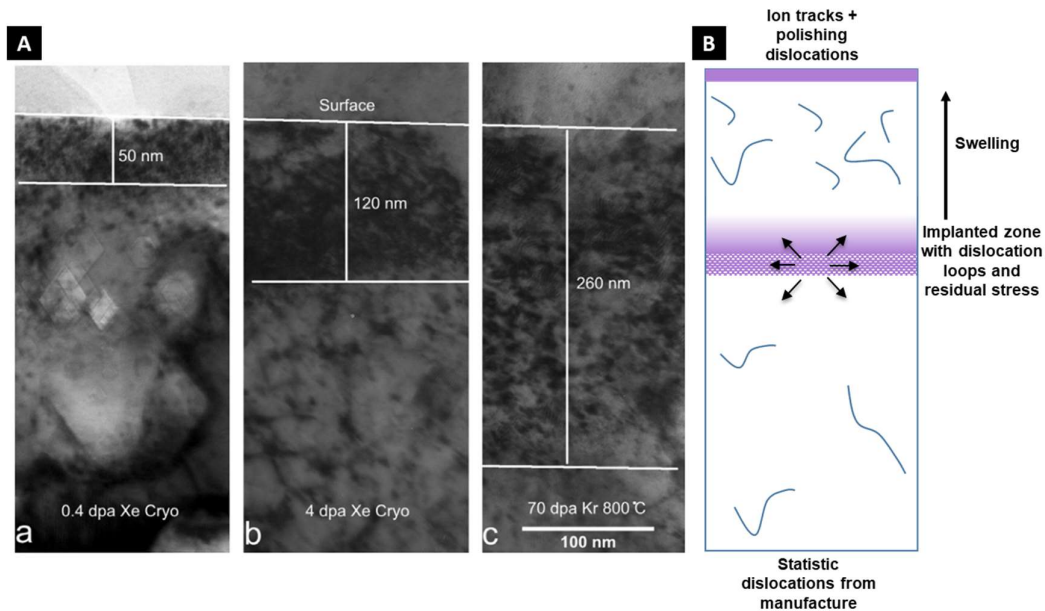


Figure 8 A Bright field TEM images from Xe^+ and Kr^+ ion implanted ZrN samples at a range of dpa's and temperatures, B schematic diagram showing typical ion implanted microstructure of ZrN [25].

From the surface to the substrate the most common features are ion tracks, dislocations implanted ions, swelling and residual stress. These features are induced in the material with a magnitude dependent on the ion species, accelerating voltage, fluence and dose.

Returning to the ion-surface interaction, first we will consider the path of the ion incident on the surface. Incident ions are backscattered or implanted; in the case of implantation the ion loses energy in the solid and is trapped in the solid as an interstitial atom [24]. There are two primary reactions between the lattice and the ion. The first is interaction with the substrate electrons leading to the emission of secondary electrons, optical photons and characteristic x-rays as shown in Figure 7. Electrons from both the substrate and incident ion can be excited to emit these forms of radiation; these inelastic effects are well known and understood in particle physics. The second interaction with the lattice is the implantation of the incident ion resulting in point defects. Further to this, ions with sufficient energy impact atoms causing the energy to be transferred back to the surface, resulting in erosion of the target through sputtering [24]. Numerous models have been developed to characterise the slowing of incident ions and the effects of ion energy transfer to the target lattice. The collisions are broken into two categories: electronic and nuclear [24]. To start the interaction of the fast ion with the lattice electron results in excitation and ionisation; this is considered an inelastic process [24]. The density of electrons is sufficiently high in the surface to result in a

continuous energy loss for the ion [24]. Models for continuous energy loss have been presented by Lindhard and Scharff (1961 and 1963) and by Whaling (1958) [24], [26]. Nuclear loss which occurs when incident ions and lattice atoms collide have been found to be more complex to model. Due to their low frequency, they are described by two body collisions where conservation of energy and momentum apply [24]. Different models are used depending on the energy of the ion. At high energies, Rutherford scattering models are used while at medium energies, Coulomb scattering models are used. At lower energies the Kinchin and Peses, 1955 model is typically used [24]. The Kinchin and Peses model is frequently recommended for stopping range of ions in matter (SRIM) simulations (see section 2.2.1) With regard to understanding ion damage of materials, it is implantation and sputtering which are most relevant.

Sputtering is an important process to consider during ion implantation. Early sputtering experiments demonstrated that sputtered material from ion bombardment is composed of uncharged atomic particles, and early theories suggested that ion irradiation caused a thermal spike; this thermal change was shown by calculating the ejected atom velocities [27]. The speed of the atoms was subsequently related to their temperature.

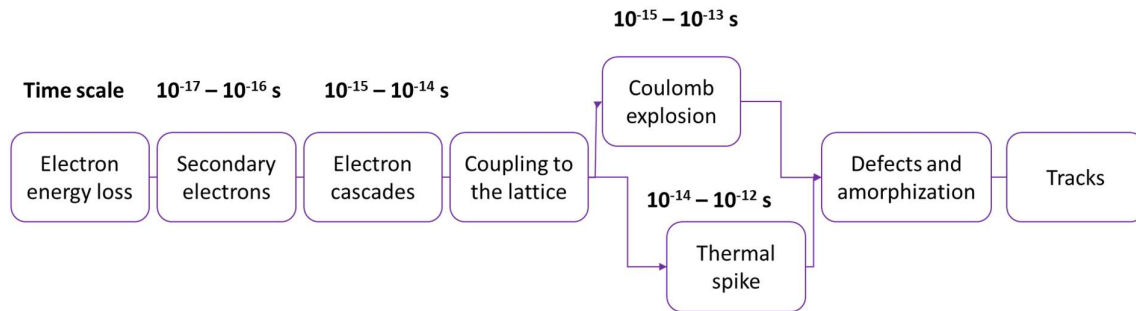


Figure 9 A time-based model for ion-surface interaction adapted from [28].

Despite the thermal spike not contributing to the ejection of atoms, there is a thermal spike which leads to the creation of ion tracks. Both experimental data and molecular dynamic modelling supports this [28], [29]. Historically there has been competition between the thermal spike and Coulomb explosion theories [29]. The consensus is moving towards the thermal spike and Coulomb explosion models being linked rather than discrete [28], [29]. Ion tracks are another feature of swift heavy ion irradiation, typically occurring in the MeV to GeV implantation ranges [30]. These are observed as nanometre diameter holes of the order of 10 s nm into the surface of the implanted substrate [30]. In-plane transmission electron microscope (TEM) lift outs are used to image these tracks' cross sections, whereby the tracks

can be observed in cross-section TEM images as band-like structures. The formation of ion tracks is proposed to be caused by the high energy, short contact time and small interaction volume of impinging ions on sample surfaces [30]. This rapid energy deposition within a small cylindrical volume leads to the ion tracks [31]. A proposed timeline for the formation of these track structures is shown in (Figure 9). These tracks often comprise of core-shell structures where the centre of the track has been amorphized and the exterior of the track is comprised of defects / disordered zone [30]. Track size and morphology are, however, dependent on the chemical composition of the material, the ion species, accelerating voltage and irradiation temperature [30].

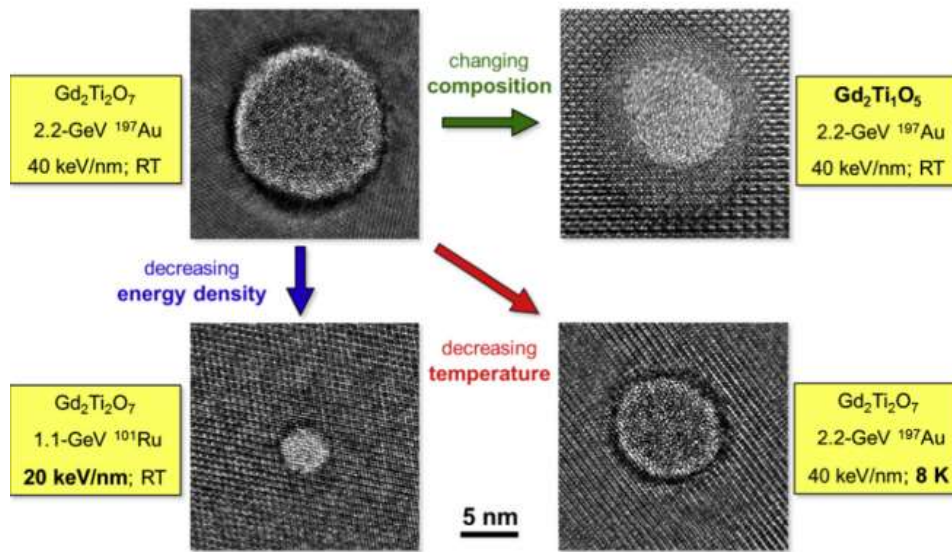


Figure 10 HR-TEM images of ion tracks under various irradiation conditions in the in-plane orientation showing the variation in track morphology based on chemical composition, beam energy density and implantation temperature [30].

There is some contention as to the mechanism behind the formation of the tracks. The proposed models both rely on the thermal spike based theory but differ in the formation of the tracks [32]. One proposed model suggests melting occurs forming a track. The other model relies on the development of defects around the track resulting in the formation of a track through collapse or rather the coalescing of the accumulated defects. The diagrams for these two models can be seen in (Figure 11) [32]:

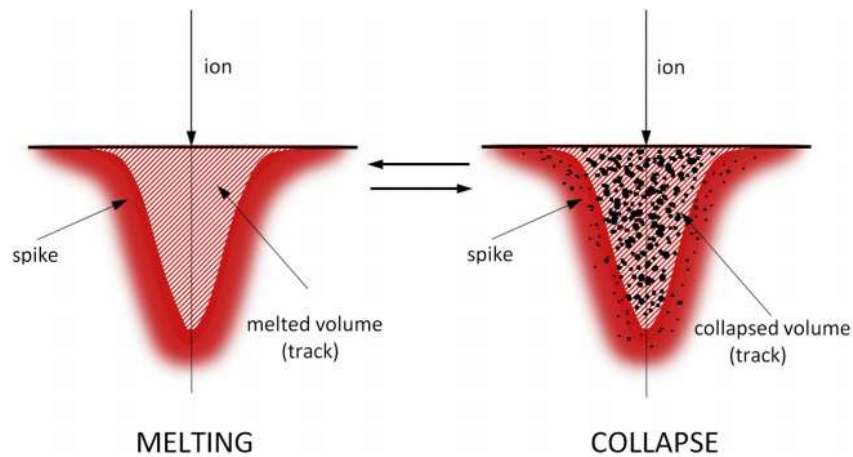


Figure 11 Two potential mechanisms for ion track formation based on melting and defect accumulation resulting in collapse [32].

Both models are a plausible system for the formation of ion tracks, and the material system may, in fact, determine which model best describes the track formation process. In Figure 8, these track features would be identifiable (if present) on the top few tens of nm. Below the ion track layer, a layer of dislocations and an implanted zone are typically observed; this layer is indicated in (Figure 8 a-c).

The characterisation of the strain below ion damaged surfaces has been approached in numerous ways. The techniques used to characterise the residual stress can be separated into mechanical and diffraction-based techniques. Indentation is a technique which has been used to determine the residual stress below ion damaged/implanted surfaces. Two indentation factors have been used: change in hardness and change in fracture toughness. Mc Hargue *et al.* applied a K_{Ic} based model presented by Lawn *et al.* to determine the residual stress induced following chromium and iron implantation in alumina single crystals [33]. It was found that ion implantation caused an increase in fracture strength up to a maximum fluence, with the peak fluence being different for iron and chromium systems. Mc Hargue concluded that compressive residual stress was imposed with a magnitude of around 1.1 GPa [33]. Further to indentation, macro scale bend testing was used by implanting the tensile face of the ten beams and four-point bend testing them. The identified residual compressive stress resulted in increased fracture strength. In the high energy implantation regime these increases were from 30-50% [33]. Despite the methodical and robust approach taken, the assumptions surrounding the indentation model limit the accuracy of the data. The ability to apply the indentation model presented to polycrystalline materials may be limited without a significant

number of indentations as the orientation relative to the crystal plane will have a large effect on the measured fracture toughness.

Wang *et al.* also used an instrumented indentation based approach to determine the residual stress caused by iron self-implantation in iron [34]. The premise of their paper is that compressive stress will result in an increase in hardness while tensile stress will result in a reduction in hardness. Following 3 MeV Fe²⁺ ions at a dose of 3×10¹⁶ cm⁻² the residual compressive stress was found to be in the order of 0.6 GPa [34]. Weng *et al.* used a similar experimental methodology to deduce the residual stress within CrN films implanted with carbon ions up to a dose of 2×10¹⁷ cm⁻², resulting in a residual compressive stress of 3.1 GPa [35]. In both cases, the link between residual stress and hardness is assumed to be linear and neglects the pinning effects of dislocations and indentation size effect.

The mechanical based techniques presented do not reveal the structure/ distribution of the stress field induced by ion implantation. Despite this limitation, in both cases, the stress state of the material is unperturbed by sectioning. For the electron and spectroscopy techniques based analysis, typically sectioning is required. Raman spectroscopy and XRD can provide surface strain values without sectioning but cannot determine the strain distribution below a surface. Very little research has been conducted on residual strain mapping in ceramics following implantation.

2.2.1. Ion beam simulation

The prediction of energy loss properties of ionising radiation in materials is essential to many areas of science, healthcare, technology and especially to the nuclear industry. To this end, a range of computer simulation packages have been developed (EDEP-1 and subsequently SRIM). These programs allow the calculation of the distance travelled by the incident particle as its energy is reduced to thermal energy (often referred to as range). The continuous-slow-down-approximation (CSDA) range can be used where there is little range variance (called straggle).

SRIM is a group of programs which calculate the stopping and range of ions (up to 2 GeV/amu) into matter using a quantum mechanical treatment of ion-atom collisions (assuming a moving atom as an "ion", and all target atoms as "atoms"). This calculation is made very efficient by the use of statistical algorithms which allow the ion to make jumps

between calculated collisions, and then to average the collision results over the intervening gap [36]. During the collisions, the ion and atom have a screened Coulomb collision, including exchange and correlation interactions between the overlapping electron shells [36]. The ion has long-range interactions creating electron excitations and plasmons within the target. These are described by including a description of the target's collective electronic structure and interatomic bond structure when the calculation is set up (tables of nominal values are supplied in the program) [36]. The charge state of the ion within the target is described using the concept of effective charge, which includes a velocity dependent charge state and long-range screening due to the collective electron sea of the target [36].

The most common measure of radiation damage in the literature is displacements per atom (dpa). Dpa can be calculated from SRIM simulation results based on the ion beam flux (ions/s.cm²), the displacements per ion per unit length (vacancies per ion per angstrom) and the atomic density of the material (atoms/cm³), as shown in Equation (2).

$$dpa/s = \frac{flux \times displacements}{atomic\ density} \quad (2)$$

Examining equation (2), it is apparent that materials of a higher density will result in lower dpa levels, and that the same dose will not result in the same dpa for each material. Despite the ubiquitous nature of SRIM calculations for dpa measurements, Nordlund *et al.* reported on a number of issues surrounding this approach [37]. The main issue identified are the need for clarity in reporting the simulation parameters as these have a significant effect on the repeatability of results [37]. Further to this, what constitutes a displacement becomes ambiguous as there are two forms of energy deposition which are separated in the calculations, “energy to recoils” and “phonons”[37]. However, most publications do not identify which has been used / if the sum has been used etc. Finally, the lack of ability in many cases to check if the dpa values are correct using another simulation is not achievable. Nordlund *et al.* uses an example of 10 keV Si ions implanted into silicon and shows how the calculated dpa could range from 0.15 to 0.48 dpa for the same irradiation condition [37]. This variation in magnitude is problematic when comparing papers, but less pronounced when comparing experimental results from the same paper. SRIM simulations also ignore athermal damage recombination, channelling effects and the filtering effects of amorphous layers on ion damage [37].

However, despite criticisms of SRIM simulations, they seem the most accessible technique for materials scientists to quantify radiation damage. Furthermore, SRIM is based on reasonable physical models which have been shown to be accurate for some materials systems.

2.2.2. Ion damage as a surrogate for nuclear damage

There are differences between ion beam and neutron damage because fundamentally the size and charge of the ions are different from that of neutrons. In nuclear damage, a neutron i.e. with a neutral charge and an atomic mass of 1 amu (atomic mass number) is incident on the surface. During gold ion irradiation the surface is bombarded with ions of a positive charge and mass of 195.96 amu. The atomic mass of each neutron and proton is around 1 amu, whereas the atomic mass of a single gold atom is the addition of its 118 neutrons and 79 protons/electrons. An ion has one less electron thus $\approx 196.96 - 1 = 195.96$ with some mass difference for binding. Thus, the key variance is that the ion has a far greater mass and is positively charged. This leads to critical differences: ion damage is shorter in range as the atomic interaction is more significant between the large ion and the surface, sputtering is more pronounced as the positively charged particle ejects/sputters more of the surface, and no helium inclusions are produced.

Ion implantation can be conducted in a more controlled manner than radiation damage, with options for selective heating and dose regimes. New research is ongoing in this area. Was *et al.* proposed an experimental procedure for accurately recreating neutron damage in Ht9 (Fe-12Cr-1Mo) steel [11]. The procedure used a heat treatment followed by a multi-energy helium ion implantation step and a subsequent elevated temperature (460 °C) ion implantation phase with Fe²⁺ [11]. SRIM was then used to calculate the implantation depth of the two steps to simulate the damage region of interest for TEM analysis [11]. Using this multi-stage approach the microstructural features in the ion irradiated sample matched those produced during reactor irradiation, as can be seen in (Figure 12) [11]. Developing and validating experimental techniques such as these seems a sensible research route. Much of the work in this field has been focused on metals; comparable work in ceramics would provide additional confidence to the development of ceramic replacement component designs.

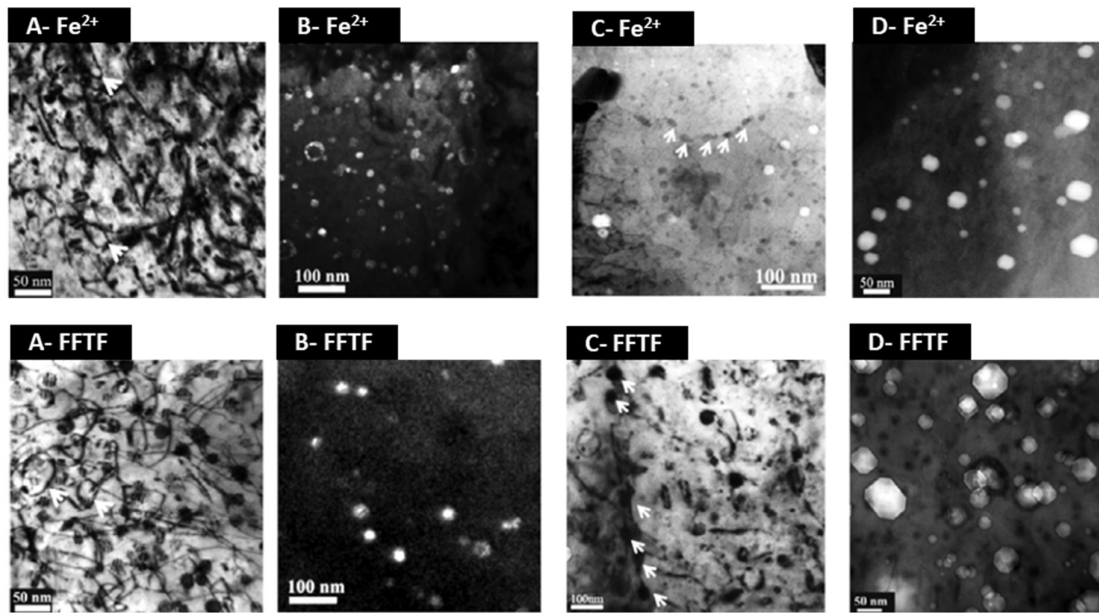


Figure 12 Comparison of irradiation microstructure in Ht9 following Fe^{2+} irradiation (460 °C:155 dpa, top images) and following reactor irradiation in FFTF (443 °C:155 dpa, bottom images): (A) bright field TEM images of line dislocations and loops, (B) dark field TEM images of *g*- phase precipitates in the matrix, (C) bright field images of *g*-phase precipitates along grain boundaries and (D) voids.

There are useful ‘rules of thumb’ in the literature suggesting that matching temperature, dose, using self-implantation and helium implantation result in microstructural features very close to neutron irradiation [11], [38]. Despite these improvements in experimental design and understanding, as outlined in ASTM E 521 – 96 “Standard Practice for Neutron Radiation Damage Simulation by Charged-Particle irradiation”, ion implantation can still only be used for research and not for material validation [39]. The key reason outlined by the ASTM committee was the rate of damage. No comprehensive scaling factor has been determined to link implantation temperature with reactor temperature and implantation rate [39]. As such it is widely considered that ion implantation studies are complementary to neutron irradiation experiments [40].

2.2.3. Summary

The production of ions and their interactions with matter has been outlined, with detail provided regarding the key microstructural features caused by ion-surface interactions. Typical effects of ion damage are ion tracks, dislocations and defects, along with swelling and an implanted zone consisting of the ion species. Ion implantation typically results in a residual compressive stress field of 0.6-3.0 GPa dependent on the material system, analysis

technique and implantation condition. Further to this, the simulation package SRIM has been reviewed with regard to its fundamental principles and uses.

Nuclear damage was shown to be dependent on dose and temperature. Higher doses resulted in higher defect levels. Nuclear damage exhibited defects which are not observed during ion implantation, and of these the lack of transmutation products such as helium is a key difference.

With the correct experimental design, ion damage is analogous to nuclear damage, which can be and has frequently been used to start to understand nuclear damage in materials, primarily because ion damage samples can be obtained promptly and are safer to work with than neutron irradiated samples. The validity of ion implantation as a surrogate for nuclear damage has been reviewed. It was found that despite ion damage producing comparable microstructural features, ion damage is not appropriate for nuclear material validation. This is due to the lack of a comprehensive scaling factor linking implantation temperature with reactor temperature and implantation rate [34]. However, ion implantation is still a first step / complementary step for material selection before test reactor exposure.

2.3. Micromechanical testing

2.3.1. Introduction

In the pursuit of greater levels of understanding and accuracy in materials characterisation, micromechanical testing has become a prevalent area of research. Since the 1920s materials scientists have been studying mechanical properties at smaller and smaller length scales [41]. By the late 2000s a greater body of research began to develop in part due to improved accessibility, capability and usability of Focused Ion Beams (FIBs), Scanning Electron Microscopes (SEMs) and Transmission Electron Microscopes (TEM). By 2011 a British standard was developed for the testing of materials used in micro electrical, mechanical systems: “BS EN 62047-10:2011”[42]. The release of this standard marks a point at which we can suggest that micromechanical testing is developing maturity as a characterisation technique.

Two main areas of research have driven the development of micromechanical testing: firstly, the production, and commercialisation of micro- and nano-electro-mechanical systems (MEMS/NEMS); secondly, the increasing requirement for higher accuracy measurements of materials properties at specific microstructural features [41]. Micromechanical testing is well suited to the accurate characterisation of the effects of specific environmental damage on materials such as is observed in nuclear reactor materials. The effects of small-scale nuclear damage on materials properties can be used to develop more precise models for lifetime prediction of components and systems [43]. Often in new nuclear reactor design, materials validation is the bottleneck [44]. Nanoindentation is frequently used to assess the properties of irradiated materials: however, the extraction of strength data from the irradiated surface sample can be challenging due to the complex stress/strain field below the indenter.

When identifying test techniques for nuclear materials, two safety principles of radiation work can be considered, which are the “as low as reasonably achievable (ALARA)” principle where the lowest radiation level materials should be tested to validate materials properties to reduce risk [35]. The second safety principle is the “time-distance-shielding (T-D-S)” principal where the minimum exposure time and maximum distance from the researcher are used along with shielding between the operator and the sample to reduce risk [35].

Micromechanical testing can also introduce a volume factor to improve both of these safety matrices by reducing the volume of material used [35].

Reducing the gauge length of test specimens seems a simple solution to the nuclear test sample size problem. Based on classical mechanics, the mechanical properties of materials should remain independent of length scales. Despite this, Fleck *et al.* identified a size effect when copper wires of different diameters were subjected to tension and torsion testing [45], [46]: as the wire diameters decreased, their flow stress increased during torsional testing. Unlike the indentation size effect identified by indentation studies, a differential strain gradient could not be attributed to changes in wire thickness [46]. These findings were echoed in the first nanopillar indentation studies conducted by Greer *et al.* Two schools of thought explaining the size effect in gold were developed. One proposal is that the volume of material is sufficiently small to cause dislocation starvation. In the dislocation starvation model, dislocations annihilate at the free surfaces of the test piece rather than multiplying [46]. Annihilation caused an increased need for dislocation nucleation which in turn results in an increased level of plastic resistance [46]. The second model suggests that smaller sample sizes are stronger, based on an undefined plasticity mechanism which is yet to be understood

[46]. The first model of dislocation starvation has gained a more comprehensive body of proof through subsequent research by Greer, Nix and others [47].

Following the work of Fleck *et al.* on wire torsion, a wide range of sample geometries and mechanical properties have been measured at the microscale. Within the literature, compression, bend, tension and torsion testing have been widely studied at the micromechanical scale. From these tests flow curves, Young's modulus, Poisson's ratio, yield strength, fracture strength, hardness, and endurance limit can be determined [41], [48]. With regards to ceramics, quasi-static compression and bend testing are the most prominent areas of research, as such this review will focus on their design, fabrication, testing and post-testing analysis.

2.3.2. Sample preparation

A range of techniques have been used to produce micropillars. This study is focused on the production of ceramic micropillars specifically in silicon carbide and zirconium nitride. Silicon carbide ceramic pillars can be fabricated through FIB, etching and chemical vapour deposition (CVD) growth. Each pillar fabrication technique has the potential to leave relics of manufacture which unchecked are likely to perturb the collection of accurate results. Chemical vapour deposition has successfully been used by Liu *et al.* to produce nanowires of beta silicon carbide at a range of diameters from 50-100 nm [49]. These nanowires could be cut, and compression tested, but such work is currently speculative. For larger pillar sizes, polycarbosilane transfer moulding in micro Polydimethylsiloxane (PDMS) moulds can be used to create a wide variety of test specimen sizes on the micron scale [50]. Jang *et al.* successfully used this technique to create amorphous silicon carbide pillar arrays of $18 \times 2 \mu\text{m}$ [50].

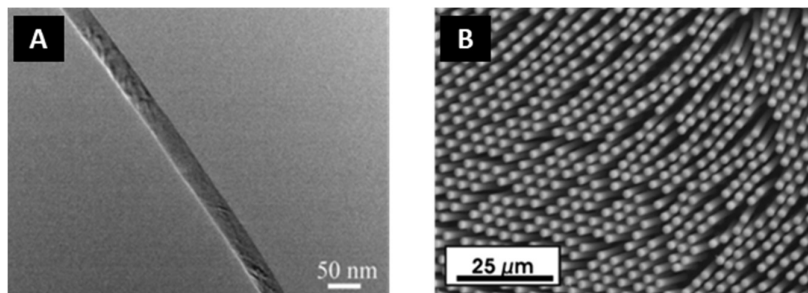


Figure 13 A- Nano silicon carbide wire [49]. B- Array of micropillars produced by polycarbosilane transfer moulding [50].

In Greer *et al.*'s, seminal work in the area of micropillar indentation both electrodeposition and FIB were used to produce gold micropillars [46]. Despite concluding that FIB fabrication produced comparable pillars to electrodeposited pillars, differences in the grain size achievable were apparent between the two techniques. Regardless of Greer's success with FIB manufacture of pillars, other researchers have identified inconsistencies in comparing differing sized FIB pillar samples, primarily in the nanometre scale [51]. Gallium ion damage in micromachined samples can result in additional dislocations, gallium ion implantation and amorphisation [51], [52]. Damage depths can be in the range of tens of nanometres dependent on the substrate and milling protocol used [51]. Shin *et al.* in 2009 concluded that FIB milling of pillars could cause significant variation in nanopillar strengths, making comparisons between pillar sizes complex [51]. Based on findings from his 2009 paper, Shin went on to develop an etching system for the fabrication of silicon carbide nanopillars [53]. Through etching and subsequent FIB refinement techniques, Shin provided a robust experimental technique which revealed useful results on the nature of SiC micropillar failure [53].

Numerous strategies to mitigate or identify the effects of ion beam damage have been developed. Laue diffraction on the microscale has been used to identify residual strain gradients in micropillars [51], [54]. However, the limitation of micro Laue diffraction is the requirement for high energy light sources making the technique inaccessible for many research institutes [55]. To reduce ion beam damage, mechanical annealing has been suggested by Kiener based on the work of Xie [48], [56]. Mechanical annealing consists of compressing and unloading nanopillars causing defects to annihilate at their surfaces [48], [56]. The validity of mechanical annealing to remove FIB induced damage is questionable, with limited evidence to date. The most accessible approach to limiting FIB induced damage is the use of optimised milling conditions and lower energy secondary milling to bring the pillar to its final shape [57]. Bei *et al.* devised a systematic nanoindentation experiment to assess the effects of ion beam conditions on hardness and modulus in molybdenum-alloy single crystals [58]. It was found that increased voltages caused hardening of the surface of the alloy. Greater accelerating voltages resulted in greater damage penetration depths and increased hardening as seen in **(Figure 14)**. Comparable indentation experiments would provide insight into the effect of ion beam conditions on ceramic micro sample fabrication.

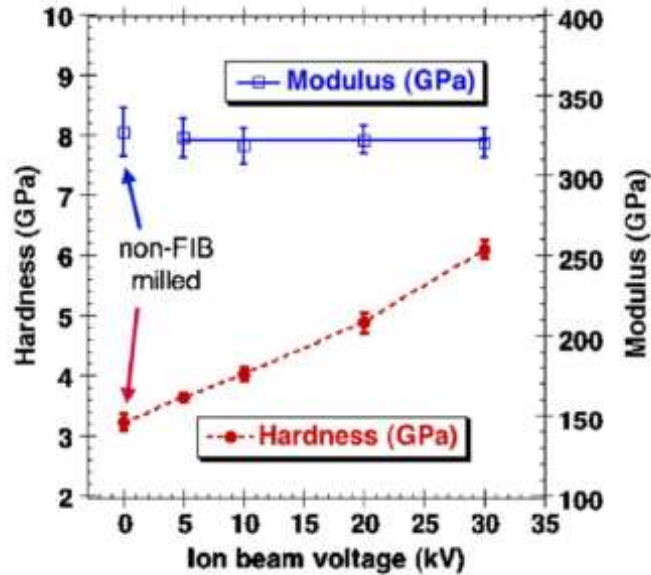


Figure 14 Plot of hardness and modulus of Mo-alloy single crystal at maximum applied load of 1.5 mN following gallium ion milling at a range of accelerating voltages (0-30 keV) [58].

The experimental design of the ion beam and indentation study conducted by Bei and Shim *et al.* exposed virgin metal surfaces to varying voltages. In real FIB milling protocols, a high accelerating voltage is required to complete milling in a timely manner and with reasonable imaging capabilities. Beyond voltage and current settings, the angle of the ion beam also affects the extent of damage and milling efficiency during sample fabrication. Inherently the change in hardness is related to the increase in defects in the lattice and induced residual strain. Korsunsk *et al.* conducted molecular dynamic simulations to recreate the residual stress induced in single crystal silicon caused by 30 keV Ga⁺ ion beam milling at 10° incident angle [59]. Korsunsk *et al.* reported that residual compressive stress of 500 MPa (max depth 8 nm) was introduced following low voltage cleaning (5 keV), as shown in (Figure 15 a) [59]. High keV cleaning (30 keV) resulted in tensile surface stress of 500 MPa (max depth 10 nm) and compressive subsurface stress of 500 MPa (max depth 30 nm) as shown in (Figure 15 b) [59]. These simulations in silicon are not directly transferable to ceramics as the bonding and ion penetration depths are significantly different.; however, this work does show how residual stress can be distributed following ion cleaning, and a plausible magnitude for residual stress caused by ion cleaning.

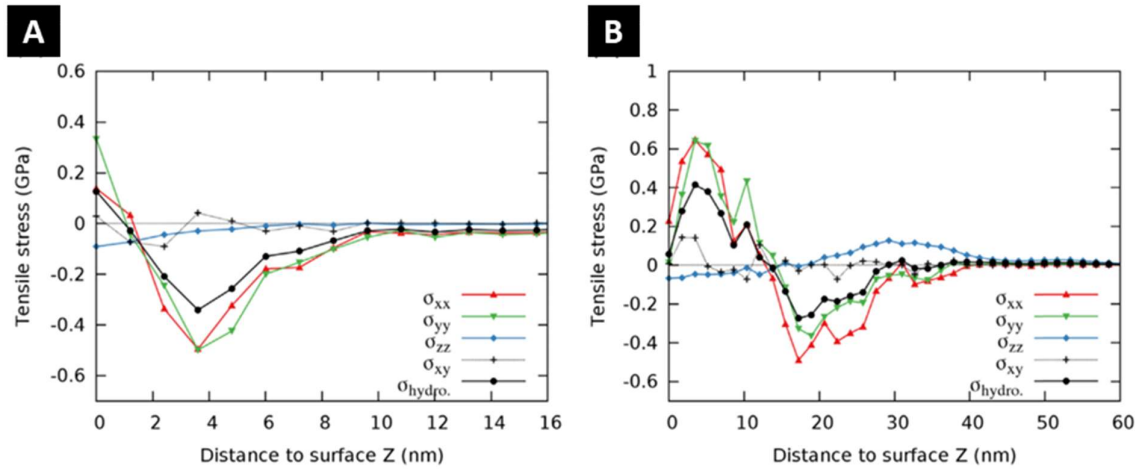


Figure 15 Residual stress profiles as a function of depth below the surface of ion beam cleaned silicon single crystal calculated by molecular dynamic modelling (MD) (a) 5 keV and (b) 30 keV.

Further to the induced residual stress, amorphisation is a frequently overlooked issue during FIB milling; amorphisation causes swelling of the milled substrate. This can cause overestimation of the cross-sectional area of test specimens [60]. Two techniques have been used to characterise the thickness of ion-induced amorphous layers: FIB cross-section followed by TEM analysis, and depth profile Auger electron spectroscopy (AES). The more accurate, albeit time-consuming, technique is FIB cross section, with TEM analysis [61]. Kelly *et al.* present a methodology for comparing the ion damage between samples prepared with gallium and xenon ions for TEM FIB lift-out samples [62]. Measurements of the amorphous layer created in silicon by a range of Ga^+ accelerating voltages are presented. Further research should be undertaken to investigate the magnitude and distribution of the ions implanted.

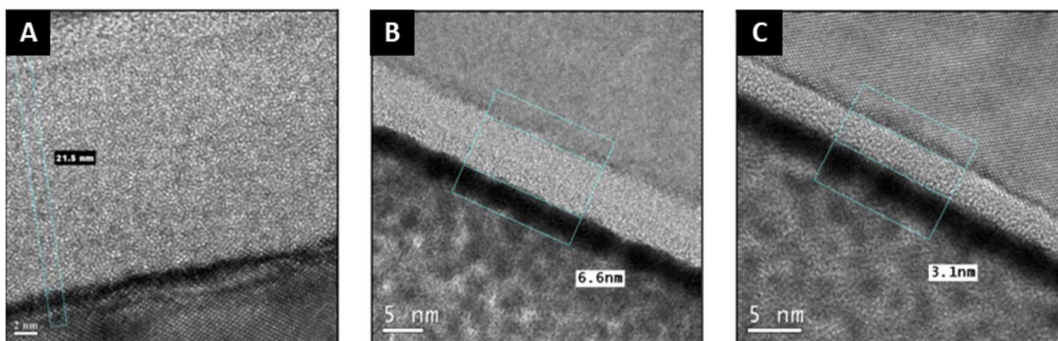


Figure 16 TEM images showing the amorphisation of silicon following A 30 keV beam, B 5 keV beam, C 2 keV gallium ion beam [62].

Kelly concludes that low voltage ion beam milling should be used to reduce sample damage. They also concluded that Xe⁺ milling can produce less damage than comparable Ga⁺ ion sources; however, while moving to Xe⁺ ion sources will reduce issues with amorphisation, it will not eliminate it. Auger electron spectroscopy (AES) was applied to ion-induced amorphisation in Zr-based metallic glasses by Lai *et al.* The depth of Ga⁺ ion signal was measured into the substrate by sputtering away the top surface; the depth of Ga⁺ was found to be 3-4 nm. Kinner *et al.* also applied AES to observe the damage depth and percentage of gallium deposited in copper [63]. It is worth noting that although AES may be convenient, the lack of ability to determine the crystal structure of the ion damaged surface is problematic when considering the effects of gallium ion damage on materials properties. Further to these options, secondary ion mass spectroscopy (SIMS) and depth-resolved micro x-ray fluorescence (μ -XRF) could plausibly be used to estimate the depth of implanted elements.

The differences in amorphisation, sputtering and implantation of materials of varying composition is complex. One common approach to estimating the effect of ions is the use of SRIM stopping range of ions in matter software [43], [51], [62]. (see section 2.2.1 Ion beam simulation, page number 21).

2.3.2.1. Design of microcantilever beams

For the purposes of this review, microcantilevers will be regarded as beams with cross sections from 200 nm to 10 μm . Particularly small “nano beams” often tested in the TEM have their own features which are beyond the scope of this review. Micromechanical bend testing of cantilever beams is unique as a test method for the testing of surface coatings in the absence of substrate effects. Fracture toughness of surface coatings is cited as a prime example of where microbeam testing characterisation provides more representative results than nanoindentation [64]. Further to this, microbeams offer a better-suited approach for the analysis of elastic properties, bend strength and the analysis of the effects of crystallographic orientation due to their small size [65].

Many of the issues associated with focused ion beam (FIB) fabrication of micropillar test specimens hold true for the fabrication of microbeams. There are two commonly used micro bend test configurations used in the literature, micro-cantilever and three-point bend. First, the microcantilever style preparation will be discussed; the FIB technique used for the milling of microcantilevers is comparable to that of a typical TEM sample preparation, see (Figure 17) . In the FIB the user selects a region of interest and mills two connected parallel trenches. The U-shaped trenches are joined to each other by milling the sample at an angle of 30° [65]. Care must be taken to remove any redeposited material following the heavy initial milling stages [65].

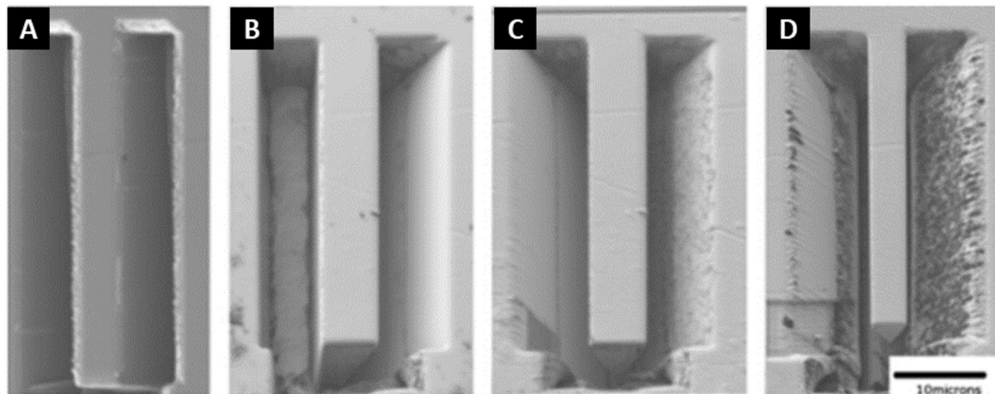


Figure 17 Microbeam fabrication in the FIB, (A) U-milling (B-C) angled milling (D) removal of redeposited material [65].

Despite the ease of microbeam fabrication by U-shaped milling, other geometries have been developed within the literature [66]. As seen in Figure 19, alternative fabrication techniques can be advantageous for imaging of the fracture point of beams.

Corner-based cutting techniques were developed by Dong *et al.* to produce cantilevers where a direct line of sight from the indenter to the beam and electron beam was required; see (Figure 18). Dong used an angled milling technique to cut the beams without the need to vent the chamber between cuts.

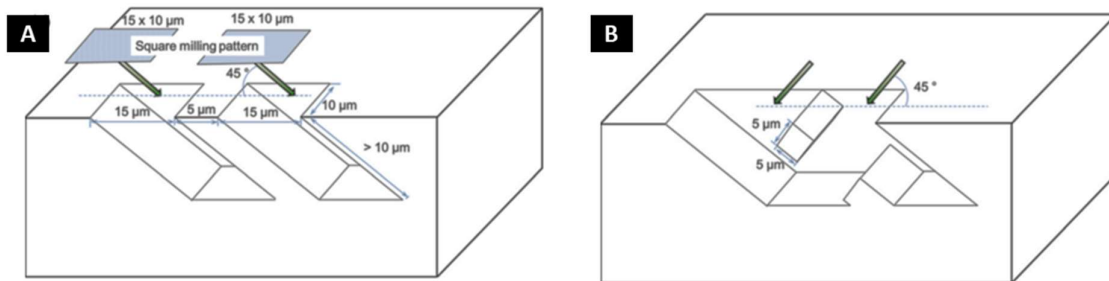


Figure 18 The parallel milling technique developed by Dong *et al.* which allows beam cutting with stage tilts and rotations rather than removing and reorienting the sample. Dong's method also allows for square cross-section cantilevers to be produced [67].

Limiting the need to open the chamber can reduce the likelihood of developing oxide scales on the test sample. For reactive metals (copper, aluminium), for instance, oxide layers could have a significant effect on tests specimens with small cross sections [63]. As shown in (Figure 19 B), true three-point bend test conditions can be recreated at the microscale.

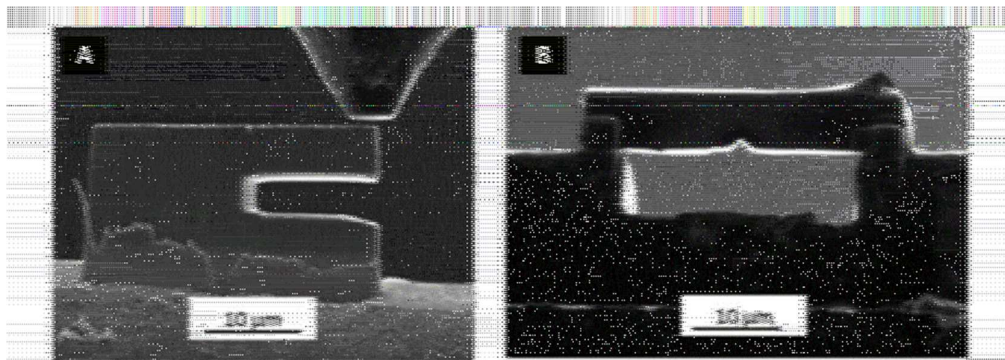


Figure 19 (A) lift out cantilever, (B) notched bend test sample [66].

The three-point bend style test can be conducted by isolating a lamellar of material, welding the lamellar to a needle and undercutting the lamellar to produce a beam [68]. This beam can then be transferred to pre-prepared mounting anvils [68]. A clear advantage of microcantilever or three-point bend testing over pillar compression testing is the ability to test

specific microstructural artefacts. One such technique is to manufacture the beam and notch across a grain boundary. The milling of beams across grain boundaries allows the testing of grain boundary strength. Recent work in 2018 has coupled the sample geometry shown in Figure 19 b with EBSD to provide grain orientation data, grain misorientation (a residual stress indicator) and grain boundary location in the specimen [68].

2.3.2.2. Testing and analysis

During micromechanical testing it is typical that a load-displacement plot is produced. Loading is commonly undertaken by a nanoindenter fitted with a flat diamond indenter or a custom-made nanoindenter like device. Flat indenters reduce the friction and damage caused by sharp indenters during loading of the specimen. In-situ probes have been developed and are commercially available for use inside SEM chambers. In-situ testing permits the use of the electron beam to track the sample under loading, whereby a selectively deposited matrices of dots can be used to compute the strain and sink in of pillars [69]. Load-displacement plots remain the most commonly used technique. With regard to bend testing, atomic force microscopy (AFM) provides a useful technique for locating samples in preparation for alignment of a nanoindenter [63], [65].

In the literature, graphical representations of the loading of pillars typically take two forms: load-displacement curves and stress-strain curves, (see Figure 20). Plotting data from differing sized pillars on the same scale assists with interpretation of the results. Figure 20 shows the transition from normal compressive behaviour to plastic deformation at the small scale, accompanied with a sample size effect where small samples are stronger [53].

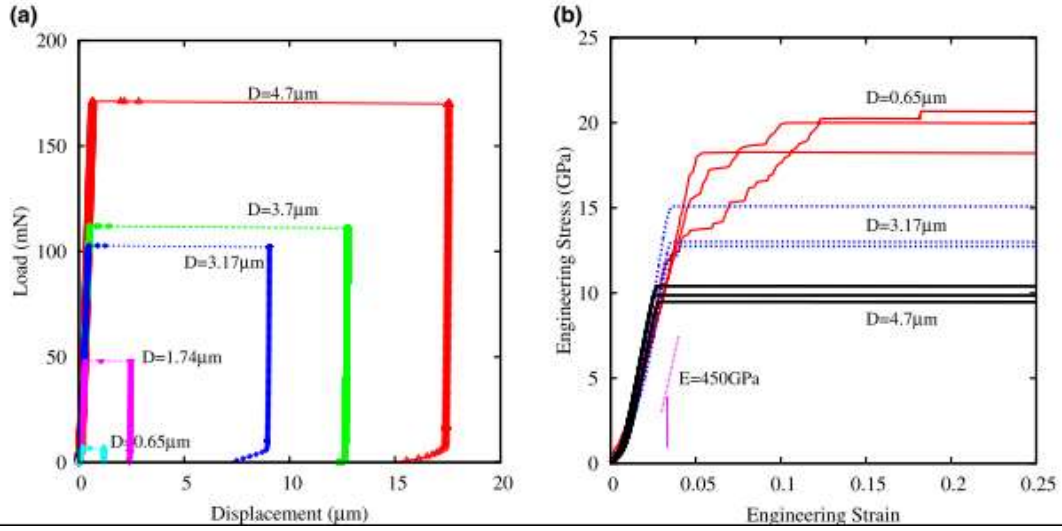


Figure 20 Load-displacement curves and engineering strain curves of 3C SiC micropillars in compression [53].

The calculation of stress and strain in micro compression testing is the same as conventional compression testing [42]:

$$\sigma = \frac{P}{A} \quad (3)$$

where σ = stress (GPa), A = area (m), P =load (N) and

$$\varepsilon = \frac{\Delta l}{l} \quad (4)$$

where ε = strain, Δl = indentation depth and l = pillar high (m).

$$E = \frac{\sigma}{\varepsilon} \quad (5)$$

where E = Young's modulus (GPa).

For pillars in which significant sink in is experienced, Sneddon's equation for the indentation of a flat punch into an infinite half space is frequently used [69]. Shin *et al.* expanded Sneddon's equation to cater for pillars which have a tapered shape, thus improving the accuracy of the calculation for micromechanical testing (see Equation (6)[43]:

$$h_{corrected} = h_{measured} - \frac{1 - \nu^2}{E} \left(\frac{P_{measured}}{D_{bottom}} \right) - \frac{1 - \nu_i^2}{E_i} \left(\frac{P_{measured}}{D_{top}} \right)$$

Where load and displacements are denoted as P_{measured} and h_{measured} , E = Pillar Young's modulus, ν = Pillar Poissons ratio and E_i = diamond indenter Young's modulus, ν_i = diamond Poisson's ratio [43].

Key to understanding load indentation curves and stress-strain curves is the analysis of the pillar post-testing. Through observation of the pillars following indentation, slip bands are often identifiable under SEM conditions. Excluding the use of EBSD and electron channelling contrast imaging (ECCI), SEM primarily offers topographical contrast and has a limited ability to quantify dislocations. With the use of platinum resists, whole pillars can be encapsulated, and FIB prepared for TEM analysis [43], [53]. Within the TEM, analysis of the plane orientation and dislocations can be undertaken, and therefore the quantity and slip plane of dislocations can be estimated. Schmid's law suggests that the slip plane, which can resolve the maximum shear stress, will activate preferentially [70]. However, based on SEM observations of body-centred cubic (BCC) metals (of a known orientation) and modelling, it has been identified that Schmid's law can become invalid at the small scale [70]. BCC pillars were found to fail in favour of the plane which offered the lowest resistance to dislocation nucleation [70]. In hexagonal close-packed (HCP) ceramics, limited research has been conducted into the conformance of failure mode to Schmid's law.

Ultimately, loading causes failure of the pillar. Post indentation analysis can take the form of debris analysis for fractured or deformed pillars [53]. Fracture debris of sufficiently small thicknesses can be placed on copper grids for TEM analysis.

Much like micropillar testing, microcantilever testing produces load displacement plots. From these plots and careful measurement of the cross-sectional dimensions of the cantilevers Young's modulus can be calculated [71]:

$$E = \frac{PL^3}{3\Delta I}$$

(7)[71]

where P is the load, L is the length between the indenter and root of the beam, Δ is the beam deflection, I is the second moment of area which is dependent on the cross-section of the beam. For a rectangular cross section second moment of area[71]:

$$I = \frac{bh^3}{12}$$

(8)[71]

Where b is the beam breadth, h is the beam height. Further to determining Young's modulus, using the peak load at fracture, the failure stress of materials can be calculated [71]:

$$\sigma_f = \frac{PL}{z}$$

(9) [71]

where σ_f is fracture stress, P is peak load, L is the beam length between loading point and fracture point and z is the moment of inertia of the beam cross section [71]:

$$z = \frac{bh^2}{6}$$

(10) [71]

One of the advantages identified by Armstrong *et al.* while testing long U pillars is the ability to tests at multiple points along the length of the beam. In the paper "Measuring anisotropy in Young's modulus of copper using microcantilever testing" Armstrong *et al.* generated hysteresis curves for bending at different beam lengths [65]. To use this multi-point bend testing method the beam must not be stressed beyond the elastic limit. Dependent on the beam size and dislocation distribution, the repeat testing may have caused mechanical annealing of the bars. The evidence for mechanical annealing caused by repeat loading may be represented in the data whereby the multiple loading moduli was shown to be lower than that of the single loading modulus. This interpretation of the results is, however, overlooked in Armstrong's discussion.

The mechanics and loading that underpin bend testing and micropillar testing are distinctly different. However Moser *et al.* provided pertinent information relating the volume of silicon microbeam and pillar samples to strength [69]. They proposed that the volume of sample irrespective of loading condition (bend or compression) results in a comparative level of strengthening [69].

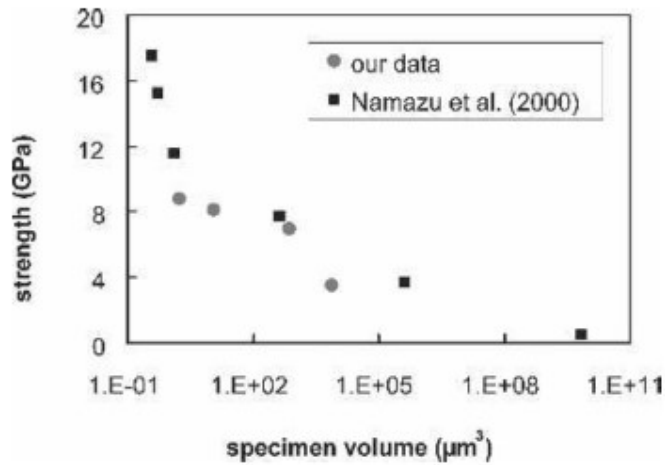


Figure 21 B. Moser *et al*'s proposed a relationship between sample volume and strength of silicon pillars [69].

From (Figure 21) a trend looks to exist between the data produced by Moser and that produced by Namazu. Based on dislocation starvation theory, the likelihood of dislocations within the volume of material tested and their ability to annihilate is controlled by the surface area and volume of the material.

2.3.3. Size effect and plasticity

Thinking of polycrystalline samples, when grain size moves from the mm to μm scale, we would expect to see a change in mechanical properties based on the effects of grain size relative to sample size. In large samples, this change in mechanical properties is referred to as the “Hall Petch relationship.” Typically, the Hall Petch relationship is exhibited when grain size is reduced and yield strength increases due to dislocation grain boundary interactions increasing [72]. Grain boundaries act as obstacles hindering dislocation glide along slip planes. As dislocation numbers increase they become piled up at grain boundaries causing a strengthening effect. The Hall Petch relationship is described by Equation (11) below, and plotted in (Figure 22) [72].

$$\sigma_y = \sigma_i + Kd^{-1/2} \quad (11)$$

where σ_y is the tensile yield stress, σ_i is the intrinsic yield stress of the grain (lattice yield stress), K is a material dependent constant and d is the grain diameter (Figure 22) shows the

formula calculated hardness increases with reducing grain size and the observed relationship which show hardness increases with reducing grain size up to critical diameter (d_c). Once the critical diameter is reached, smaller grains result in lower hardness values.

In the case of reducing the sample size in polycrystalline mechanical test samples, a “smaller is softer” relationship is well documented where the Hall Petch relationship no longer holds as the number of grains relative to the sample thickness becomes small, as shown in Figure 22:

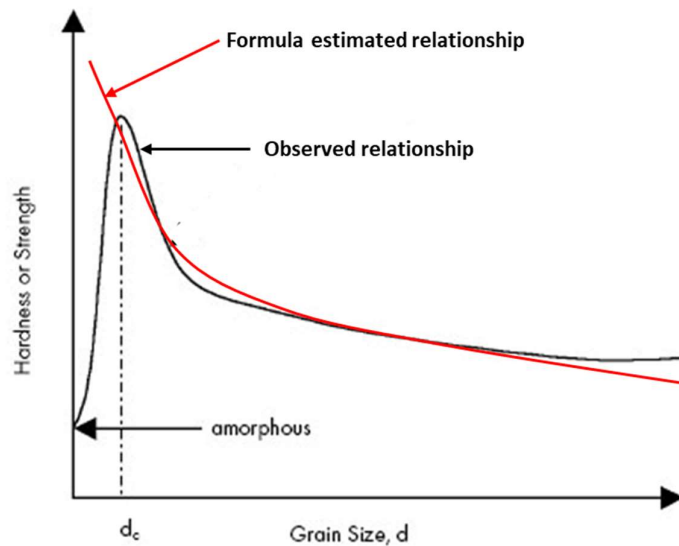


Figure 22 Plot of Hall Petch relationship between grain size and hardness, showing the observed and calculated hardness grain size relationship. Adapted from [73].

For FCC materials literature, values of sample thickness to grain diameter between 3-15 are suggested to perform in a poly/multi crystalline manner. When specimen thickness to grain diameter tends to one, the performance of the sample is that of a quasi-single crystal. How this Hall-Petch relationship relates to irradiated and un irradiated samples is critical for understanding how micromechanical test results scale to full size components.

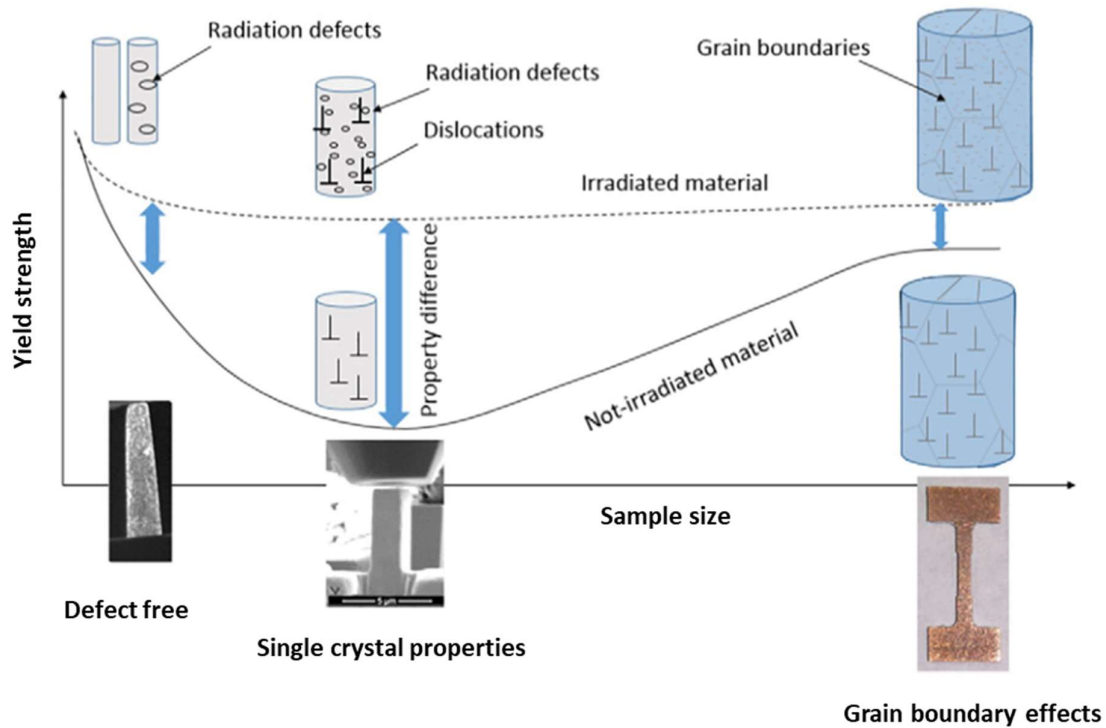


Figure 23 proposed size effect of irradiated and unirradiated materials [53][44].

Hosemann *et al.* postulated that alloy steel yield strength changes with sample size according to (Figure 23) [44]. The figure shows that micromechanical testing does not initially follow the Hall-Petch relationship. Rather, there is a minimum strength dependent on the relationship between grain size and sample size. These zones can be broken into defect-free samples (nm scale typically tested in the TEM), single crystal samples typically on the μm size where samples comprise of a single crystal and macro samples where multiple grains are included [44]. Moving between the single crystal and macro regime, the Hall-Petch relationship becomes more pronounced.

The Hall-Petch relationship works well in metals and can explain the size effect appropriately. For ceramics or “brittle” materials the Hall Petch relationship may not always be correct; however, plastic transition sizes can be observed in SiC, Si and GaAs [53], [74]–[76]. These transitions are where sample size is sufficiently small such that plastic deformation can occur. Gerberich *et al.* proposed three key reasons why ceramics can display plasticity at the small scale at room temperature [74]:

1. Small volumes, particularly single crystals, are relatively free of stress concentrations allowing high stresses before crack propagation [74].
2. Very high stresses can nucleate dislocations at free surfaces in ceramics at low temperature [74].
3. The activation energy for nucleating a dislocation is much smaller at high stresses, allowing both nucleation and propagation of dislocations to produce plasticity when normalized by structure size [74].

It is worth noting that the mathematic models proposed by Gerberich are derived from diamond-like structures not hexagonal structures such as SiC [74], [77]. Despite this they raise an interesting point. Due to the small samples size, small defects at the surface are likely to be the only initiation point for failure. In grown or sintered samples, the surfaces defects could be as small as 2 nm; as such in a typical ceramic with fracture toughness $\approx 2 \text{ MPa}\cdot\text{m}^{1/2}$ a stress of 25 GPa would be required to initiate failure [74]. Before failure, dislocations would initiate from these small stress concentrations. These dislocations arising from the stress concentrations could build up and act as a form of work hardening [74]. Gerberich postulates that this system could be repeated in a cycle: as stress is applied more “shielding” dislocations are formed allowing higher stress tolerance and allowing further plastic deformation[74].

2.3.4. Summary

Ceramic micro cantilever sample preparation methods and some experimental challenges, including size effect and plasticity, have been explored in this literature review.

Micromechanical testing is a plausible technique for the characterisation of radiation damage layers and has widely been used in metals. Further work will be required to use micro bend testing to determine the effects of radiation damage on ceramics. The effects of experimental set up are not trivial matters and have not been well explored in the literature for ceramics. The sample preparation of ceramic cantilevers is limited to etching and focused ion beam milling. The choice of sample size has been shown to have a substantial effect on the outcome of micromechanical tests. Following this review, the effects of ion beam milling and sample size will be explored in a model material (SiC) before their application to an ion damaged material.

2.4. Sharp indenter indentation

A brief critical review is presented below regarding the indentation test methods used in this thesis. Indentation allows the extraction of materials properties in an essentially non-destructive manner. Using indentation, very small surface areas can be used to evaluate materials properties with good statistical significance when compared with the volumes of material required for bend or compression testing. Despite its advantages (such as speed and ease of use) indentation results in a complex stress field, making analysis and the extraction of strength data complex. This complex stress field also makes linking microstructural features and mechanical properties challenging. The test techniques are presented in order of material volume tested

2.4.1. Micro-indentation

Hardness measurement consists of pressing an indenter of a known geometry into the surface of a material with a known load and holding time. Equation (12), which is used to calculate hardness, is shown below:

$$H = \frac{P_{max}}{A_e} \tag{12}$$

where H = hardness, P_{max} =maximum force applied and A_e = projected contact area. Hardness can be considered as a material's ability to resist plastic deformation. During hardness testing a load is selected for testing, and the projected area of the indentation is measured following indentation. Based on the known geometry of the indenter used for Vickers indentation, the projected area is calculated by measuring the length of the diagonal corners of the indentation. A schematic representation of a standard Vickers indenter system is shown in Figure 24:

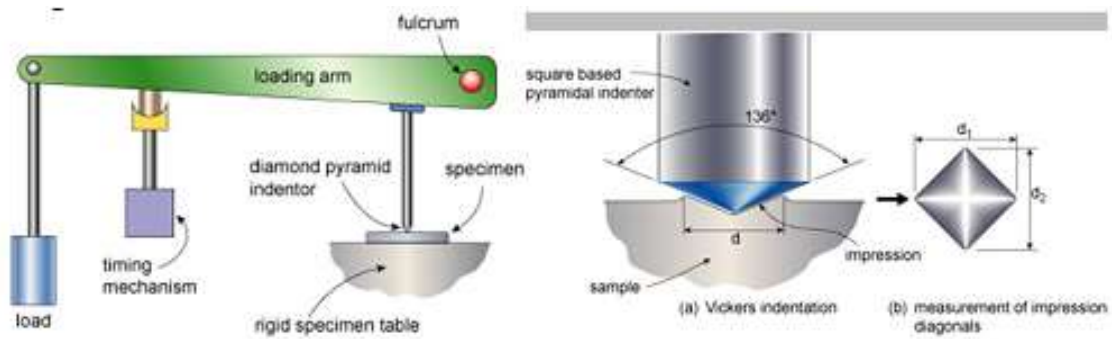


Figure 24 Vickers indenter system diagram showing the arrangement of the indenter and load along with the standard measurement procedure for Vickers indents [78].

Quasi-static Vickers indentation initiates both cracking and plastic deformation. This is widely agreed to be an appropriate measure of contact damage, particularly for brittle materials [79]. Indentation initiates plastic deformation, in ductile metals facilitated by the nucleation of shear-induced dislocations in the lattice of the material. In ceramics, this process is hindered by the strong ionic and covalent bonds between the atoms of the material. The cracking of material during testing changes the test from one which is a measure of plastic deformation to one which is multifactorial. (Figure 25) shows a guide to crack nomenclature which enables the discussion of Vickers cracks more easily. These descriptors can also be used for 3 sided indenters [80].

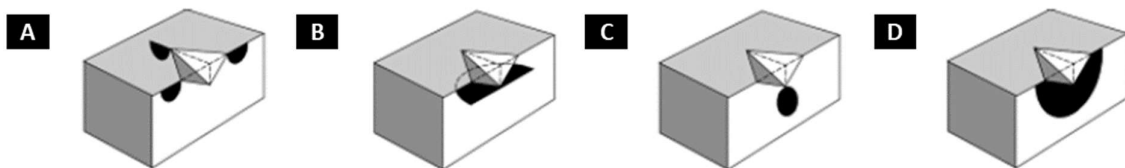


Figure 25 Macro-scale crack systems typically exhibited by Vickers indentation: (a) radial cracks, (B) Lateral cracks, (C) median cracks, and (D) half-penny cracks [80].

2.4.2. Size effect of hardness measurement

In both metals and ceramics, an indentation size effect (ISE) has been identified whereby increasing test loads result in a decrease in measured hardness [79]. This size effect was touched on during the micromechanical testing section (page 38 of this review). Mechanical properties should be independent of length scale; however, mechanical testing and indentation studies frequently identify a size dependency. The size effect equations (see

Equation(13) [81] based on geometrical necessary dislocations set out by Nix & Gao are often used for metallic samples:

$$H \approx Gb[\rho_{SSD} + \rho_{GND}]^{\frac{1}{2}}$$

(13) [81]

where G is the shear modulus, b is the magnitude of the Burgers vector, ρ_{SSD} is the statistically stored dislocation density and ρ_{GND} is the geometrically necessary dislocation density [82].

Based on strain gradient plasticity theory, as the indenter presses on the material the strain at the tip will be high and low at the edges, as shown in **Figure 26**. This gradient between the tip and edges is referred to as the strain gradient. Due to the strain gradient plastic deformation occurs where geometrically necessary dislocations (GNDs) accommodate the geometric change in the surface.

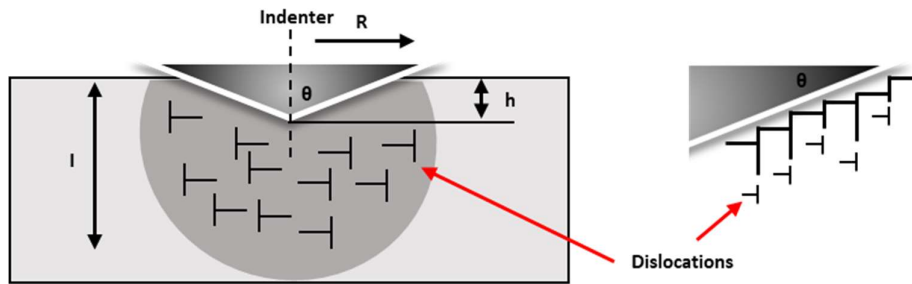


Figure 26 Geometrically necessary dislocations created by a ridged conical indenter, where the dislocation structure is modelled as circular dislocation loops. Adapted from [81].

Statistically stored dislocations are generated by homogeneous deformations. Examples of SSDs are the dislocations developed during the plastic deformation in a uniaxial tension test. We can consider that GNDs make up the strain hardening component that causes the indentation size effect and the specimen size effect observed in micromechanical testing. In metals, there is typically a large amount of SSDs which are subsequently increased by GNDs in the event of a strain gradient. During loading, plastic flow readily occurs with dislocations slipping over long ranges. Ceramics, however, have a low number of statistically stored dislocations. They are capable of some plastic deformation; however, due to their strong bonds ceramics often fracture at the largest flaw. Common failure nucleation points are grain boundaries, pores and flaws. As such strain hardening is not so readily observed in ceramics.

Due to this lack of strain hardening, proportional specimen resistance (PSR) models have been developed. Kick developed a basic principle which has been the starting point for the majority of ceramic PSR / indentation size effect models [83]:

$$P = \text{constant} \times d^2 \tag{14}$$

where P is load and d is an indentation dimension.

This law is useful as it can be applied independently of indenter type. Despite the ease of use of Kick's law, the exponent of 2, although logical (based on load per unit area), has not been observed experimentally [83]. The use of an exponent n was subsequently used by Meyer. In Meyer's law n is observed to be $1 < n < 2$. To address the issues associated with both Meyer's and Kick's law, namely the lack of meaning behind the constants and exponents, Li and Bradt suggested a proportional specimen resistance (PSR) model [79]:

$$P = a_1 d + a_2 d^2 \tag{15}$$

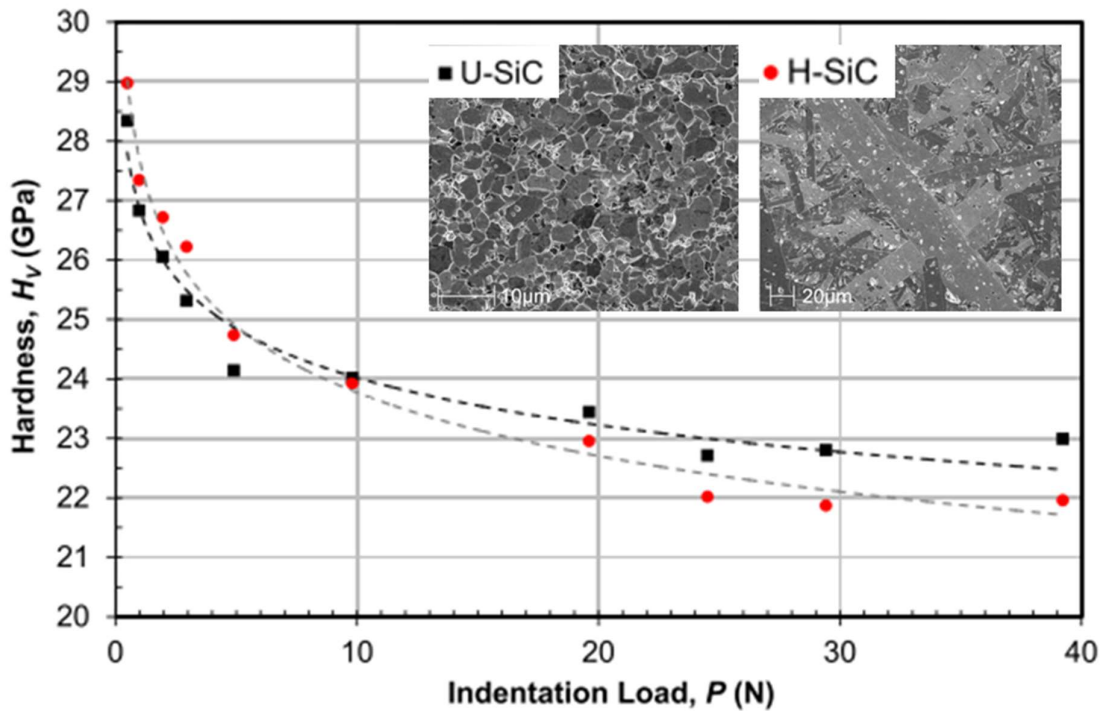


Figure 27 Plot of hardness against indentation load showing the indentation size effect differences between in U-SiC (uniform grain size) and H-SiC (heterogeneous grain size). Adapted from [79].

(Figure 27) shows the ISE and fitted PSR curves for two silicon carbide ceramic samples with different grain structures as presented by Wade *et al.* By fitting the PSR equation to hardness values from a range of loads two individual values can be resolved.

The two values resolved are the a_1 and a_2 , where it is accepted that the a_1 value is a function of the energy per indentation area typically related to cracking [83]. The a_2 value is attributed to the energy per indentation area associated with plastic deformation [83]. Wade *et al.* refers to these values more specifically as the a_1 magnitude of cracking and a_2 magnitude of plasticity [79]. An observation from Li and Bradt's work suggests that the a_1 value is in part affected by the friction of the surface being indented. This could have implications for the testing of porous ceramics. However it is clear from the crack lengths recorded by Wade *et al.* that cracking is the dominant determinant of the a_1 value [83], [84]. Wade *et al.* proposed that the a_2 value remains unaffected by grain structure, and therefore it could be suggested that the a_2 value is a property of the chemical composition and microstructure of the ceramic. Although a limited deviation in a_2 is commonplace in silicon carbide ceramics, a_2 values for alumina can vary more widely. Wade *et al.* demonstrated these variations. The original data used to develop the PSR model were from amorphous glass, but the properties of glass are very different to those possessed by polycrystalline ceramics. Despite this, the model is a useful technique to characterise the indentation-based deformation of ceramics.

2.4.3. Strength estimation from indentation

A materials strength is required for the design of components under load. Nano indentation or macro indentation cannot give a direct strength value but has often been used as an estimator of strength. The general formula is given by Equation (16) [85]:

$$H_v \approx 3\sigma_{ys} \tag{16} [85]$$

where H_v is Vickers hardness and σ_{ys} is yield strength. This relationship is broadly accepted for steels and metals with medium to fine grain [85]. Polycrystalline engineering ceramics often have correction coefficients much higher than 3, with strength values far below their hardness [85]. As such the formula is not suitable for typical polycrystalline engineering ceramics. However, strength values measured by micro mechanical testing are frequently closer to their theoretical value. Micro bend samples contain very few / smaller defects, thus their strength values fall much closer to the three times correction factor making the formula

a useful tool for designing experiments. It should be noted that this approach should not be used for the design of components.

2.4.4. Fracture toughness

Fracture toughness is the ability of a material to withstand crack propagation. In the case of ceramics, fracture toughness “ K_{IC} ” is a central property required for the design of components. Chevron notched three-point, or four-point bend specimen testing is the preferred technique for determining fracture toughness [86]. Using the equations developed by Lawn *et al.*, indentation can be used as a controlled method of inducing cracking in ceramics to estimate fracture toughness. Indention can efficiently be conducted on small samples, making it ideal for materials science researchers.

Lawn’s equations link the average corner crack length from an indentation to mode one (opening mode) fracture toughness. Lawn identified that the halfpenny crack length (see Figure 25) in glass related to fracture toughness based on Equation (17) [87], [88]:

$$K_{IC} = \nu \left(\frac{E}{H} \right)^{1/2} \frac{F_m}{c^{3/2}}$$

(17) [87], [88]

where ν is Poissons ratio, E is Young’s modulus, H is hardness, F_m is maximum load and c is the average crack length from the centre of the indentation to the crack tip.

The validity of this technique has received scepticism in the literature due to concerns as to the differences between unstable and stable cracking [89]. The deficiency of certainty as to the stress field induced during indentation, and a lack in crack pattern uniformity undermining the universality of the indentation methodology, have also been questioned [89]. However, as Marshall *et al.* made clear in their review paper, the ease of indentation to determine fracture toughness outweighs the potential limitations of the model [89].

2.4.5. Nanoindentation

Nanoindentation has provided a step change in materials scientists’ and engineers’ ability to study materials properties at the nanometre scale [90]. The basis of nanoindentation is the

inference of mechanical properties through indentation of an instrumented indenter. The load cell and displacement sensor linked to the indenter produces a load-displacement curve (Figure 28). By using an indenter of a known geometry, these load indentation plots are typically used to determine both elastic modulus and hardness.

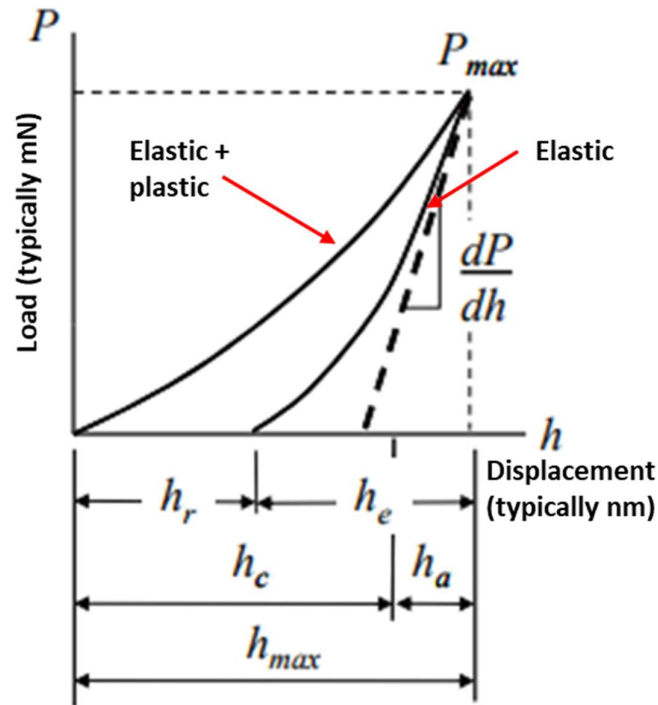


Figure 28 Nanoindentation plot with maximum load P_{max} and max depth h_{max} . The slope of the elastic unloading dP/dh , h_r depth of the residual impression and h_e is the displacement associated with elastic recovery.

During nanoindentation two modes are commonly used, load controlled and depth controlled indentation. Once the required force or depth has been reached the load is then released, and an impression is left due to plastic deformation in the material. In conventional indentation, this is measured and converted to hardness (see Equation (12)). The plastic impression is fixed in place due to deformation in the material, but the size of the indent left does not account for the elastic recovery of the indented material. In the case of nanoindentation, the displacement of the indenter is recorded, thus on unloading of the indenter the elastic recovery of the material can be measured. Analysis of the initial portion of this elastic unloading gives an estimation of the elastic modulus of the indented material, where:

$$S = dP/dh$$

(18) [91], [92]

where dP is change in load and dh is change in depth (as per Figure 28). Based on relationships developed by Sneddon a geometry independent relation using contact stiffness can be used to determine elastic modulus:

$$S = 2\beta \sqrt{\frac{A}{\pi}} E_r$$

(19) [92]

where β is a indenter dependent constant, A is contact area and E_r is the reduced elastic modulus which is a composite of the deformation from the sample and indenter. E_r can be given by the common form:

$$E_r = \frac{1 - \nu^2}{E} + \frac{1 - \nu_i^2}{E_i}$$

(20) [91], [92]

where E and ν are the elastic modulus and Poisson's ratio for the sample and E_i and ν_i are the modulus and Poisson's ratio of the indenter.

These calculations require a known contact area; the unloading part of the curve and calibrated tip can be used for this purpose. The unloading section of the curve is best fitted with a power law as found by Olliver and Pharr [91]. A solution to this non-linearity was proposed by Doerner and Nix:

$$P = B(h - h_f)^m$$

(21) [91], [92]

where B and m are empirically determined fitting parameters. This part of the calculations is typically carried out by dedicated nanoindentation software. The unloading stiffness can then be determined by differentiating equation 21 at the maximum penetration depth:

$$s = \left(\frac{dP}{dh}\right)_{h=h_{max}} = Bm(h_{max} - h_f)^{m-1}$$

(22) [91], [92]

Suitable area functions can then be used for each indenter type as per Table 5; An expanded form is described in (Equation (23) [91], [92]):

$$A_c = 24.56h_c^2$$

(23) [91], [92]

Further allowances can be made to adjust for indenter bluntness, and more qualitative information can be gathered from analysis of the indentation plot. Pop-in events on loading part of the curve can signify non-linear events such as cracking, phase transformation and delamination of thin films. On unloading, similar features can be identified such as pressure-induced phase changes [93]. Displacement changes at peak load can identify creep or thermal drift in the sample or setup.

2.4.6. Continuous stiffness measurement (CSM) nanoindentation

During nanoindentation, a direct current is applied to a coil driving an indenter into the surface of the test media. A recently developed variant of nanoindentation, continuous stiffness measurement (CSM), uses a small sinusoidally varying signal on top of the standard DC signal. This additional loading and unloading allows the calculation of stiffness and hardness at a range of loads very rapidly. An example of how a CSM indentation plot is developed is shown in Figure 29:

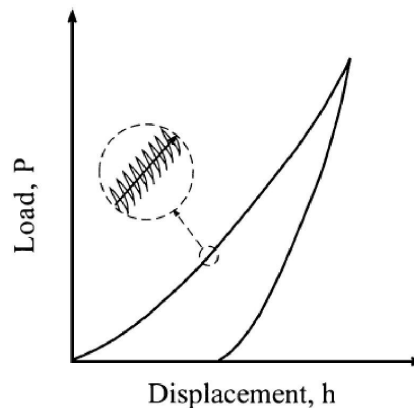


Figure 29 Continuous stiffness measurement (CSM) nanoindentation plot showing the DC and AC sections of the indentation [92].

A typical CSM test on “hard” materials use a driving frequency of 45 Hz and a peak amplitude of 1-2 nm [92], [94]. Especially for low load testing, the choice of amplitude must be made carefully with the lowest amplitude capable of exceeding the signal to noise ratio being recommended [95]. The use of repeated loading and unloading with short time constants allows the testing of thin surface features during the loading phase. Continuous measurement also permits the testing of multilayer, graded and implanted/irradiated materials

more easily. However, the mechanical description of CSM is different from conventional nanoindentation due to the harmonic loading. Thus to calculate the contact stiffness, the dynamic response of the indentation system has to be accounted for. To do this the mass of the indenter m , the spring constant of the leaf spring supporting the indenter K_s and the stiffness of the indenter frame must be considered [92]. The stiffness of the support frame is described as $K_f=1/C_f$, where C_f is the compliance of the loading frame and the dampening coefficient C due to the air gaps in the capacitor plate displacement sensing system [92]. These factors, along with contact stiffness S , make up the response of the sample indenter interaction. Contact stiffness S can be calculated from the displacement signal:

$$\left| \frac{P_{os}}{h(w)} \right| = \sqrt{\{(S^{-1} + K_f^{-1})^{-1} + K_s - mw^2\}^2 + w^2 C^2} \quad (24) [91], [92]$$

where the driving force $P=P_{os} \exp(iwt)$ and the displacement response of the indenter is $h(w)=h_0 \exp(iwt+\Phi)$ [92]. The phase difference between the force and displacement signals can also be used where Φ is phase angle:

$$\tan(\phi) = \frac{wC}{(S^{-1} + K_f^{-1})^{-1} + K_s - mw^2} \quad (25) [91], [92]$$

Where in the two equation's P_{os} is the magnitude of the force oscillation, $h(w)$ is the magnitude of the resulting displacement oscillation, w is the frequency of the oscillation and as stated Φ is phase angle [92]. Equations (23) [91], [92] and (25) [91], [92] can be solved for contact stiffness, S :

$$S = \left[\frac{1}{\frac{P_{os}}{h(w)} \cos\phi - (K_s - mw^2)} - K_f^{-1} \right]^{-1} \quad (26) [91], [92]$$

The damping caused by the capacitor air gap damping is calculated by Equation (28) [91], [92], the damping provided by the sample is treated as negligible.

$$wC = \frac{P_{os}}{h(w)} \sin\phi$$

(27) [91], [92]

By substituting Equation (24) [91], [92] into Equation (20) [91], [92] we can derive:

$$S = 2\beta \sqrt{\frac{24.56}{\pi}} E_r h_c$$

(28) [91], [92]

As such hardness and modulus can be calculated from load-displacement data from CSM indentation. Presented in (Figure 30) are typical CSM curves from a range of material types:

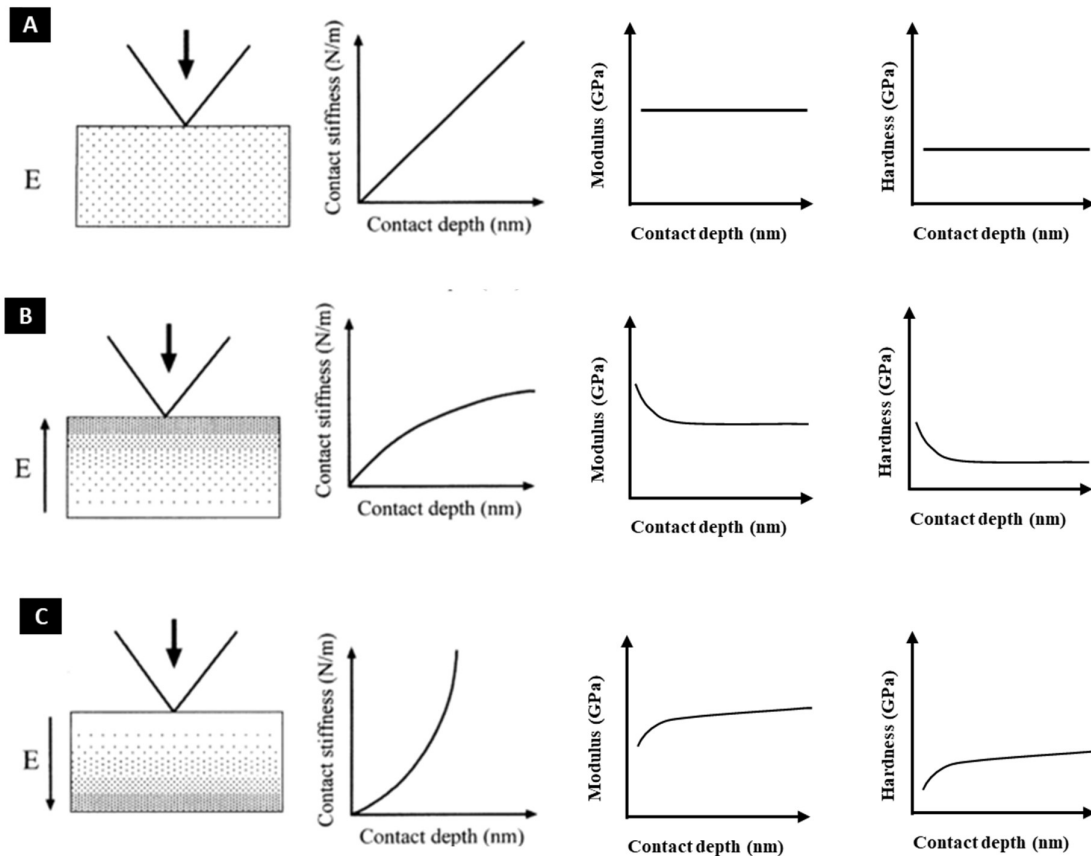
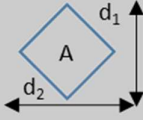
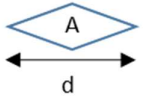
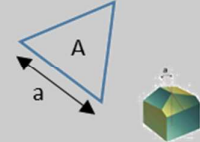
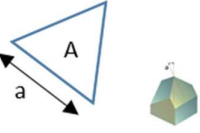


Figure 30 Example CSM indentations stiffness response (A) consistent modulus, (B) high modulus on a low modulus substrate (graded), (C) low modulus material on a high modulus substrate (graded) [92].

2.4.7. Indenter design and geometry

Berkovich indenters are typically used for nanoindentation. The configuration of a three-sided indenter such as the Berkovich is simpler to manufacture to a higher tolerance than that of a four-sided indenter such as a Vickers indenter [96]. Despite their differences in shape and manufacturability, the projected area of Vickers and Berkovich indenters are the same. At the atomic scale, indenters are a spherical shape with a radius of 50-150 nm. To extrapolate materials properties from load-displacement curves, a detailed knowledge of the actual indenter geometry is required. To assess the indenter shape, a system of area function fitting must be completed before testing. Further to area fitting, compliance of the sample and sample holder must be calibrated. The correct operational procedure and preparation before nanoindentation can reduce the likelihood of inconsistencies and inaccuracies in results. Further potential errors consist of worn indenters, surface oxides, indenter misalignment, creep and thermal drift [48]. To ensure repeatable and comparable results, it is typical to scale loading rates relative to maximum test load to ensure the number of test points ascertained is comparable between low and high load tests [91].

Table 5 Reference table of indenter details and calculations for contact area and hardness [80], [97].

Indenter name and description	Indenter shape	Contact area	Hardness formula
Vickers- square pyramid with a centre line to face angle of 68°		$A = \frac{d^2}{\left(2 \times \sin \frac{136}{2}\right)}$	$H_v = 1.854 \frac{P}{d^2}$
Knoop- Dimond pyramid with centre line to face angle of 86.25° and 65°		$A = \frac{d^2}{\left(2 \times \cot \frac{172.5}{2} \tan \frac{130}{2}\right)}$	$H_k = 14.23 \frac{P}{d^2}$
Berkovich- Triangle pyramid with a centre line to face angle of 65.3 °		$A = a^3 \sqrt{3/2}$	$H_B = \frac{P}{a^3 \sqrt{3/2}}$
Cube corner- Triangle pyramid with a centre line to face angle of 35.26 °		$A = a^3 \sqrt{3/2}$	$H_C = \frac{P}{a^3 \sqrt{3/2}}$

As discussed, Berkovich indenters are more readily ground to a point. This allows for the probing of materials properties at the smallest possible scale. Cube corner indenters are also easily ground and are capable of displacing more than three times the volume of substrate materials as Berkovich indenters at the same load [92]. Cube corner indenters subsequently produce considerably higher stresses and strains at the contact area, causing a reduction in the cracking threshold [92]. Subsequently, this makes the cube corner indenter useful for the estimation of fracture toughness at relatively small scales compared with other indenters. (Figure 31) shows the difference in pileup nature between both Berkovich and cube corner indenters in irradiated and unirradiated materials:

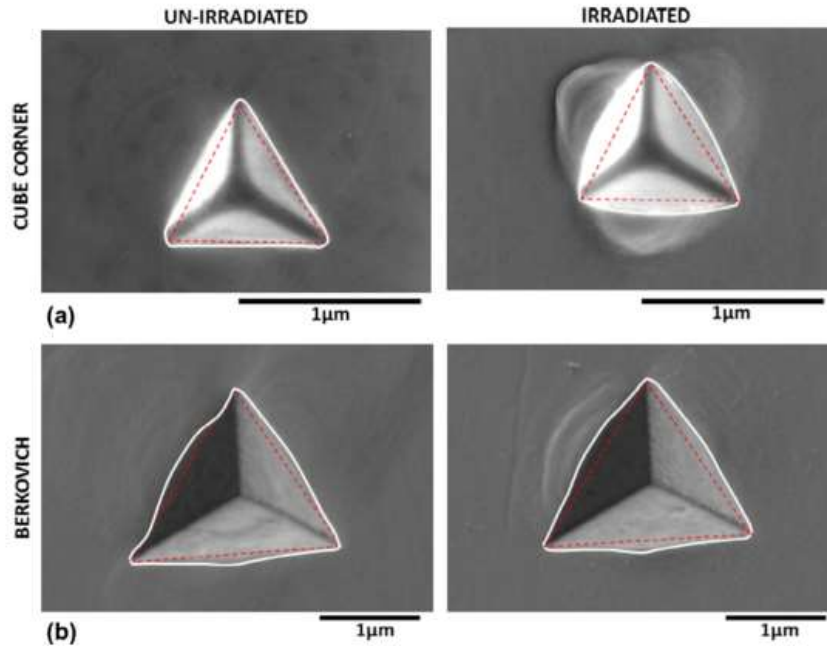


Figure 31 The comparison above between un-irradiated and irradiated steel (Fe12%Cr) samples indented to a depth of 250 nm with cube corner and Berkovich indenters. The chain dotted red line denotes the contact area from the nanoindenter, and the solid white line shows the contact area measured in the SEM [98].

Knoop hardness testing is commonly used for ceramics. Knoop indentation uses an asymmetric pyramidal indenter while Vickers uses a symmetric pyramidal point 136° indent angle. Knoop testing provides a more repeatable indent whereas Vickers indentation results in more clear changes in fracture mode [99]. Knoop testing can be used to selectively initiate slip systems by testing in a range of orientations [100]. Pyramidal indenters are preferred to spherical indenters for ceramics hardness testing. Due to the lack of a stress singularity, spherical indenters can produce wholly elastic indentations at low loads [90]. At higher loads, spherical indenters produce elastic-plastic contacts, making them well suited to the examination of yielding and work hardening [92]. The pileup nature of damage caused by spherical indenters is different to that experienced by sharp indenters. This must be considered when interpreting results. Finally, the precision with which spherical indenters less than $100\ \mu\text{m}$ can be manufactured is limited, making their applications more limited [92]. Despite the relative simplicity and maturity of nanoindentation, experimental skill is still required to ensure that reliable accurate and repeatable results are collected. Nanoindentation is extremely sensitive to environmental influences, including thermal changes and mechanical vibration/interference.

2.4.8. Indentation / nanoindentation of ion and neutron damaged materials

Nanoindentation is widely used for the characterisation of ion, neutron and proton damaged surfaces. It is understood that irradiation causes a hardening in metals caused by increased defect clusters known as Frenkel pairs [94]. This increase in dislocations leads to an increase in yield strength and a subsequent reduction of ductility for most materials. For metals, the increase in hardness is quoted as increasing yield strength, σ_y through the relation $H = 3\sigma_y$ [94]. A more general form of this equation has been presented by Tarbor as $H_v = c\sigma$ where c is a material dependent constant [101], [102]. This hardening phenomenon is known as radiation embrittlement. Other more complex factors such as radiation induced precipitation and helium bubble generation may also occur and contribute to changes in mechanical properties. Nanoindentation allows the characterisation of this change in mechanical properties, making screening of potential nuclear materials viable. A common procedure would be to irradiate a sample with a mask, then nanoindent the irradiated and unirradiated area of the sample with the same equipment and parameters and compare the results [94]. Due to the costs and hazards associated to working with “hot” samples, and the time required to produce such samples, ion damage surrogacy is often favoured for screening materials. Ion damage can produce highly damaged samples in a number of days rather than years. The length scale of ion implantation is typically 0.5-5 μm , while nanoindentations are on the 0.05-2 μm scale, as such the two techniques overlap well. Despite the comparative ease of ion beam irradiation and “hardness testing” there are a number of issues associated to the nanoindentation of ion damaged materials. First, we will, discuss in plane testing, as illustrated in (Figure 32):

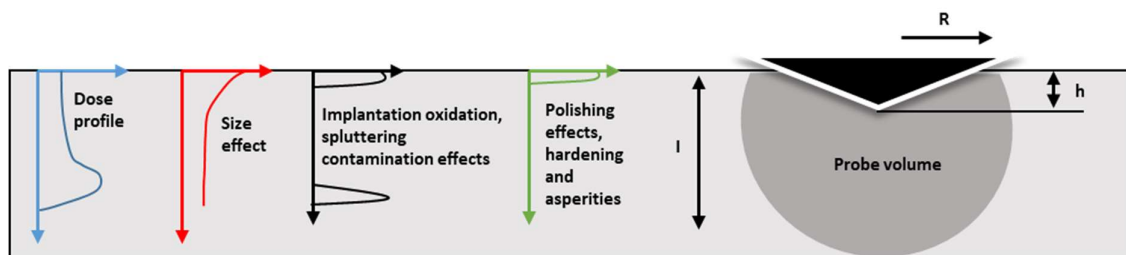


Figure 32 A visual representation of the effects which must be considered when nanoindentation is performed on ion damaged materials. The blue line shows an idealised dose

profile of ion damaged. The red line shows size effect, the black profile shows additional ion damage effects, and the green line shows potential surface finish effects. Adapted from [103].

The issues with nanoindentation of irradiated materials are presented in (Figure 32). The inhomogeneity of the ion damaged layer or “dose profile” is a significant issue. Ion damage often exhibits as a concentrated layer below the surface due to the ions being implanted at a singular exciting voltage, however, this distribution does not reflect typical neutron irradiation damage. To overcome the inhomogeneity, in ion implantation researchers are moving to multi-energy irradiation experiments [101]. In these tests, samples are implanted with ions at a range of energies, thus extending the thickness of the damaged layer and improving its homogeneity. Further to the inhomogeneity produced by ion irradiation, ion implantation, surface oxidation, sputtering, phase transformation and contamination are all additional effects which must be considered. Despite improving experimental techniques for ion irradiation, the complexities of nanoindentation still exist. Size effect is characterised by low load indentations resulting in increased hardness and modulus values, as covered in section 2.4.2. Another surface-based issue with the potential to result in erroneous or increased hardness values is sample surface finish. Grinding and polishing result in a layer of dislocations on the surface of the material. However, provided polishing is conducted well, finer grit finishes result in lower dislocation zone thicknesses, and density: 0.04 μm colloidal silica finishes are typical. Many studies led by S.G. Roberts use shielding to produce an irradiated and unirradiated area on the same sample face [98]. The main point is that the same polish should be used on the bulk and irradiated surfaces.

The probe size of indentation is a contentious issue within the literature, with plastic zones below indenters being modelled at 2-10 times the depth of indentation depending on material [94]. This uncertainty regarding the strain field below indenters makes the interpretation of indentation curves to microstructural features difficult. A number of models have been proposed based on the use of indentation size effect differences between irradiated and unirradiated plots along with ion simulation data to isolate mechanical properties through nanoindentation [94].

An alternative to conducting in-plane nanoindentation is the use of cross-section indentation. Cross section indentation requires an additional cross-sectioning step to cut the sample and polish to the irradiated zone. Indents can then be placed on the cross section in a matrix to map the change in mechanical properties as shown in (Figure 33):

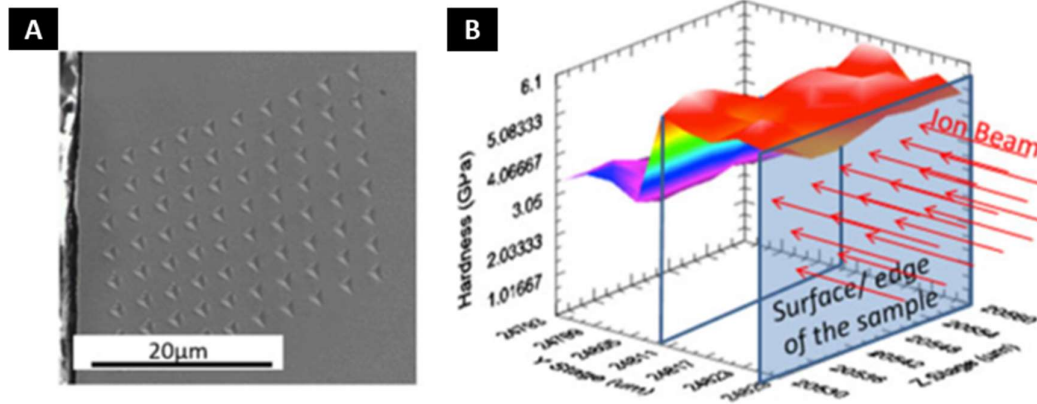


Figure 33 (A) SEM image of indent map on a cross-sectioned ion irradiated surface. (B) 3D plot of hardness data measured versus irradiation depth on 304ss irradiated to 10 dpa at 360°C [66].

The cross-section technique has many issues if not conducted correctly. Indentations too close to the edge of the sample may produce low hardness values, and insufficient indent spacing can cause variation in properties due to residual stress/interaction of strain fields from previous indentations. Surface finish effects caused by polishing the irradiated layer may also modify values artificially.

To simulate in-service conditions as closely as possible, high-temperature vacuum or inert gas flushed chambers are used. High-temperature testing is beyond the capability of most research facilities and as such will not be discussed further. To conclude, the magnitude of material property change due to irradiation is a function of sample dose, the experimental setup, indenter tip and loading conditions and, as such, should be compared with care [98].

2.4.9. Comparative analysis of indentation and micromechanical testing

With regards to micromechanical testing, the selection of the correct test methodology goes beyond reducing sample size. These test techniques are laborious and expensive, so before testing begins some consideration has to be taken as to the time and expertise in sample testing and analysis/modelling. Hosemann presented trade offs between sample preparation time and the modelling efforts required to interpret nano/micro mechanical test results (see **Figure 34**). As can be seen in the figure, the closer the experiment to macro scale testing the

less modelling required; this advantage come at the cost additional equipment costs and sample preparation time.

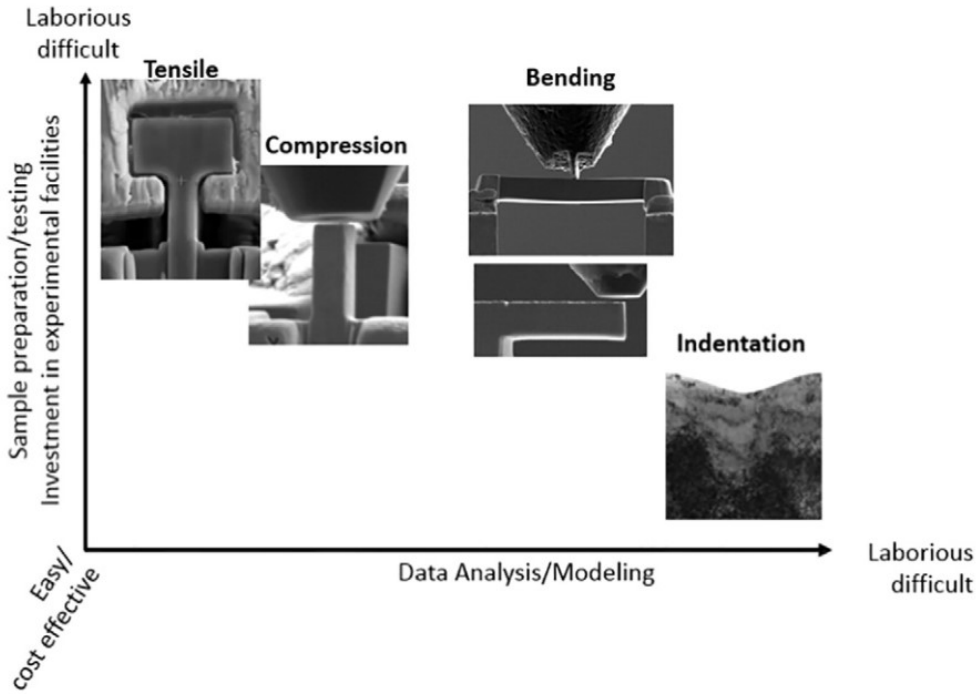


Figure 34 Schematic representation of difficulty levels of small-scale mechanical-testing techniques and nanoindentation [44].

The time required for sample preparation of micromechanical tests results in few samples being produced; as such, the standard deviation is often high especially when coupled with the range of experimental factors at play. Nanoindentation based techniques can be collected in a far timelier manner, with some researchers conducting tests with hundreds of data points. The ease of collection is inversely proportional to the ability to determine engineering properties such as yield strength and flow stress.

Indentation has its limitations as does micromechanical testing. Below, (Table 6), macro indentation nanoindentation and micromechanical testing are compared. The length scales quoted are based on ceramic testing. For metals, length scales may be much broader.

Table 6 Comparison between indentation, nanoindentation and micro mechanical test techniques.

Materials property	Macro indentation length scale	Nano indentation length scale	Micro mechanical testing length scale	Test validity
Hardness	$\mu\text{m} - \text{mm}$	$\text{nm} - \mu\text{m}$	-	Widely used but comparison between different loads and indentation techniques is not advised.
Young's modulus	-	$\text{nm} - \mu\text{m}$	$\text{nm} - \mu\text{m}$	Instrumented indentation makes the calculation of modulus possible.
Fracture toughness	$\mu\text{m} - \text{mm}$	$\text{nm} - \mu\text{m}$	$\text{nm} - \mu\text{m}$	Vickers indentation crack length analysis has been shown to be a weak determinant of fracture toughness: however it is a commonly used technique. Nanoindent crack length measurements have issues similar to Vickers crack length. Macro and micro bend testing can be used to calculate fracture toughness.
Compressive strength	-	-	$\text{nm} - \mu\text{m}$	Micro and macro-mechanical testing can yield compressive strengths. Micromechanical testing can also provide crystallographic orientation relationship data to compressive strengths.
Bend strength	-	-	$\text{nm} - \mu\text{m}$	Micro and macro-mechanical testing can yield bend strengths. Micromechanical testing can also provide crystallographic orientation relationship data to compressive strengths.
Tensile strength	-	-	$\text{nm} - \mu\text{m}$	Micro-tensile tests are possible but prone to error due to miss alignment.

To conclude, indentation cannot provide a complete picture of the materials properties of ceramics. When Nanoindentation is used in conjunction with micro and macro mechanical testing, a great deal of detailed information can be gathered as to the response of ceramics to loading in tension and compression.

2.5. Measuring strain at the microscale

2.5.1. Introduction

Engineering strain, “gauge length divided by the change in gauge length”, Equation (4), can be relatively easily measured during traditional mechanical testing. However, determining residual strain can be significantly more challenging. In the case of mechanical testing, a known load is applied, and a resultant strain can be measured to determine mechanical properties. In the case of residual strains, the measurement of the applied load is typically unknown while the mechanical properties are known. Measurement of the residual strain in the material allows the calculation of the residual stress in the material. Residual strain can be induced in materials through a range of phenomena. With regards to ceramics, the residual strain caused by sintering and ion damage is of interest for this project.

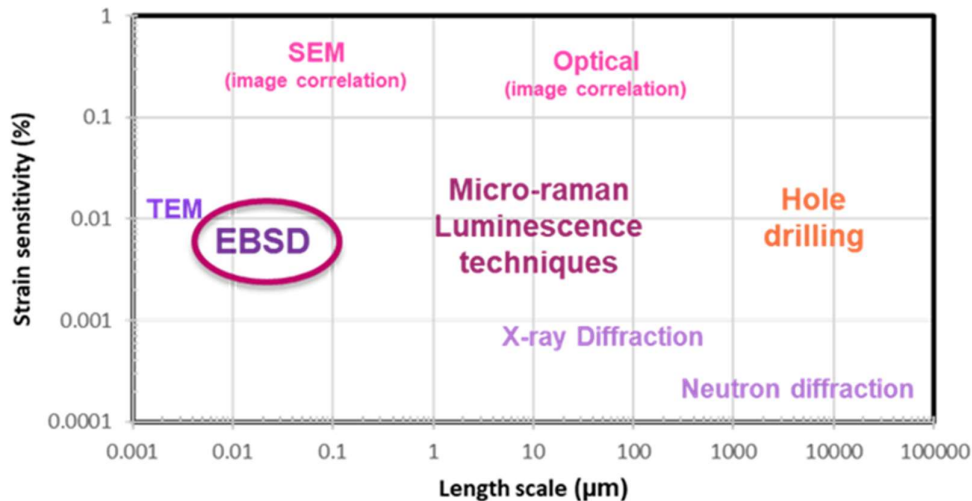


Figure 35 Chart showing the strain sensitivity and length scales resolvable by various strain measurement techniques. Adapted from [104].

From the literature review it can be seen that ion damage layers are on the micro to nano meter length scale and induce stresses of a few GPa. As can be seen in (Figure 35), for ion beam damage assessment, image correlation, hole drilling and x-ray/ neutron do not have sufficient strain sensitivity or spatial resolution. For these reasons TEM, EBSD and, to a lesser extent, Raman will be the focus of this study.

2.5.2. HR-EBSD

The discovery of the fundamentals on which electron backscatter diffraction (EBSD) is based can be traced back to 1928, when Shoji Nishikawa and Seishi Kikuchi directed a beam of 50 keV electrons from a gas discharge on to a cleavage face of calcite at a grazing incidence of 6° . Diffraction patterns were recorded on photographic plates; these patterns were described as “black and white lines in pairs due to multiple scattering and selective reflection.” With improvements in microscope, camera and computer capabilities, EBSD is now a commonly utilised technique. The analysis of strain through EBSD post-processing has been a developing field since the start of commercial EBSD system development. At present HR-EBSD can provide strain and special resolution data which only TEM is capable of bettering (with higher special resolution), see (Figure 35).

Elastic and plastic deformation within a crystal lattice causes deformation of the lattice thus causing a change in the spacing or order of the atoms. For diffraction techniques in their basic form, we can consider the atoms as a diffraction grating, when electrons pass through or in this case, are backscattered. The reduction or expansion of the lattice spacing causes a reduction or expansion of the distance between the diffracted/backscattered pattern; deformation can also result in rotation of the electron backscatter pattern (EBSP).

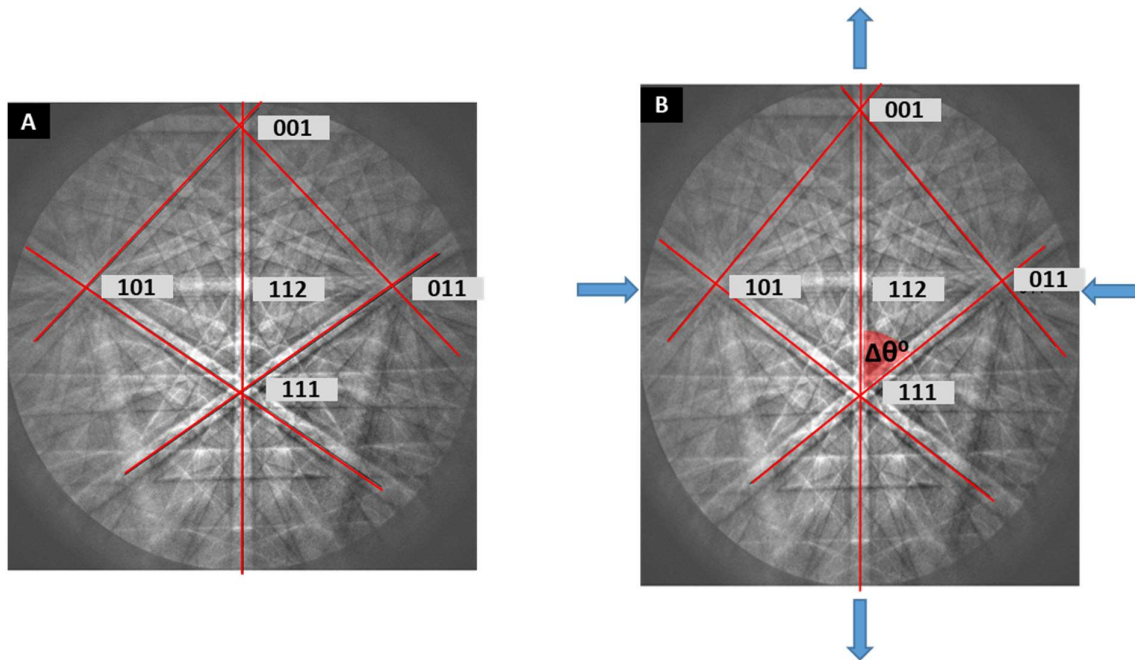


Figure 36 Example indexed electron backscatter diffraction pattern. [A] shows a reference EBSP. [B] Shows a highly strained EBSP [104].

With a crystal orientated in such a way that a symmetry axis was parallel to the tensile axis, an EBSP such as the one in Figure 36 could be recorded. Tensile strain on the sample in the vertical direction would cause the zone axis [001] to move upward and apart from the [111] axis. The consequent contraction of the sample due to the Poisson effect would cause the axes [101] and [011] to move towards the vertical band. These movements would be minimal. The angle between [001] and [111] is 54.67° if the strain was 0.001, then this angle would change to 54.70° . Thus, to measure the strain to 1 part in 1000, a change in angle between these two zone axes of just 0.03° degrees would have to be measured. If an EBSP image contained 1000 pixels top to bottom, then a 0.03° shift would result in a 0.26 pixel distance movement. To quantify such small shifts, cross-correlation methods are required. Cross-correlation compares two slightly different images, and statistically analyses the pixel changes to give an average displacement between the two images. Cross-correlation can map these changes with sub-pixel resolution. To interpret strain data and HR-EBSD strain data specifically, first Hooke's law must be considered Equation (29):

$$\sigma_{ap} = E\varepsilon \quad (29)$$

where σ_{ap} = applied stress, E= Young's modulus and ε = strain.

With HR-EBSD, Young's modulus can be used as an input with the measured strain state to calculate the applied or residual stress. In the case of testing 3-dimensional objects, Hooke's law is not sufficient to describe stress and strain due to Poisson's effect. Consider a box in compression (see Figure 37); the sides expanding have a value of strain along with the compressed faces (due to Poisson's effect), so stress and strain must be described by vectors.

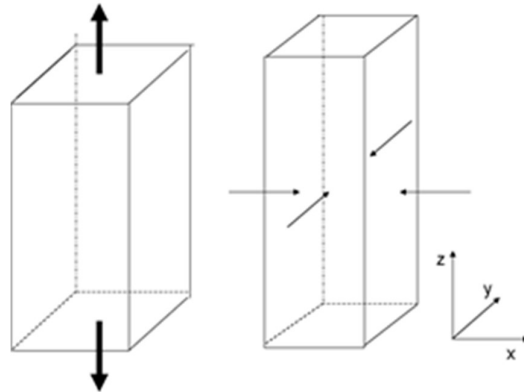


Figure 37 The effects of tensile force on a bar of material with reference to the coordinate system used by Crosscourt 4 HR-EBSD software [104].

Due to the coupling effects in the sample, a 3x3 matrix is used to describe strain in the sample. In this system, X, Y and Z are represented numerically as 1, 2 and 3. For a strained sample in tension, the strain term would be e_{33} : the first subscript describes the axis being strained (Z) and the second subscript denotes the strain is in the direction of the Z-axis. Other examples of this are e_{11} and e_{22} : these are tensile or normal strain. Where the subscripts are in opposing axis, shear components are described i.e. e_{13} , e_{31} ; due to symmetry in the strain tensors these two values are interchangeable. Shear of a plane causes crystal distortion: crosscourt4 deals with this shear and resultant rotation using the physics rather than engineering definition; thus we will continue to use the symbol E. As vector values are used, vector modulus values are also required; these are the C_{11} the longitudinal compression Young's modulus, C_{12} transverse expansion and C_{44} shear modulus as illustrated in Figure 38 [105]:

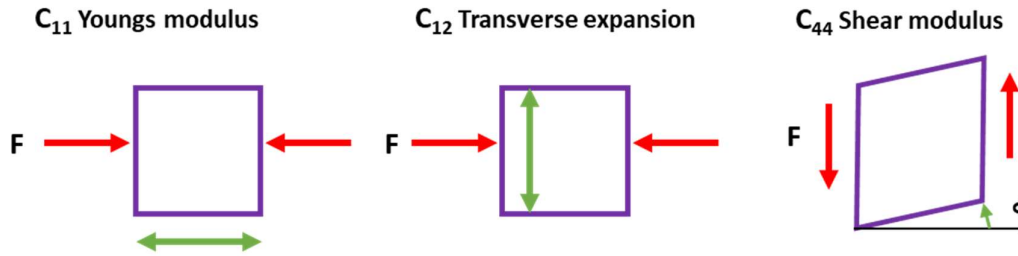


Figure 38 Schematic describing the physical meaning behind the Young's, transverse and shear modulus [105].

From these constants, the stress in the material can be determined. However, to determine the stress at a given location in the sample, first a reference position must be sought to compare each EBSP against. For this comparison and conversion of pattern shifts to stress maps, Cross court software can be used. Crosscourt began development in 2004 by David Dingley, Angus Wilkinson and Graham Meaden [106]. Angus Wilkinson had published a technique for mapping small changes in EBSD patterns for strain mapping using a semi retracted EBSD camera. Working together they developed a modified technique which could use a fully inserted camera [106]. With the EBSD camera fully inserted, different pattern centres were cross correlated to map the distortion tensor in the sample [106].

Crosscourt 4 has fitting procedures for choosing an unstrained area as a reference for the strained areas. However, EBSP pattern simulation software is not yet capable of producing sufficiently accurate simulated patterns for comparing strained samples to simulations (without additional camera length calibrations). This internal calibration requirement creates a problem when testing fine-grained and highly deformed materials as low strain reference points within each grain are not available. In instances where the reference patterns are from a strained area, a map of relative strain rather than absolute strain is generated.

With regards to residual strain following ion implantation, very little work has been published using HR-EBSD. Some work has been published on indentation size effect, and residual stress around indentations; precipitate residual stress and twinning have also been reported upon [107]–[109]. Kareer *et al.* advocated the use of HR-EBSD to determine the effective probe size of indentations made in ion-implanted steel, but are yet to publish such data [94].

Zaafaran *et al.* conducted one of the first 3D HR-EBSD experiments on copper indented with a spherical indenter to validate a crystal plasticity finite element simulation [110]. Britton *et al.* demonstrated the ability of HR-EBSD to quantify residual strain at grain boundaries, slip bands and around a cracked carbide precipitate [111].

To conclude, both transmission and backscattered electron, strain measurement techniques have been reviewed with emphasis on determining the residual stress in ion implanted ceramics.

2.5.3. Transmission electron microscopy (TEM)

As shown in (Figure 35), TEM can offer the highest sensitivity to strain measurement at the highest special resolution. There are four main strain measurement techniques used in the TEM: convergent beam electron diffraction, precession, geometric phase analysis (GPA) and selective area diffraction.

Convergent beam electron diffraction (CBED) produces Kikuchi patterns when focused on a single crystal area of a TEM lamella. The brightness and contrast of these patterns depend on the sample thickness and disorder. The camera length of the microscope can be varied to produce broad higher order Laue zones (HOLZ), and the angle of the HOLZ lines can be measured to map strain. Convergent beam electron diffraction can offer higher special resolution due to the small spot size deliverable by TEM (<1nm). Further to the reduced spot size of the electron beam as a transmission microscopy technique, the interaction volume of the electron beam is limited to the thickness of the TEM lamella Typically, TEM lamellar can be prepared in the FIB from a thickness of 300 nm to 50 nm. Convergent beam analysis offers large area analysis with some microscope systems offering a mapping function. Where mapping is required but not possible with CBED, geometric phase analysis (GPA) can be used.

GPA is a high-resolution TEM technique where an atomic resolution image is processed to identify the differences in atomic spacing, thus inferring the strain at each point/area [112], [113]. To calculate the lattice strain, a virtual aperture is used to produce selective areas, these areas are then processed with Fourier transforms [113]. The resultant diffraction patterns are analysed and compared to produce a displacement field. As a HRTEM technique, the area which can be mapped is typically very small (fields of view around 100 x 100 nm are common). Where a larger field of view is required, dark field electron holography (DFEH) may be utilised; DFEH has a slightly lower spatial resolution than GPA. DFEH requires a bi-prism to interfere an object wave with a reference wave and produce an electron hologram. Due to the additional requirement of the biprism, DFEH is not available for most

microscopists due to the additional cost. Further to this, exceptionally high stability and source coherency are required, further limiting DFEH access for researchers. DFEH is a state-of-the-art technique, yet as time passes it will likely become more commonplace [114]. Due to the thin nature of TEM lift out samples, lamella relaxation must be considered when conducting strain analysis in the TEM. Strain variations from lamellar relaxation are quoted at a maximum of 30% [115].

2.5.4. Summary

A brief review of the most ubiquitous and appropriate residual strain measurement techniques has been conducted with regards to residual strain in ceramics. A summary of these techniques is presented in (Table 7):

Table 7 Summary of the residual strain mapping techniques discussed [114].

Technique	Spatial resolution	Strain variation	Field of view/ mapping area
HR-EBSD	60 nm	1×10^{-4}	$100 \times 100 \mu\text{m}^2$
CBED	2 nm	1×10^{-3}	Specialist setup required for mapping
HRTEM (GPA)	2 nm	6×10^{-4}	$100 \times 100 \text{nm}^2$
Dark field electron holography (DFEH)	4 nm	2×10^{-4}	$1 \times 0.25 \mu\text{m}^2$

Ion-induced residual stress is likely to consist of an area of a few micrometres and have a magnitude around 1-0.5 GPa. Due to the volume and magnitude of stress induced by ion implantation, HR-EBSD is a plausible technique for the measurement of residual strain in ceramics. TEM based techniques such as geometric phase analysis (GPA) could be used to estimate the residual stress around localised precipitates or damage regions in the microstructure. While offering high spatial resolution lift out/ TEM based strain measurements are susceptible to lamellar relaxation due to the thin nature of the specimen. Due to the limitations of TEM and EBSD based strain measurement both techniques should be cross checked with modelling or analogous results to ensure the validity of measurements.

2.6. Silicon carbide (SiC)

2.6.1. Introduction

As previously stated, silicon carbide (SiC) is widely used as TRISO fuel coating and is being explored for use as a metal part replacement for a range of nuclear applications. SiC is also widely used as an engineering and armour ceramic. SiC was primarily manufactured as an abrasive material and later developed into a structural ceramics. Silicon carbide can be described as providing low density, high hardness, high Young's modulus, low thermal expansion, high thermal conductivity, and good chemical stability. These properties, coupled with a high melting temperature, thermal shock resistance, and high oxidation resistance, make SiC the material of choice for a wide range of extreme engineering environments. Following the Fukushima event in 2011, a number of research organisations recognised the need to improve fuel rod nuclear damage tolerance [116]. SiC/SiC composites consisting of SiC and SiC fibres were identified as a candidate material for fuel rods [116].

Beyond engineering uses, SiC is also used for the manufacture of nano/micro electro mechanical systems (NEMS/MEMS). These nano/micromachined structures integrate transistor-like nano-electronics with mechanical actuators, pumps and motors, thus forming physical, biological and chemical sensors [117]. A key example of such components is the accelerometers used in smartphones. These devices are made in large volumes and require high levels of repeatability. Many accelerometers and pressure sensors are manufactured from silicon; however, for high temperature and harsh environments, such as gas turbine control and in the oil industry, silicon carbide offers the necessary combination of thermal and chemical resistance required [118]. Critical to the design of NEMS/MEMS devices is an understanding of Young's modulus at a range of length scales and how length scale effects modulus. This modulus for design is referred to as the effective modulus [117].

Silicon carbide forms around 250 different crystallographic structures. Of these the most common is 6H polytype (alpha SiC). 6H silicon carbide consists of a hexagonal close-packed (HCP) structure. 6H is widely used for polycrystalline armour and structural materials produced through hot pressing and reaction bonding. Single crystal forms of 6H SiC are manufactured using physical vapour transport (PVT). Also of notable interest is the 3C (beta-

SiC). This polytype forms a cubic structure. Cubic 3C is more commonly formed using chemical vapour deposition (CVD), as is used on TRISO fuel coatings.

Regarding non-stoichiometry, SiC is predominantly covalently bonded but has slight ionic bonding due to the electronegativity difference between silicon and carbon [119]. Due to this mix of bonding, stable SiC compounds are only obtained at stoichiometry [119]. Excess carbon is typically observed in a graphitic structure, while excess silicon is found in the metallic form in the microstructure. As discussed, SiC forms around 250 polytypes, and the stability of each polytype varies depending on pressure and purity. Further to this, solid state transformations are possible based on periodic slip and diffusional rearrangement [120]. Characterised polytype transformations are $2H \rightarrow 3C \rightarrow 6H$ $6H \leftarrow 4H$; transformations have also been observed in boron-doped materials [120]. HRTEM is one of the established techniques for identifying variation in polytype as it provides sufficient spatial resolution to resolve small changes in polytype [120].

2.6.2. Manufacture of SiC

2.6.2.1. *Sintered silicon carbide manufacture*

Processing of silicon carbide for commercial armour/engineering materials consists of two main routes: hot pressing, and pressureless sintering. Green body techniques and vapour deposition methods are capable of forming SiC, but hot pressed and pressure-less sintered SiC is commercially preferred for engineering applications. Whether hot pressing or pressure-less sintering, the initial manufacture steps in the production of dense ceramics are similar. First, the SiC powders, sintering aids/additions and a solvent are selected and milled to an appropriate particle size and distribution [121]. It is widely accepted that finer initial particle sizes result in smaller sintered grain sizes; however, small particle sizes do not press well [122]. For this reason granulation or spray freeze drying can be used to produce powders which flow into pressing dies well and, when pressed, result in a more homogeneous green body [122]. Process dependent, these granulated powders are then uniaxially pressed, ready for hot pressing. For pressureless sintering, an additional isostatic pressing step is often utilised to achieve higher densities.

Due to the covalent nature of the silicon-carbon bonds and the low self-diffusion coefficient, sintering aids are required for both hot pressing and pressureless sintering to achieve fully dense ceramics [123]. Typically consisting of boron, carbon, yttrium oxide, aluminium or aluminium oxide, sintering aids reduce the oxide (SiO_2) layer around the silicon carbide grits making densification thermodynamically possible through solid-state sintering [124], [125]. Through the use of partial sintering studies, it has been found that boron sintering aids do not form at grain boundaries, but are found within the grain [126]. Some evidence suggests that carbon sintering aids react with the SiO_2 layer around the SiC particles, forming SiC crystallites [126]. Due to the agglomeration of small particles and cost of fine milling, researchers also use standard and ultra-fine SiC together to act as sintering aids [123].

Solid-state sintering is dependent on material transport by volume diffusion consisting of movements of atoms or vacancies along grain boundaries, surfaces, or the volume of the material. The driving forces behind solid state sintering are the difference in free energy or chemical potential between free surfaces of particles and the points of contact between adjacent particles. (Figure 39) shows a schematic of solid state material transport:

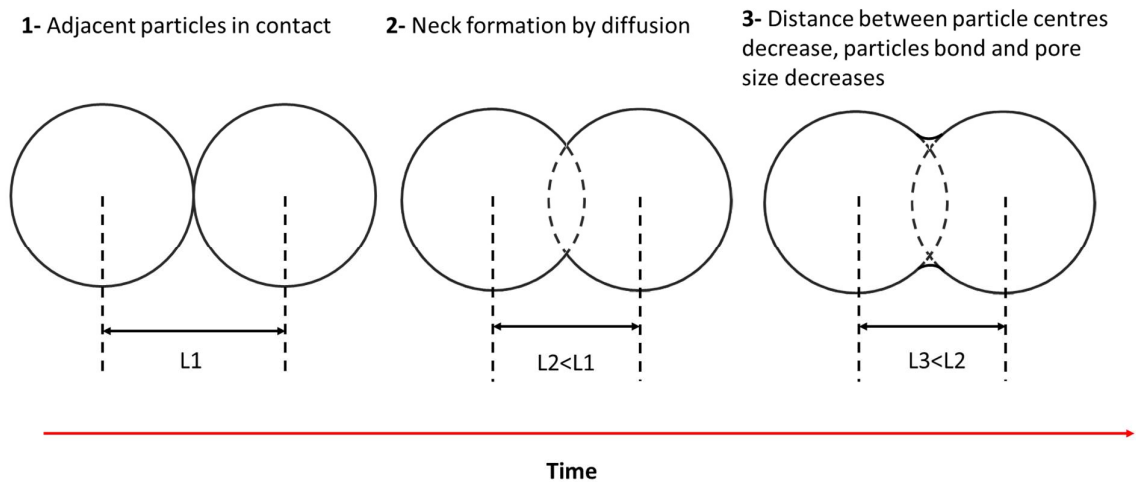


Figure 39 Mechanism of solid-state sintering through material transport, as time increases the particles coalesce. Adapted from [127].

Aside from ultra fine SiC sintering aids, carbon/boron sintering aids can be used. Carbon and boron segregate at grain boundaries and contribute to the grain boundary strength [125]. On a wider scale, the quantity and blend of sintering aids used controls the sintering temperature and pressure, which in turn affect grain size, aspect ratio and distribution [128]. Excessive

use of sintering aids can result in a weakening of the grain boundaries, resulting in poor materials properties especially at high temperatures [123].

Hot Pressing is often used as the application of pressure allows for reduced processing temperatures, thus reducing processing time, temperature and minimisation of residual porosity [129]. Reduced processing temperatures minimise grain growth, which is seen as advantageous to maintain high material strength [129]. Despite the advantages of hot pressed SiC, sintered SiC offers economic benefits in reduced processing costs [79], [130]. Further to this, hot pressing introduces a level of anisotropy to sintered components where flaws in the component are typically elongated plate shapes perpendicular to the pressing direction [131].

2.6.2.2. *Physical vapour transport (PVT) silicon carbide*

It is common for semiconductor materials to be manufactured in a crystal pulling or seeded solidification process whereby a melt is used to produce a large boule. However, due to thermodynamic considerations, these processes are not appropriate for SiC as huge temperatures and pressures would be required (10^5 atm and $>3200^\circ\text{C}$) [132]. For these reasons, physical vapour transport (PVT) makes up 90% of silicon carbide manufacture [132]. PVT is conceptually relatively simple. A powder bed of SiC is heated to form a vapour that rises within the furnace, cools, and condenses on a seed crystal forming a crystal of SiC [132] as shown in Figure 40:

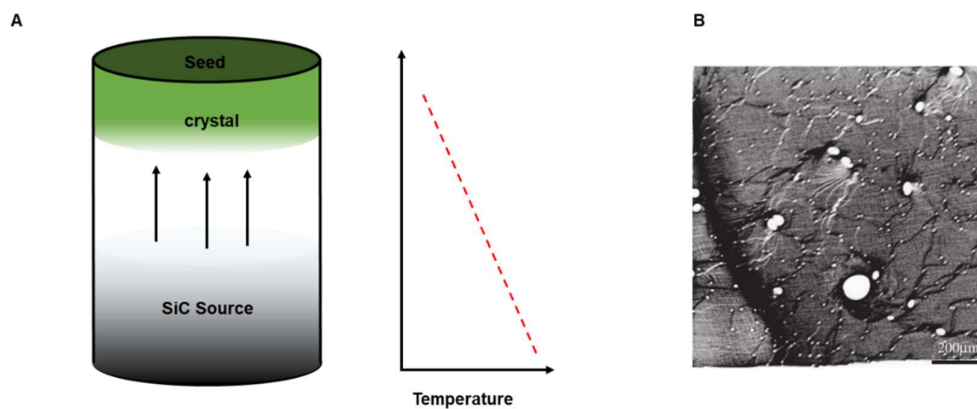


Figure 40 [A] PVT furnace schematic [132], [133], [B] micropipe and dislocation imaged with synchrotron white beam x-ray topography[134].

To sublime significant quantities of the SiC powder, temperatures above 2150-2500 °C are required [133], [135]. These high temperatures mean that the crucibles are typically manufactured from graphite and use inductive heating [132]. The purity of both crucible graphite and the SiC source are critical to the purity of the crystals grown [135]. Partial vacuums and inert gas (Ar, He, N₂) atmospheres are also used to limit Si/C vapour reactions with oxygen in the air. Key research is required in the reduction of micropipe density, reduction of residual dislocations, stress, and the manufacture of increased crystal diameters [133]. Micropipes consist of open core dislocations: these can be seen in Figure 40 [B]. Defects of these types have been reduced by technological advances in manufacture. However they must be considered when undertaking micromechanical testing on single crystal SiC [134]. Another key factor for mechanical testing is polytype instability. The accepted growth model for PVT is a terraced model. An analogous explanation of the terrace model is people filling a cinema: initially, people fill from the back but over time disorder and reordering occurs depending on the supply of people/seats etc. In SiC growth this manifests as a switching of polytype based on the supply (flux) of SiC / C and the substrate temperature [136]. It is believed that under Si-rich conditions and low supersaturation conditions the preferred poly- type will be 6H SiC (or 15R-SiC) on the Si-face, as well as C-face, of SiC (0001) [137]. While in the case of Si-excess and high supersaturation, 3C SiC is formed preferentially [137].

2.6.2.3. *Chemical vapour deposition (CVD) silicon carbide*

Increasingly, chemical vapour deposition is being used to produce high purity (99.9999%) silicon carbide. A range of reaction chemicals, heating systems and process conditions can be conceived to produce CVD silicon carbide. The primary principle of chemical vapour deposition involves the decomposition of a precursor chemical at an elevated temperature to condensate a surface substrate [125]. Deposition rates vary from 6-75µm/hour dependent on the system parameters; higher deposition rates will likely see decreasing prices and increased use of CVD SiC [138].

2.6.3. Mechanical properties of SiC

Polycrystalline properties are in part dependent on the grain size, density and composition of the ceramic tested. Typical values are presented in **Table 8**:

Table 8 Silicon carbide mechanical properties.

Material property	6H -single crystal	3C -single crystal	Poly crystalline 6H
Density (g/cm ³)	3.215 [119] - 3.14	2.215-3.166 [119]	3.10 [139], [140]
Poisson's ratio	0.24 [141]- 0.018 [142]	0.318-0.328 [143]	0.14 [140]
Hardness (GPa) (Vickers)	25-33 [57], [142]	31.2±3.7 [144]	19.3 – 27.3 [119]
Young's modulus (GPa)	415 - 450 [57], [142]	433±50 [144]	410-430 [139], [140]
Yield/ failure strength (GPa)	10 [141]	-	
Flexural strength (GPa)		-	0.38-0.55 [139], [140]
Compressive strength (GPa)	7.8 [57]	-	3.90 [139]
Fracture toughness (MPa.m ^{1/2})	3.3 [142]	1.59 ± 0.21[144]	2.0 – 5.4 [119]
Melting point (K)	3000 [57]	-	-

Table 9 bulk modulus of each crystallographic plane have specific stiffness values as shown [145], [146].

	C11	C33	C12	C13	C44
6H (hexagonal) Modulus (GPa)	503-500	564-552	109-92	-	168-160
Transformed Modulus (GPa)	479	521	98	56	148
Cubic Modulus (GPa)	351.5	-	140.4	-	232.9

The bulk modulus of each crystallographic plane has specific stiffness values as shown in **Table 9**. Further to this, the modulus of 6H SiC has some variation in the literature depending on the experimental or modelling technique used to develop the data set (see Table 9).

2.6.4. Crystallography and damage in SiC

Silicon carbide (SiC) is a compound of silicon and carbon. SiC has over 200 polytypes caused by a one-dimensional disorder, allowing different stacking sequences. Among these polytypes, 3C- SiC has the cubic symmetry (β -SiC), and the others have either hexagonal or rhombohedral structure (α -SiC). Figure 41 depicts the crystal structure of common polytypes of SiC, where the structure and periodicity of the atomic stacking is shown [147]. Each diagram shows the periodicity of the lattice, i.e. in 6H six repeating units of silicon and carbon make up each unit. As a point of reference, 6H-SiC (a polytype of α -SiC) has a wurtzite crystal structure and is sometimes referred to as moissanite.

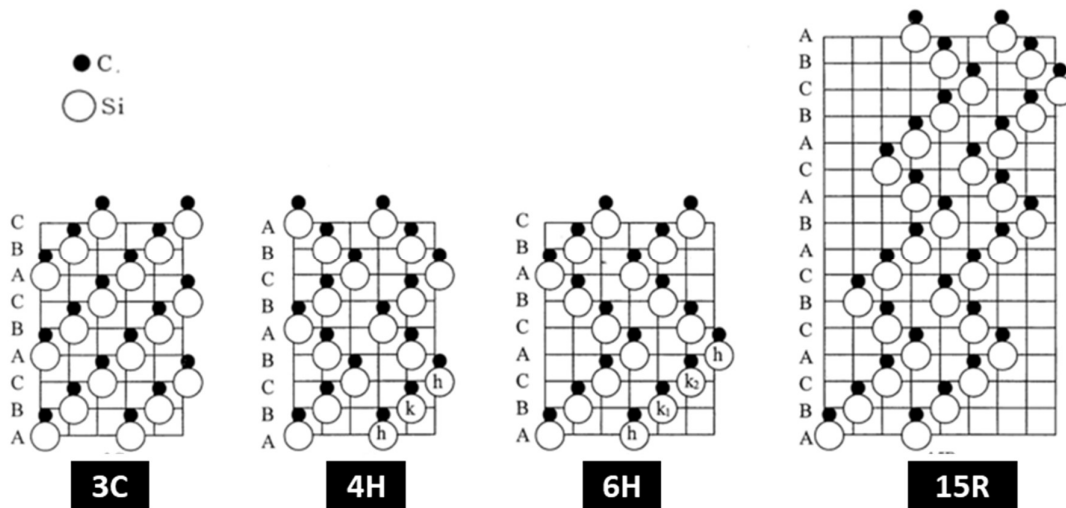


Figure 41 crystal structure of 3C, 4H, 6H and 15R sic from left to right [147], [148].

6H SiC is hexagonal where $\alpha=90^\circ$, $\gamma=120^\circ$ with lattice constants of $a=3.07300 \text{ \AA}$ and $c=15.0800 \text{ \AA}$. 6 atoms of carbon and 6 atoms of silicon make up each unit cell.

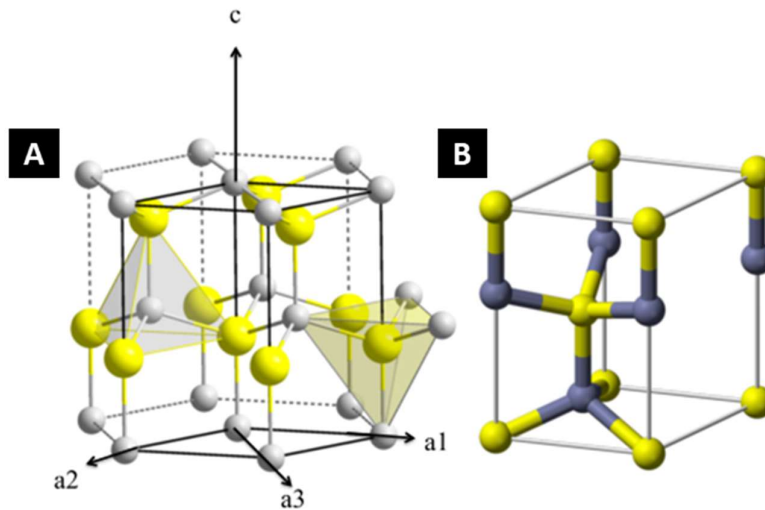


Figure 42- A) wurtzite crystal structure. B) wurtzite unit cell [149].

3C SiC is cubic in structure with a lattice constant of $a=4.3596 \text{ \AA}$. Based on its cubic structure, 3C is relatively simple to index using typical (hkl) notation, 6H is hexagonal, thus requires the use of a four-axis Miller indices. In this four-axis system vectors are notated as a_1, a_2, a_3 and c . Miller indices for planes (reciprocal of planes intersect with axes) are represented by (hkil) where $i=-(h+k)$.

Direction is expressed as; $d=ua_1 + va_2 + ta_3 +wc$ where $t= -(u+v)$.

Conversion of (UVW) in the 3 axis system to the 4 axis system is;

$u = 1/3 (2U-V), v = 1/3(2V-U), w = W$ and $t=-(u+v)$ four axis Miller indices.

The conversion of the plane (hkil) to the corresponding direction normal is;

$[uvtw] = (hki3/2(c/a)2l)$ in a hexagonal structure.

Unlike face and body centred cubic materials, hexagonal close-packed materials have a very limited number of slip systems. The range of available slip systems for HCP materials are shown in Figure 43 [150]:

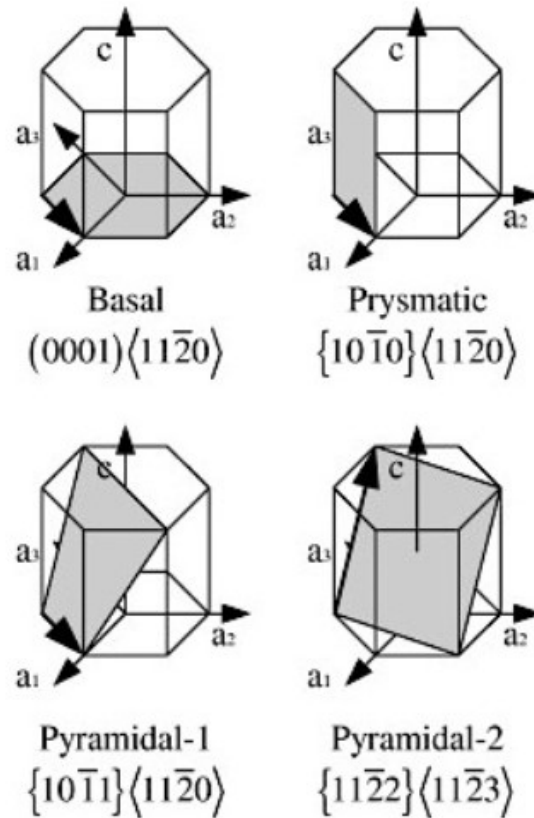


Figure 43 Common slip systems in hexagonal close-packed crystal structures [150]

Yan *et al.* presents the available slip systems in SiC as $(0001)\langle 1\bar{2}10 \rangle$, $(0001)\langle 01\bar{1}0 \rangle$, $\{10\bar{1}3\}\langle 1\bar{2}10 \rangle$ and $\{10\bar{1}0\}\langle 1\bar{2}10 \rangle$ [151]. Of these systems, dislocations are most likely to occur on the $(0001)\langle 1\bar{2}10 \rangle$ and $(0001)\langle 01\bar{1}0 \rangle$. K. Nihara used Knoop indentation to determine the preferential slip plane in single crystal SiC over a range of temperatures [100]. The $\{10\bar{1}0\}\langle 11\bar{2}0 \rangle$ slip system was found to be preferential at room temperature. This matches well with the finding of Yan *et al.* Under specific conditions cross slip may also occur on the $\{10\bar{1}3\}\langle 1\bar{2}10 \rangle$ and $\{10\bar{1}0\}\langle 1\bar{2}10 \rangle$ planes.

2.6.5. Effects of ion damage on SiC

Due to the ubiquitous use of SiC for nuclear fuel (TRISO) cladding, ion and neutron damage of SiC has been investigated in detail. Regarding neutron damage, Snead *et al.* conducted a detailed review of the properties of SiC for fuel performance modelling [119]. SiC has a very low amorphisation threshold. Snead *et al.* investigated the amorphisation of 6H, 3C and Hexalloy (a commercial grade of SiC) following carbon ion (3 MeV), silicon ion (0.56 MeV)

and neutron irradiation at a range of temperatures [152]. Combining these results and the results of others, a plot of amorphisation dose threshold and irradiation temperature was developed (see Figure 44) [152]:

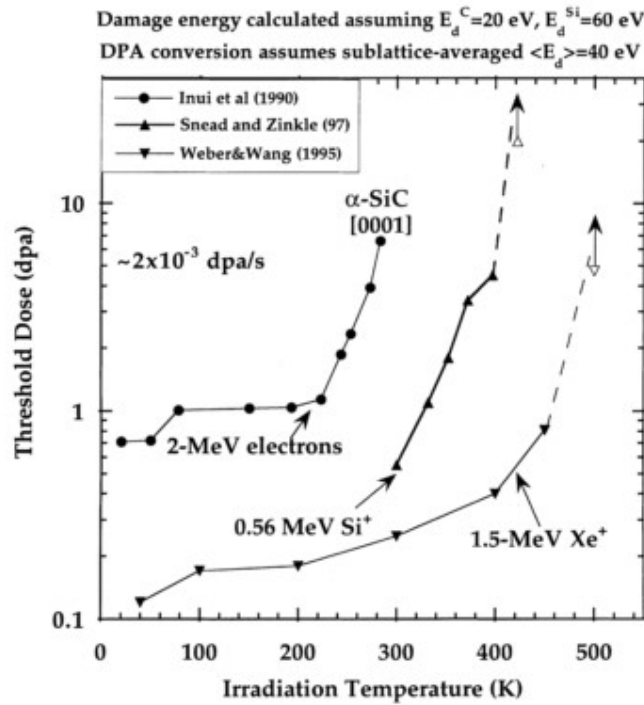


Figure 44 Temperature dependence on the critical amorphisation threshold of SiC and Si following irradiation with a range of ion species [152].

Further to detailing the amorphisation of SiC, Snead also characterised the amorphized microstructure of the 6H SiC lattice following ion irradiation, using high-resolution transmission electron microscopy (HRTEM) [152]. (Figure 45) shows the effects of ion implantation perpendicular to the c axis. Image A shows the onset of amorphisation with islands of disorder forming, followed by image B where large areas are amorphized:

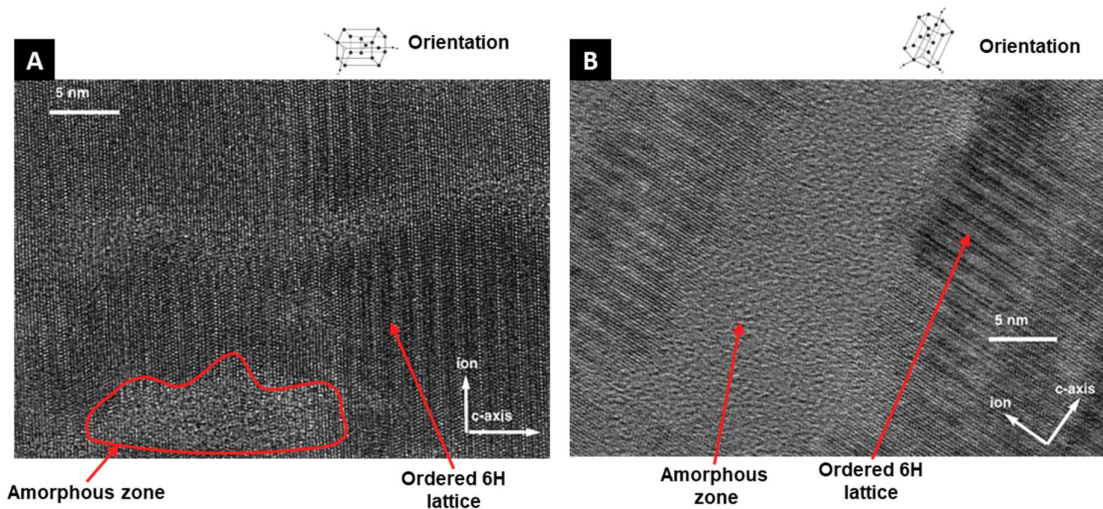


Figure 45 [A] The onset of amorphisation of SiC following Si ion implantation. [B] extensive amorphisation of SiC following Si ion implantation [152].

Debelle *et al.* explored the ion irradiation induced disorder in 6H and 3C single crystals: 100 keV Fe ions up to 0.7 dpa were used to cause amorphisation [153]. 0.45 dpa was identified as the amorphisation threshold; the formation of interstitials before amorphisation induced tensile elastic strain up to 4 % [153]. Debelle theorised that this residual stress caused the destabilisation of the microstructural defects to cause amorphisation [153]. Costantini *et al.* used a similar range of samples to Snead *et al.* with 4.0 MeV Au and 4.0 MeV Xe ion. On all accounts plane expansion was found to increase with ion dose, as did lattice disorder [154].

2.6.6. Micromechanical testing of SiC

No papers have been reported concerning micro bend testing of 6H single crystal SiC; however, some research has been conducted on compression testing of 6H SiC and 3C CVD SiC. This work will be reviewed. When specifically looking at slip systems, referring to other 6H covalently bonded materials may also be useful. High-temperature results will be avoided as temperature-induced plasticity is well known.

6H micro-compression

There are two key papers on the micro-compression of 6H SiC: “Dislocation glide- control room temperature plasticity in 6H SiC single crystals.” Kiani *et al.*, and “Room temperature yield and fracture strength of single crystalline 6H silicon carbide.” Kwon *et al.* The samples used in both cases were 6H single crystals cut along the $\langle 0001 \rangle$ and at a 45° or 40° angle to the plane $\langle 0001 \rangle$ [57], [155]. In Kiani’s research, the compression tests were conducted in the TEM with pillars < 300 nm while Kwon produced a range of pillars from $1.17 - 2.13$ μm which were tested in the SEM [57], [155]. Subsequent research has shown that electron beams such as those employed in the TEM can facilitate dislocation movement: this is important when comparing the two papers [156]. Both researchers analysed their compressed micropillars in the TEM. Through TEM analysis and MD simulations, Kiani concluded that plastic deformation in room temperature 6H SiC is controlled by glide rather than dislocation nucleation [57]. Kwon identified that plastic deformation was size dependent, where pillars below 0.49 μm would deform plastically, and concluded that in the case of angle cut pillars slip traces and dislocations were located on the basal plane [155]. In both experiments plastic deformation occurred near the top of the pillar. In both cases, it could be suggested that this was due to indenter misalignment. In the brittle fracture range, Kwon measured the compressive fracture strength of 6H SiC to be 23.8 GPa, and the CRSS was found to be 9.85 ± 0.69 GPa [155]. No phase transformations to the zinc blend SiC structure were observed during testing of the 6H SiC, despite tests stresses reaching close to the required 10 GPa critical stress (refer to SiC nanoindentation for further detail) [151].

3C micro bend

Due to differences in the number of available slip systems in 3C SiC, 3C SiC micro mechanical results are not comparable to those conducted in 6 or 4 H SiC; however, points of interest can still be identified, along with examples of experimental best practice.

Zhao *et al.* performed lift-out style micro bend tests on 3C CVD silicon carbide coatings on alumina spheres. Beams were milled to a length of 20 μm , width of 2.2 μm , and breadth of 2 μm ; final thinning was conducted at a beam current of 6.5 nA using a gallium ion FIB. A nanoindenter was used to bend the cantilevers, and a modulus of 421 ± 24 GPa was calculated from 5 beams [7]. The beams were notched and fractured to calculate the fracture toughness in different directions relative to the microstructure. All the beams failed elastically with a fracture toughness from $3.47 - 6.72$ $\text{MPa m}^{1/2}$ and Zhao comments that the

fracture toughness was higher than previously reported values [7]. These conclusions match well with those reported by Frazer *et al.* in their study of CVD SiC/ SiC composites [157], in which the matrix of the 3C CVD SiC was characterised by nanoindentation and microcantilever testing in orientation parallel and perpendicular to the grain structure. The modulus was found to be 473 ± 15.23 GPa parallel and 470.21 ± 19.35 perpendicular to the SiC shell, while the parallel fracture toughness was reported as 3.37 ± 0.36 MPa m^{1/2} and 2.29 ± 0.31 MPa m^{1/2} for the perpendicular direction [157].

3C micro-compression

Shin has researched both irradiated with 5.4 MeV Si²⁺ to 14 dpa and unirradiated 3C CVD SiC micropillars with a range of sizes and aspect ratios [43], [53]. To reduce high keV FIB implantation and improve manufacture speed, a lithography and etching process was used to manufacture the compression specimens. Dependent on the study intent, etching was followed by FIB machining using low voltage and current to remove etching artefacts. FIB milling was shown to have no effect within experimental error, as was the irregular etching patterns caused by the lithography technique. In the unirradiated micro-compression paper, pillars with diameter from 0.65 to 4.7 µm were fabricated [53]. Pillar diameter was linked to size effect, and pillars sub 0.65 µm diameter displayed plastic flow before fracture [53]. Up to 12 % strain was accommodated in the pillars before fracture. Loading was accompanied by discrete strain bursts, and TEM linked these bursts to slip on the $[\bar{1}1\bar{1}]$ plane. As discussed previously, the plastic deformation transition for 6H SiC has been identified as 0.59 µm diameter, and the value for 3C and 6H is very similar. The authors of the study refer to this transition as a new form of brittle to ductile transition caused by the small size of the pillar. Other authors have commented on a similar transition concept in Si and GaAs [74], [76].

With regard to the ion implanted samples, a strengthening effect was observed despite the high ion damage levels (14 dpa) [43]. These findings are contrary to the threshold value identified by Costantini *et al.* (Figure 47), who postulated 0.4-0.8 dpa as a sufficient dose to cause amorphisation in SiC resulting in a reduction of hardness and modulus [154].

2.6.7. Nanoindentation and indentation of SiC

Yin *et al.* presented a paper on the effects of polishing 6H SiC with various diamond abrasives [142]. Plastic deformation in low load (400 mN) Vickers indentations was observed, while cracking and edge chipping was observed at loads greater than 5 N [142]. SEM was used to link indentation damage structures and polishing damage structures. Without TEM to identify the dislocation densities and types caused by indentation and the various polishing regimes, the paper lacks conclusive evidence [142]. Niihara produced some detailed experimental data linking Knoop crack length to the active slip systems in 6H SiC at a range of temperatures [100]. It was found that at room temperature the active slip system is $\{10\bar{1}0\}\langle 11\bar{2}0\rangle$, while at high temperature $> 400^\circ\text{C}$ $(0001)\langle 11\bar{2}0\rangle$ is preferred [100]. These results match well with those of some previous researchers, and are commonly cited in the literature.

In a later paper, Qian *et al.* used macro indentation to identify a size effect in 6H SiC [158]. A peak hardness at low load was measured to be 29.4 GPa (Knoop hardness) and a plateaued hardness at a high load of 19 GPa [158]. Further to this, the crack length of the indentations was used to determine the fracture toughness of the single crystal to be $K_{IC} = 1.8 \text{ MPa} \cdot \text{m}^{1/2}$ with no size dependency identified over the load range [158]. The variation in results between Qian and Page are likely to be related to differences in the preparation of the SiC wafers. In Page *et al.* paper wafers were cleaned with hydrofluoric acid, resulting in the etching of any surface flaws and resulting in increased fracture toughness. Low load indentations were conducted, and SiC was found to exhibit popin events during nanoindentation [159]. Page concluded that SiC, along with alumina, displays both elastic and plastic deformation rather than simply densification [159]. Shim *et al.* recorded similar hardness data from Berkovich nanoindentation and also used a novel angled indenter technique to extract the flow properties of SiC [141]. Using FEA, the yield strength of 6H SiC was calculated to be 10 GPa [141]. None of these researchers had identified the conversion of 6H SiC (zinc blend) to a cubic structure (salt blend) or to an amorphous structure; however, researchers using SiC as anvils and during molecular dynamic modelling have identified the conversion of SiC [151], [160]. Yan *et al.* conducted a TEM study on a

Berkovich indentation into a SiC wafer to explore the conversion of SiC further, see **Figure 46** for cross section TEM:

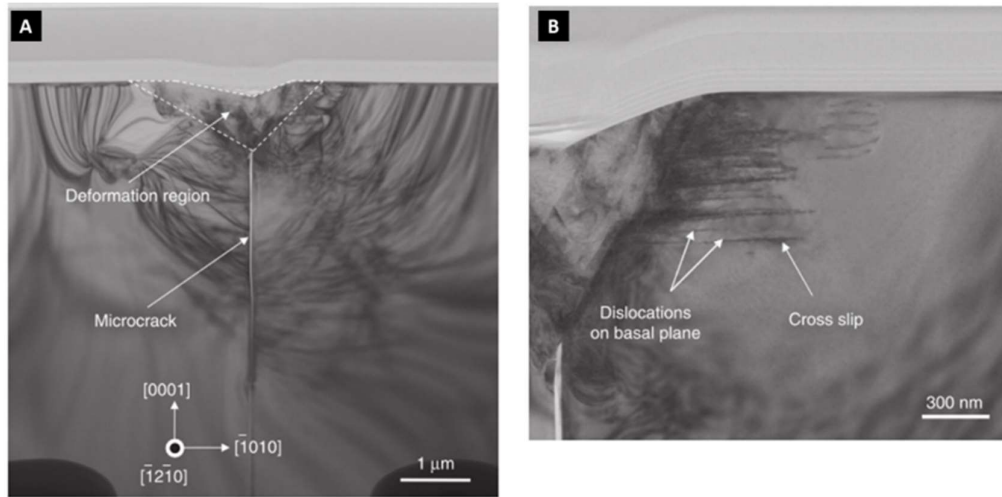


Figure 46 [A] cross-section TEM sample from a 100 mN Berkovich indented SiC wafer, showing microcracking, the deformation region and sample orientation. [B] shows the disordered centre of the indent surrounded by basal dislocations and some cross slip of the dislocations [151].

Based on selective area diffraction from inside and outside of the indentation, Yan *et al.* concluded that no amorphisation took place but that indentation caused severe disorder to the lattice. Further to this, he suggests that at the centre of the indentation the SiC becomes polycrystalline and transforms phases upon loading [151]. At 105 GPa the lattice may convert to salt blend (cubic) to allow the movement of dislocations: upon unloading the lattice reverts to zinc blend 6H [151]. It seems that the identification of microcracking and grain refinement caused by nanoindentation are well substantiated and match with other research; however, the conversion and recovery of the lattice are not fully substantiated.

Nanoindentation tests have been conducted on 4 MeV Xe⁺ and 4 MeV Au²⁺ ion irradiated 6H and 3C SiC by Costantini *et al.* Intriguingly, SiC was found to exhibit an ion softening trend where modulus and hardness reduced with increasing ion dose (see Figure 47):

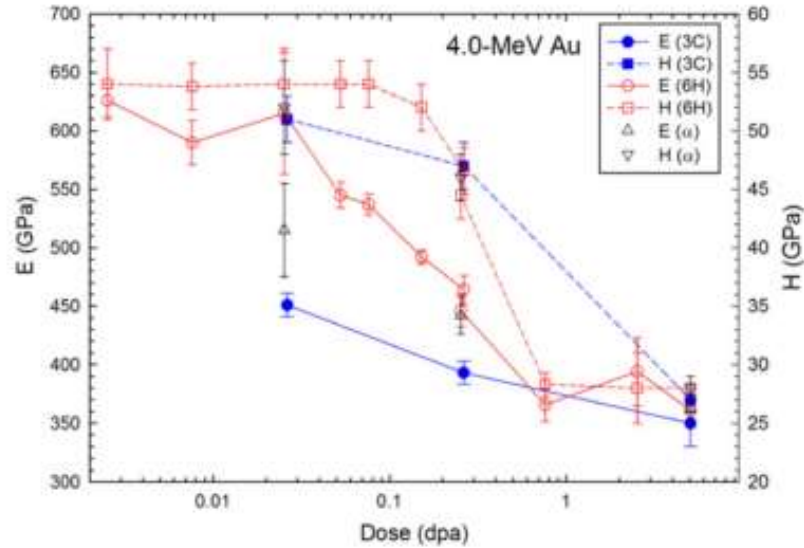


Figure 47 Young's modulus and hardness as a function of 4.0 MeV Au²⁺ dose. Blue symbols show 3C SiC, red markers denote 6H SiC and grey denotes Hexoloy α-SiC [154].

At low doses using Xe ions, the 6H SiC was hardened, but nevertheless the general trend was ion softening. Ion-induced amorphisation was attributed to this change in mechanical properties [154]. Critical doses of 0.2 and 0.8 dpa were identified as sufficient to cause amorphisation. This information is worth noting when conducting FIB milling on SiC for the preparation of microbeams. The points of difference between the amorphisation threshold and subsequent reduction of mechanical performance can be put into context by studying macro neutron damage tests in CVD SiC. Under neutron irradiation from 0.6 to 4.6 dpa, a modest increase in flexural strength and reduction in modulus (~ 50 GPa) can be observed in CVD SiC [161]. Testing at higher fluences, up to 28 dpa, reports a modest reduction in modulus and flexural strength for 3C CVD SiC [162]. Lattice expansion caused by neutron damage is attributed to these changes in mechanical properties [161]. It is worth considering that the effect of ion damage with heavy ions may be more aggressive than the damage caused by neutrons.

2.7. Zirconium nitride (ZrN)

2.7.1. Introduction

Zirconium, carbides, borides, oxides and nitrides were initially researched for nuclear applications and later developed during the space race. Ultra-high temperature ceramics (UHTCs) are a range of borides, carbides and nitrides coupled with early transition metals. These transition metal nitride ceramics, such as titanium, chromium, hafnium, tantalum and zirconium, are of interest to industry due to their unique properties [163]. Transition metal nitrides have been used with great success for cutting tool coatings, diffusion barriers for microelectronics and abrasion resistant layers on optical and mechanical components [164]. Further to industrial applications, ZrN is a candidate material as an inert matrix in fast reactor fuels for the incineration of plutonium and micro actinides [165], [166]. Zirconium nitride, carbide and boride also have potential for use in cooling rod assemblies in next-generation nuclear power plants.

2.7.2. Manufacture of ZrN

For nuclear applications, both monolithic and coatings of ZrN are of interest. ZrN can be obtained by employing various deposition techniques such as magnetron sputtering, ion beam assisted sputtering, reactive ion beam sputtering, vacuum arc deposition, pulsed laser deposition and chemical vapour deposition [164]. However, for monolithic material, manufacturing routes will be the focus of this research. ZrN requires long holding times and/or high applied load due to its high melting point, strong covalent bonding, low self-diffusion coefficient and the presence of a monoclinic oxide layer (ZrO_2) on the ZrN powder surface [163], [167]. To produce bulk materials of a high density, hot (2000°C) isostatic pressing is used resulting in densities >99% [163]. Powder sintered ZrN samples have been produced by milling ZrN particles, followed by pressing and sintering from 1300-1600°C for around 10 hours in a range of atmospheres [168]. Most notably, argon atmospheres allow ZrN to be sintered to a dense state at temperatures as low as 1600°C [167].

Gribaudo *et al.* developed a Zr-N phase diagram Figure 48 to show the conditions temperature and atomic % at which thermodynamically distinct phases occur and coexist at equilibrium in the zirconium nitrogen system. Ermoline *et al.* also developed a similar phase diagram for ZrN and ZrO_2 , and Zr_3N_4 [169].

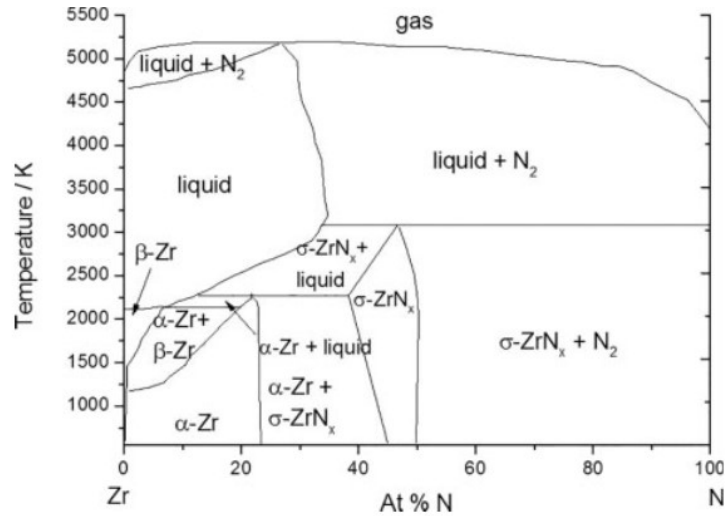


Figure 48 Calculated phase diagram of Zr-N [170], [171].

From the phase diagram (Figure 48), it is clear that ZrN forms a stable structure from 45-50 % nitrogen. In practice the phase diagram of ZrN and indeed the structure of ZrN often include oxygen due to oxygen abundance during processing/manufacture. Hot pressed and magnetron sputtered samples have been identifying as containing ZrN, Zr₃N₄, Zr₂ON₂ and ZrO.

Carvalho developed a ternary phase diagram to describe the multi-phase nature of Zr, N, O based materials, see Figure 49 [172]:

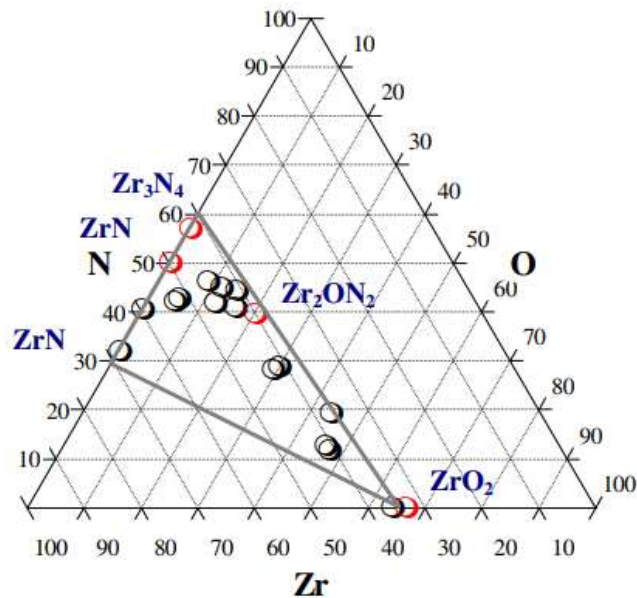


Figure 49 Ternary phase diagram of Zr-N-O red point show known chemical composition of ZrN + O constituents while black points show experimentally identified compounds following magnetron sputtering [172].

TEM analysis was not able to identify these grain boundary segregates; however, grazing incidence X-ray diffraction with Rietveld analysis could detect small quantities of this phase along with trace amounts of oxynitrides at the surface sample [163].

2.7.3. Mechanical properties ZrN

(Table 10) lists the mechanical properties of the phases commonly found in hot pressed zirconium nitride:

Table 10 Mechanical properties of ZrN and Zr, O, N phases.

Material property	ZrN	ZrO ₂
Density (g/cm ³)	7.09	6.05-5.51 [173]
Poisson's ratio	0.25	0.3-0.23 [173]
Hardness (GPa)	20-25 [25]	
Young's modulus (GPa)	380-400 [25]	215-205 [173]
C11 (GPa)	471	
C12 (GPa)	88	
C44 (GPa)	138	
Failure strength		
Flexural strength		
Compressive strength (GPa)		
Fracture toughness (MPa. m ^{-1/2})		20-6 [173]
Melting point (°C)	2 980	
Thermal conductivity (W.m ⁻¹ .K ⁻¹)		3-2 [173]

Mechanical property data was sought regarding the properties of Zr²ON², but insufficient literature was found.

2.7.4. Crystallography of ZrN

ZrN has a face centred cubic (FCC) crystallographic structure $Fm\bar{3}m$, where the arrangement of the atoms is comparable to NaCl (see Figure 50). Through nanoindentation and cross section TEM studies, Egeland *et al.* identified the preferential slip plane for dislocations to be the $\{011\} \langle 0\bar{1}1 \rangle$ [163], [174]. The results from Egeland and others suggest that the preferential slip plan of ZrN is dependent on the stoichiometry of the compound [163].

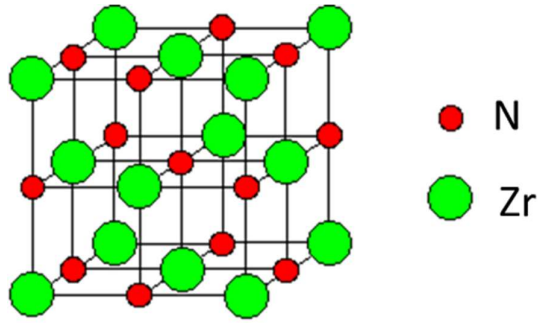


Figure 50 ZrN unit cell where Zr is represented by green spheres and nitrogen is represented by red spheres.

Zirconium nitride (ZrN) has a lattice perimeter of (4.578 Å), as given by JCPDS Card (35-0753). ZrN can form a remarkably broad range of nonstoichiometric compounds with a wide homogeneity range (ZrN_{1-x} , where $0 < x < 0.35$) [167]. Ashley *et al.* investigated the relationship between lattice parameter and non-stoichiometry in ZrN using computer simulation based methods [167], [175]. The following equation was derived to describe the relationship between these factors:

$$\lambda(ZrN_{1-x}) = \lambda(ZrN) - 0.0254x \quad (30) [167], [175]$$

Where the lattice parameter of $\lambda(ZrN_{1-x})$ is the lattice parameter of the subject material, x is the composition and $\lambda(ZrN)$ is the ideal lattice parameter. The small magnitude of the constant (-0.0254) is a testament to a limited change in lattice parameter caused by non-stoichiometry [175].

2.7.5. Effects of ion damage on ZrN

Very little work has been undertaken by researchers on the ion irradiation effects on ZrN with gold ions, although a wide range of experiments has been performed with krypton, xenon and protons. Further to this, very high dose experiments have seldom been reported in the literature. The table below summarises the limited research findings available at this point; furthermore, an example of typical microstructural features following ion irradiation in ZrN is shown in Figure 8 page 17.

Table 11 Experimental literature review for ZrN ion damage.

Title	Sample type	Irradiation source and dose	Observations
Proton irradiation study of GFR candidate ceramics [176]	Hot pressed CERCOM ZrN pre-prepared to a TEM sample (Zr to N ratio 0.85)	Proton beam 1.8 dpa at 800 °C fluence of 2.75×10^{19} protons/cm ³	<ul style="list-style-type: none"> - No significant microstructural changes. - Some evidence of ZrO₂ precipitates. - Very minor/no lattice expansion.
Radiation tolerant nanocrystalline ZrN films under high dose heavy-ion irradiations. 2015 [177]	Thin film 9 nm and 30 nm grain size tested	900 keV Fe ²⁺ ions at a 40° incidence angle to a fluence of 6×10^{15} ions/cm ²	<ul style="list-style-type: none"> - Clear size dependency between small and large grains, where smaller grain size materials exhibited a significantly lower density of defect clusters. - Smaller grains appeared to effectively curtail grain growth, mitigate irradiation softening, and irradiation-induced variation of electrical resistivity.
Heavy-ion irradiation defect accumulation in ZrN characterized by TEM, GIXRD, nanoindentation, and helium desorption. 2013 [25]	ZrN HIPed sample Zr:N 0.894 >99% theoretical density	Xenon and krypton 450 keV-70 keV acceleration voltage and flux of 1×10^{16} ions/(cm ² h) Temperatures – liquid nitrogen, 350°C, 580°C, 800°C	<ul style="list-style-type: none"> - Nanoindentation did not show linear increase increasing effect to dpa of radiation exposure. - No amorphisation up to 200 dpa. - Nitrogen loss occurred at the surface. - An ion implantation threshold effect was observed at 800 °C where depth went from 120nm to 260 nm. - No bubbles or loops observed.
Radiation stability of ZrN under 2.6 MeV proton irradiation. 2009 [178]	Commercial grade ZrN rods from CERCOM I. HIPed Zr:N 0.803	2.6 MeV proton beam at 800 °C	<ul style="list-style-type: none"> - ZrN had lower densities of faulted dislocation loops than in ZrC - lattice variation induced - No radiation-induced voids or bubbles for a dose up to 0.75 dpa - No irradiation induced amorphisation or precipitates were detected at a dose of 0.35 or 0.75 dpa

	96.3% of theoretical density		<ul style="list-style-type: none"> - Microstructure dominated by a high density of dislocation loops and point defects - Radiation hardening was found for doses of 0.35 and 0.75 dpa - Dislocation density @ 0.35dpa = $8.36 \times 10^{15} \text{m}^{-2}$ loop 2.23nm - Dislocation density @ 0.75dpa = $1.12 \times 10^{16} \text{m}^{-2}$ loops 2.35nm
The effect of He and swift heavy ions on nanocrystalline zirconium nitride. 2014 [166]	Arc-vapour deposition ZrN with grain size 4 nm.	First implanted He ions 30 keV 10^{16} - $5 \times 10^{16} \text{cm}^{-2}$ Followed by irradiation with 167 MeV Xe 5×10^{13} to $1 \times 10^{14} \text{cm}^{-2}$ or 695 MeV Bi ions, $1.5 \times 10^{13} \text{cm}^{-2}$	<ul style="list-style-type: none"> - An amorphous surface may have been formed which is not easily observable by TEM causing a decrease in surface melt temperature. - Surface blistering identified.

2.7.6. Micromechanical testing of ZrN

No literature was found regarding micromechanical testing of ZrN. As ZrN is commonly used for machine tool coatings, most test data is on thin films [170]. Due to the high modulus of ZrN, samples are often characterised by vibrational techniques as bend/ tensile testing is too challenging to perform [170].

2.7.7. Nano-Indentation of ZrN

Some research has been conducted into the nanoindentation response of ZrN and ion irradiated ZrN. No evidence was found of studies involving ZrN and gold ion damage using micromechanical bend tests or nanoindentation. Egeland *et al.* conducted an extensive set of nanoindentation experiments exploring the effects of surface finish on plasticity in ZrN, and identified the major slip plane ZrN [174]. It was found that residual dislocations from polishing facilitated plastic deformation [174], while colloidal polished samples with low dislocation densities performed elastically up to a threshold value, at which point they

underwent instantaneous penetration and plastic deformation [174]. ZrO_2 crystallites were identified as potential dislocation point sources for Frank Read loops [174]. The major slip system identified in ZrN was $\{011\} \langle 0\bar{1}1 \rangle$ [174]. In a later paper, Egeland *et al.* explored the effects of heavy ion (Xe) on ZrN using TEM, grazing incident angle XRD and nanoindentation. Surface plasticity was not studied in this later paper due to an alternative experimental set up; rather, the change in hardness due to ion implantation was the focus of the study [25]. A plot of nano-hardness against displacements per atom (dpa) was developed, see Figure 51:

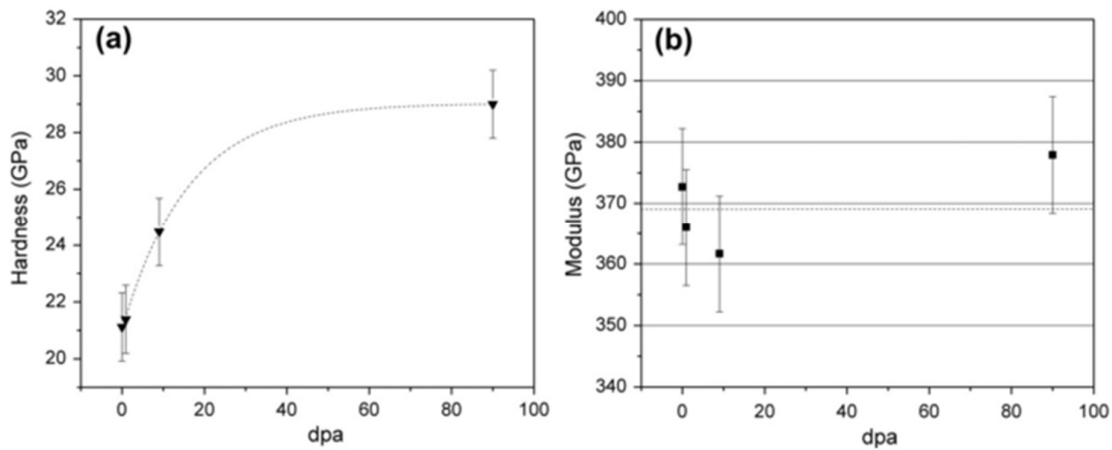


Figure 51 Nanoindentation results from Egeland *et al.* paper where hot pressed ZrN was exposed to 300 keV Xe ions at cryogenic temperatures. [A] shows the hardness against dpa. [B] shows modulus against dpa [25].

The hardness of ZrN was shown to increase with ion damage; the increase in irradiation-induced defects resulting in the pinning of dislocations and slip was attributed to the change hardness increase [25]. Modulus changes were within error: therefore, modulus is independent of ion damage. The remaining hardness/nanoindentation research conducted on ZrN was conducted by Yang *et al.* In their paper on “Radiation stability of ZrN under 2.6 MeV proton irradiation”, it was shown that the Knoop hardness of ZrN increases with dpa [178]. Yang also discusses the hardening of ZrN due to point defects, strain fields and dislocations [178]. Due to differences in experimental set up, comparing the hardness change between the two studies is ill-advised. However, from the data presented we can conclude that, up to a fluence of 100 dpa, ion implantation increases the hardness of ZrN.

Numerous other papers have discussed the hardness of magnetron sputtered ZrN films. Due to differences in microstructure (namely grain size), comparisons between hot pressed and

sputtered films is ill-advised. But to highlight this work, hardness of films has been recorded up to 39.5 GPa [164]. Plastic deformation is observed under nanoindentation conditions facilitated by glide dislocations and subsequent microcracking [179].

2.8. Concluding remarks

In producing a detailed review of the literature available for micromechanical testing and ion damage in 6H SiC and ZrN, some areas deficient in knowledge have been identified:

1. The effects of FIB machining on the mechanical properties of ceramic microbeams has not been explored.
2. A plastic deformation threshold size has been identified for compression and nanoindentation in 6H SiC, but has not yet been identified during micro bend testing.
3. There is a limited quantity of work comparing nanoindentation and micromechanical testing of ceramics following ion irradiation
4. The mechanical properties of ZrN following high dose ion irradiation has not been fully explored.

3. Experimental procedures

This chapter details the experimental methodologies used to obtain the results of the experimentation in this study.

3.1. Raw materials

3.1.1.1. Silicon carbide (SiC)

Single crystal 6H SiC was selected as a model material to develop the micro bend test technique. Single crystal SiC allowed the micro beams to be tested with consistent crystallographic orientation, no grain boundaries and a limited number of defects. By isolating these experimental factors, it was expected that the effects of sample size and ion beam cleaning could more clearly be evaluated. 6H single crystal SiC was sourced from Marketech International (Port Townsend, USA).

The crystals were provided as $0.3 \times 6 \times 6$ mm wafers with a polished top face parallel to the 0001 plane. Six samples were purchased; nano indentation, XPS and micro bending were conducted on individual wafers. SEM was conducted on the nano indentation specimen before indentation. An image of a 6H SiC wafer is shown in Figure 52:

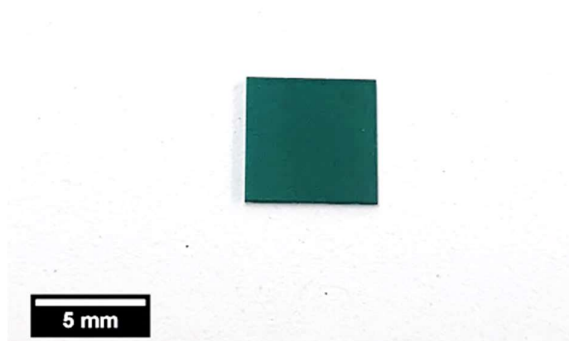


Figure 52 As supplied 6H SiC wafer

3.1.1.2. Zirconium nitride

All zirconium nitride (ZrN) samples were provided by Dr Guo-Jun Zhang (Donghua University/Shanghai Institute of Ceramics, Shanghai, China).

ZrN materials were manufactured by hot-pressing commercial ZrN powder (Beijing Dk Nano Technology Co., Ltd., Beijing, China). The as-purchased powder had a lattice parameter of 4.5783 Å (D50=800 nm, D90=1000 nm). The ZrN content was 95 wt%; the other chemicals in the powder are listed in **Table 12**, as claimed by the supplier:

Table 12 Chemical composition of other chemicals in ZrN powder.

Ingredient	Hf	Na	Fe	O
wt%	2.6	0.8	0.3	1.0

The as-purchased ZrN powder was dispersed in ethanol in a polyethene plastic bottle with silicon nitride spherical balls (~10 mm) included. The weight ratio of ZrN to milling medium was 2:1. After sealing, the bottle was ball milled at 120 rpm for 24 hours. Following ball milling, the slurry was dried at 60°C in a vacuum using a rotary evaporator. The dried powder was sieved through a 200-mesh screen to eliminate large lumps. The milled powder was filled in a graphite die coated with boron nitride. Graphite sheets were set between ZrN powder and punches. The sintering procedure involved the following steps: firstly the furnace was pumped down to a vacuum of 10 Pa while the temperature was raised to 1300°C in order to remove absorbed gases from the powder. Secondly, Ar gas was purged into the chamber. Finally, hot-pressing was accomplished in a flowing Ar environment at 2000°C with a dwelling time of 1 hr and normal pressure of 30 MPa.

The surface scale of the as-manufactured ZrN samples was ground off. Their densities were measured using the Archimedes method, giving an average of 7.17 g/cm³, equivalent to 98% of the theoretical density (7.32 g/cm³). Samples with a size of 5 × 5 × 5 mm³ were cut from an as-ground block. The surfaces to be irradiated were finished by polishing with diamond slurry with an average grit size of 2.5, 1 and 0.5 μm successively (UNIPOL-802, Shenyang Kejing Auto-instrument Co., Ltd., China).

A 4 MeV Au²⁺ ion beam was used for irradiating ZrN on the PKU Tandem Accelerator at room temperature with an accumulated ion fluence of 5×10¹⁶/cm². The chamber was kept at a

vacuum below 10×10^{-3} Pa, and the direction of ion beam was perpendicular to the surface of bulk ZrN.

For the experiments conducted, samples of irradiated and unirradiated ZrN approximately $5 \times 3 \times 2$ mm were supplied. The locations of the samples within the original hot-pressed sample is unknown. Some variation in properties maybe related to the position of the sample within the original sample. Furthermore, due to the small volume of material tested, the results should be viewed conservatively. An image of the ZrN samples is shown in **Figure 53**:



Figure 53 Mounted samples of irradiated and unirradiated ZrN.

3.2. Sample preparation

Where necessary, samples were sectioned with a Pace technologies diamond cut off wheel using an Accutom-5 sectioning saw (Struers, Cleveland, USA). A disc speed of 8000 rpm and feed of 0.01 mm/min was used while the sample and disc were flushed with polymer coolant. Samples were then hot or cold mounted dependent on their intended purpose.

Sample polishing was conducted with a Labopol-30 with Labopress-100 (Struers, Cleveland, USA) autoloading and dosing system see Table 13 . Polishing times were reduced if sufficient material was removed, and loads were reduced for samples with a low surface area. Where electron backscatter diffraction (EBSD) was to be conducted, polishing with Struers, OP-S 0.04 μm colloidal silica ((Struers, Cleveland, USA) was added on to the standard polishing

regime. Where appropriate, samples were cleaned with Acetone and ozone cleaned with a ZONE sample cleaner (Hitachi high tec, Toronto, Canada).

Table 13 Sample polishing regime.

Plate name	Plate (rpm)	Sample (rpm)	Time (min)	Load (N)
MD-Piano 220 grit	300	150	15	45
MD-Piano 500 grit	150	150	3	35
MD-Piano 1200 grit	150	150	5	25
MD-Plan 9 µm	150	150	5	15
MD- Dac 3 µm	150	150	2	10
MD-Plan 9 µm	150	150	5	15
MD- Dac 3 µm	150	150	2	10
MD- Nap 1 µm	150	150	2	10
MD- Chem + colloidal silica	150	150	10	10
Water- flooding to remove remaining silica	150	150	30 s	Decreasing to 2 N

3.3. Characterisation

The schedule of characterisation for SiC and ZrN are detailed in (Figure 54 and Figure 55) respectively. These figures are supplied to elucidate the purpose, order and aims of each test:

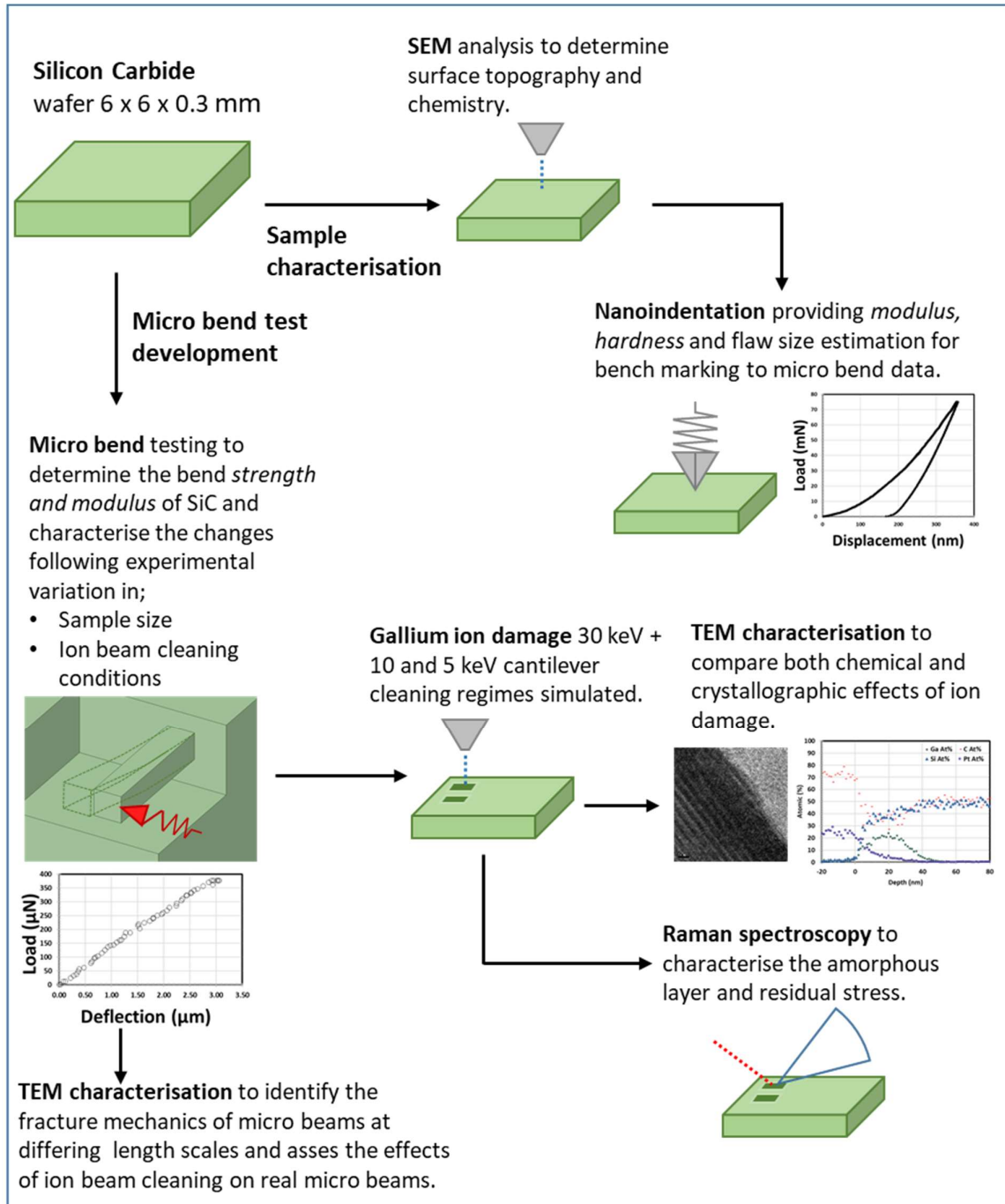


Figure 54 Characterisation schedule for SiC detailing the initial sample characterisation steps to confirm the quality, and benchmark mechanical properties and subsequent micro bend test technique development, including size effect analysis and ion beam cleaning effect analysis.

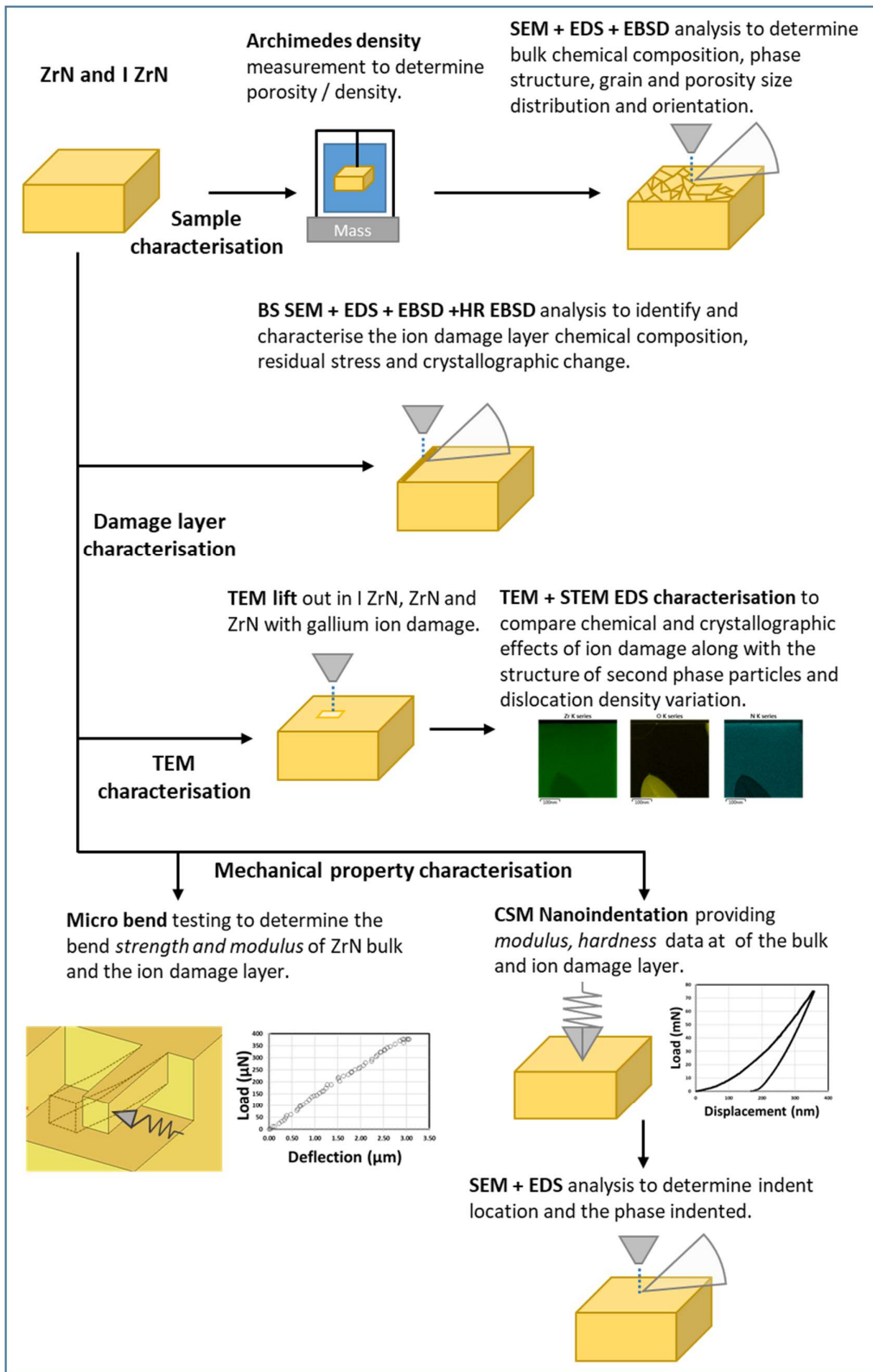


Figure 55 Characterisation schedule for the ZrN and irradiated ZrN samples. Initial sample quality was assessed with SEM and TEM; following this the damage layer was characterised mechanically with micro bend testing and nanoindentation.

A summary of the sample and experimental techniques used is presented in (Table 14) where the details of the experimental aims are detailed:

Table 14 Table of experiments and samples, with attention to the aims of each experimental technique.

Technique	Sample			Aims
	6H SiC	ZrN	I ZrN	
XRD		×	×	ZrN- Identify constituent phases and lattice parameter.
XPS	×			SiC- Identify composition, oxide layers and suitability for nanoindentation.
SEM				SiC- Characterise surface topography for nanoindentation and measure nanoindentation sizes.
	×	×	×	ZrN- Identify grain structure, ion damage layer and characterise nano indents.
SEM-EDS				SiC- Confirm composition and check for impurities.
	×	×	×	ZrN- Identify phase composition, ion damage and nano indent locations.
SEM-EBSD				ZrN- Characterise grain structure, grain boundaries, texture and residual stress caused by ion implantation.
		×	×	
Nanoindentation				SiC – Characterise Young's modulus and assess size effect.
	×	×	×	ZrN- Characterise effects of ion damage and identify Young's modulus and size effect
X section TEM				SiC- Nano indent dislocation / slip plane analysis.
	×	×	×	ZrN – Ion damage characterisation.
STEM-EDS				ZrN- Chemical composition analysis of each phase and the ion damage layer.
		×	×	

Ga implantation+ X section TEM + STEM EDS	×	×	×	SiC + ZrN- Effects of gallium ion damage on structural integrity. Characterisation of damage layer depth.
Ion beam cleaning micro bend tests	×			SiC- Characterise the effects of ion beam cleaning on micro bend strength and modulus.
Micro bend size effect	×			SiC- Characterise the effects of cantilever size on strength and modulus.
Micro bend testing	×	×	×	SiC- Characterisation of modulus and strength. ZrN / I ZrN- localised effects of gold ion damage on Young's modulus and strength in ZrN
Raman	×			SiC- Assess the effects of gallium ion damage and amorphisation.

3.3.1. Scanning electron microscopy (SEM)

Scanning electron microscopy has been pivotal to this project for the characterisation of topography, chemical and crystallographic change in both materials systems. This is due to the wide range of interactions electrons have with matter, as shown in Figure 56:

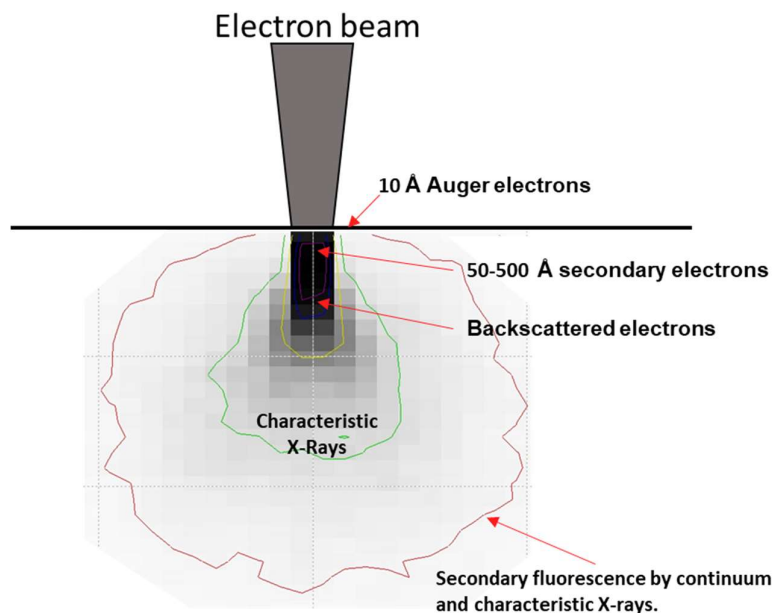


Figure 56 Schematic diagram of electron beam surface interaction, developed in CASINO V2.

Electron images are formed from both secondary and backscattered (BSE) electrons. These images provide topographic and atomic mass contrast, while the characteristic x-ray produced can be used to determine chemical composition. Crystallographic orientation maps can also be developed with the use of electron backscatter diffraction (EBSD).

Electron microscopes consist of an electron source in a vacuum chamber with a detector such as an Everhart Thornley (EHT). The EHT detector uses a negatively charged grid to accelerate secondary electrons to the detector; backscattered electrons have considerably more energy, thus they travel to the detector based on line of sight. These differences in electron motion cause a sense of perspective in electron beam images dependent on where the detector is placed. As well as perspective, the effects of interaction volume of the electron beam with the sample results in edge contrast formed by the additional signal from the larger relative surface area of edges to surfaces. During micromechanical testing, edge, effects and image perspective have potential to introduce error. To limit the effects of perspective, microbeams were tested with the length of the beam perpendicular to the EHT. Using an in-lens detector removes any perspective effects but is not feasible in all systems, due in part to the electromagnetic forces around the lens. There are many factors which affect the edge brightness of the microcantilevers during testing. Current and voltage affect edge brightness, and reducing both reduces the brightness but results in an extended image acquisition time. An acceptable compromise between image quality, edge brightness/contrast and acquisition time must be achieved, based on the sample size material and microscope specification.

Scanning electron microscopy was utilized to measure indent dimensions and microstructural features, and to determine chemical and crystallographic properties of samples. SEM was conducted with a JMS-7800F field emission (Jeol, Tokyo, Japan) equipped with backscatter (BSD) detector (SM84030SRBE, Jeol, Tokyo, Japan), electron backscatter detector (EBSD) (Nordlys Nano, Oxford Instruments, Oxford, UK), and energy dispersive spectroscopy detector (EDS) (Oxford X-Maxⁿ 80, Oxford Instruments, Oxford, UK). Backscatter electron images were taken at 5-15 keV and image analysis was conducted using ImageJ. When imaging for measurement purposes, the area of interest was magnified to fill the imaging window as much as possible to allow easy measurement of the feature of interest. Image contrast and brightness were tuned in the SEM to ensure areas were not 100% black or white in any region of interest. When required, post processing was used to improve image contrast; however, selective contrast or brightness modification have not been used.

3.3.1.1. *Energy dispersive spectroscopy (EDS)*

EDS mapping consists of an electron beam scanning across a sample surface. The electron beam causes elements in the specimen to become ionized and emit characteristic X-rays. By detecting the energy spectrum of emitted X-rays, elements in the specimen can be identified. Measuring X-rays within a specific energy window across the scanned surface allows elemental maps to be obtained. The focused electron spot of a typical field emission (FEG) SEM is around 10 nm, while the resolution of EDS mapping is fundamentally limited by the interaction volume of the electron beam within the sample. This is usually much larger than the focused electron spot when working at typical analytical conditions; beam energy > 15 keV results in a spot size of around 10 nm. Simulated probe size estimates have been compiled in Table 15 below. By reducing the beam energy / accelerating voltage, the electron spot size and EDS probe size can be matched. Reducing probe size results in extended scan times. Further to this the low input energy only excites lower energy states, making mapping of heavy elements more challenging while improving resolution to light elements.

For the EDS analysis of the ZrN samples, the bulk material was scanned at 5 keV to provide sufficient signal while providing information on the nitrogen and oxygen content of the sample. Probe currents from 1-10 nA were used to provide sufficient signal, while dwell times of 1000 ns were used to limit collection time and sample drift. Typical scan times were 3-6 minutes. To identify the gold implanted region, mapping at higher accelerating voltages (10-20 keV) was tested attempted.

Following collection, EDS maps were processed with Oxford Aztec software (Oxford Instruments, Oxford, UK). Each map was converted to atomic % and coloured using the “normalised” mode. Unless stated, both M and L spectral lines have been used to fit the spectra.

CASINO v2 (Sherbrooke, Quebec, Canada) software was used to estimate the probe size of each of the materials systems studied at a range of accelerating voltages. An idealised set up was used for the simulation with a consistent spot size of 10 nm. 100,000 electrons were simulated from 5-30 keV in 5 keV increments for each material (an example simulation is shown in Figure 57 below). Based on these simulations, the energy distribution was plotted

and the 50th percentile diameter measured for each of the materials and accelerating voltages, as suggested by Child *et al* [180].

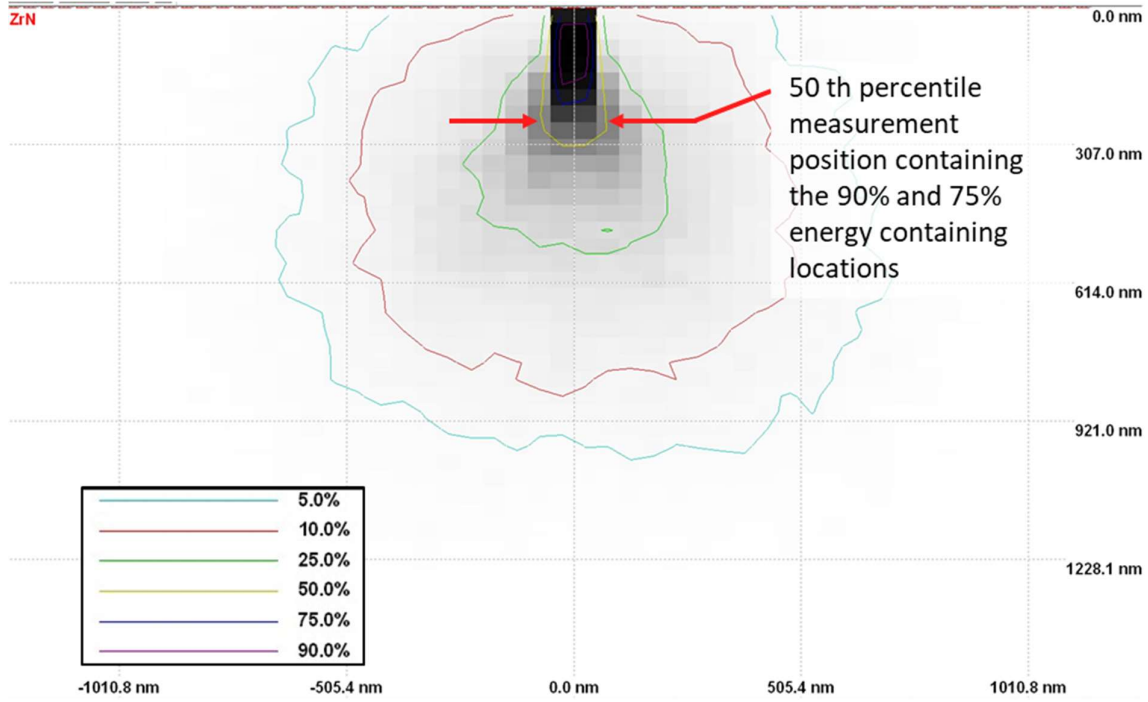


Figure 57 Energy distribution plot from ZrN at 20 keV in cross-section showing the location at which the electron beam probe size was measured, calculated in CASINO v2.

Table 15 Energy distribution plot 50th percentile diameter for each material system simulated with CASINO V2 Monte Carlo software and tabulated for each accelerating voltage.

	SiC	ZrN	ZrO ₂	Zr ₂ ON ₂
Density (g/cm³)	3.14	7.1	5.68	3.67 *
Accelerating voltage (keV)	50 th percentile energy diameter (nm)			
5	17	53	33	18
10	72	52	64	74
15	116	56	162	149
20	240	146	162	244
25	428	171	356	457
30	295	322	363	366

*calculated theoretical density of Zr₂ON₂ as no literature was available.

The main point to take from these simulations is that the probe size difference will be large between the ZrN and any oxide based particles. For all the material systems, images of features from 70 nm in thickness should be resolvable.

3.3.1.2. *Electron backscatter diffraction (EBSD)*

EBSD is conducted by tilting a sample to 70° (20° to the electron beam) and applying an electron beam 10-30 keV at a probe current of 1-20 nA. If the sample surface is sufficiently defect free, electrons will be backscattered from the surface in a spherical nature. These patterns are used to excite a phosphor screen, and these interrelations are recorded by a digital camera. The patterns relate to the crystal orientation of the sample. By rastering the electron beam across the surface and indexing the collected patterns, orientation maps can be developed. A schematic representation for the EBSD setup is shown in Figure 58:

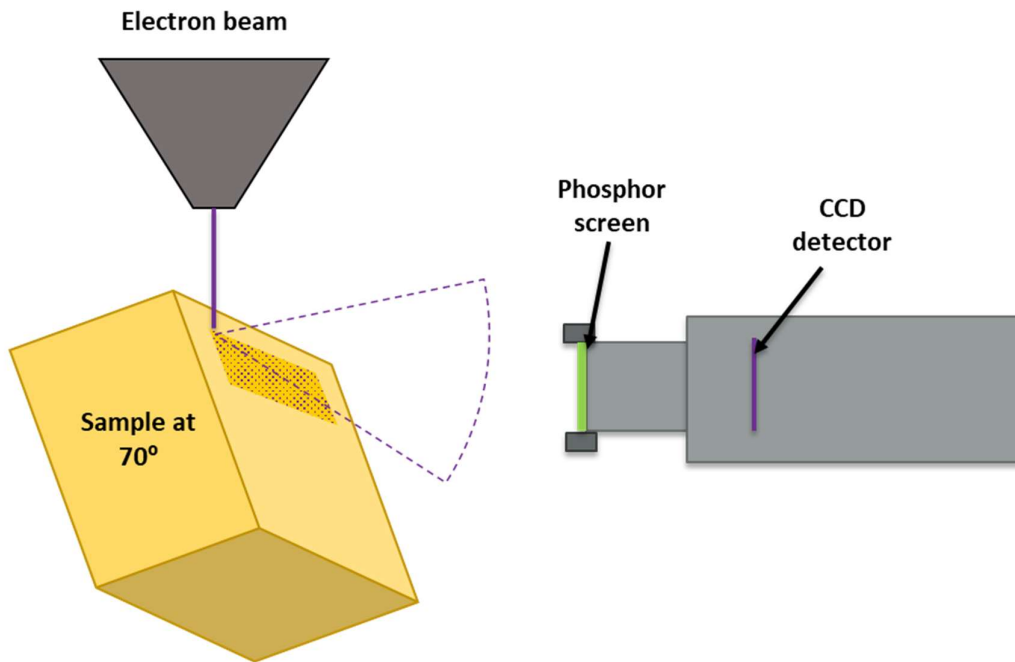


Figure 58 Schematic diagram showing a standard electron back scatter diffraction microscope setup.

EBSD patterns were collected at 20 keV with a probe current of 12-20 nA and specimen tilt of 70° . Binning of 6×6 was used to balance pattern quality and collection time (13.56 ns per pixel). Background images of the detector were used to reduce effects of contamination on the phosphor screen. A step size of $0.3 \mu\text{m}$ was used, and scanning took 1 hour 30 minutes.

The ZrN sample was found to be dual phase, comprising of ZrN and Zr₂ON₂. Both these phases are FCC, making indexing challenging; therefore, EDS assisted EBSD was used to resolve the two phases. The JEOL 7800 SEM is capable of producing a spot size of 10 nm diameter at 20 keV; the probe size in ZrN is around 0.15 μm and a step size of 0.3 μm was deemed sufficient for grain and orientation mapping. This setup offered limited drift while producing high-quality data in a timely manner. Example un-indexed and indexed patterns can be seen **Figure 59**:

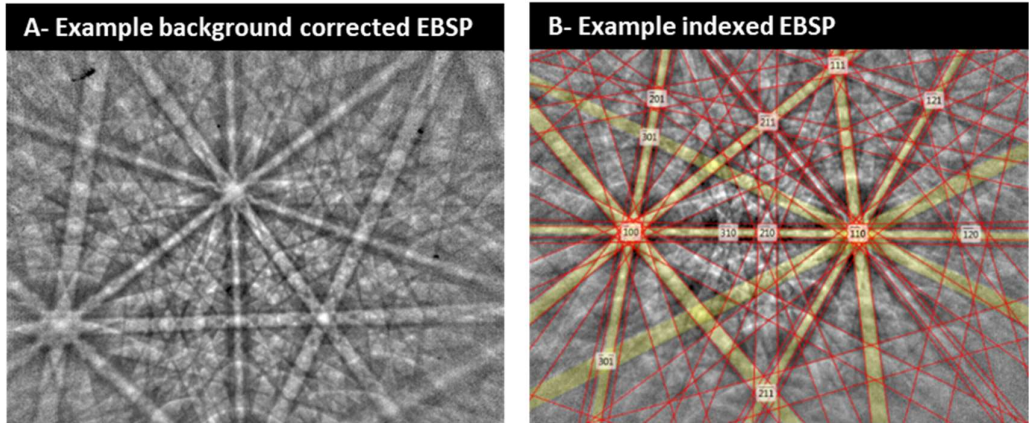


Figure 59 A- Example electron backscatter patterns (EBSP) collected from ZrN at 20 keV 1x1 binning. B- indexed ZrN EBSP.

EBSD data analysis was performed with the Tango and Mango processing tools (Oxford Instruments, Oxford, UK). From the patterns collected, grain size and grain orientation were calculated along with data specific to the quality of the Kikuchi patterns.

Grain orientation was calculated by identifying a pattern with a 10° difference to its nearest neighbours. This variation in orientation was used to identify each grain. Each grain was then characterised by its length in the x and y dimension, thus providing each grain's equivalent circle diameter and aspect ratio. For accurate quantitative grain size/distribution based on EBSD >200, grains are recommended with around 100 points per grain [181].

Below are the definitions and explanations of EBSD terms using Oxford instruments naming/processing conventions for pattern quality;

- Mean angular deviation (MAD) is an angular deviation value generated by comparing the simulated Kikuchi band and the collected band. Here, lower values are preferred indicating a good fit [131].

- Band contrast (BC) is derived from the Hough transform that describes the average intensity of the Kikuchi band with respect to the overall intensity of the pattern [182]. These values are scaled to a byte range 0 to 255, where 0 is low contrast (poor quality) and 255 is high contrast (high quality) [182]. These values plotted black to white in 2D give analogous results to SEM images, as grain boundaries have low contrast while grains with good signal produce bright regions. BC is affected by the diffraction intensity of a phase; dislocations / crystallographic defects and orientation are a component of this brightness.
- Band slope (BS) is calculated in a manner similar to BC; however, BS is concerned with the sharpness (maximum contrast gradient) of the Kikuchi bands [182]. BS is more sensitive to strain but less sensitive to small orientation changes than BC.

Pattern quality as a technique for determining strain in a quantitative manner is no longer widely used, as reference samples are required to calibrate the grey value to a strain level [181]. Wilkinson *et al.* conducted a range of EBSD pattern analyses on strained aluminium to determine the effect of strain on pattern quality [183]. Wilkinson concluded that band contrast was reduced with deformation in a nonlinear fashion, with a dependency on the orientation of the crystal analysed [183]. Plastic deformation strain measurements in metals have been widely conducted using intragranular misorientations which result from the residual dislocations accumulated during plastic straining [181].

3.3.1.3. *High-resolution electron backscatter diffraction HR-EBSD*

High-resolution electron backscatter diffraction (HR-EBSD) patterns were collected in essentially the same manner as standard EBSD patterns. Due to the increased pattern quality required, a few steps were taken to ensure accurate HR-EBSD analysis was possible. For HR-EBSD analysis 1×1 binning was utilised and all patterns were saved for post-processing in Crosscourt 4 (BLG Vantage, Bristol, UK). For HR-EBSD, pattern size is directly linked to stress resolution; as such, 1000 x 1000 sensors are preferred. A Helios G4 PFIB CXe (FIB), (FEI, Oregon, USA) equipped with a Symmetry: EBSD Detector, (Oxford Instruments, Oxford, UK) was used for the collection of the HR-EBSD data. This had the added benefit of reducing scanning times, resulting in limited sample drift.

The microscope magnification was set to 13000 x magnification with an accelerating voltage of 20 keV and 13 nA. Scans of 2 μm x 3 μm were conducted with a step size of 0.04 μm . The pattern collection time used was 43 ms. To improve spatial resolution the sample was rotated to scan the side of the sample, rather than scanning from the ion irradiated surface to the bulk, as shown in **Figure 60 A**:

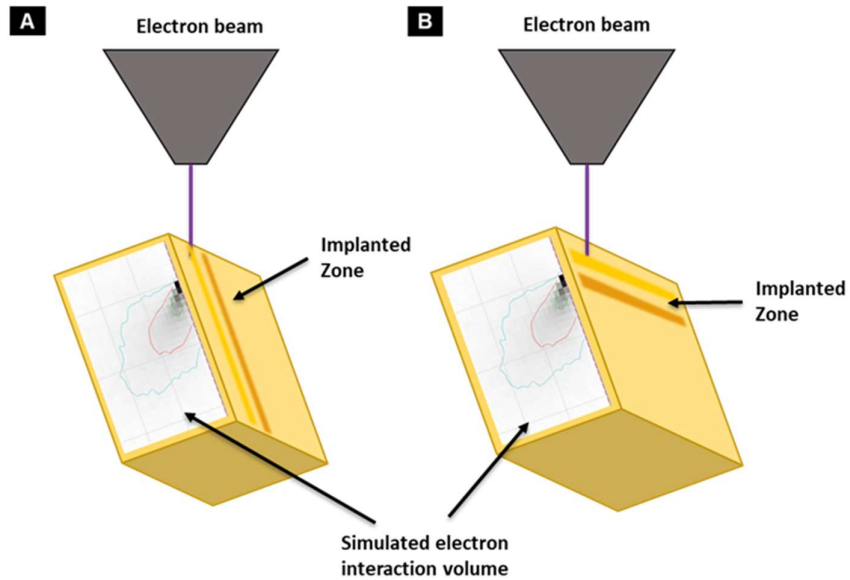


Figure 60 Schematic representation of [A] optimised sample orientation for HR-EBSD, [B] typical sample orientation for EBSD.

Due to sample tilt, the interaction volume in the z direction is greater than x and y; as such rotating the sample will improve the spatial resolution for layers parallel to the surface. For HR-EBSD scanning beyond 3 μm in the Y direction of the sample, calibration of the beam is required to account for beam stigmatism caused by the tilt angle of the sample. 3 μm was deemed sufficient to characterise the bulk below the ion damage zone. Before scanning, a phosphor background image was collected. The screen was clear of contamination.

Before map collection, the field of view was assessed to identify potential single grain areas and areas with indexable high-quality patterns. Particles of the second phase (Zr_2ON_2) were avoided to make processing simpler.

Based on the tutorials and literature provided by BLG, the EBSD patterns were processed; reference points were located using kernel average misorientation to identify areas of potential low strain. These data points are denoted on the maps as a pixel with a cross within it. Following this, the FFT processing was addressed; based on the work of Tong *et al.* and

the BLG software guide, a low frequency cut off 8, width LF 8, High frequency cut off 29 and width HF was used [184]. 20 regions of interest (ROI's) with an area of 256 x 256 pixels per region were used, and these regions were distributed in a circle automatically by the software. BLG recommends a minimum of 4 regions is used for cross-correlation; analysis was conducted with 20 ROIs as is suggested in the software and literature. Robust fitting was used rather than least squares regression. Robust fitting is recommended in samples with dislocations, as were identified in the ZrN irradiated and polished surfaces. Results are presented with the conventions laid out in **Figure 61**:

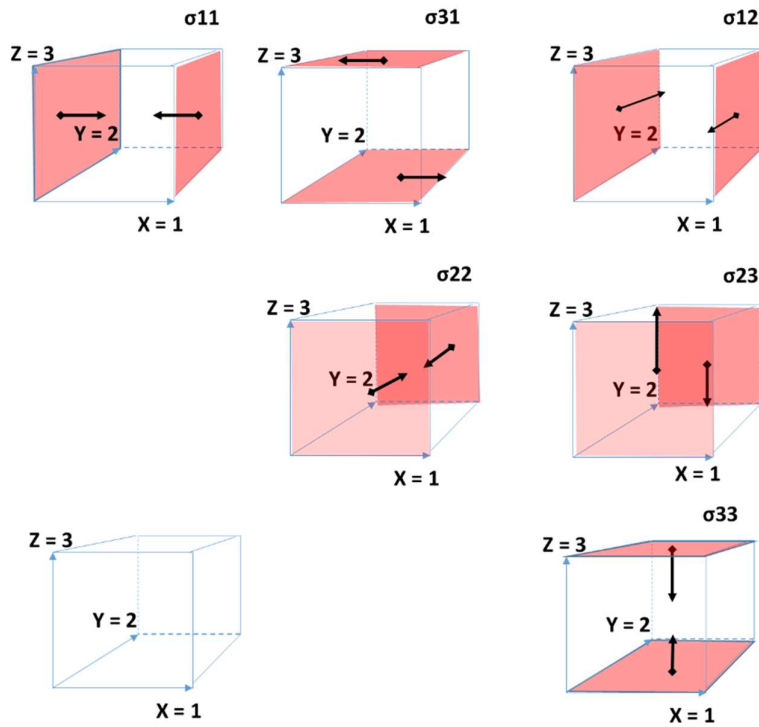


Figure 61 Graphical representation of each of the stress states. The red faces denote the face in which the stress is acting and the arrows denote the direction of the stress. For clarity, the z-direction is the plane out of the sample (the electron beam direction).

3.3.1.4. Image quantification

To measure features in the SEM, images were scaled and measured in ImageJ using the measure tool. Where appropriate, grey values have been plotted using the ImageJ plot profile feature, and using the box tool to produce averaged profiles where necessary.

To determine the porosity of the ZrN samples, 20 backscatter electron images were batch scaled and thresholded. Following thresholding, each image was checked by eye to ensure the

process had identified the porosity. Image J's particle counting tool was then used to identify the residual porosity. Grain size analysis was conducted using a liner intercept method, whereby a random grid of up to 7 lines was drawn on each micrograph. The length of the line and number of grain boundary intersections were recorded. The line length was divided by the number of intersections and the average value is presented as the grain size.

3.3.2. X-ray diffraction (XRD)

Phase identification and lattice parameter determination were carried out by X-ray diffraction (XRD) using a Bruker Phaser D2 (Bruker, Massachusetts, USA) with a Cu-k α source and a nickel detector cover. Large samples were mounted in plasticine and rotated during analysis. Small samples were mounted on a wafer of silicon and not rotated during analysis. International Centre for Diffraction (ICDD) cards embedded in the Bruker analysis software were used to identify the sample phases. XRD processing included minor smoothing and background removal PeakFit (Systat Software Inc, California, USA) was used to characterise the peak position and full width half maximum (FWHM) of each peak.

3.4. Transmission electron microscopy (TEM) Analysis

3.4.1. TEM Sample preparation

A dual beam Nanolab 600 FEI focused ion beam (FIB),(FEI, Oregon, USA), which combines a focused ion beam and field emission gun scanning electron microscope (FEGSEM), was used for preparing transmission electron microscope samples.

To prepare TEM samples, first a platinum layer was deposited to protect the lamellar from ion damage and to improve milling consistency. For previously ion damaged samples or samples with surface layers of interest, an electron beam layer of platinum 0.5 μm was deposited before a 1.5 - 2 μm layer of ion beam platinum was deposited. For unirradiated samples, a layer of ion beam platinum only was deposited. Following this, staircase cuts were made on either side of the platinum at 20 nA current. The lamellar was then cleaned to 1 - 2 μm in thickness with successively lower beam currents (see **Figure 62**). At low beam currents (1 nA or less), the sample was cleaned at $\pm 1.5^\circ$. Once reduced in thickness, the lamellar was milled from the bulk material and platinum welded to a micromanipulator. The lamellar was then platinum welded to a copper half grid, the probe removed and the sample thinned to

250-100 nm in thickness (see **Figure 62** E-F). Lamellar sizes ranged from $20 \times 9 \mu\text{m}$ to $10 \times 5 \mu\text{m}$ depending on the purpose of the lift out. Samples that were to be analysed with STEM-EDS were placed on flag post positions on the grid to limit copper signals on the EDS spectra.

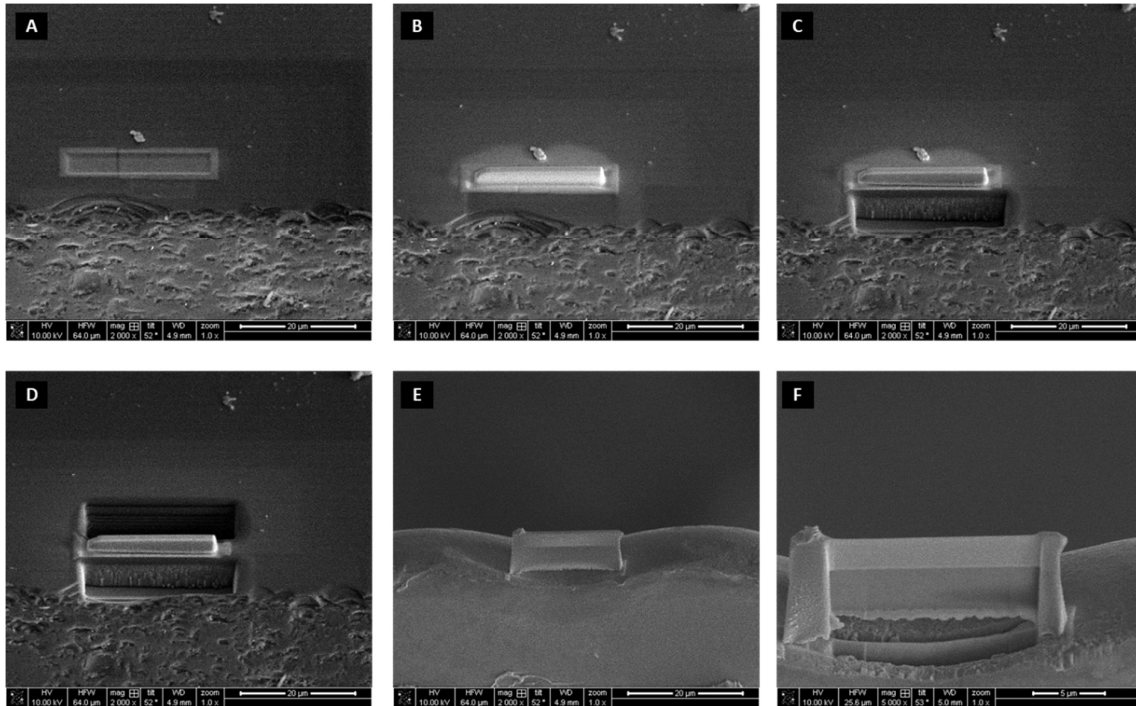


Figure 62 Focused ion beam lift out process (A-F) A shows the ion damage phase and electron beam platinum deposition. B shows the ion beam platinum. C-D shows the staircase cutting either side of the lamella. E-F shows the thinning of the lamella on a "V" grid position.

To assess the effects of gallium ion damage, lamellar were lifted from areas exposed to controlled doses of gallium ions. Initially, a $2 \mu\text{m} \times 20 \mu\text{m}$ box was milled at 30 keV, 3 nA to a depth of $0.01 \mu\text{m}$ to remove any surface damage or redistribution. The left side of the box was then capped with a layer of electron beam platinum. The central region was exposed to 10 keV, 50 pA for 20 s over an area of $20 \mu\text{m}^2$. Once each step was completed, the area was capped with electron platinum to mitigate any potential ion damage from depositing ion beam platinum. This process was repeated with 5 keV 70 pA over an area of $20 \mu\text{m}^2$. A standard TEM lift out was then conducted on the area as shown in Figure 63:

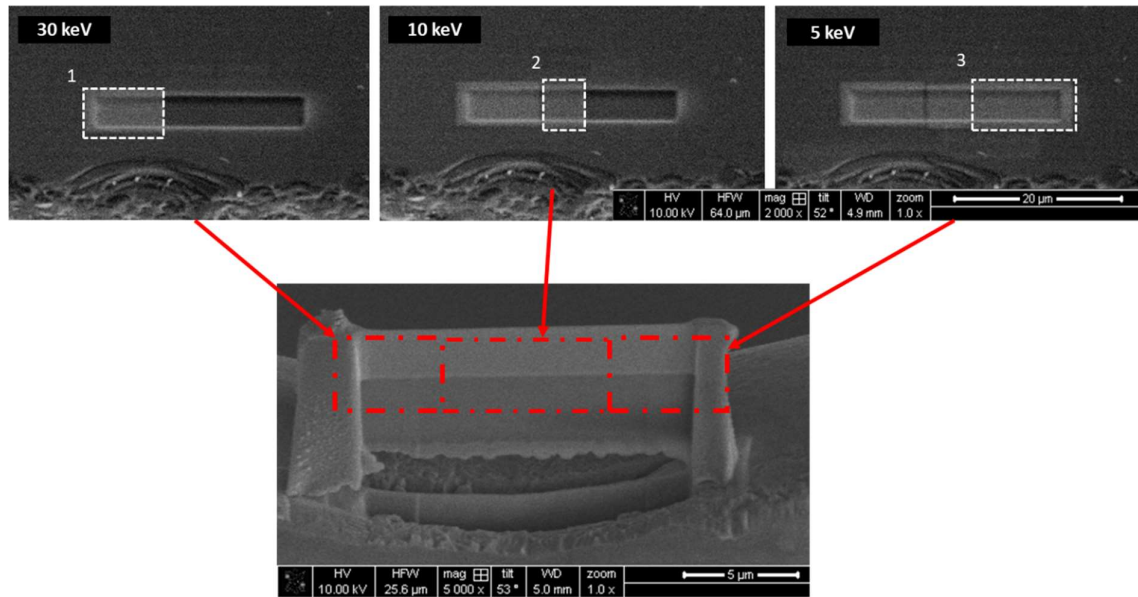


Figure 63 Selective gallium ion damage lamellar preparation showing the location of each of the ion beam implanted areas located in the TEM lamellar.

3.4.2. Conventional transmission electron microscopy

Much of the conventional transmission electron microscopy (TEM) imaging and selective area diffraction (SAD) was undertaken on the JEOL JEM 2000fx (JEOL, Tokyo, Japan). Image capture was undertaken with a charged coupled device (CCD) Erlangshen (Gatan, Pleasanton, USA) camera mounted in the middle position (at 100 cm). TEM imaging and SAD were used to identify ion beam damage layers, quantify dislocation densities and assess crystallographic orientation and phase. Dislocation quantification was conducted using the linear intercept method whereby random lines were drawn on a scaled image and the number of dislocations intersecting with the lines is counted, and a dislocation density given by:

$$\rho = \frac{2n}{Rt}$$

(31) [185]

where ρ is dislocation density, n is the number of line dislocation intercepts, R is the total line length over the micrograph and t is lamellar thickness (150 nm estimated).

Regression analysis was conducted to determine the appropriate number of lines to place on each micrograph. A simple dislocation counting method was also tested: however, it was found to be more laborious and susceptible to user error.

The d spacings of samples were measured using the linear distance between the bright spots in single crystal diffraction patterns. Equation (32) gives the d spacing value:

$$d = \frac{L\lambda}{R} \tag{32}$$

where L is the camera length (100 cm JEOL TEM, 255 cm Tecni TEM), λ is the wavelength of the electron beam at the accelerating voltage used to record the image $200 \text{ keV} = 0.00273 \text{ nm}$, and R is the distance between two bright spots or radius of the amorphous ring.

Calibration of the TEMs was undertaken by the Loughborough materials characterisation centre (LMCC) TEM microscopy technician; however, rotation calibration on the JEOL is user calibrated. For this molybdenum trioxide rotation calibration was undertaken; using a calibration sample from Agar Scientific, a rotation of -8° (anti-clockwise) was identified from images to diffraction patterns

3.4.3. High-resolution electron microscopy (HRTEM)

High-resolution imaging was conducted in the Tecni TEM; firstly, the sample was orientated close to an indexable zone axis. Once in an appropriate orientation, the magnification was increased to $600,000 \times$ magnification. Live FFT processing was then used to tune the objective focus. This simplified HRTEM operating procedure was feasible due to the pre-alignment of the beam. Where appropriate, HRTEM images were processed with Digital micrograph FFT processing (Gatan, Pleasanton, USA).

3.4.4. Scanning transmission electron microscopy and Energy-dispersive X-ray spectroscopy (STEM-EDS)

EDS mapping and line scans were undertaken in the STEM. STEM-EDS has a higher resolution when compared to SEM. This is primarily based on the lower interaction volume

of the sample due to the small lamellar thickness. Further to this, the increased excitation voltage results in a higher resolution to heavy elements when compared to the SEM-EDS. All EDS data processing was conducted with Aztec for TEM software (Oxford Instruments, Oxford, UK). Element maps and scans were converted to atomic percent and counts.

3.5. Microbeam testing

3.5.1. Focused ion beam microscopy

Ions are distinctly heavier than electrons: the lightest ions are 250 times heavier than an electron, while larger ions are 2000 times more massive. Ions are particles where the number of electrons and protons are not balanced, resulting in a positive or negative charge. For convenience, gallium ion sources are common. Due to the large size of ions, their interactions with surfaces when accelerated are quite different to those of electrons, as discussed in the literature review.

Unlike electrons, ions cause milling/sputtering of the surface, along with implantation and amorphization, and can be used to break down gases to provide enhanced milling or welding capabilities. Ion images have more channelling contrast than electron beam images. For micromechanical testing ions, beams can be used to manufacture microbeams through milling. However, the introduction of surface damage during ion milling must be considered. Focused ion beam (FIB) systems use an electron column and ion beam column to allow the cutting and imaging of samples. A layout of this type of system is shown in Figure 64:

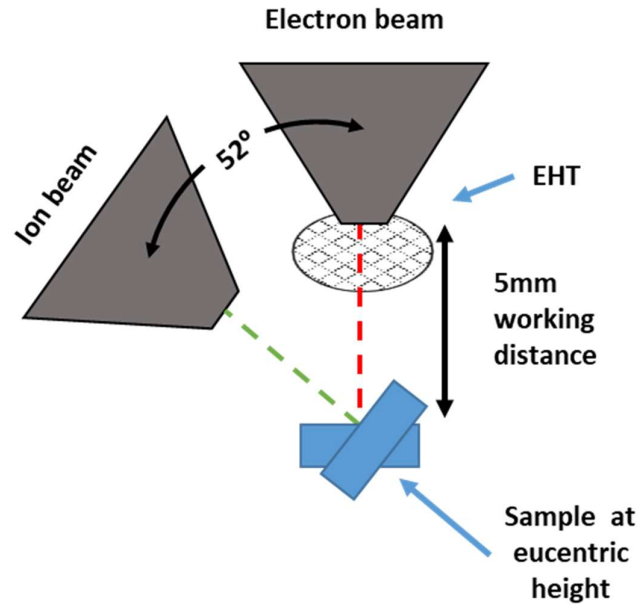


Figure 64 Focused ion beam schematic showing the location of the ion beam and electron beam relative to the sample.

The position of the EHT at the back of the chamber explains the shadowing effects that can be observed in secondary electron images.

The various techniques used to prepare microbeams and TEM cross-section lift outs in the FIB are detailed in the following sections.

3.5.2. Microbeam preparation

The silicon carbide and zirconium nitride microcantilever beams were prepared using an FEI focused ion beam (FIB) system. To ensure the prismatic planes of the SiC beams were parallel to the 0001 plane of SiC, a three-stage milling technique was developed. At the corner of the sample, two rectangular areas were milled 4 μm deep parallel to each other leaving a central area approximately 4 μm x 15 μm . This formed a lamella. Milling was conducted at 30 keV with diminishing currents from 20 nA to 0.3 nA, dependent on the volume of material removal required. Following this, the sample was removed from the FIB and re-orientated to allow undercutting of the beam. Once undercutting to the required dimensions was complete, the bottom faces of the beams were cleaned at 30 keV 0.3 nA, 10 keV 50 pA 20 s and 5 keV 70 pA 30 s respectively. Three micro beams were bent at each

cleaning voltage. Once cleaned, the sample was reoriented and returned to the FIB for final sizing, cleaning and testing. Due to the Gaussian distribution of the low current gallium ion beam, a tilt angle of 1° was used to preserve the parallelism between the opposing faces of the microbeams. (**Figure 65**) details the milling steps undertaken to manufacture the SiC microbeams:

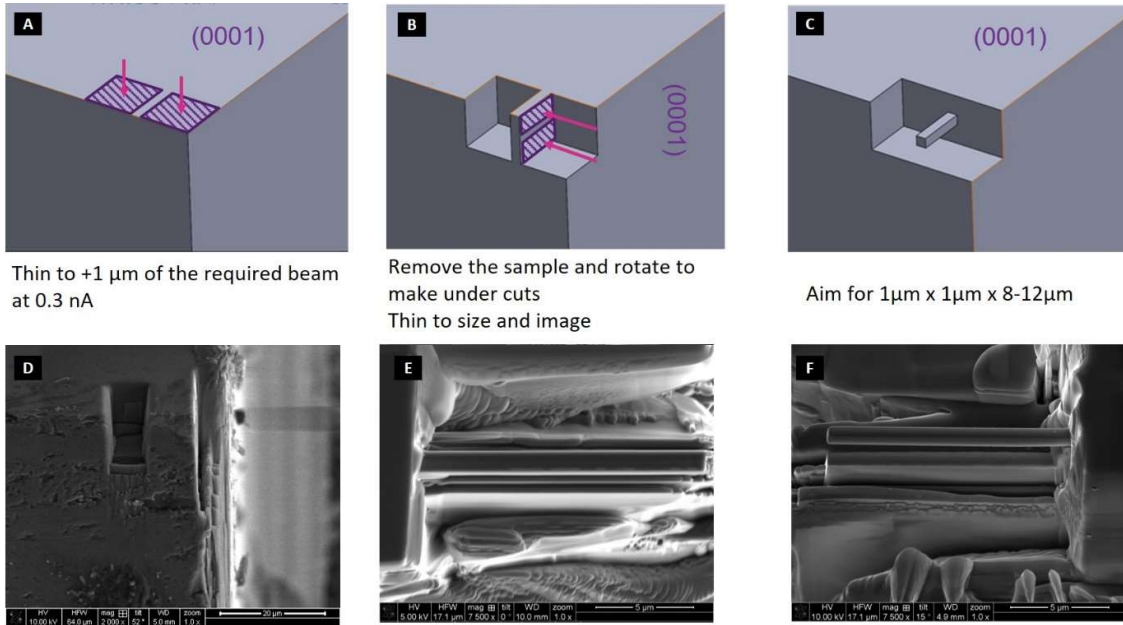


Figure 65 (A-B) shows a CAD representation of the micro bend preparation technique used for the SiC sample. (D-F) shows the corresponding steps in the FIB.

This method of manufacture results in a true cantilever with all faces fully constrained. For the ion damage samples or ZrN, the microbeams were cut from the surface of the material, making the top face semi unconstrained.

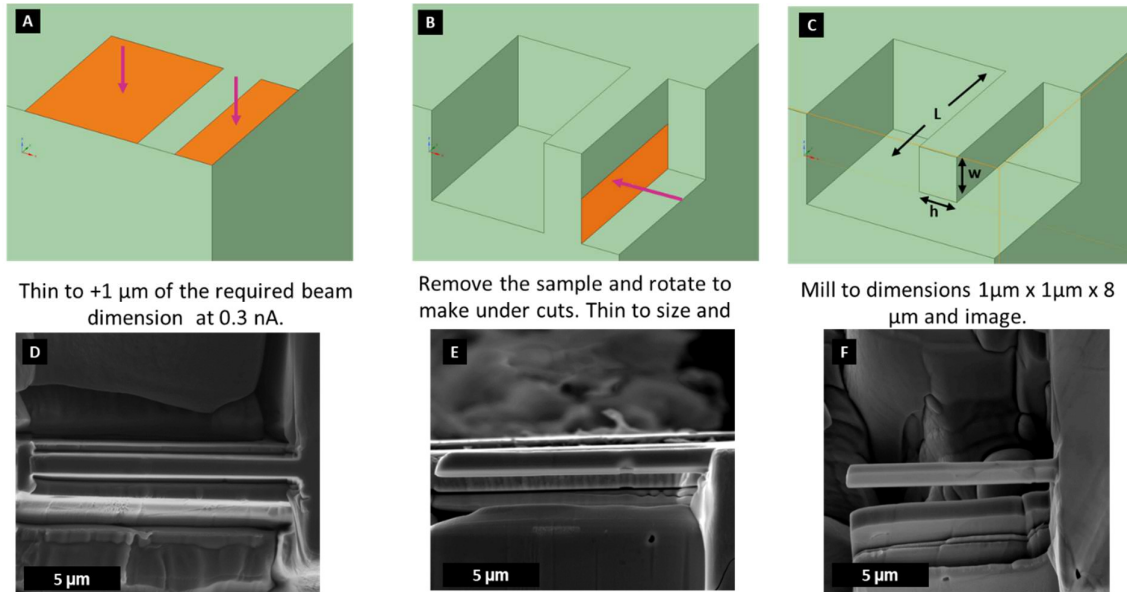


Figure 66 (A-B) shows a CAD representation of the micro bend preparation technique used for the implanted and un implanted ZrN sample. (D-F show representative images of the milling stages in the FIB. E and F show the beam on the surface rather than submerged.

Although the change in manufacture from the SiC to ZrN cantilevers was subtle, it was necessary to ensure the beam contained the ion damaged region and residual stress layer. Care was taken to measure the height and breadth of the beams to ensure the highest accuracy values were recorded as permitted by the system: as such (slow scan) 10s scan images were taken, height and breadth measurements were repeated at 3 positions on each beam at high magnification. The tests were conducted over a 24-month period. The FIB system is recalibrated every 6 months and no appreciable change in dimensional calibration was identified. Ion beam aperture widening was identified over the course of testing and, where suitable, alternative apertures were used to provide comparable milling currents.

3.5.3. Microbeam testing

For micro bend testing, a microprobe (FMT 120, Kleindiek Nanotechnik, Germany) was installed in the FIB. The Kleindiek consists of a tip with three degrees (x,y,z) of freedom with a MEMs chip mounted on the tip (Figure 67). The chip acts as a piezoelectric load cell whereby deflection causes a voltage change at the silicon tip. To convert the voltage change to a force, the chip is calibrated with a copper wire as per the manufactures instructions. Average calibration values were $48.072 \pm 2.56 \mu\text{N/V}$. The maximum tip force is $360 \mu\text{N}$

dependent on the initial calibration. Higher loads are measurable, but 360 μN maximum is guaranteed for each indenter tip. The tip resistance is specified from 500 to 650 Ω with a sensitivity of $18.8 \times 10^{-3} \text{ mV/nm}$ at $V \text{ bridge} = 2.5 \text{ V}^2$. The system offers a force resolution of 10 nN. Part of the experimental design and test development was to ensure that tests were conducted within an appropriate and comparable range of the load cell. The indenter was machined to a rounded tip to improve toughness and reduce the sliding friction between the tip and the microbeam.

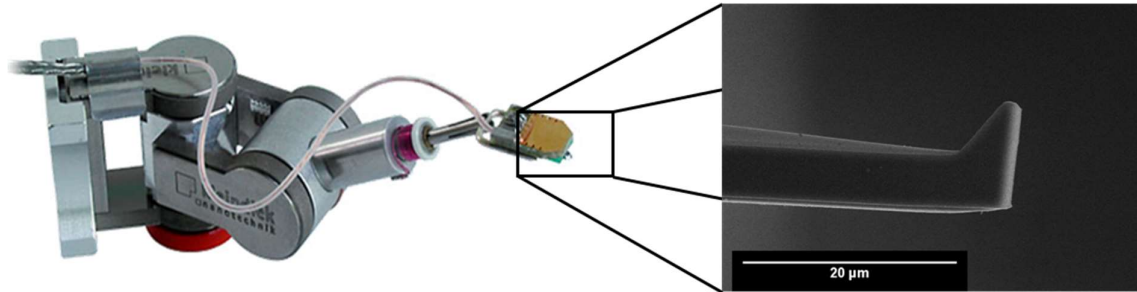


Figure 67 Kleindiek Nanotechnik microprobe with a SEM magnified image of the silicon probe tip [186].

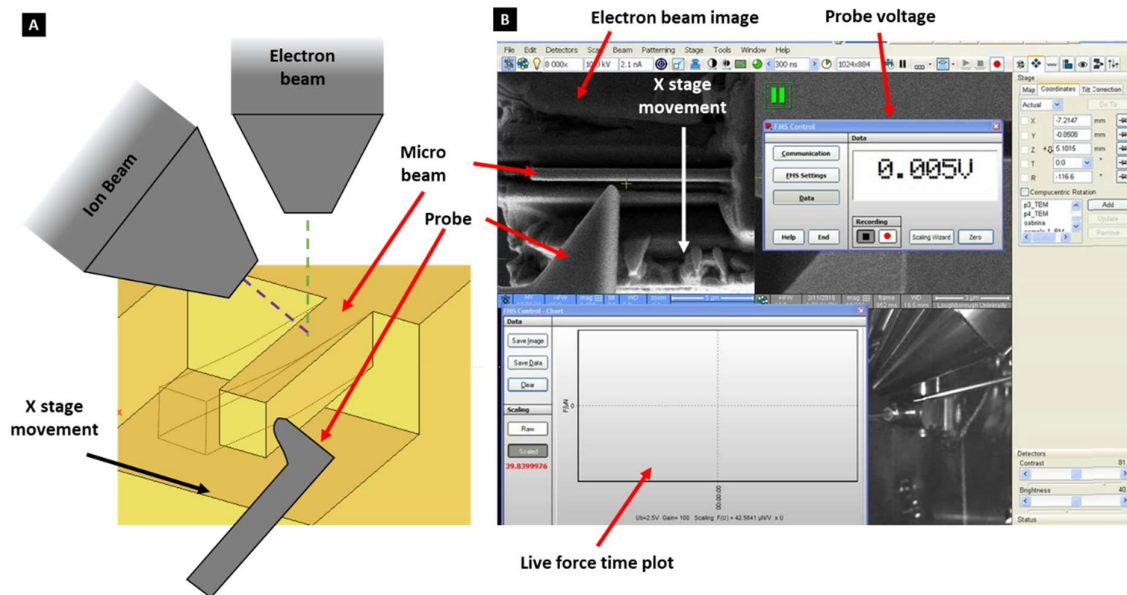


Figure 68 (A) Schematic representation of the location of the micro cantilever and indenter relative to the electron beam. (B) Example operating screen of the FIB during testing showing the SEM image, micro probe feedback and stage position.

The loading tip was brought into contact with the cantilever using the electron beam to determine x and y position and the ion beam to determine the height (z) position of the

indenter relative to the cantilever (schematic representation shown in **Figure 68**). A simple script indexed the piezo-driven microscope stage towards the indenter 100 nm every 0.5 s: this allowed a 1024 x1024 TIF image frame to be taken in-between 2-3 stage moves. For beams of cross-section less than 1 μm , an extended time between frames was used as detailed in the results section.

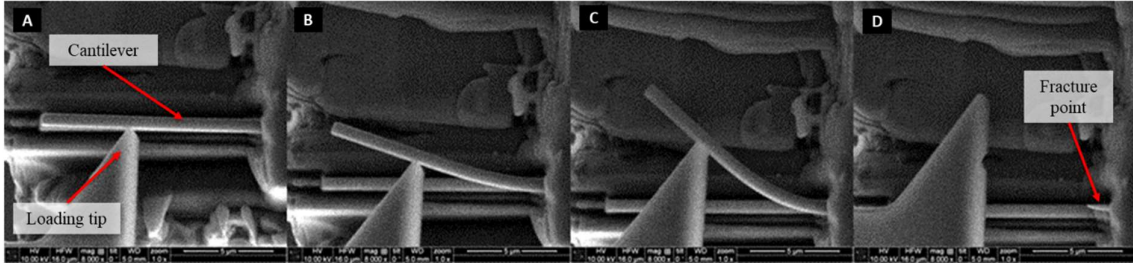


Figure 69 Micro bend test (A-D) shows micro bend test progressing in SiC to failure. (A) initial contact (D) failure.

During testing, a screen capture video was taken of the stage position and microprobe voltage. This helped synchronise the load-displacement measurements. A “.bat” script was used to extract the image frame time of each image. The image timestamps and load cell time stamps were matched using “vlookup” functions in Excel (Microsoft, Washington, USA). This workflow provided a quick system for synchronising images and loads.

3.5.4. Data analysis and mechanics of microcantilevers

As discussed, each micro bend test was processed to give a load displacement graph (**Figure 70**). The micro probe produces a force time graph. The SEM images of the beam displacement at the centre of the indenter at the surface of the beam was then used to calculate the beam displacement (**Figure 69** A-D shows typical micro beam displacement images).

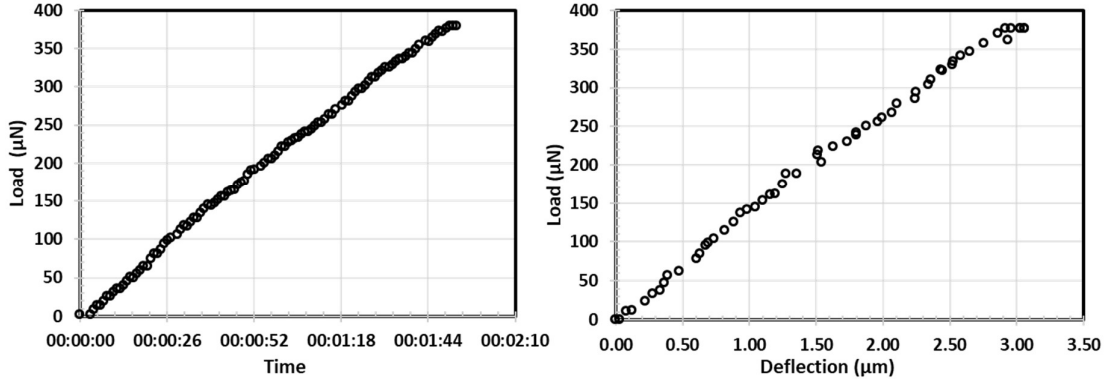


Figure 70 Force time and force-displacement graphs of “pillar 10”, $1 \times 1 \mu\text{m}$ 30 keV.

From the load deflection graph, the gradient of the first portion, approximately 20% of the total number of data points (10 points for $1 \times 1 \mu\text{m}$ beams) of the graph, is used to determine the Young’s modulus of the microbeams as per Equation (7). The least squares regression function in Excel was used to determine the gradient of the initial deflection of the microbeams. Where R^2 values less than 0.85 were calculated, the number of points was varied to increase the R^2 value. The standard modulus calculation for small deflections in bending calculation was used [71]:

$$E = \frac{PL^3}{3\Delta I} \quad (7) [71]$$

where P is the load, L is the cantilever length from the root to the indenter contact point. One of the boundary conditions of the equation is that the deflection of the beam is small, thus the beam length is consistent through the test. Δ is the beam deflection, I is the second moment of area which is dependent on the cross-section of the beam. For a rectangular cross section second moment of area is described by Equation (8) [71]:

$$I = \frac{bh^3}{12} \quad (8)[71]$$

where h is the height of the beam (top face during testing) and b is the beam breadth (the side of the beam during testing). Further to this, the modulus of each beam at each displacement was plotted against the percentage of completion of the microbeam using Equation (7).

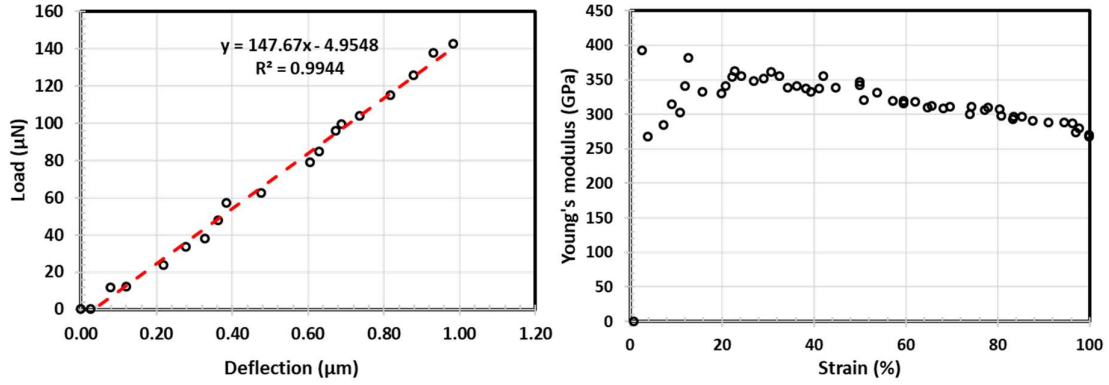


Figure 71 Load-displacement graph showing the liner nature of the deflection of the beam, and Young's modulus strain graph showing the change in modulus over the test.

The modulus strain graphs provided information on the change in modulus during the test. Using the initial micro beam length does not account for indenter slip to or from the cantilever root. Therefore, the modulus strain plots are calculated with the indenter position measured to account for these changes. Flexural strength calculations were conducted using the standard formula:

$$\sigma_f = \frac{PL_0}{z} \quad (9) [71]$$

where σ_f is stress, P is peak load, L_0 is the beam length between loading point and the root of the beam and z is the moment of inertia of the beam cross section. Moment of inertia z is calculate by Equation (10) where b is beam breadth and h is beam height as previously defined.

$$z = \frac{bh^2}{6} \quad (10) [71]$$

Where the microbeams failed midway through the beam, an adjusted formula (33) was used to compensate for the fracture position:

$$\sigma^a = \frac{PL}{z} \times \frac{L_0 - x}{L_0} \quad (33)$$

where σ^a is the adjusted strength, L_0 Is the beam length from root to loading point, x is the length from the fracture point to the root.

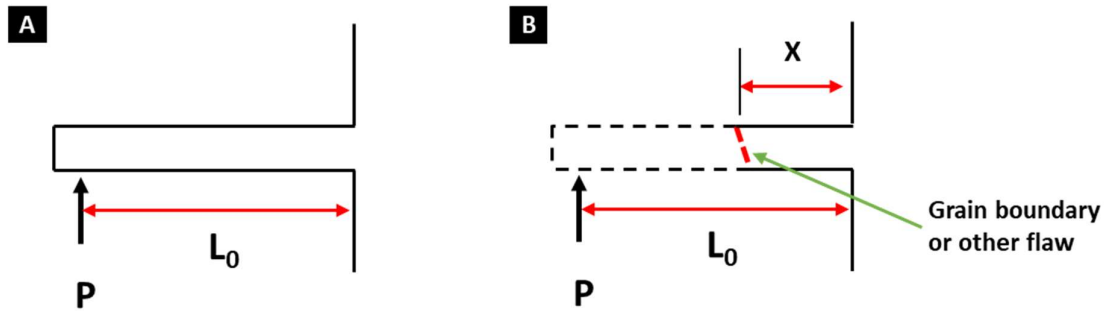


Figure 72 schematic (A) showing L_0 and (B) showing the measurement of x from a fractured microbeam.

This adjusted fracture length calculation is required when estimating the strength of grain boundaries or flaws situated mid-way along the microbeams. Flaw size estimation calculations were also made using equation (34):

$$K_1 = C \sigma \sqrt{\pi a} \quad (34) [71]$$

where K_1 is comparable to K_{1c} at fracture, C is a constant 1, σ is the strength or adjusted strength of the beam and a is the flaw size of the material. The equation was rearranged to estimate the flaw size of the material.

3.6. Nanoindentation

3.6.1. Nanoindentation of single crystal 6H silicon carbide

To determine hardness and Young's modulus, a Berkovich indenter was installed for testing using the Nano-test 600 indentation system (MicroMaterials ltd., Wrexham, UK). The indentations were conducted at room temperature (25.0°C) and an ambient humidity level of 31.8%.

For the single crystal SiC nano indentations, a SiC wafer measuring 0.3mm × 6mm × 6mm was hot wax mounted and polished on colloidal silica for 5 minutes. Following this, the sample was remounted on a large polycrystalline block of SiC for nanoindentation. A 40x optical magnification light microscope was used to locate the indentation sites. Following this, the system was set to indent at loads of 25 mN, 50 mN, 75 mN, 100 mN, 150 mN, 200 mN and 250 mN. A loading rate of 0.5 mN/s and unloading rate of 5 mN/s was used with a

dwelt time of 30 s. Each indentation was repeated ten times with an appropriate distance between each indentation depending on the indentation size. Following testing, modulus and hardness were calculated with the micro materials software and all data exported as CSV files. Tests with hardness or modulus values great than 3 standard deviations from the mean results were discarded; each load and displacement graph was plotted and the quality of the data analysed. Erroneous loading profiles were excluded, along with noisy plots and plots which were not started at 0 load 0 displacement (example shown in **Figure 73**):

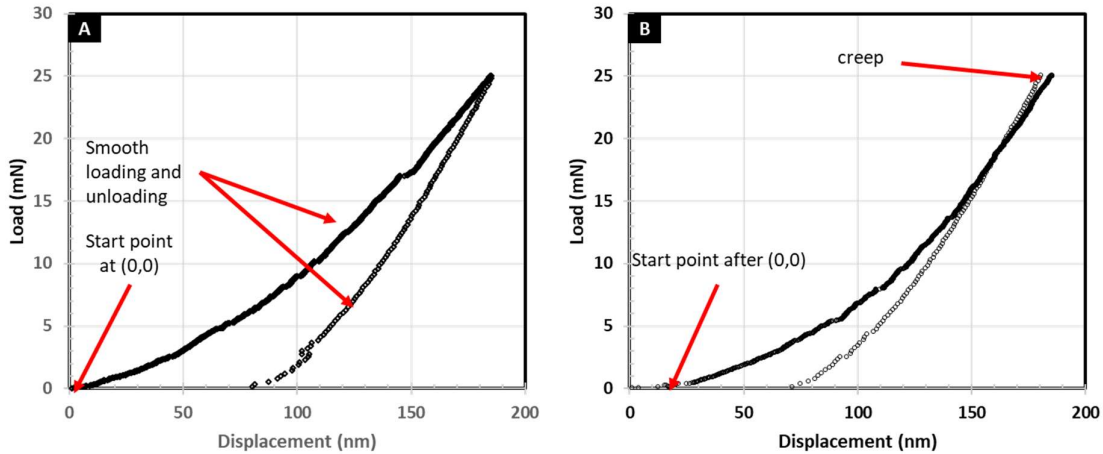


Figure 73 Example plots of acceptable data and rejected load-displacement data.

Indenter cleanliness was found to be critical to taking precise measurements. Initial test results were not satisfactory due to indenter contamination. Cleaning of the indenter was conducted by pressing the diamond tip into polystyrene and imaging with the SEM. The micro materials indenter outputs modulus as reduced modulus, which is the combined modulus of the sample and the indenter. These values were converted to Young’s modulus using Equation (20). All indentations presented were conducted with a diamond indenter. The indenter manufacturer’s values for Young’s modulus and Poison’s ratio used for the reduced modulus conversion were $E_i = 1114 \text{ GPa}$ and $\nu_i = 0.07$.

Following indentation, the indents were located by using a tilted stage in the SEM (JEOL 7800) to increase the surface topography effect. Once identified, the indents were imaged at 5 keV using backscatter electron imaging. SEM-based hardness was calculated using image J processing. Each image was scaled and the area from each corner was measured using the “polygon selection” function (as shown in Figure 74). Hardness was calculated using Equation (12).

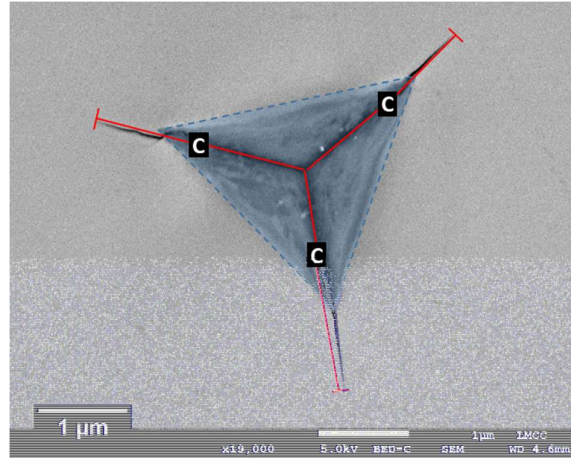


Figure 74 Annotated SEM showing how the measurement of area and crack length was conducted/defined. The blue triangle denotes the area of the indentation while the “C” values indicate the crack length.

SEM crack length measurements were made using the SEM images of the indentations. Much like the area, the crack length was measured using imageJ, using the “line” tool (see **Figure 74**). Length was measured from the indent centre to the crack tip. Equation (17) was used to determine fracture toughness:

$$K_{IC} = v \left(\frac{E}{H} \right)^{1/2} \frac{F_m}{c^{3/2}} \quad (17) [87], [88]$$

where v is Poisson's ratio, E is Young's modulus, H is hardness, F_m is max force or peak load and C is average crack length [87], [88], [187]. Modulus, hardness and peak load values were calculated from the nano indenter data output. “c” average crack length was measured from the SEM images and a literature-based value for Poisson's ratio was used (0.018) [124].

3.6.2. ZrN nanoindentation

All the ZrN nanoindentations were conducted in Donghua University/Shanghai Institute of Ceramics, using an Agilent G200 nano indenter, (Agilent Technologies, USA). Continuous stiffness measurement (CSM) was used for the indentation with a diamond cube corner indenter (Micro Star Technologies B-style). This indenter was factory inspected and calibrated; each facet angle was accurate to $\pm 0.025^\circ$. For the indentation of the ZrN ceramic, initial attempts were made at a cross-sectional indentation study as discussed in the literature. This approach typically yields hardness and modulus data, which would have fit well with the

HR-EBSD strain mapping work. However, in-plane indentation was settled upon as this provided the required hardness and modulus data in fewer tests and with less ambiguity in the results.

15 indentations were made on the unirradiated and irradiated ZrN faces. Before testing, both faces had been polished to a 1 μm finish. The tests were conducted in depth control mode to a depth of 1500 nm with a surface approach velocity of 10 nm/s, strain rate of 0.05 1/s, and harmonic displacement of 2 nm at a frequency of 45 Hz. The calculation of modulus and hardness was conducted by the Agilent software using a Poisson's ratio of 0.25 for the ZrN. The indenter software outputs Young's modulus rather than reduced modulus.

Following indentation, the indents were located by using a tilted stage in the SEM (JEOL7800) to increase the surface topography effect. Once located the indents were imaged at 10 keV with backscatter imaging. This provided channelling contrast, highlighting the grains and oxide phase. Further to backscatter imaging, EDS, (JEOL 7800 with Oxford instruments detector as detailed in the SEM section) was conducted to verify the location of the oxide particles. The same analysis of crack length and indentation area was conducted, as detailed in the SiC indentation section.

4. Results and discussion

4.1. Micromechanical characterisation of 6H single crystal silicon carbide

4.1.1. Surface inspection

4.1.1.1. Silicon carbide surface morphology

Secondary electron and backscatter imaging were used to image the surface of the as-supplied 6H silicon carbide wafers. The wafers exhibited very little surface topography apart from some scratches $\approx 0.1 \mu\text{m}$ in width. No sub-grains or defects were discernible on the surface of the material.

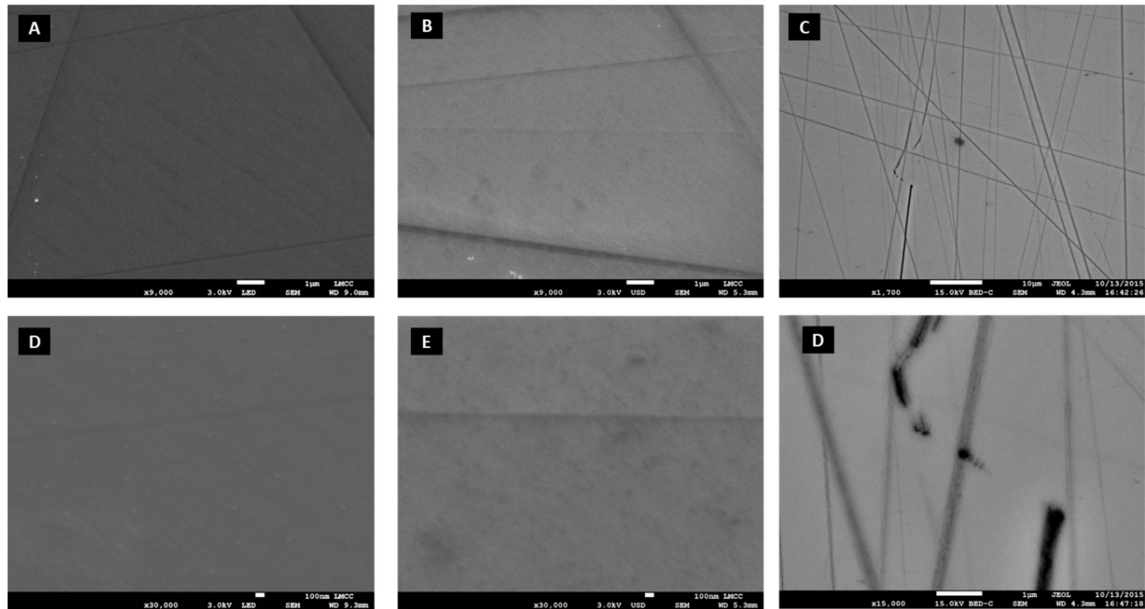


Figure 75 SiC surface as supplied imaged secondary electrons (LED images A and B), in lens/upper secondary electron detector (USD images E and F), and backscatter imaging (BED images C and D).

The surface of the single crystal was found to be similar to those identified by Malherbe *et al.* and Suvorova *et al.* under secondary electron imaging conditions [188], [189]. Suvorova *et al.* demonstrated the ability of secondary electron imaging to identify band gap differences in 4H and 6H polytypes [189]; however, no such variations in polytype were identified in the samples. Backscatter images provide atomic number contrast and crystallographic orientation contrast through channelling and dislocation contrast. The image in (Figure 75 D) shows dark

points/bands which could relate to dislocations in the matrix. These images compare well with the literature examples of dislocations identified by electron channelling contrast imaging (ECCI). Further analysis of the SiC samples would be required to confirm the validity of these claims. Based on the secondary electron images, the surface roughness of the single crystal was deemed sufficiently low for nanoindentation.

4.1.2. 6H single crystal silicon carbide bulk chemistry

EDS mapping at 15 keV was undertaken to check for bulk impurities in the crystal. Results can be seen in **Figure 76**:

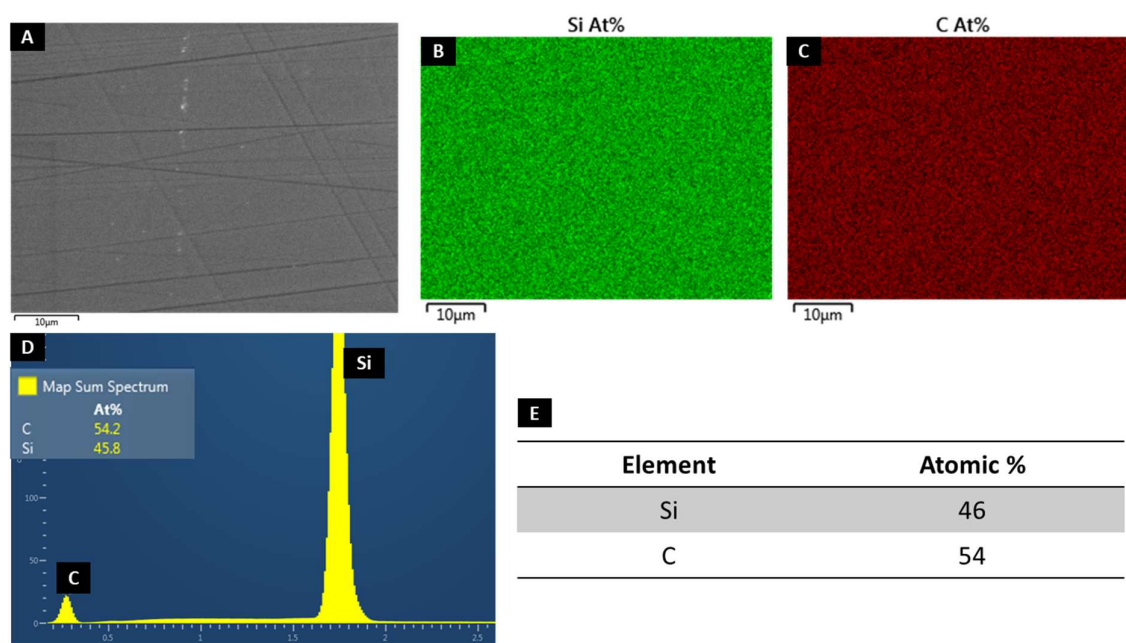
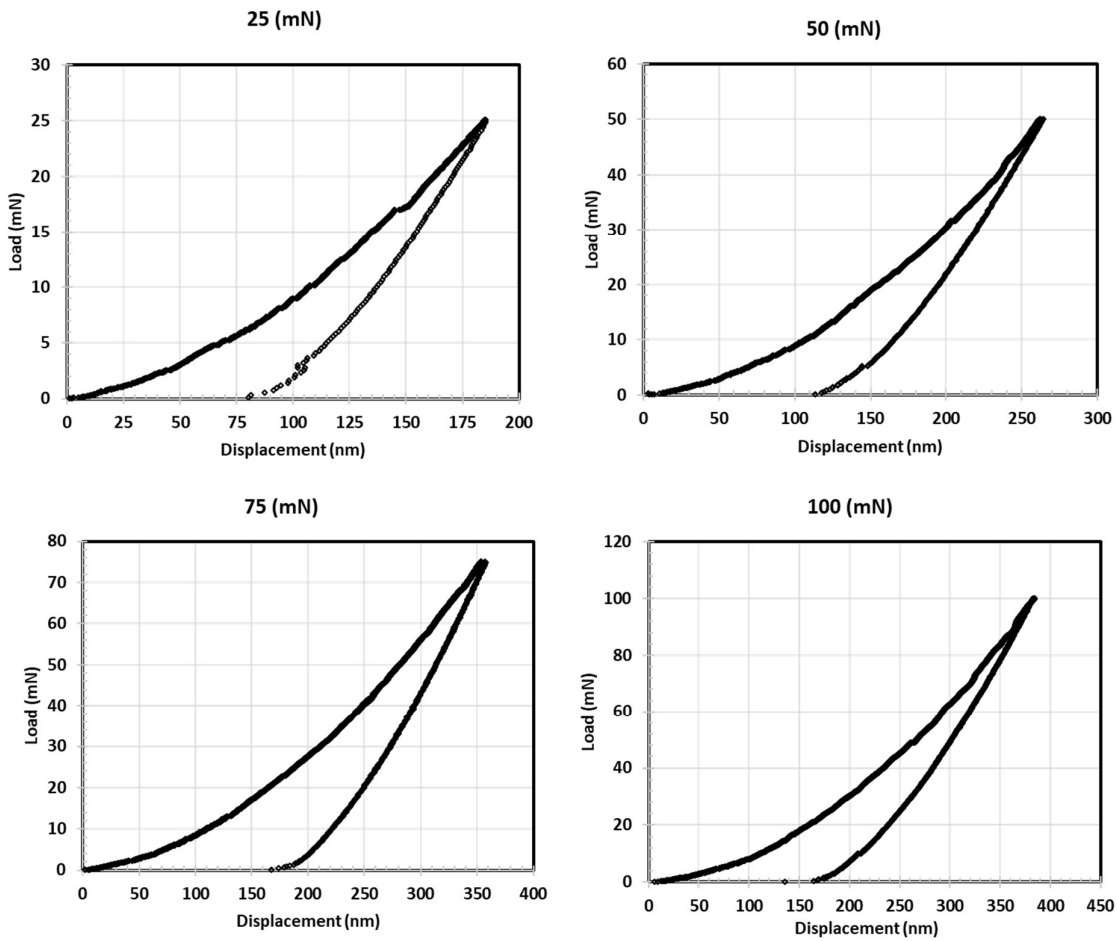


Figure 76 EDS SiC 10 keV, (A) SEM image, (B) Si and (C) C atomic maps, (D) spectra and (E) atomic % table.

EDS showed the SiC wafers are composed predominantly of silicon and carbon in a ratio close to stoichiometry. The excess of carbon measured was likely due to surface carbon contamination. Due to interaction volume effects, EDS could not be used to identify surface impurities or oxide layers. Therefore, XPS was conducted. Data from these experiments are presented in the appendix. In essence no significant oxide species were identified on the surface, indicating that the samples would not have an artificial depth dependence during characterisation.

4.1.3. Nanoindentation of 6H single crystal silicon carbide

A range of loads from 25 mN to 250 mN was used to assess the Young's modulus, hardness and fracture toughness of the 6H SiC sample. By using a range of loads, the single crystal size effect was also investigated (see Figure 77 for typical plots). As discussed in the experimental section, any curves with excessive noise or erroneous features were excluded from the data (around 2-3 plots per data set). Low load (10 mN) indentations were conducted; however, the results were not sufficiently consistent for presentation.



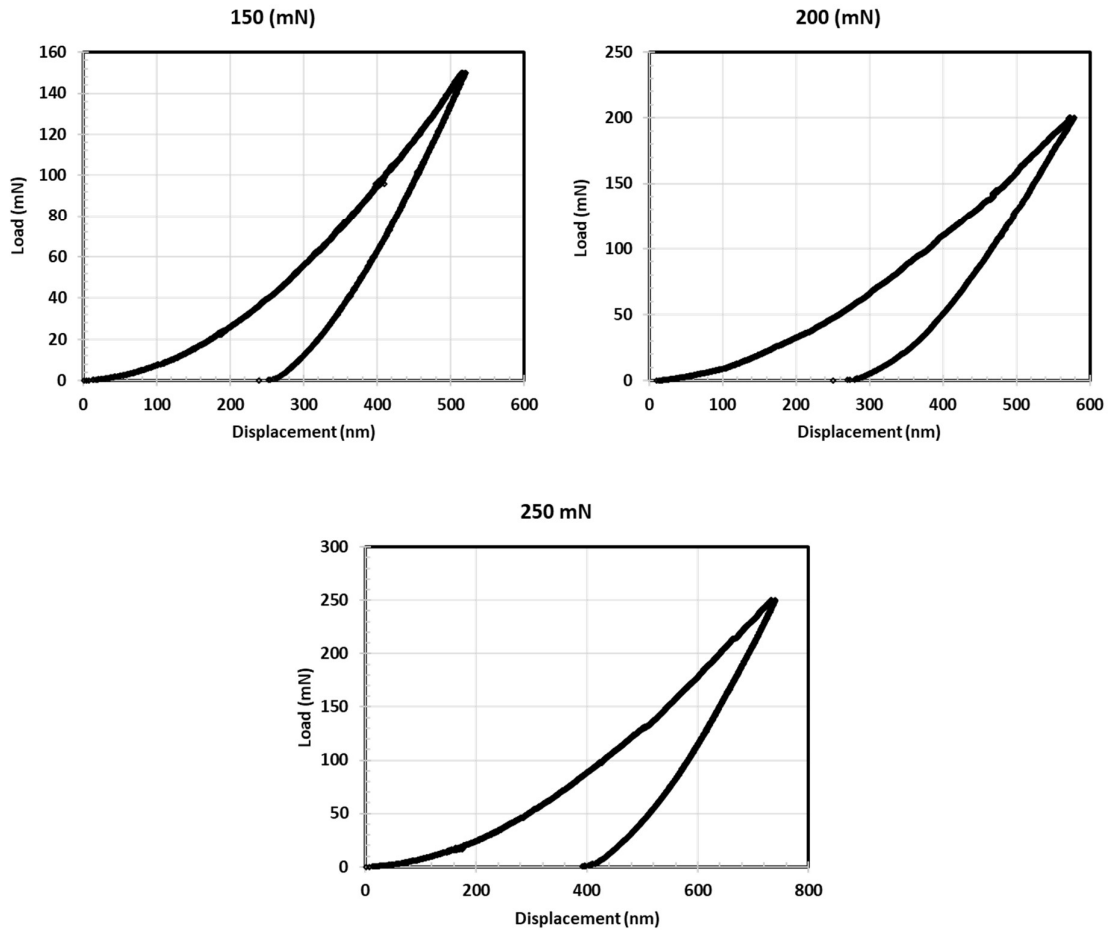


Figure 77 Example nanoindentation data from 6H SiC indented with a Berkovich indenter at 25 mN, 50 mN, 75 mN, 100 mN 150 mN, 200 mN and 250 mN loads.

Pop-in events frequently occurred during the 25 mN tests, with the first pop-in event occurring at 2.31 ± 0.7 mN. These low load pop-in events were accompanied by less frequent but greater in magnitude pop-in events at 19.52 ± 2.4 mN. These results match well with those reported by Page *et al.* in their 1992 paper on the deformation of ceramic crystals at low loads [159]. During the 50 mN tests, pop-ins were identified at the 30.72 ± 4.8 mN range; higher load tests exhibited pop-ins but not at repeatable points during loading. Pop-ins are typically associated with cracking / fracture of the indented material. Other than the pop-in events at low load, no consistent trends in the nanoindentation curve were identified.

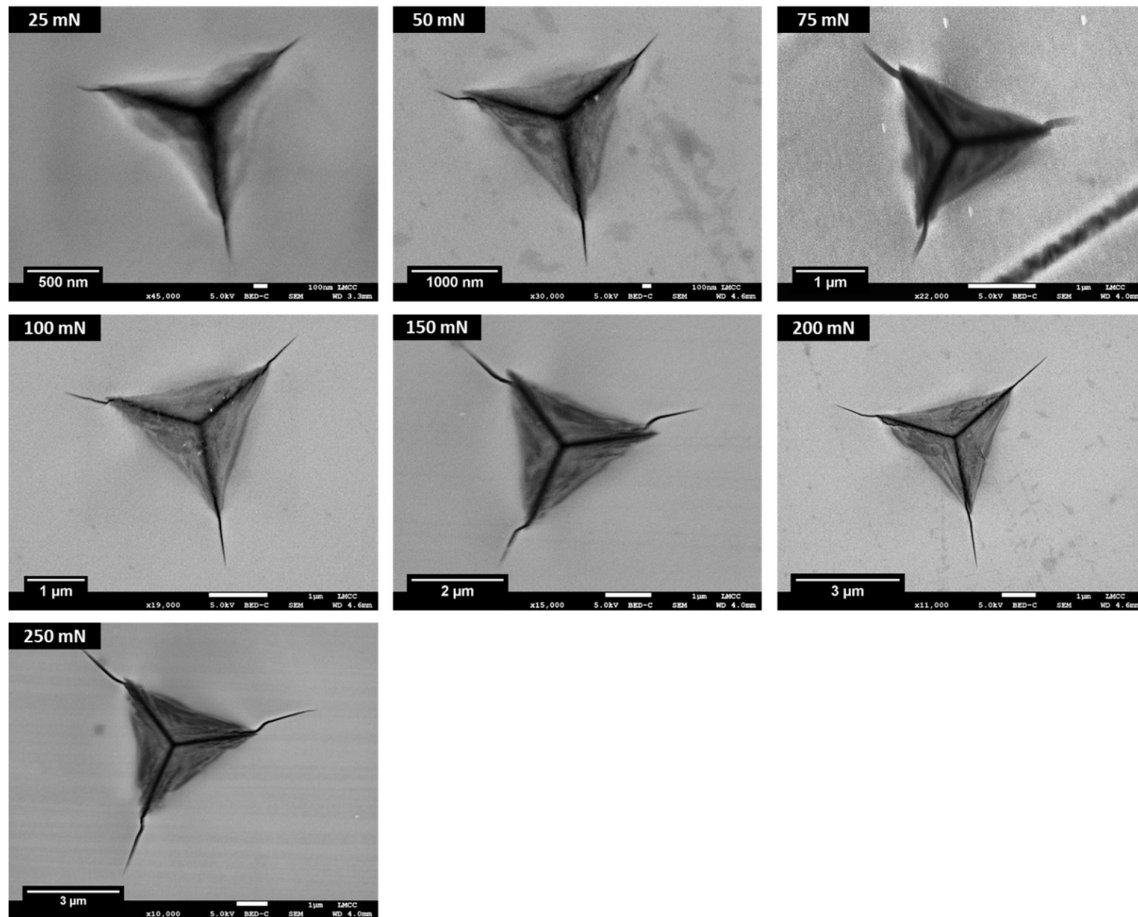


Figure 78 SEM images captured with backscatter electron imaging at 5 keV and 3-4 mm working distance of the nanoindentations from 25 – 250 mN. The magnification used to image each indent was modified to best fit the size of the indentations.

Some trends were observed in the nanoindentations images. The corner crack length of each indentation increased with load. This is typical of nanoindentations where low load tests are dominated by plastic deformation. Lower load indentations exhibited some minor pinching at the corners of the indentation, as had been identified by Page *et al.* in their paper on the deformation of ceramic crystals at low load [159]. Pinching refers to a reduced angle at the corner of an indentation. Page *et al.* postulated that the slip bands located parallel to the indentation edge were the cause of indentation size effect [159]. No such bands were identified during imaging of the 6H SiC crystal studied.

Pang *et al.* did not identify corner cracking during nano indentations on the basal plane of 6H SiC with a load of 30 mN [190]. These results contrast to others reported in the literature and our findings. The use of AFM to measure the indents may have obscured the cracking in the

material. Other experimental variations such as surface finish or differences in dislocation density could have caused this variation.

The corner crack C (see Figure 79) of the indents was typically longer than the top two corner cracks A and B. This variation in crack length may have been caused by a slight indenter misalignment: rotation of the sample could have been used to test this hypothesis. Preferential fracture can also be caused by the alignment of the indenter to a preferential slip plane. Hiihara used this technique to demonstrate that the preferential slip plane of SiC at room temperature in 6H SiC is $[10\bar{1}0] \langle 11\bar{2}0 \rangle [100]$. At low loads, the corner cracks were observed to initiate from the corners of the indentation. At higher loads, the corner cracks initiated from within the indentation and frequently kinked, as shown in **Figure 79**:

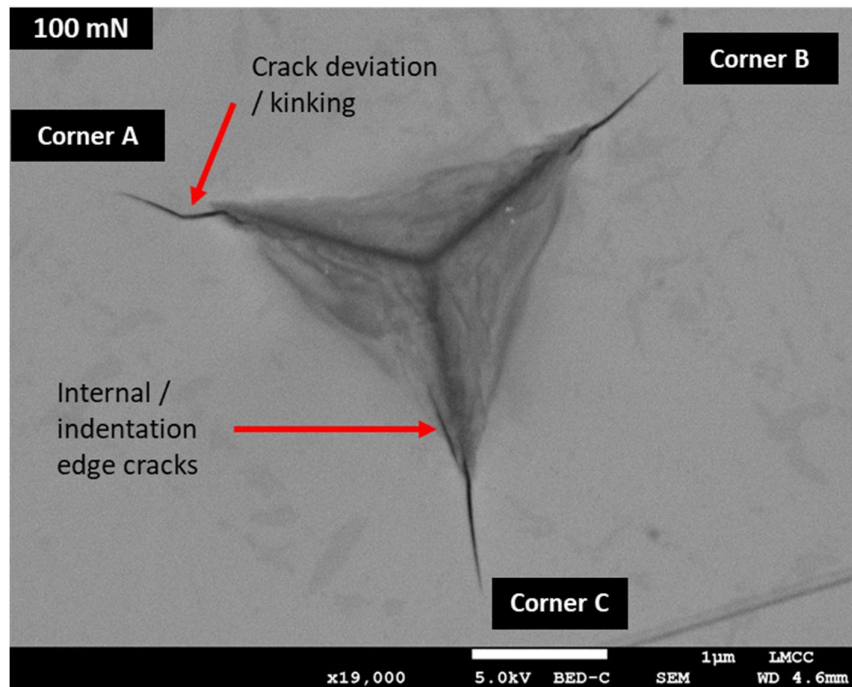


Figure 79 100 mN Berkovich nanoindentation into 6H SiC showing cracking within the indentation along with crack deviation and kinking.

An expansion of this work and that of Hiihara would be to use HR-EBSD and single crystal diffraction to prove the orientation of the preferential slip plane and map the stress around the indentations. This, along with electron channelling contrast imaging (ECCI) could be used to link dislocation density to residual stress and cracking. This could provide a deeper insight into the source of the indentation size effect in ceramics. Demir *et al.* outlined a similar work schedule for identifying the size effect in copper [191]. Locating stress fields and dislocation

densities can assist in the development of better FEA models for the simulation of component designs.

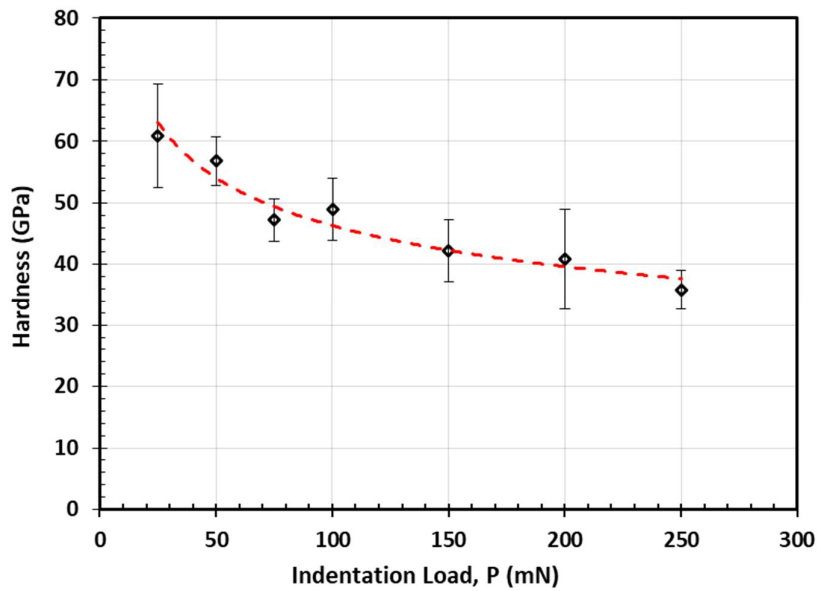


Figure 80 Hardness against indentation load for Berkovich nanoindentations in 6H SiC perpendicular to the 0001 plane.

Figure 80 shows a plot of indentation load against hardness. There is an apparent size effect with low load indentations resulting in increased hardness. The data from the 75 mN nanoindentation was not as consistent with the size effect trend. As can be seen in (Figure 78), the images of the 75 mN load indentations were slightly rotated. This rotation potentially resulted in the indenter corners interacting with a different set of slip planes causing variation in the observed size effect. A similar effect can be seen in the load against modulus plots. Based on the strength estimation equation discussed in the literature review, Equation (16), ($H_v \approx 3\sigma_{ys}$) an estimated fracture strength value from 20-11 GPa can be expected from the micro bend tests; this result can be used to inform the microbeam experimental design.

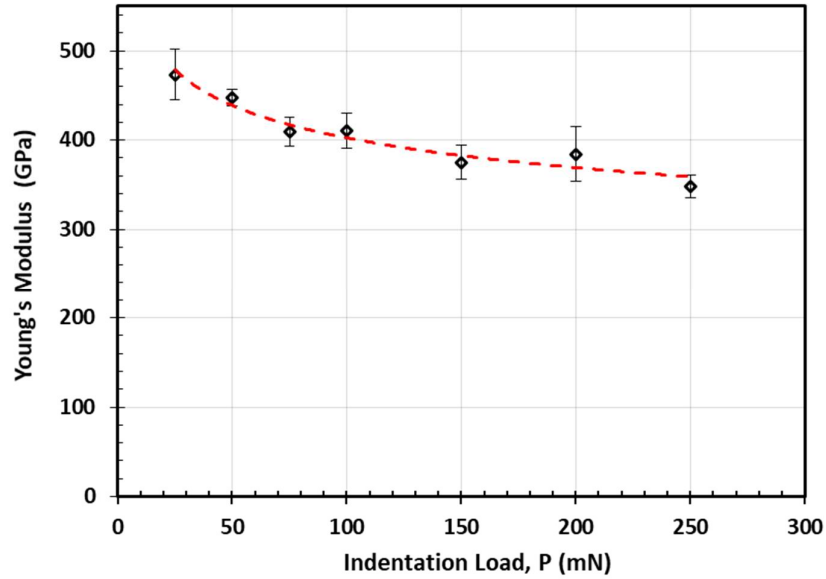


Figure 81 Young's modulus against indentation load for Berkovich nanoindentations in 6H SiC perpendicular to the 0001 plane.

A size effect was identified in both Young's modulus and in hardness (see Figure 80 and Figure 81). To confirm the observed size effect in hardness, Meyer's law was applied based on the methodology used by Wade [80]:

$$P = Ad^2 \quad (35) [80]$$

To calculate the exponents, equation (35) can be used in the form shown in below:

$$\log P = \log A + n \log d \quad (36) [80]$$

where P is load in Newtons, A is the intercept, d is the indentation diameter and n is the gradient of the line where values tending to 2 having no size effect. The log load against log diameter plot is (shown in **Figure 82**):

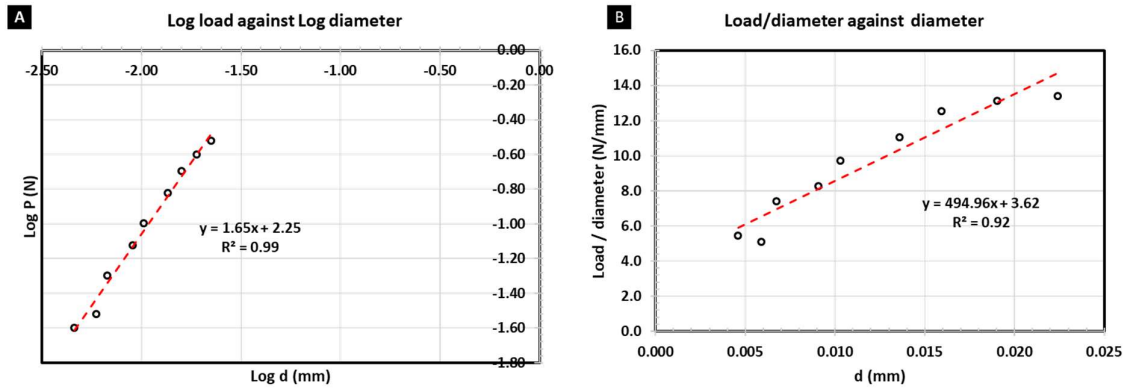


Figure 82 (A) Log (load) Log (diameter) plot for 6H SiC nanoindentation results with regression analysis and (B) Load- diameter plot for 6H SiC nanoindentation results with regression analysis.

Using Excel based regression analysis, the gradient was found to be 1.65 indicating a strong size effect, while the intercept value was 2.25 N and the R^2 value was 0.99, indicating a good correlation. Wade *et al.* discusses the validity of Meyer's law for determining indentation size effect (ISE). He postulates that Meyer's law is sufficient to identify size effect, but the proportional specimen resistance model is more useful as it provides a size-independent hardness value, a_1 and a_2 values, which can be attributed to the degree of plastic deformation and cracking. Next, the proportional specimen resistance (PSR) model was applied:

$$P/d = a_1 + a_2 d \quad (15)$$

where P and d are load and diameter respectively. a_1 is the cracking dependent deformation and a_2 is plastic deformation dependent component. The R^2 value associated to the fitting of the line was 0.92, suggesting a less successful fit compared to that of Meyer's law.

Table 16 Meyer's law and PSR model for nanoindentation size effect.

	Meyer's law			PSR		
	n	A	R^2	a_1	a_2	R^2
6H SiC	1.65	3.22	0.99	14.01	7426	0.92

As shown in **Table 16**, both Meyer's law and the PSR model show that there is a size effect when hardness testing single crystal 6H SiC. Further work in the same loading range would be required on other materials to make a comparison as to the difference magnitude of the

size effect. The values of a_1 and a_2 are within the same range (a_1 22-29, a_2 11532-11918) as those recorded by Wade *et al.*; however, the extreme differences in experimental conditions make comparisons difficult [79], the key differences being loading magnitude and indenter geometry differences between the Vickers and Berkovich indenters.

The crack length of each indentation was measured to determine the fracture toughness of the wafer. Further to this, the effects of load on fracture toughness measurement were also of interest. Fracture toughness was determined as discussed in the experimental and literature review sections (pages 47 and 120).

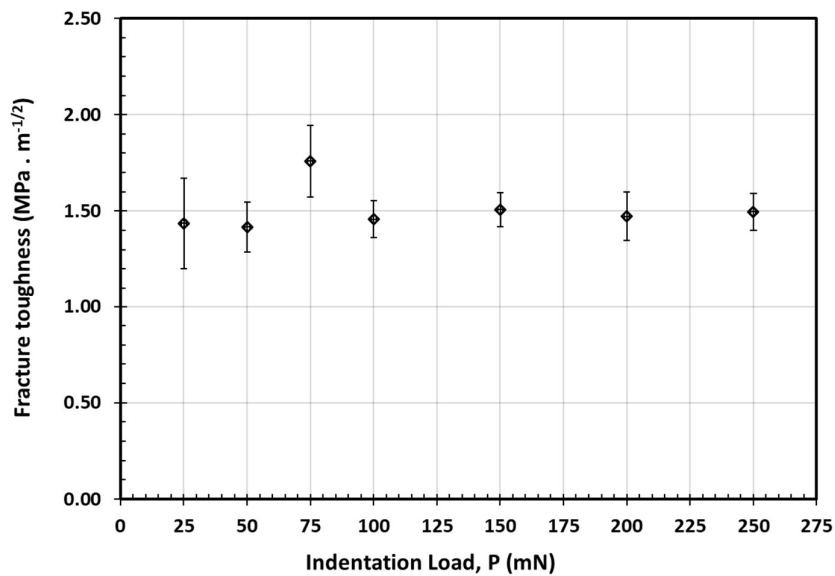


Figure 83 Plot of fracture toughness against indentation load calculated based on crack length measurements.

It was identified that fracture toughness based on crack tip measurements was size independent between 25 mN and 250 mN, as shown in Figure 83. The data point for 75 mN was slightly above the general trend of the data. The lack of size effect in the data matches well with the findings of Anstis *et al.* in their seminal work on indentation fracture toughness [88]. The average value of fracture toughness was calculated to be 1.50 ± 0.1 MPa · m^{-1/2}. These results match well with those presented by Leatherbarrow *et al.* in their paper on the nano indentation of brake disc materials, including 3C SiC. The original indentation fracture toughness formula was developed in amorphous glass where there are no slip systems. Due to the geometric and crystallographic differences in the model and application, the values

presented should be considered estimates. The TEM lift out of a nano indentation did not show the half penny type crack pattern suggested by the model presented by Lawn. TEM is not ideal for the reconstruction of cracking, and a serial sectioning or polishing approach as undertaken by Hallam *et al.* would be more appropriate for determining the crack morphology below the indentations [192].

A TEM lift out was conducted on a 250 mN nanoindentation through one of its lines of symmetry (as shown in Figure 84). The lamellar contained the majority of the deformation zone and two macrocracks, this large crack at the base of the indent increased in size during the lift out procedure. Below the nanoindentation was a high number of microcracks and dislocations. At the surface of the sample were a number of cracks including cracking on the basal plane. The slip and basal plane dislocations extended to a diameter of 4.5 μm , with the highest density region below the indenter extending to a low-density region composed of long dislocation loops and lines. The cracking observed in the lamellar matched the cracking observed in the SEM analysis of the interior of the indentations, with angled cracks emanating from the indented surface at an angle of 30°. As discussed in the literature review, the slip systems of hexagonal single crystal SiC are $(0001)\langle 1\bar{2}10 \rangle$, $(0001)\langle 01\bar{1}0 \rangle$, $\{10\bar{1}3\}$ $\langle 1\bar{2}10 \rangle$ and $\{10\bar{1}0\} \langle 1\bar{2}10 \rangle$ [151]. Of these systems, dislocations are most likely to occur on the $(0001)\langle 1\bar{2}10 \rangle$ and $(0001)\langle 01\bar{1}0 \rangle$. The corresponding Schmid factors under a load in $[0001]$ direction are 0.378, 0.282, 0.019 and 0.131, respectively [151]. The cracks along the 30° plane could indicate pyramidal slip.

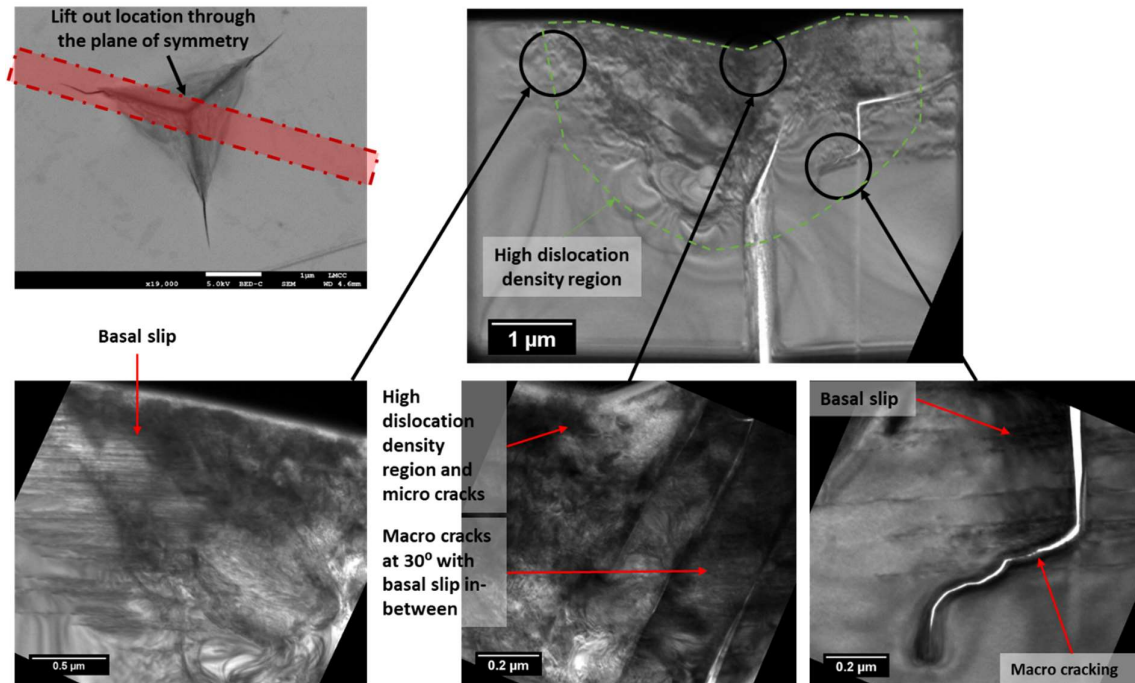


Figure 84 TEM image showing an overview of the 250 mN nano indent lift out location, bright field image overview and magnified sections showing basal slip, high dislocations below the indenter and micro cracking.

Microcracking below and around the indentation likely caused a reduction in material integrity. Based on a law of mixtures, this affects Young's modulus on un-loading portioning of the indentation resulting in an apparent reduction in modulus. The high levels of macro and microcracking matches well with TEM analysis of SiC nanoindentations in the literature [151]. The high levels of microcracking also match well to the PSR model analysis of the nanoindentation data. Literature accounts of SiC nanoindentation suggest that no amorphisation is caused by indentation, but some reduction of the single crystal to a polycrystalline form may occur [151]. Selective area diffraction did not identify amorphisation below the indentation. Based on measurements of the plastic zone identified by the green line in Figure 84, Kramer's cavity model for Berkovich indentation was used to estimate the yield strength of the single crystal SiC [193], [194]. Kramers cavity model equation (37) was rearranged to determine the yield strength based on the plastic deformation zone and applied load:

$$c = \sqrt{\frac{3P}{2\pi\sigma_{ys}}} \quad (37)$$

where P is load, c is plastic zone radius and σ_{ys} is yield strength.

In this case $P = 250$ mN, $c = 2.40$ μm , from these values the yield strength of the crystal will be around 20 GPa. The previous estimates for yield strength based on hardness were from 10-20 GPa; as such the cavity model (20 GPa) matches well with these estimates.

Based on these preliminary nanoindentation results, a modulus of 473-348 GPa was expected from the microbend tests, dependent on beam size, while a yield strength / fracture strength of 10-20 GPa was estimated. These values were used to inform the experimental design of the microbend tests and for comparison of the validity of the test results. Further to this, the calculated fracture toughness of the single crystal could be used to estimate the flaw population in the micro bend tests.

4.1.4. Gallium Ion milling effects on SiC micro bend testing

Based on the hypothesis that ion beam milling has a deleterious effect on micromechanical test results, three beams were prepared at three milling voltages. Each micro beam was cut using 30 keV gallium ions, and the final milling was conducted at 0.3 nA. The low accelerating voltage micro samples were then tilted $\pm 2^\circ$ and milled for an additional 30s (at 10 keV, 50 pA and 5 keV 70 pA). Low voltage milling of this nature is typically referred to as a cleaning step in TEM lamellar preparation and is designed to remove any amorphous layers on the exterior of the sample. Details of each microcantilever are presented in **Table 17**:

Table 17 Table of pre-tests microbeam samples and maximum load/deflection data.

	Ion beam voltage (keV)	Ion beam current (Amp)	Cleaning time (s)	Height (μm)	Breadth (μm)	initial length (μm)	length at failure (μm)	Area (μm^2)	Volume (μm^3)	load at failure (μN)	Deflection at failure (μm)	K_{Ic} (Mpa $\text{m}^{1/2}$)
P 10	30	0.3 nA	Na	1.06	1.11	9.60	8.94	1.18	11.33	373.0	3.10	1.8
P 13	30	0.3 nA	Na	0.91	1.02	9.98	9.41	0.93	9.30	292.2	3.80	1.8
P 18	30	0.3 nA	na	0.88	0.97	9.63	9.03	0.85	8.22	278.4	4.41	1.8
P 11	10	50 pA	20	0.95	0.86	8.46	7.41	0.81	6.86	402.	3.23	1.8
P 8	10	50 pA	20	0.78	1.05	6.45	6.46	0.82	5.27	235.7	1.76	1.8
P 14	10	50 pA	20	0.88	0.98	8.06	7.35	0.87	7.00	377.0	4.23	1.8
P 7	5	70 pA	30	0.71	1.08	7.54	7.13	0.77	5.79	178.3	3.90	1.8
P 9	5	70 pA	60	0.97	0.73	6.89	6.89	0.71	4.88	275.5	1.44	1.8
P 12	5	70 pa	60	0.91	0.75	6.97	6.45	0.68	4.74	334.9	2.66	1.8

Maintaining consistent beam dimensions was challenging due to the nature of ion beam milling. Where necessary, the length of the microbeams was modified to compensate for variations in cross-section. This was intended to ensure that similar ranges in the load cell were used each time. From each micro bend test, a load-displacement plot was generated along with Young's modulus-strain plot.

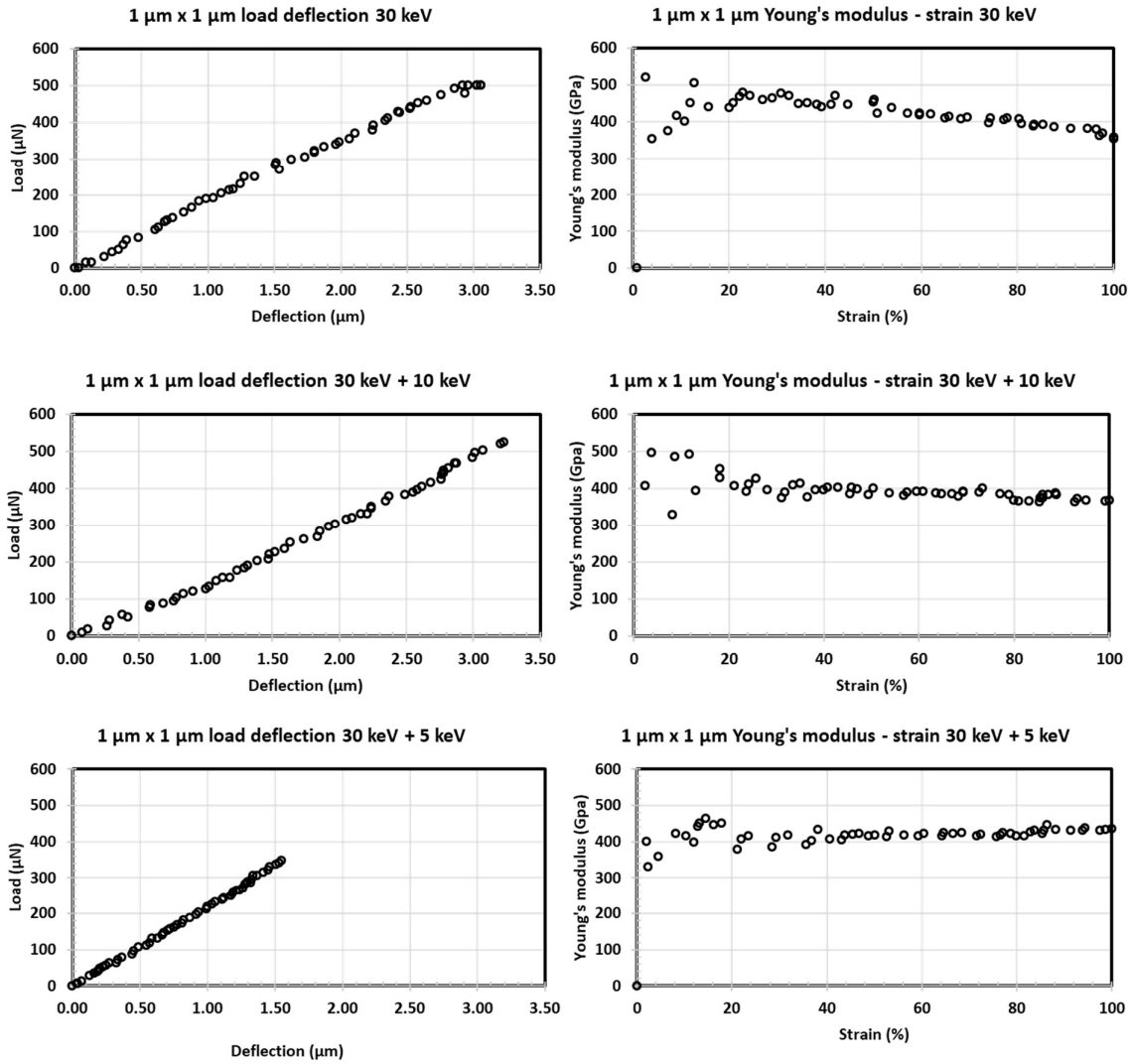


Figure 85 Example results from each of the milling regimes applied to the 6H SiC micro cantilevers, showing the 30 keV milled samples, 30 keV + 10 keV and 30 keV + 5 keV samples.

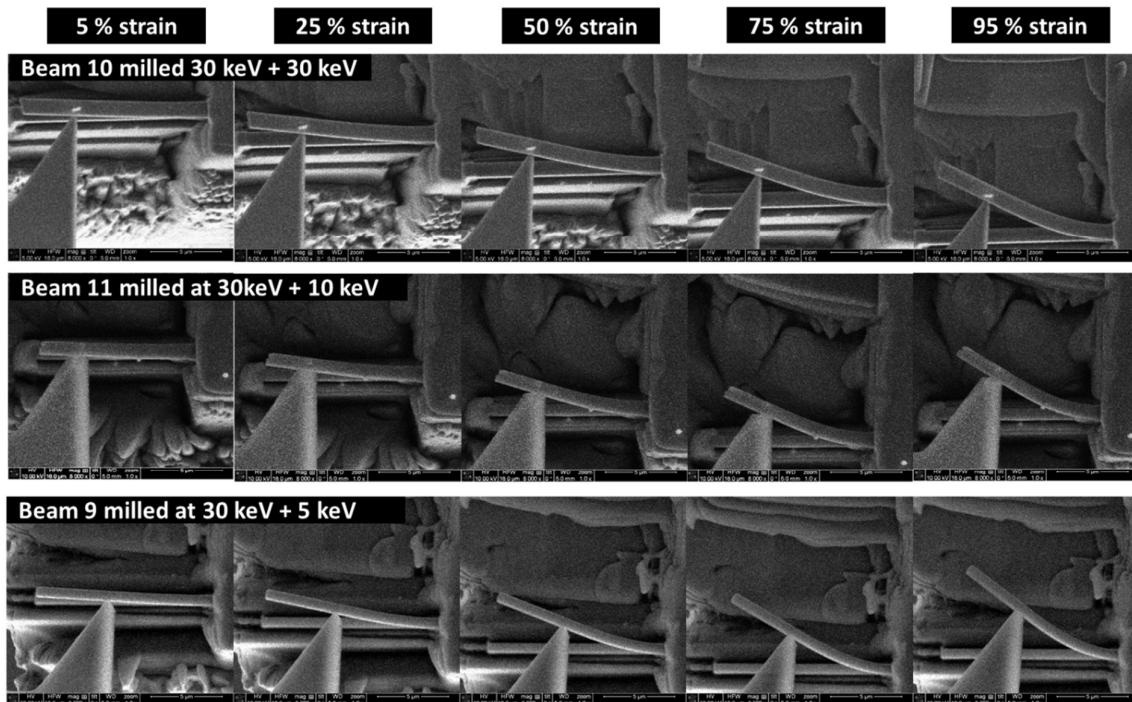


Figure 86 Representative micro bend test still images and incremental stages during micro bend testing from 5-95 % strain. Images shown represent each of the ion milling regimes.

The plots in Figure 85 show the general trends identified during micro bend testing of the various ion cleaned surfaces. Both the load-deflection and Young's modulus-strain graphs illustrate the force response variation at the point of initial contact between the micro-beam and indenter. From an experimental view, this initial contact has the highest error as the measurements being made are very small. The video images were recorded at 1024×943 pixels with frame widths up to 25 μm , resulting in a minimum pixel width of 0.025 μm (Figure 86 shows example image sequence from micro bend tests). Deflections less than 0.025 μm would require subpixel measurement during post-processing. All the beams exhibited a predominantly linear force-deflection relationship. Some sticking points were noted in the load-deflection graphs; however, the SEM images do not offer high enough frequency or resolution to identify these points as pop-in events as have been identified by other researchers using nanoindentation to deflect microbeams. The Young's modulus strain displacement graphs show that a gradual reduction in modulus occurred during the tests. Based on the beam length measurements, it was clear that part of this reduction in modulus was due to indenter slip. Either slip occurrence pushed the indenter towards the root of the beam, or in the early stages of test slip could have caused the indenter to drift away from the root of the beam. Both forms of slip are potential sources of error as they contain unquantified stress resulting in additional compressive or tensile force, dependent on the

direction. Evidence of the difficulties in measuring small deflections can be (seen in **Figure 85**) where there is a high variance in mechanical properties. Further to this, the images of the microbeams at 95% strain show the considerable deflection on the beams beyond that which would be typical of a macro sample. This significant curvature of the microbeams also contributes to the reduction in observed modulus. The mechanics of micro bend testing are often simply characterised by the small deflection equations. The premise of these equations is that the beam deflection is minimal, otherwise the effective length of the point of contact of the indenter to the root the beam is variable. As discussed in the experimental section, to negate the effects of large deflection the modulus of the micro beam was calculated based on the initial deflection of the beams.

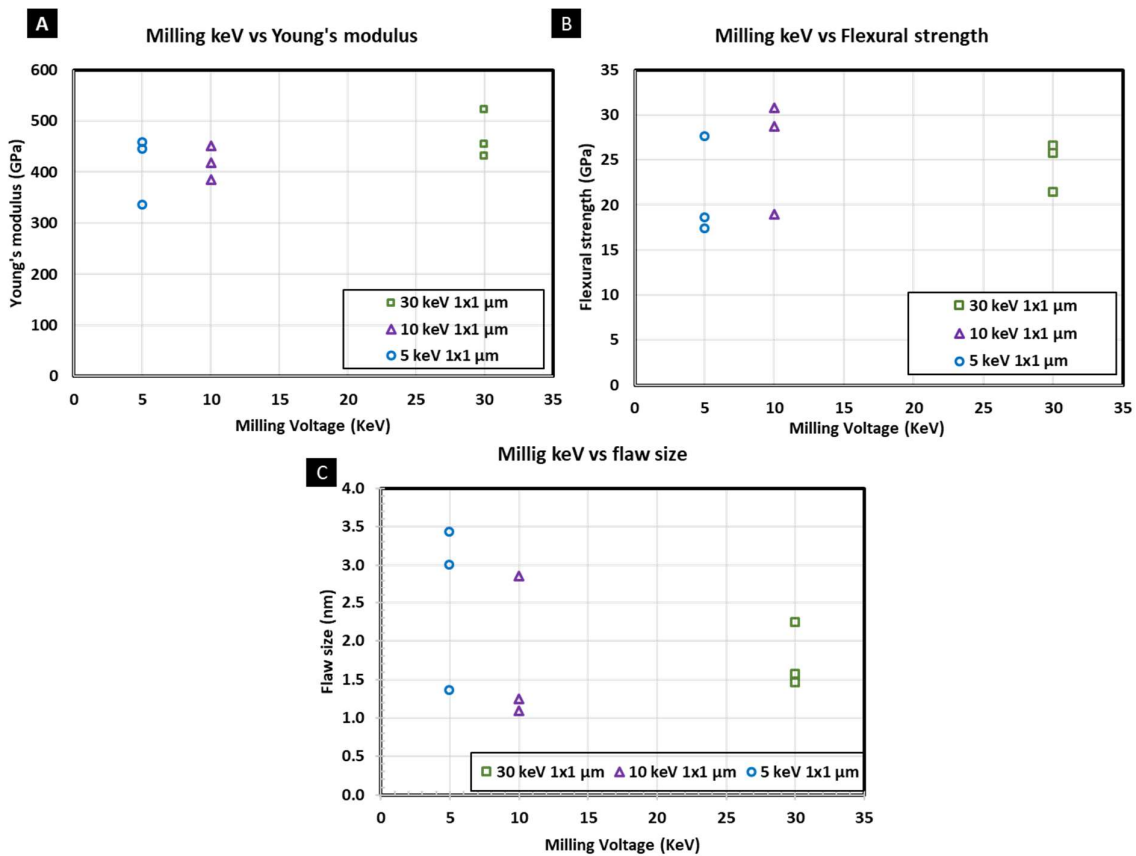


Figure 87 Results of Gallium ion microbeam milling study: effects of cleaning on Young's modulus, flexural strength and estimated flaws size.

Table 18 Summary of SiC micro bend milling study results.

Milling keV	Average Young's modulus (GPa)	Standard deviation (GPa)	Average strength (GPa)	Standard deviation (GPa)	Average flaw size (a) (nm)	Standard deviation (nm)
30	469	47	24.6	3	1.8	0.4
30 + 10	418	32	26.2	6	1.7	1
30 + 5	412	67	21.1	6	2.6	1

The results from the micro bend tests with varying ion milling parameters are summarised in Figure 87 and Table 18. The 30 keV milling regime resulted in the highest modulus and flexural strength results. Additional low voltage milling resulted in a minor reduction in modulus and no significant change in flexural strength. The modulus values recorded, 469 ± 47 GPa (30 keV), were within the bounds of the modulus calculated during nanoindentation 473-348 GPa and below the literature values for Young's modulus of 6H silicon carbide 414-450 GPa. The flexural strength 24.6 ± 3 GPa was recorded. Literature values for flexural strength for single crystal are not readily available. Values from 10 GPa are plausible. The values recorded for strength matched well with the estimated strength based on the nano indentation results.

During manufacture of the microbeams, it was identified that low voltage cleaning caused some geometric changes in the microbeam's cross section, (see Figure 88). This effect was more pronounced with the 10 keV milling steps. The sides of the microbeams became angled and the corners rounded. This rounding of the beams introduces another source of error in the calculation of the beam's true cross section. Further to this, it was noted that the poor image resolution offered by low keV milling reduced the repeatability of the cleaning technique due to difficulties in placing the milling area accurately. These changes in the microbeam shape and potential sources of error explain some of the variation in the modulus and flexural strength data recorded.

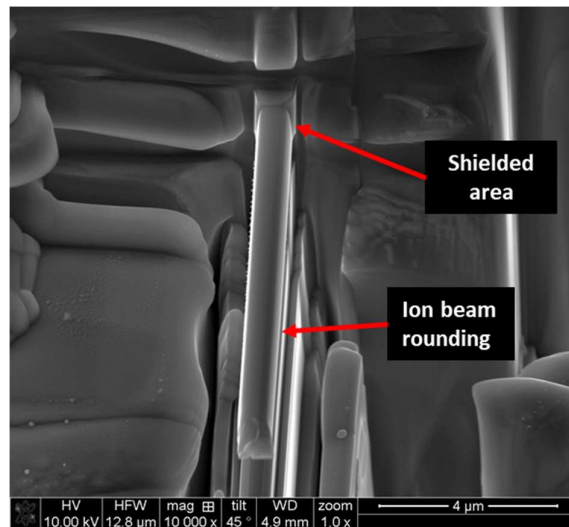


Figure 88 Beam rounding caused by 30 keV + 10 keV milling.

Despite these changes, the error between the tests was comparable to the results reported by other researchers in the field. Standard deviations of around 5-15% of the modulus are not uncommon for micro mechanical testing [195].

The fracture faces of each of the micro bend samples were analysed. The fracture faces were consistent in their presentation. As expected, the beams failed at the tensile face leaving a root of material on the compression face. The root thickness was less than half the thickness of the original beam. The fracture pattern of the micro beams (see **Figure 89**) matched well with those predicted by brittle bend test models reported in the literature:

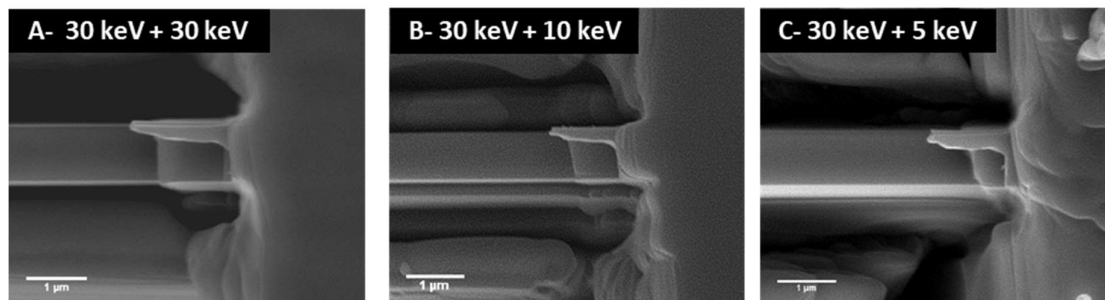


Figure 89 Fracture faces of 6H SiC 1×1 μm bend test samples cleaned at 30 keV, 10 keV and 5 keV.

No overarching trend was identified between the fracture faces of the 30 keV, 30 keV+ 10 keV and 30 keV + 5 keV milled faces. Irrespective of the final milling voltage, the fracture mode of the microbeams was repeatable.

Based on these results 30 keV, 0.3 nA milling will be used on any subsequent micro beams, because, the bend test results did not provide enough evidence to conclude that low voltage milling resulted in superior micro mechanical performance, and observations were made which suggest that low voltage cleaning reduced the repeatability and modified the cross section of the microbeams. Additional TEM analysis was conducted to identify the microstructural effects of ion beam milling on the SiC samples.

4.1.4.1. TEM study of ion milling voltage on SiC

To better understand the effects of the three microbeam milling schedules, TEM lamellar were prepared. As described in the experimental section 3.4.1, the TEM lamellar consisted of an area exposed to 30 keV + 30 keV, 30 keV + 10 keV and 30 keV + 5 keV. The exposure times used at each milling voltage were matched to the the milling protocols used on the microbeams. Figure 90 shows STEM images of the ion-implanted layers topped with electron and ion beam deposited platinum. The implanted layer shows a contrast band mid to halfway; a similar contrast band can be seen in side wall cross section TEM images of Si milled with gallium and xenon ions reported by Kelley *et al.* [62]. The contrast band and implanted depth were measured and detailed in **Table 19**, where the “first contrast band” is referred to as the dark layer in the amorphous zone.

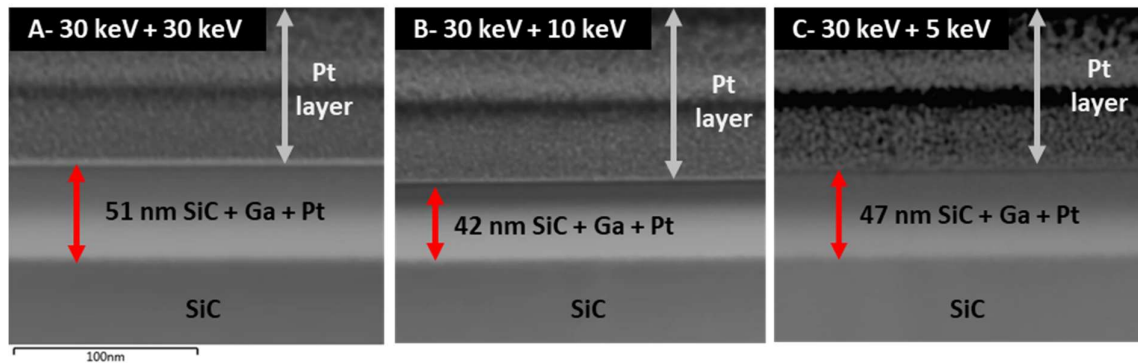
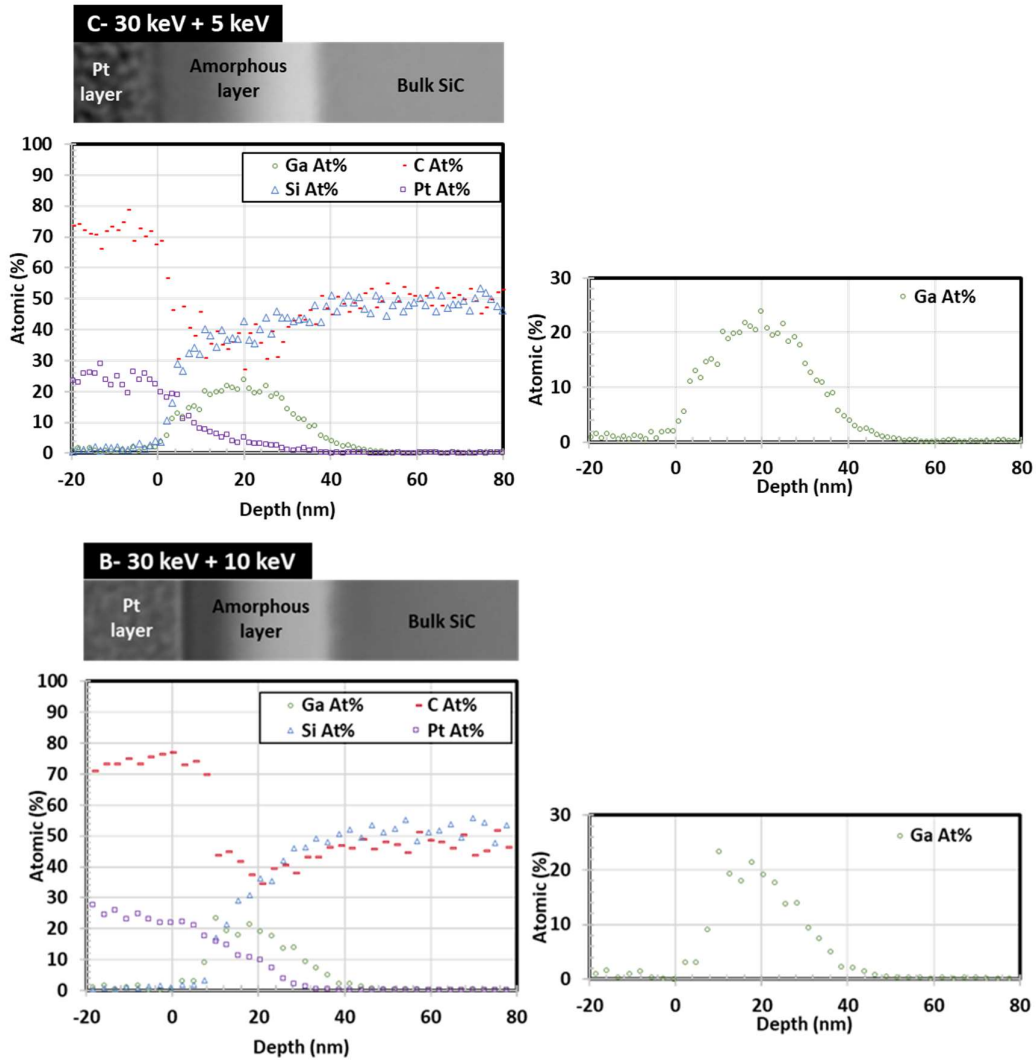


Figure 90 STEM BF images of the gallium ion damage layer introduced when ion milling single crystal 6H silicon carbide at 30 keV followed by 10 keV and 5 keV cleaning steps.

It is apparent the 30 keV sample exhibited the greatest damage layer depth (51 nm, **Figure 90**); this was expected as accelerating voltage is linked to ion penetration depth. The 30 keV + 10 keV and 30 keV + 5 keV milled areas were reduced in thickness by 9 nm and 4 nm respectively.

STEM EDS line scans were used to identify the trends in element distribution following gallium ion milling. The EDS data confirmed that a damaged layer is formed, comprising of gallium, silicon carbide and some residual/carried over platinum from the protective layer.



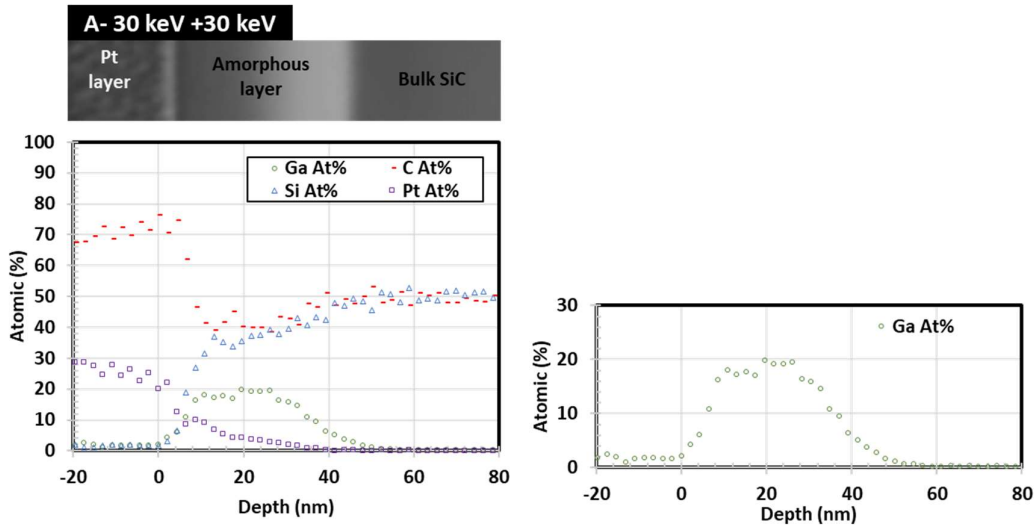


Figure 91 STEM-EDS data from gallium ion milling experiments on 6H silicon carbide with ion beam milling at 30 keV + 5 Kev, 30 keV + 10 keV and 30 keV + 30 keV.

The 30 keV + 10 keV milling procedure reduced the initial 30 keV damage layer most significantly. As can be seen in Figure 91, the width of the gallium ion peak was clearly reduced. The quantity of gallium present in the two cleaned (30 keV + 10 keV, 30 keV + 5 keV) areas was increased: this can be explained as due to the differing implantation depths of the low voltage milling steps. The difference in implantation depth can be simulated using SRIM: the results from the SRIM simulated milling of SiC are shown in Figure 92. The simulations show the ion range dependent on the accelerating voltage of the gallium ion beam. The gallium ions are implanted in a skewed distribution and, when milled with two different accelerating voltages with two overlapping distributions of ions, are implanted in the material. This overlapping implantation results in an additive effect, causing an increase in implanted gallium. It is expected that some of the gallium ions are implanted and remain in the lattice [61]. As discussed in the literature review, the high energy gallium ions cause the SiC lattice to become disordered and amorphous.

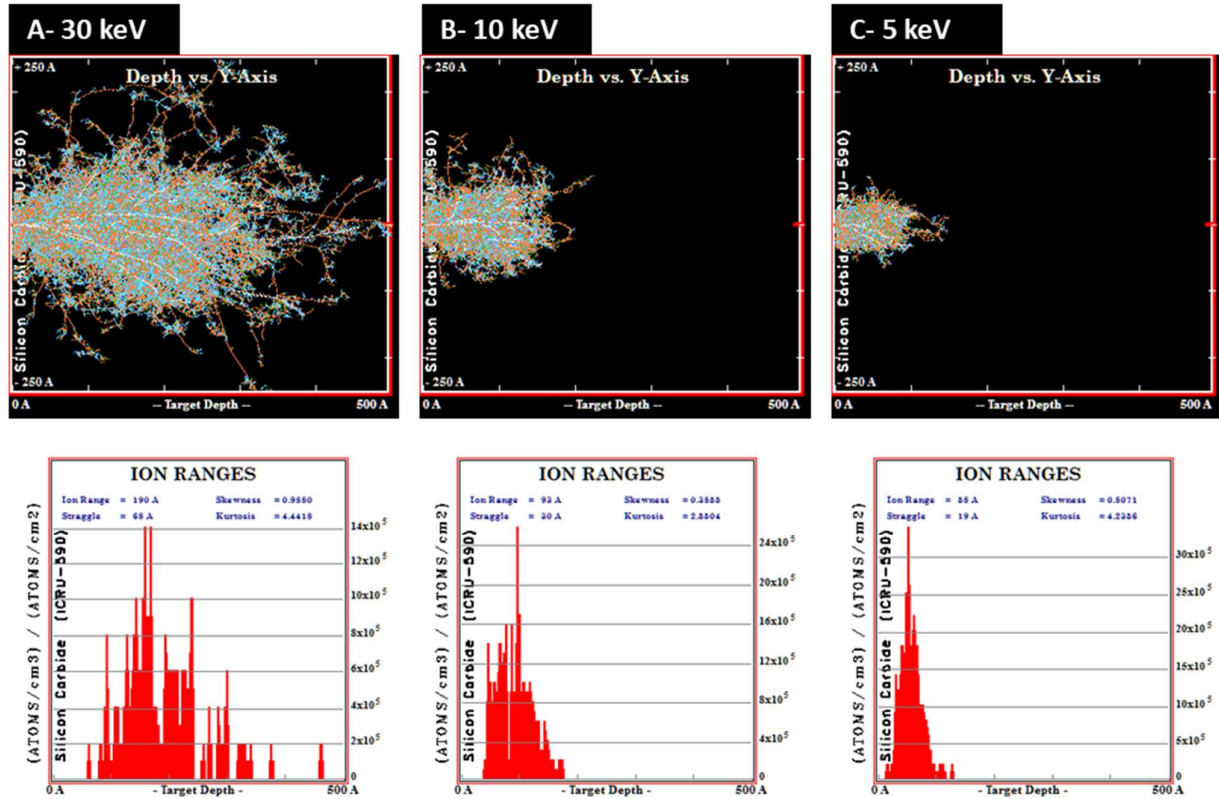


Figure 92 SRIM simulations from 100 gallium ions at (A) 30 keV, (B) 10 keV and (C) 5 keV incident on silicon carbide at 0° .

Piecing together the bright field TEM image interpretation, EDS data and SRIM simulations, a summary table of measured gallium ion distributions developed:

Table 19 Summary table of TEM and SRIM simulation results from single crystal 6H sic implantation with gallium ions at a range of accelerating voltages.

Accelerating voltage (keV)	Depth of contrast band 1 (nm)	Amorphous layer thickness (nm)	EDS atomic % gallium centre (nm)	EDS atomic % gallium max depth (nm)	SRIM simulated ion range (nm)
30 + 5	24	47	19	59	5.9
30 + 10	17	42	18	45	9.3
30 + 30	26	51	21	61	19

Tabulating the data, the contrast band observed in the bright field TEM images and the central position of the gallium ion distribution measured with EDS are well matched. The SRIM simulation data for the 30 keV milling matches with the contrast band 1 and the EDS atomic centre. The depth of the amorphous layer also corresponded well with the detectable depth of the gallium ions in the material.

SRIM was used to simulate the ion ranges of gallium ions in SiC. The modelling fitted closely with the results from the 30 keV implantation lamellar, with the centre of the gallium implanted band sitting close to the simulated position. The model also illustrated the implantation range differences between the 30 keV, 10 keV and 5 keV ions.

As low voltage cleaning techniques are commonly used to refine TEM lamellar, a greater degree of removal of the amorphous layer was expected. The minor change in damage layer thickness can be attributed to the small sputter yield from low keV milling, the angle of milling and the time period used. For experimental simplicity, all cleaning/ implanting steps were conducted with the gallium ion beam perpendicular to the SiC sample. However, when ion milling micromechanical test samples, an angle of 1-5° is used to improve sputter yield and reduce implantation. SRIM can be used to model the effects of ion angle on sputter yield and implantation depth:

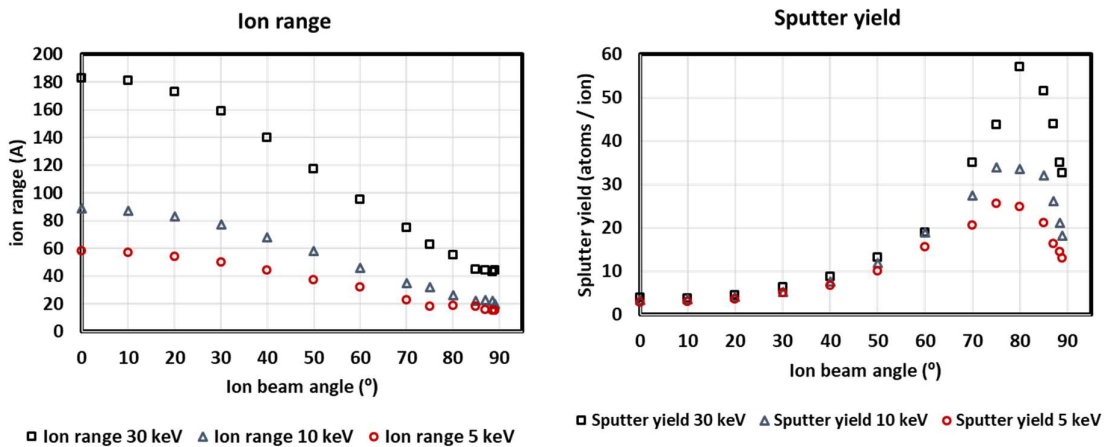


Figure 93 SRIM simulation results from 30 keV, 10 keV and 5 keV gallium ions incident on silicon carbide at a range of angles from 0° to 90°.

SRIM simulations were performed to relate the effects of ion beam angle to ion range and sputter yield (Figure 93). A tilt of 1.5° is a commonly used ion milling angle; this is frequently cited as assisting in compensating for the Gaussian distribution of the ion beam. The simulations show that angled milling also reduces the ion range and increases sputter yield of the SiC substrate. The range at 0° was 180 Å and 20 Å at 98.5°. Using this data, along with the micro beam lift out that was subsequently conducted, as a guide, it can suggest that the ion damage layer is approximately 25 nm around the microbeams.

SRIM simulations have a number of key limitations; the most relevant in this case is the lack of inclusion of channelling effects, the omission of re-disposition and amorphisation.

The crystallography of the ion-implanted layer was of interest with regards to understanding the effects of ion cleaning on micromechanical bend strength. High-resolution transmission electron microscopy (HR-TEM) was used to identify the nature of this layer.

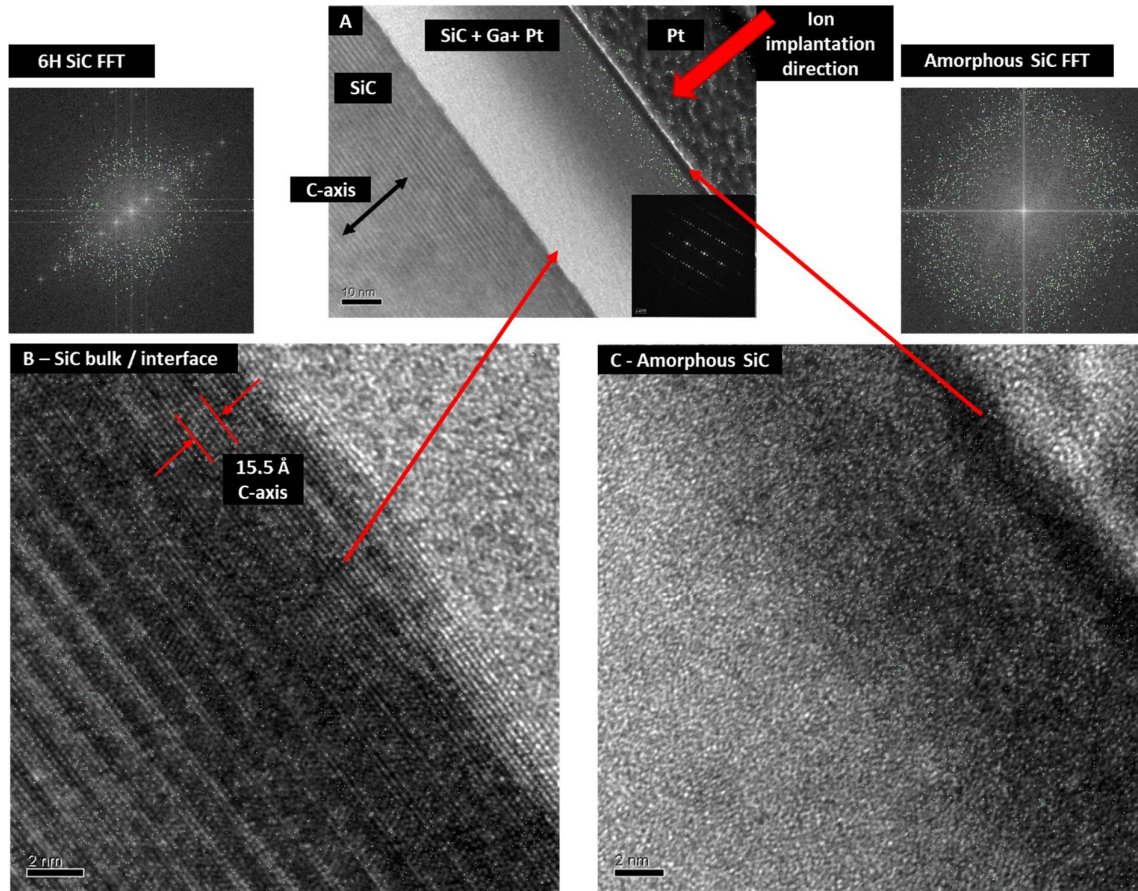


Figure 94 A – Overview of the gallium ion damage layer showing the locations of the higher magnification images (taken from the 30 keV + 10 keV milled area. The 30 keV and 30 keV + 5keV exhibited similar microstructural features). The FFT of the bulk SiC also shown. (B) SiC lattice structure topped with an amorphous layer; the image shows the 6H repeating units of SiC and c axis lattice parameter. (C) Shows the amorphous layer and platinum with the contrast band and the FFT of the amorphous zone.

The HRTEM images in Figure 94 show that the gallium ion beam amorphized the top layer of the 6H SiC as was anticipated. There is a sharp transition between the amorphous and ordered 6H structure beneath it. The atomic spacing of the 6H lattice was measured from the top face into the bulk. No statistically significant change was measurable (average 15.5 Å). No measurable change were observed in the planes perpendicular to the surface due to the lack of resolution to the smaller “a” lattice parameter. Some topography is visible in the bulk amorphous layer interface; however, this is likely related to the change in the surface of the

sample in the TEM beam direction. FFT processing of different regions below the amorphous layer was conducted. No clear conclusions could be drawn as to the residual strain below the layer, for further analysis geometric phase analysis (GPA) could be used to identify the residual stress below the amorphous layer of the 6H SiC crystal.

The mechanical properties of amorphous SiC have not received much attention in the literature. However, Li *et al.* have performed a range of nanoindentation tests on 6H SiC following Xe⁺ ion irradiation up to 2 dpa [196]. They identified that before amorphisation, ion damage caused a hardening effect, with an increase in hardness of up to 20%. At the point of amorphisation, the hardness of the SiC wafer decreased by around 35 % [196]. No modulus data was provided; despite this, we can be certain that comparable reductions in modulus could be expected as hardness and modulus are linked. Further to this, amorphisation is a function of atomic disorder: atom spacing has a direct relationship with modulus. To expand on the work of Li *et al.* low load nano indentation was attempted on the gallium ion damaged SiC areas to determine the modulus following amorphisation, however, no sufficiently robust data could be collected due to the noise from the low loads required to characterise the small (50 nm) thickness of the amorphous layer.

To conclude, the TEM analysis conducted on the ion milled faces, showed that the SiC lattice was amorphised during ion milling. This amorphisation was likely to be part of the slight reduction in modulus and bend strength following ion cleaning. The change in micro beam cross section from a square to rounded square shape is also a probable contributory factor to changes in strength. Based on the TEM analysis and SRIM simulations, a damage layer of around 25 nm can be predicted to form around the micro beams.

4.1.4.2. *Silicon carbide ion milling summary*

Gallium ion milling with 10 keV was shown to reduce the amorphous layer caused by high voltage gallium ion milling. The parameters used in the tests conducted were not sufficient to cause a significant modification of the micro bend strength or modulus of the silicon carbide. Larger-scale effects, such as microbeam corner rounding, introduced additional error into the experimentation causing an increased variation in results. TEM was conclusive in showing the gallium ion beam had caused the SiC to become amorphized, and the strength and modulus of the beams were likely also reduced due to this amorphous layer.

The results from Raman spectroscopy could not be used to identify the state of the gallium in the matrix or to define the residual stress caused by the ion damage. These results can be seen in the appendix (page 232). The Raman data matched well with the TEM data in showing the amorphisation of the SiC following ion beam implantation.

Based on this research, it is concluded that the use of 30 keV 0.3 nA or 100 pA cleaning where possible should be used to reduce the gallium ion damage on microbeams. A damage layer of 25 nm around the beams was estimated based on the TEM and SRIM analysis.

Drawing from the work of Kelly *et al.* it is also suggested that the use of xenon plasma ion beam milling could be utilized to produce lower levels of ion beam damage [62].

4.1.5. Micro bend size effect in single crystal 6H SiC

To understand the microbeam size effect and plasticity in silicon carbide, a range of micro bend tests were conducted on microbeams of cross section 1 x 1 μm , 0.6 x 0.6 μm and 0.3 x 0.3 μm . These samples sizes were chosen to pass through the so-called brittle to ductile size transition identified in the literature [53]. Based on the previous work, the microbeams were finished with a 30 keV and 0.3 nA gallium ion beam milling to avoid sample geometry variation; Table 20 shows the samples properties recorded:

Table 20 SiC size effect microbeam data pre-test.

Name	Preparation	Height (μm)	Breadth (μm)	Initial length (μm)	Length at failure (μm)	Area (μm^2)	Volume (μm^3)	Load at failure (μN)	Deflection at failure (μm)
P6	30 keV 1x1 μm	0.84	1.18	7.27	6.24	0.99	7.22	182	1.92
P10	30keV 1x1 μm	1.06	1.11	9.60	8.94	1.18	11.33	500	3.10
P13	30 keV 1x1 μm	0.91	1.02	9.98	9.41	0.93	9.30	387	3.80
P18	30 keV 1x1 μm	0.88	0.97	9.63	9.03	0.85	8.22	369	4.41
P15	30 keV 0.6x0.6 μm	0.46	0.61	4.13	4.05	0.28	1.16	80	2.79
P16	30 keV 0.6x0.6 μm	0.39	0.63	2.78	2.52	0.24	0.68	117	1.13
P19	30 keV 0.6x0.6 μm	0.60	0.50	3.79	3.48	0.30	1.15	159	1.01
P17	30 keV 0.6x0.6 μm	0.33	0.54	2.95	2.69	0.18	0.53	212	1.01
P21	30 keV 0.3x0.3 μm	0.23	0.38	2.09	1.92	0.09	0.18	36	1.25
P22	30 keV 0.3x0.3 μm	0.35	0.31	2.25	2.12	0.11	0.25	57	0.64
P24	30 keV 0.3x0.3 μm	0.26	0.33	2.10	-	0.08	0.18	-	-
P25	30 keV 0.3x0.3 μm	0.30	0.29	1.81	1.64	0.09	0.16	74	0.67

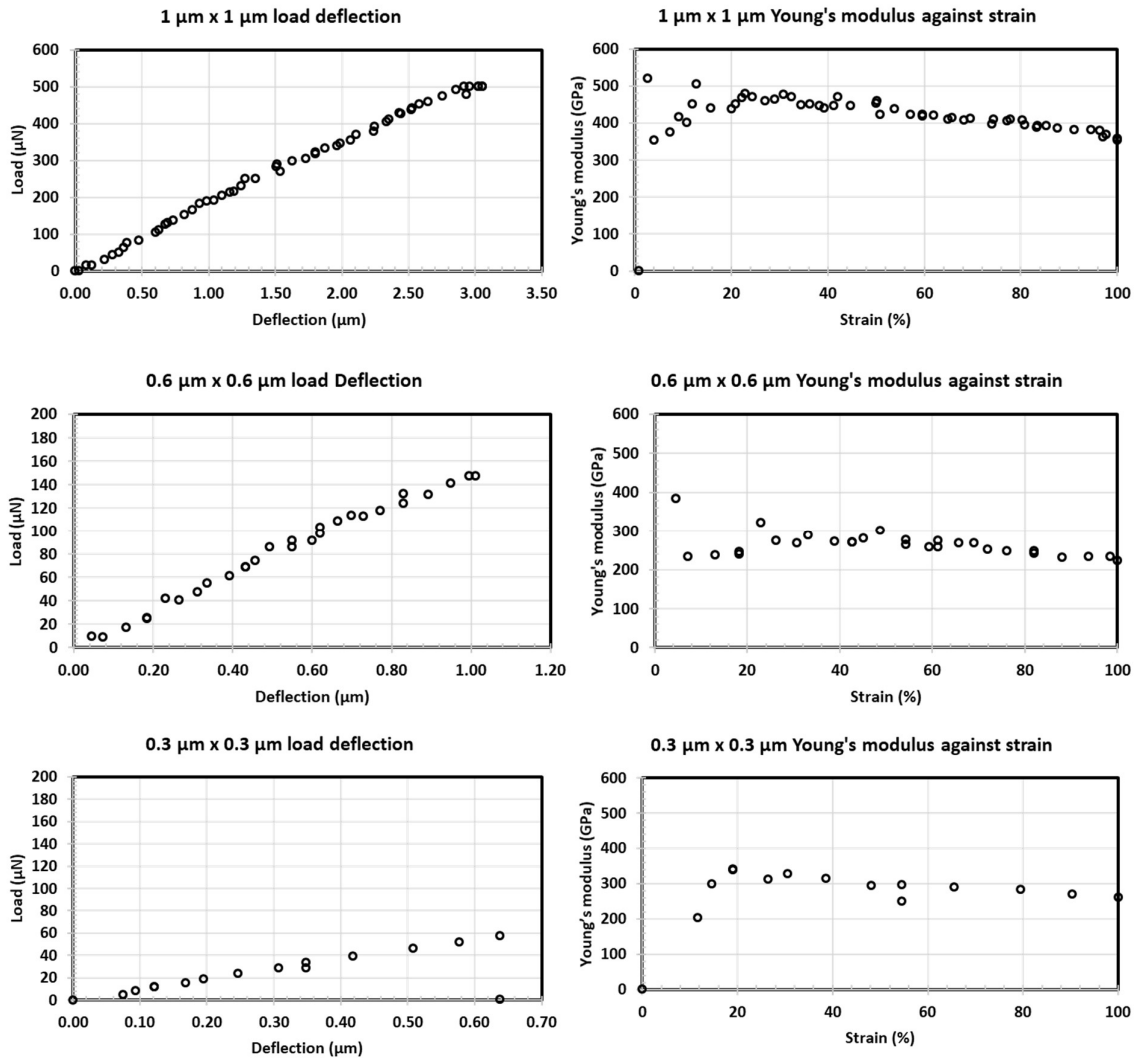


Figure 95 Example load deflection and Young's modulus against strain plots from each of the sizes 6H SiC micro bend tests.

The plots in Figure 95 show the general trends identified during micro bend size effect testing. Both the load-deflection and Young's modulus against strain graphs illustrate the variation at the point of initial contact between the micro-beam and indenter. From an experimental view, this initial contact has the highest error as the measurements being made are very small. As previously discussed, the video images were recorded at 1024×943 pixels with frame widths up to 25 μm resulting in a minimum pixel width of 0.025 μm. Deflections less than 0.025 μm would require subpixel measurement during post-processing. As the beam size reduced the ability to determine the edge of the beam, subsequent deflection became more challenging. Further to this, the number of data points before fracture of the smaller beams was reduced, making the results more sensitive to each data point. An additional

source of error may have been the compliance of the silicon tip of the indenter. As shown in Figure 96, there was slight variation in the indenter shape as the indenter was machined in-between tests to correct any damage to the tip. These variations will have modified the tip contact area and the frictional forces between the indenter and micro beam.

All the beams exhibited a predominantly linear force-deflection relationship, with the $0.3 \times 0.3 \mu\text{m}$ beams exhibiting some non-linearity. Sticking points were noted in the load-deflection graphs; however, the SEM images do not offer sufficient spatial or temporal resolution to identify these points as pop-in events as have been identified by other researchers using nanoindentation to deflect microbeams. The Young's modulus strain displacement graphs show that a gradual reduction in modulus occurred during the tests. Based on the beam length measurements, part of this change in modulus was based on indenter slip. Indenter slip is a potential source of error as it produces unquantified stress resulting in additional compressive or tensile force in the beam. A second source of error is in the equations used, which assume the deflections in the cantilever to be small and elastic: as the tests progressed the deflections became considerable with the indenter position being quite different to the original length. Plasticity was also identified in the $0.3 \times 0.3 \mu\text{m}$ micro beams, making modulus estimates at large deflections incorrect. As previously discussed, the modulus values presented are averages from the initial phase of the tests, which should be elastic irrespective of micro beam size.

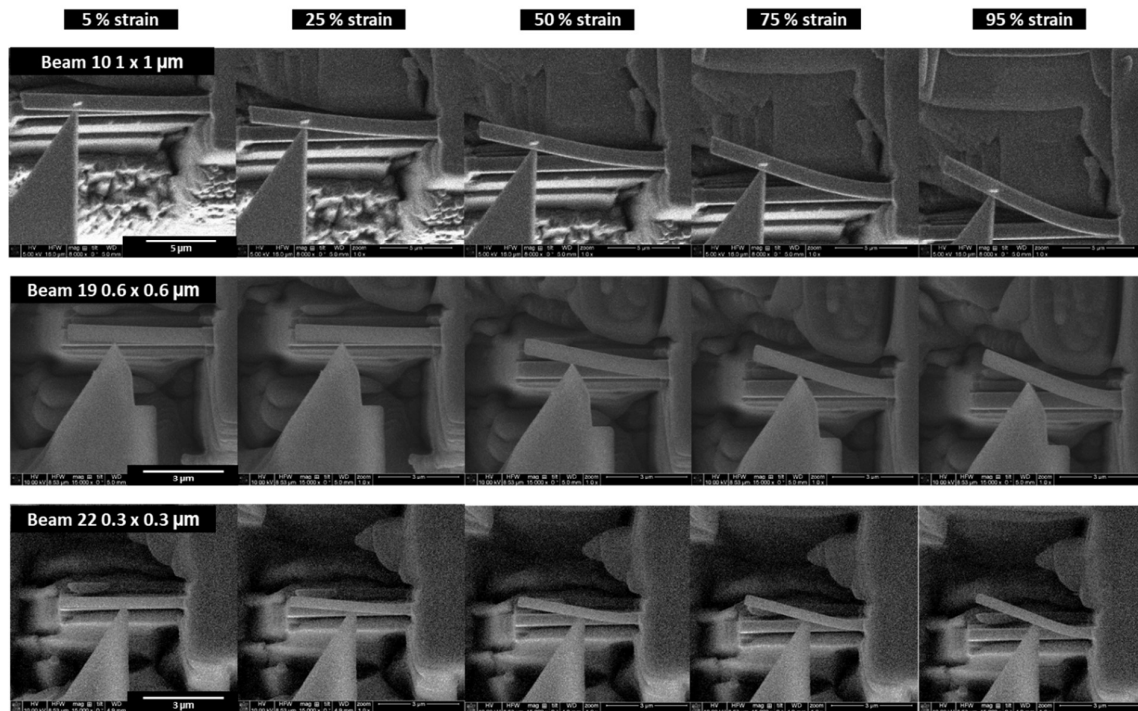


Figure 96 Representative micro bend test still images from the size effect study.

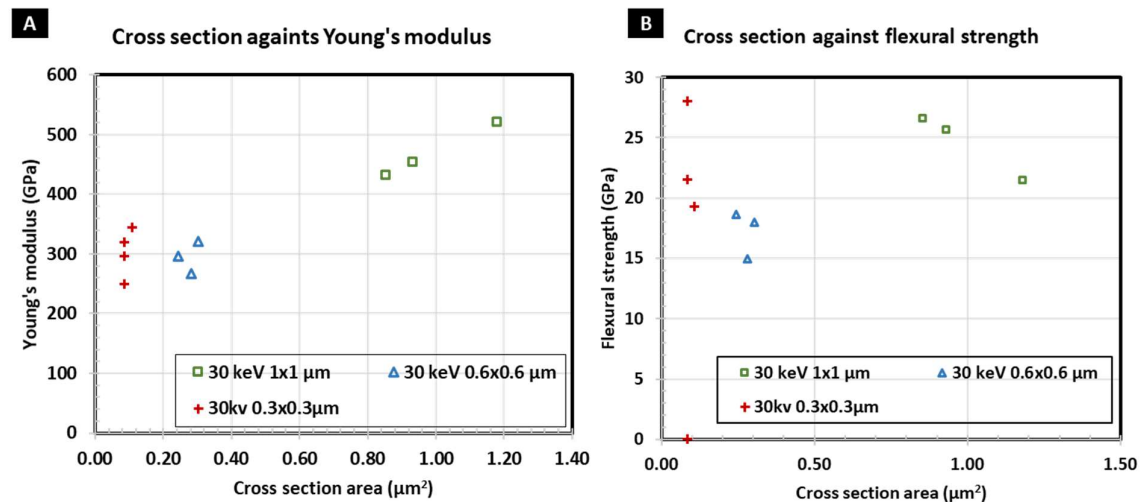


Figure 97 Micro bend size effect plots of 6H SiC, (A) Young's modulus against cross-section, (B) flexural strength against cross-section.

An inverse size effect is shown in Figure 97: modulus reducing with sample cross-section is contrary to the general trend observed in the micromechanical testing literature. The trend in the strength data is less clear, with the 0.3 μm beams performing better than the 0.6 μm beams.

Based on the in-depth TEM study of the effects of gallium ion damage on SiC, this trend is understandable as smaller beams are consumed by a greater percentage of ion damaged material. Based on the literature, this material will have a significantly lower modulus and strength compared to the bulk. To compensate for the ion damaged caused by microbeam manufacture, 25 nm was subtracted from each face during the modulus and strength calculations. The mechanical tests results were re-processed with this compensation for FIB damage. The data can be seen in Figure 98:

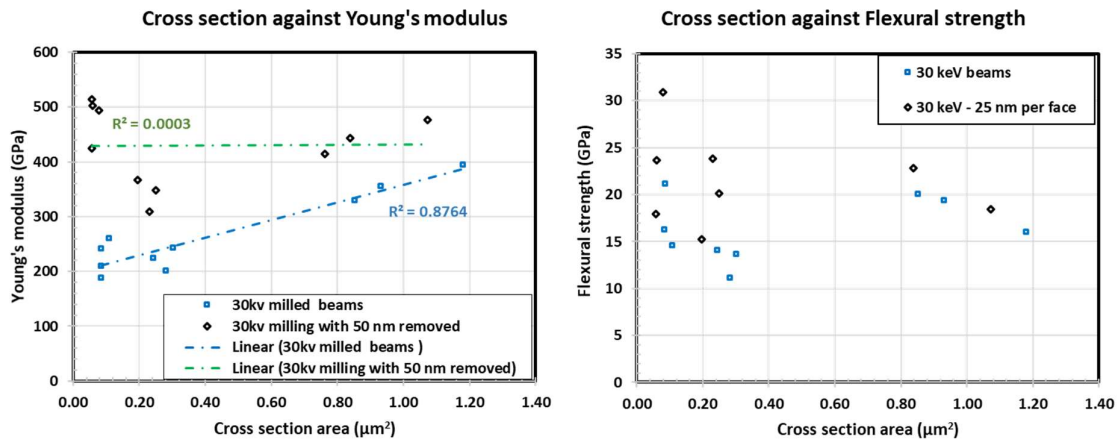


Figure 98 Micro bend size effect plots of the adjusted and original micro bend test data. Plots show Young's modulus and flexural strength against area.

By adjusting for the ion damage at the surface of the microbeams, the results are increased and therefore closer to the literature values for Young's modulus and closer to the modulus measured during nanoindentation as shown in :

Table 21:

Table 21 Microbeam size effect average Young's modulus and failure strength.

Micro beam preparation condition and size	Average Young's modulus (GPa)	Average adjusted Young's modulus (GPa)	Standard deviation (GPa)	Average strength (GPa)	Average adjusted strength (GPa)	Standard deviation (GPa)
30 keV 1x1µm	469	579	47	25	29	2
30 keV 0.6x0.6µm	295	426	27	17	24	2
30 keV 0.3x0.3µm	302	681	40	23	40	5

The strength values achieved reached the calculated estimated strength based on the nano indentation results ≈ 20 GPa. The modified cross sections showed the classic size effect, with smaller samples having higher mechanical properties. However the modulus and flexural strength of the adjusted $0.6 \mu\text{m}$ cross section microbeams did not conform well to this general trend. As discussed in the subsequent section (4.1.5.1 Plasticity in single crystal 6H SiC), the $0.3 \mu\text{m}$ may have performed better due to the sample deforming plastically. This plastic deformation would not have been accounted for by the mechanics for small beam deflection.

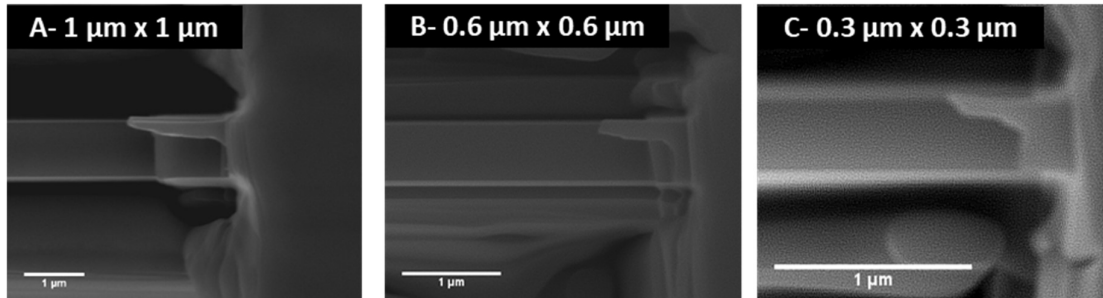


Figure 99 Representative fracture faces from $1 \times 1 \mu\text{m}$, $0.6 \times 0.6 \mu\text{m}$ and $0.3 \times 0.3 \mu\text{m}$ microbeams.

The fracture of the SiC beams was very repeatable with the shape of the fracture and the root length scaled with the thickness of the beam. The $0.3 \times 0.3 \mu\text{m}$ beam fracture roots exhibited a slight deflection from parallel. This deflection of the root may indicate some plasticity before failure.

4.1.5.1. Plasticity in single crystal 6H SiC

Based on the load displacement plots and initial hysteresis testing of the $0.3 \times 0.3 \mu\text{m}$ microbeams, it was identified that the microbeams were deforming plastically. To characterise the plastic deformation, hysteresis testing was undertaken (as shown in Figure 100). The beam was loaded and unloaded resulting in permanent deformation of $0.12 \mu\text{m}$. The permanent deformation can be observed in the graph in Figure 100 and image sequence in Figure 101:

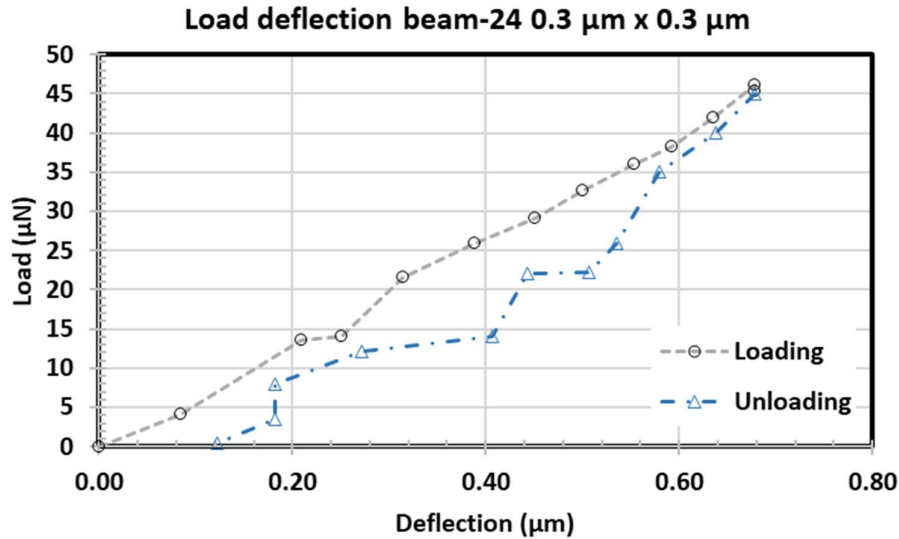


Figure 100 Load deflection graph from a $0.3 \times 0.3 \mu\text{m}$ SiC hysteresis micro bend test. The loading phase is denoted by the grey line and circles while unloading is shown by the blue line and triangles.

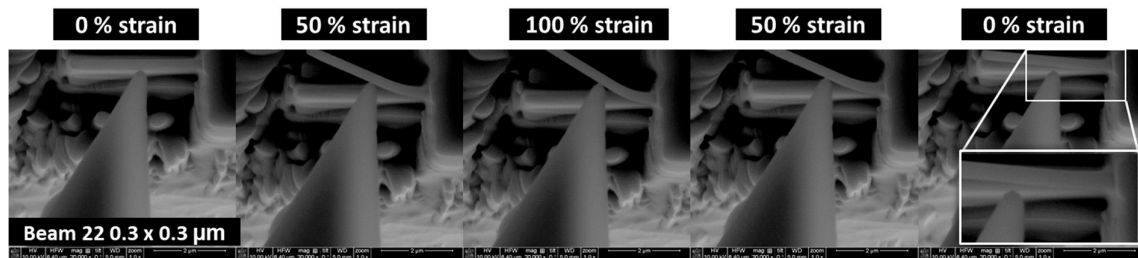


Figure 101 SEM images from the micro bend hysteresis tests showing the residual displacement of the microbeam following testing.

During the literature review it was identified that a plastic to brittle transition can be identified in SiC and other brittle materials (Si GaAs) [76]. The transition cross section identified in SiC was $0.3 \times 0.3 \mu\text{m}$. The ability for the beams to deform plastically suggests that the strength equations for brittle failure were not appropriate for the calculation of strength in the size effect study. This potentially explains the high strength values calculated from the $0.3 \times 0.3 \mu\text{m}$ tests. FEA would be a more suitable approach for calculating the strength of the micro beams. FEA was deemed beyond the scope of this project.

Following hysteresis testing, the plastically deformed microcantilever was coated in platinum and lifted out for TEM analysis. The microbeam was lifted out from the indented face of the beam, parallel to the basal plane. Due to the thin nature of the microbeam, it was challenging

to ensure the lamella was cut from the central portion of the microbeam. Upon TEM analysis it was found that the end of the microbeam was fully amorphous. During the lift out and subsequent TEM analysis, it was concluded that the end of beam was amorphized during lift out rather than before or after testing. The root of the beam remained crystalline and was indexed as [0001] relative to the electron beam.

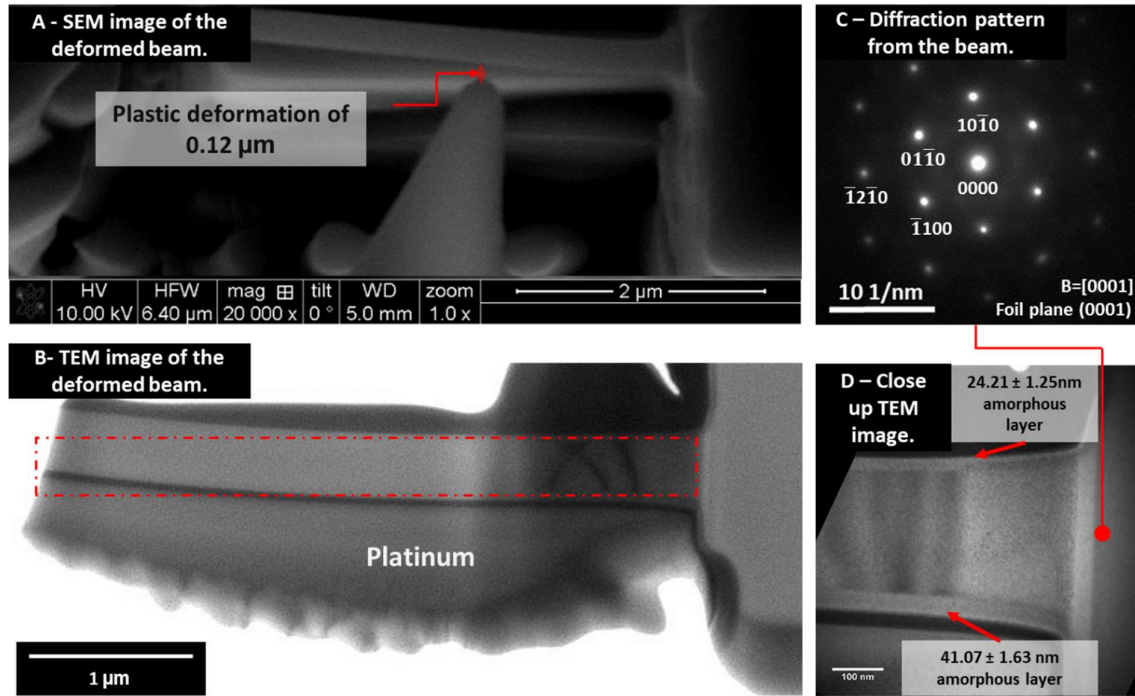


Figure 102 (A) SEM image of the plastically deformed SiC microbeam. (B) TEM images of the lifted out microbeam showing the original and deformed shape of the beam; with diffraction contrast, some diffraction bands are present. (C) diffraction pattern from the root of the micro beam. (D) higher magnification images of the root of the microbeam showing the amorphous outer layer and interior of the beam.

The [0001] basal plane is one of the available slip systems in the 6H lattice making deformation more favourable. The root of the microbeam exhibited few resolvable dislocations. These dislocations emanated from the tensile stress face seen at the bottom of the Figure 102. Slip on the prismatic plane could have facilitated deformation of the cantilever; the orientation of the dislocations (in Figure 102) suggest this may have been possible. SEM analysis of the beam after testing did not show any signs of slip traces on the top face.

An amorphous layer was identified on the exterior of the beam forming a core shell structure. The compression face of the beam had an amorphous layer thickness of $24.21 \pm 1.25 \text{ nm}$, while the tensile face had a thickness of $41.07 \pm 1.63 \text{ nm}$. The thickness of the amorphous layer

around the beam was comparable to the estimated damage layer thickness determined in section 4.1.4. The top face of the microbeam would be expected to have the highest damage layer thickness, as it would have been exposed to ion damage during imaging of the beam and during milling. Based on the TEM images from the cross sectioned micro beam, the side faces have a damage layer thickness between 24 – 41 nm. The stress concentration is higher on tensile face of the beam, making the amorphous layer thickness of 41 nm significant in reducing the strength and modulus of the micro beams.

4.1.6. Single crystal 6H silicon carbide micro mechanical characterisation conclusions

In this section, the surface topography and chemical composition of the 6H SiC wafers have been characterised. Due to the low roughness and consistent composition, the wafer was deemed suitable as a model material for the development of the micro bend test technique. Nano indentation was used to determine the Young's modulus and hardness of the wafers purchased, such that micro bend tests results could be cross referenced to Young's modulus results from the same samples.

A range of indentation loads from 25 mN to 250 mN was used for indentation. Nano indentation determined the Young's modulus of the wafers to average from 349-473 GPa dependent on load, and the hardness was found to be 36-60 GPa. Based on the crack tip length measurement method, the fracture toughness of the wafer was found to be 1.43-1.76 MPa.m^{-1/2}. Young's modulus and hardness of the wafer were found to vary with load. The size effect was characterised using the Meyer's law and the PSR model. Fracture toughness was found to be independent to load, as suggested in the literature.

Micro bend testing was conducted, and a range of beam sizes and milling voltages were used to cut the micro beams. Varying ion beam milling voltage was not found to have a significant effect on the modulus or strength of the micro beams. Through TEM analysis it was identified that ion milling caused amorphisation of the surface of the SiC, with a thickness of 42-50 nm. Furthermore, it was identified that prolonged ion milling resulted in rounding of the micro beams, reducing their effective cross section. Average Young's modulus ranged from 320–469 GPa, and average fracture strength ranged from 17–26 GPa. The Young's

modulus values determined through micro bend testing and nano indentation were within error.

Micro beam modulus was found to reduce with cross section; based on the amorphisation of the micro beams, this trend was expected as smaller beams consist of a greater percentage of amorphous material. As the micro beams tended towards $0.3 \times 0.3 \mu\text{m}$, plasticity was identified. Once bent, the micro beams could remain plastically deformed, and a lift out of a deformed micro beam was conducted. In the TEM sample of the plastically deformed micro beam, very few dislocations were visible.

Based on these findings, future tests with high young's modulus ceramics ($\approx 400 \text{ GPa}$) will be conducted with a consistent cross section $\approx 1 \times 1 \mu\text{m}$ and length $\approx 10 \mu\text{m}$. Furthermore, Ion beam milling voltage will be maintained at 30 keV, due to edge rounding caused by additional low voltage milling steps.

4.2. Characterisation of zirconium nitride (ZrN) and ion implanted ZrN

4.2.1. Introduction

In this section, hot pressed ZrN and gold ion implanted ZrN are characterised to determine grain size, porosity, effects of ion damage including gold ion distribution, dislocation density and residual stress.

4.2.2. SEM analysis of ZrN and ion implanted ZrN

4.2.2.1. Grain structure of ZrN

Backscatter imaging was used to identify the grain size and residual porosity of the zirconium nitride samples. The dark grains reflect stronger channelling, while the lighter ones have weaker channelling. Despite both the virgin and irradiated samples being cut from the same hot-pressed sample, SEM identified the considerable difference in porosity between the two samples, as shown in **Figure 103**:

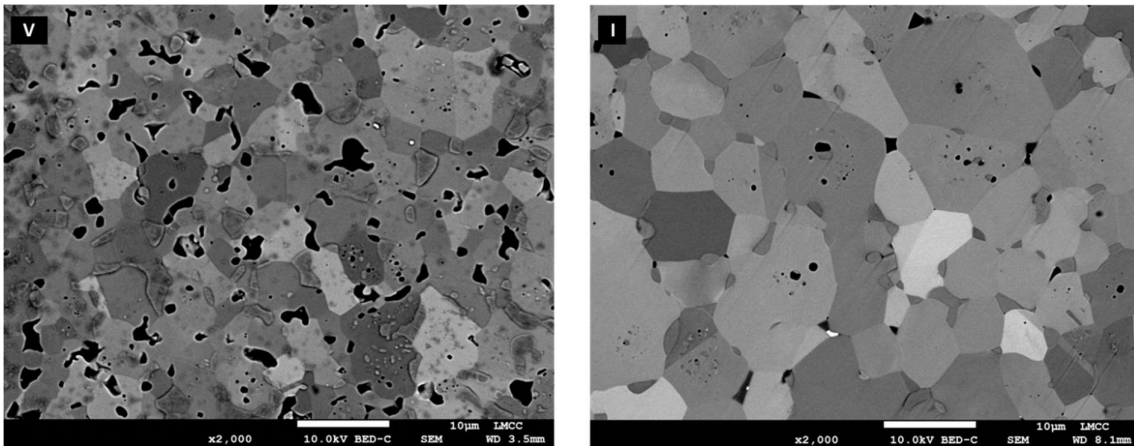


Figure 103 Backscatter image of (V) virgin and (I) irradiated ZrN showing residual porosity distribution.

The grain size of the virgin sample was calculated to be $7.4 \pm 3.9 \mu\text{m}$, while the grain size of the irradiated sample was $6.1 \pm 2.0 \mu\text{m}$. Due to the differences in porosity, the remainder of

the virgin area analysis (EDS and EBSD) was conducted on the irradiated sample in areas away from the ion implanted zone. Backscatter imaging suggested that the sample may be dual phase, as some smaller darker grains were distributed through the microstructure. This phase could not be isolated using thresholding and, as such, could not be characterised by imaging alone. Researchers in the literature have reported ZrN samples containing ZrN, Zr₃N₄, Zr₂ON₂ and ZrO [172]. The second phases will be thoroughly characterised by combined EBSD and EDS.

The virgin sample exhibited 6.6 ± 1.4 % porosity with an average pore size of 0.48 ± 0.1 μm , while the irradiated sample had a porosity of 0.9 ± 0.3 % with an average pore size of 0.13 ± 0.04 μm over 20 images covering an area of 0.054 mm^2 . Porosity measurement images were taken at $2000\times$ magnification. Each pixel = 0.05 μm at $2000\times$ magnification; thus the resolution to porosity at this scale could have been characterized more accurately by using a mix of high and low magnification images. The manufactured density of the ZrN sample was calculated to be 98% based on the Archimedes method (data provided by Donghua University/Shanghai Institute of Ceramics). The SEM porosity findings match reasonably well with the Archimedes density data. The porosity distribution was not homogeneous within the virgin sample and the irradiated sample. Density inhomogeneity is not uncommon in hot pressed ceramics due to strain gradients during pressing [127]. Further to this, the Archimedes density measurement may have underestimated the density of the ZrN sample due to open porosity at the surface of the hot-pressed sample.

Grain boundaries, triple points and porosity within the grain were identified along with twinning, (see Figure 104). The microstructure identified compares well with other hot-pressed samples in the literature, including triple point porosity as identified by Yang *et al.* [178]. The porosity levels in the samples were comparable to those achieved by other researchers using hot pressing. Wheeler *et al.* produced ZrN samples as a surrogate for actinide nitride fuels [168]. For surrogacy of actinide nitride fuels, it was recommended that a microstructure containing large open porosity with high mechanical properties be sought [168]. The open porosity would allow the release of helium caused by the alpha decay of neutrons subsequently limiting sample swelling and cracking [168].

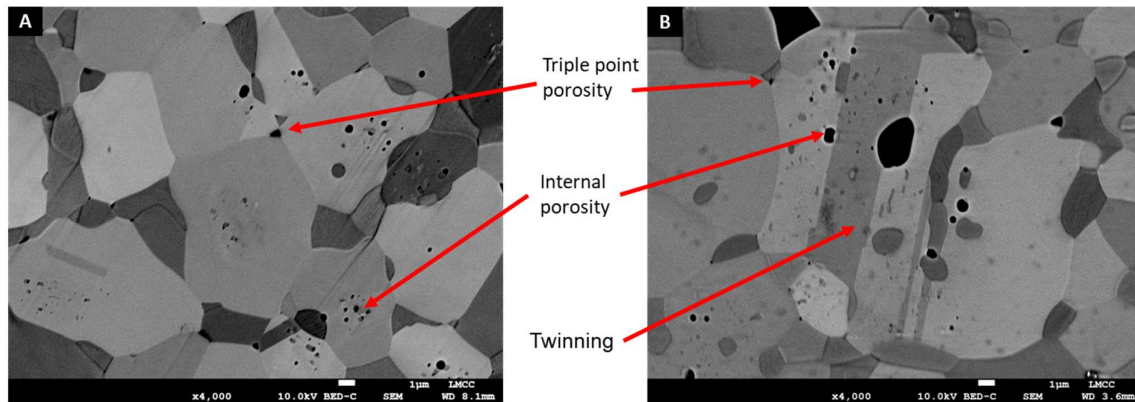


Figure 104 Backscatter images of ZrN showing porosity and twinning (A) shows triple point porosity and internal grain porosity. (B) shows a large twin with an internal pore.

In both the virgin and irradiated samples, the ZrN matrix did not exhibit dislocation lines while the second phase often featured dislocations lines (see **Figure 105** and **Figure 106**). Dislocation lines in the second phase were also identified by Yang *et al.* The source of the contrast is due to backscatter channelling contrast as is used in electron channelling contrast imaging (ECCI) [178], [197].

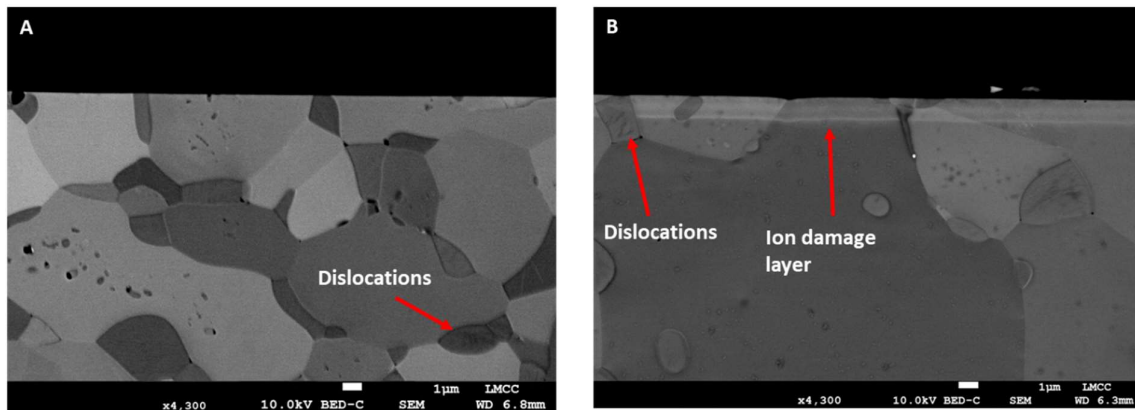


Figure 105 (A) Un-irradiated ZrN, (B) gold ion irradiated ZrN showing a contrast band on the top face.

The ion damaged surface was identified using backscatter imaging. As shown in **Figure 105** and **Figure 106**, the ion layer is visible as a bright layer on the surface of the bulk. Unirradiated faces of the sample were checked to ensure that this contrast band was unique to the ion damaged face and not related to polishing or hot pressing (as shown in **Figure 105**).

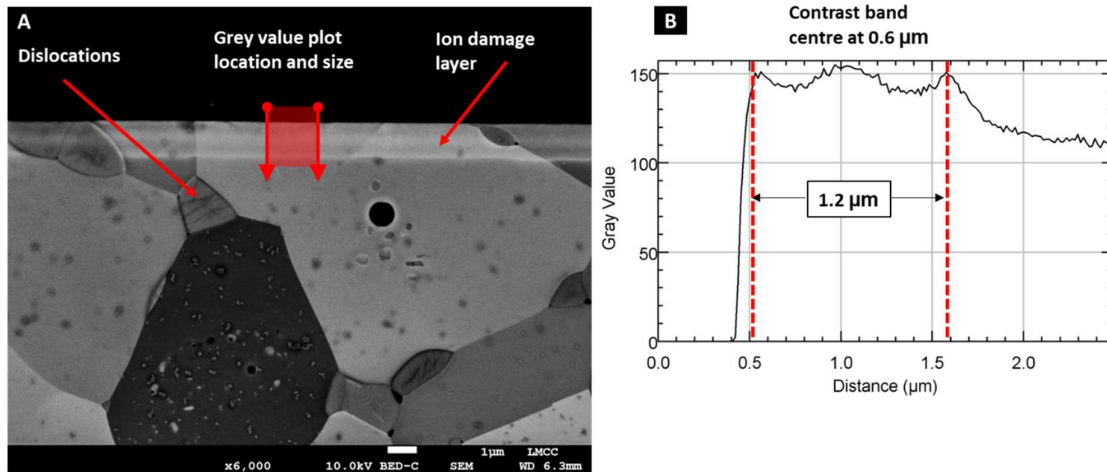


Figure 106 (A) Ion damaged ZrN backscatter SEM image annotated with the ion damage layer and dislocations in the second phase. (B) a averaged grey value plot from the surface of the sample through the ion implanted layer into the bulk; the plotted area is shown in red box in image A.

Very few researchers have characterised ion damage cross sections using backscatter SEM. Analysis of the ion irradiated face samples is more common in the literature [188]. This technique proved to be a quick, easy way to evaluate ion beam damage before conducting detailed TEM analysis. One significant point is that polishing may have enhanced the contrast to the ion damage due to additional dislocations and surface pull out. This phenomenon is common in indentation cross-section studies [198]. Within the ion damage contrast band there is a second bright layer (as shown in the image [A] and grey scale plot [B] **Figure 106**). The grey value plot uses an averaged value from the area denoted. The grey scale contrast plot identified the central contrast band within the bright layer, and the location of the central band was found to be at $\approx 0.60 \mu\text{m}$ with a normal distribution. The width of the contrast band was around $1.20 \mu\text{m}$. Backscatter imaging is sensitive to changes in crystallographic orientation based on channelling contrast, atomic mass, dislocations, and density. Electron backscatter diffraction and energy dispersive spectroscopy were subsequently used to confirm the source of the contrast band. To further confirm the source of the contrast band and validate its relationship to the ion damage, focus ion beam (FIB) lift outs and transmission electron microscopy (TEM) were conducted on the surface of the sample.



Figure 107 Photo montage showing the consistency of the ion damage layer across the sample.

A photo montage was used to show that the ion damaged layer is persistent across a large area of the sample (over 100 μm shown, see Figure 107). The ion damaged layer was consistent across the whole sample with minor variations in thickness where grain boundaries, porosity or multiple grains were included in the surface layer. The thickness of the layer was measured over ten images and calculated to be $1.20 \pm 0.15 \mu\text{m}$. Grey points were occasionally present in the micrographs. These areas were confirmed as contamination from polishing and not a constituent of the microstructure.

4.2.2.2. *Energy dispersive spectroscopy (EDS) of ZrN*

Energy dispersive spectroscopy (EDS) was used to identify the chemical composition and relation of chemical composition to microstructure of the irradiated ZrN sample. The bulk of the material was mapped (see Figure 108). Low accelerating voltage EDS was subsequently utilised to gain better resolution to oxygen and nitrogen content, see Figure 109:

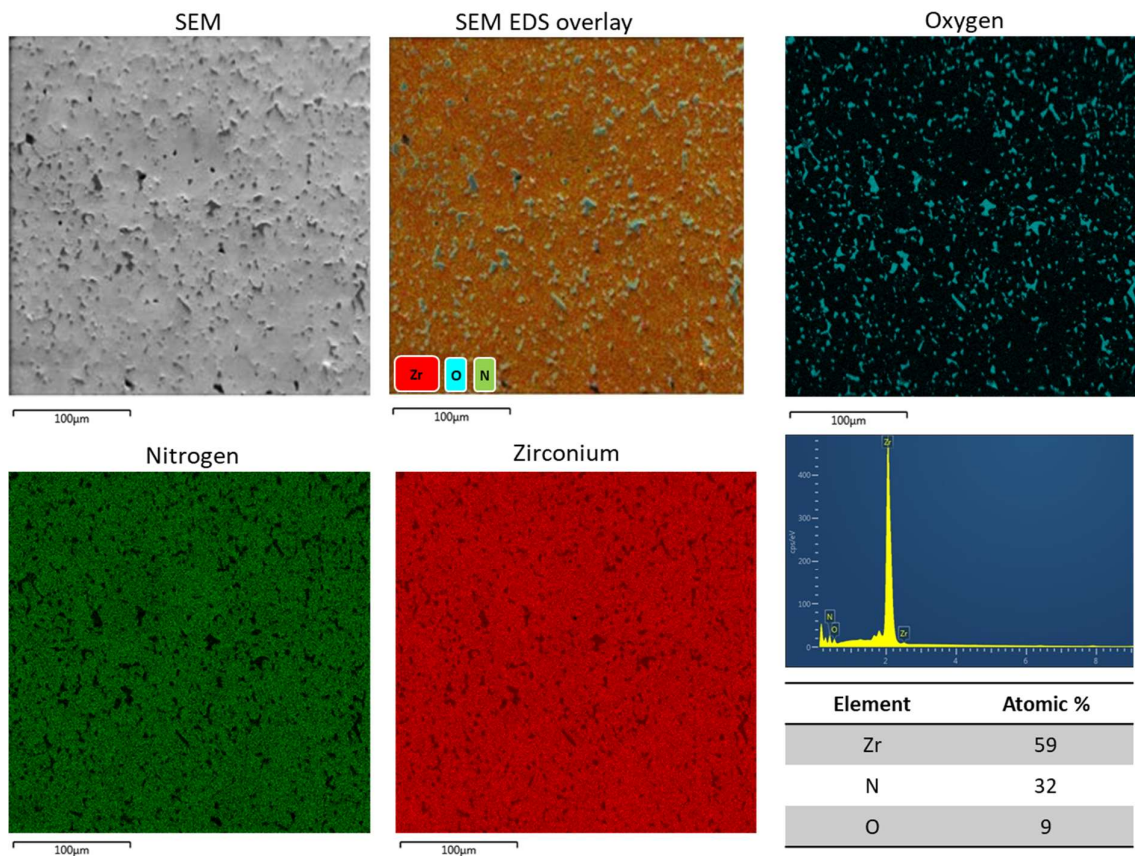


Figure 108 EDS scan from the bulk of the ZrN sample conducted at 20 keV showing each element distribution, spectra and summary elemental table by atomic %.

The surface of the ion irradiated ZrN was EDS mapped. The stoichiometry between zirconium and nitrogen was found to be $ZrN_{0.9}$. The results match closely to the bulk material, apart from the additional carbon from the sample mount. The implanted gold layer was not discernible by EDS, as gold and zirconium K alpha spectra overlap.

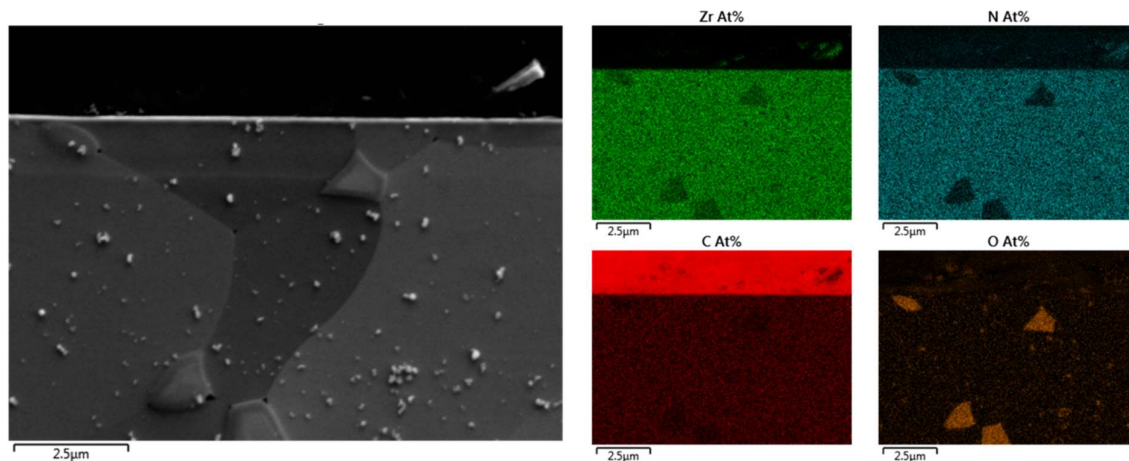


Figure 109 EDS scan from the surface of the irradiated ZrN sample conducted at 5.0 keV showing each element distribution.

EDS scans were performed at higher accelerating voltages to excite higher energy gold peaks; despite this, gold could not be identified in the implanted surface. The EDS suggests the samples were comprised of a dual-phase material consisting of ZrN and ZrO or Zr₂ON₂ oxide particles. The SEM images show that the oxide particles may have a core-shell structure.

4.2.2.3. Electron backscatter diffraction (EBSD) of ZrN

EBSD was performed on the bulk and ion irradiated surface of the ZrN sample. Grain orientation was calculated by identifying patterns with a 10 ° difference to their nearest neighbours. Different colours are used to denote adjacent crystallites having orientation difference, and the same colour in a continuous region represents same crystal orientation. Two scans of the bulk material were conducted, providing orientation data and grain size data (see Figure 110). The sample size included 1807 whole grains in a frame size of 200 × 200 μm. The combined EDS and EBSD found that the sample comprised of ZrN and Zr₂ON₂.

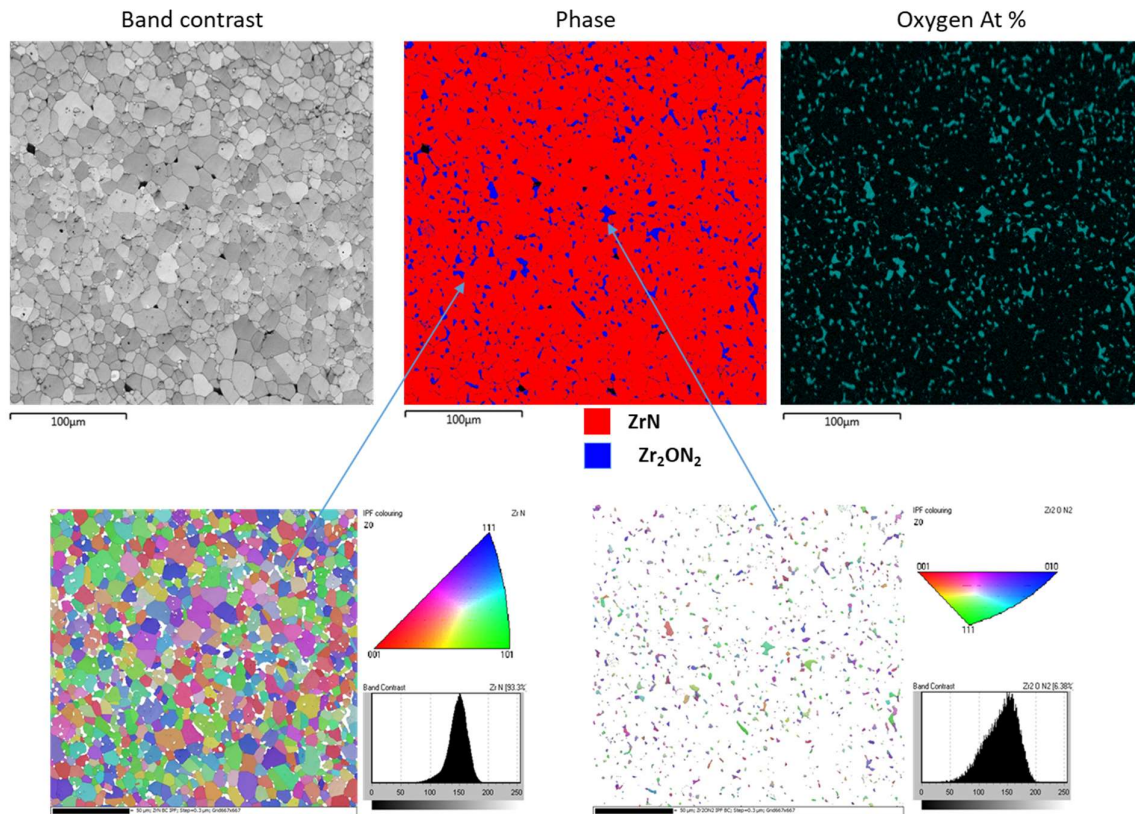


Figure 110 EBSD map of ZrN showing the two phases ZrN and Zr₂ON₂. The phase map and oxygen map show good agreement with the oxynitride phase aligned to the oxide regions.

Through EBSD mapping, we showed that the ZrN polycrystalline sample consisted of 93.3% ZrN and 6.4% Zr₂ON₂ in the examined region. The ZrN bulk was found to be untextured; the average grain size was calculated as $5.29 \pm 3.31 \mu\text{m}$. The grain size of the Zr₂ON₂ phase was found to be $1.60 \pm 0.63 \mu\text{m}$. This matched well with the initial linear intercept-based measurements of grain size. The numbers of grains (1195 + 631) were sufficient to regard the data as statistically representative of the sample microstructure. Observationally, some areas of the sample did contain more porosity; however, regarding grain size, this data is sufficiently representative. The average grain aspect ratio was 1.74 ± 0.75 , suggesting the ZrN grains were close to equiaxial in shape. The aspect ratio of the Zr₂ON₂ was similar at 1.99 ± 0.72 also suggesting an equiaxed shape. Neither phase was identified as having a preferential orientation. EBSD band contrast images matched well with the backscatter imaging where twinning was identified, along with porosity at triple point junctions and within grains; further work could be done to quantify these features.

Table 22 Table of grain properties for ZrN and Zr₂ON₂ based on EDS assisted EBSD.

ZrN	Area [μm ²]	d [μm]	Xcg	Ycg	Aspect ratio	No of grains
Average	30.59	5.29	337.24	336.47	1.74	1195
Standard deviation	39.39	3.31	203.65	193.15	0.75	
Max	600.30	27.65	665.27	665.69	8.37	
Min	0.90	1.07	0.47	0.21	1.00	

Zr ₂ ON ₂	Area [μm ²]	d [μm]	Xcg	Ycg	Aspect ratio	No of grains
Average	2.31	1.60	333.75	319.43	1.99	613
Standard deviation	2.68	0.63	199.23	176.61	0.72	
Max	33.66	6.55	665.22	663.53	5.53	
Min	0.90	1.07	1.20	1.36	1.02	

As observed, the Zr₂ON₂ had a smaller grain size and grain size distribution when compared to the ZrN matrix (see Table 22). The linear intercept method for calculating grain size matched well with the large grain frequency distribution (5-6 μm), but underestimated the smaller grain population. Additional higher magnification and potentially lower keV EBSD (with lower interaction volume) could be conducted to provide further detail on the small grain distribution.

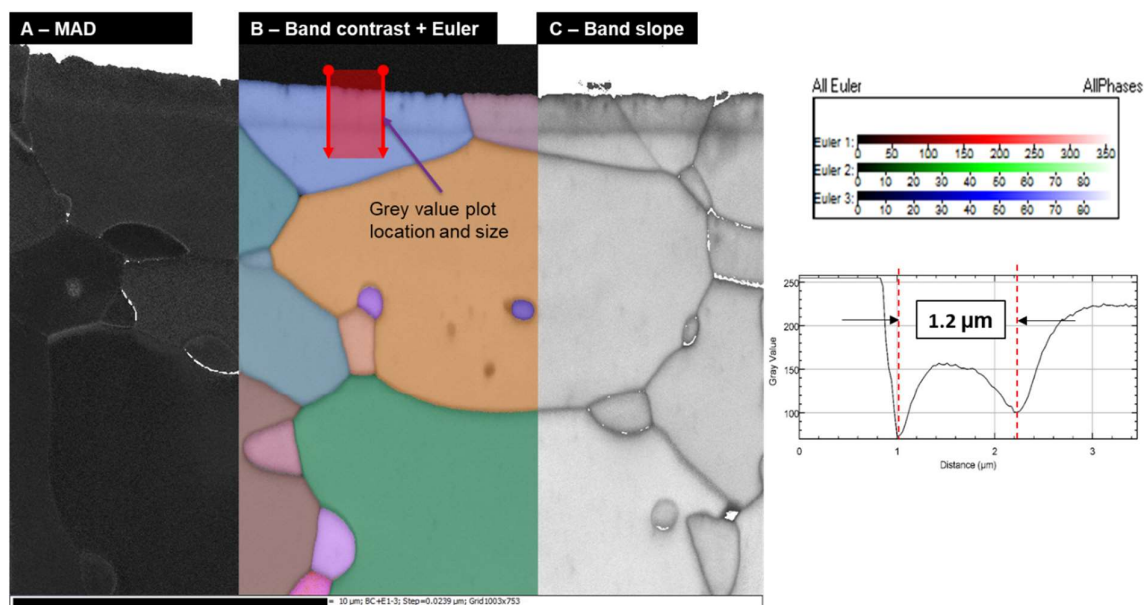


Figure 111 Gold ion irradiated ZrN cross section prepared by polishing examined with EBSD at 20 keV. (A) mean angular deviation map (MAD), (C) Band contrast with grain orientation, (D) Band slope.

EBSD of the surface gold ion implanted layer exhibited a contrast band at 1.20 μm from the surface (see Figure 111). This band was identified in the band contrast plot (as shown in Figure 111), band slope and MAD images. The width of the band was around 1.2 μm in thickness. This dimension for the implanted layer matches well to the layer observed in the backscatter images in Figure 106. In the band slope image, the area above the contrast band was darker across the whole surface; this indicates a reduction in EBSP sharpness. This reduction in sharpness, contrast, and change in orientation are all typical of residual strain and a modification of the crystallographic orientation. Band slope and band contrast are no longer used as a method of calculating residual stress, as its quantification requires calibration for each material. High-resolution electron backscatter diffraction (HR-EBSD) is now a more popular and accurate alternative. The surface layer did not show the central contrast band previously identified during BS imaging in Figure 105 and Figure 106. This suggests that the central layer is not formed due to crystallographic change, but instead is due to atomic mass change from the additional gold.

4.2.3. High-resolution electron backscatter diffraction (HR-EBSD) of ZrN and ion implanted ZrN

High-resolution electron backscatter diffraction (HR-EBSD) was used to assess the residual strain and stress distribution before and after gold ion implantation. Subsequently, the stresses below both polished cross-section faces of the ZrN sample and the cross-section of the gold implanted ZrN were determined. One of the issues with using HR-EBSD for the analysis of lattice deformation is the need for a reference area. In the case of ion damage in ZrN, the grain size (5-6 μm) is significantly larger than that of the damage layer (1.20 μm). This makes the location of a strain-free reference significantly easier. Further to this the as-sintered ZrN has relatively few dislocations (section 4.2.5 page 181) making the reliability of the magnitude of the stress higher.

Regarding the HR-EBSD data processing, a range of FFT and ROI settings were tried to assess the effects of processing on the results and their repeatability. Processing was conducted as per the experimental section, with a custom FFT appropriate for the patterns collected along with 20 regions of interest per electron backscatter pattern (EBSP).

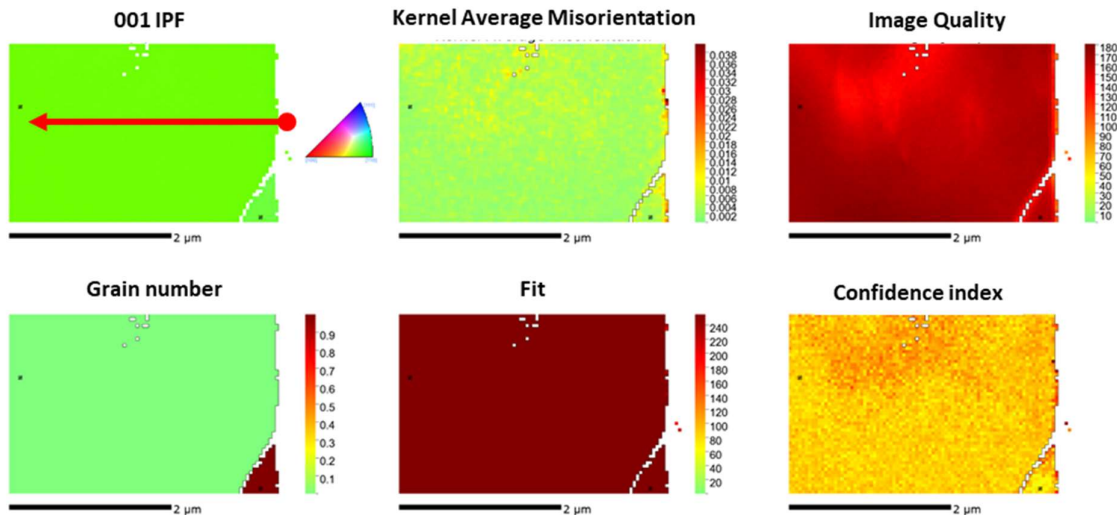


Figure 112 Pre-analysis summary of polished face cross section high-resolution EBSD. Cross court 4 processes Aztec EBSD data as: image quality = band contrast, fit = band slope, confidence index = MAD.

In **Figure 112**, the ZrN cross section shows very little pattern quality change from the polished face to the bulk. A slight contrast change in the first grain at its centre is observable; this variation may have been caused by small un-indexable Zr_2ON_2 particles at the start of the

scan. The reference points in both the polished and gold ion irradiated surfaces were identified by the Cross Court software using the minimum kernel average misorientation value. Minimum kernel average misorientation assesses the similarity in orientation between diagonal pattern neighbours and selects a pattern most similar to its neighbours.

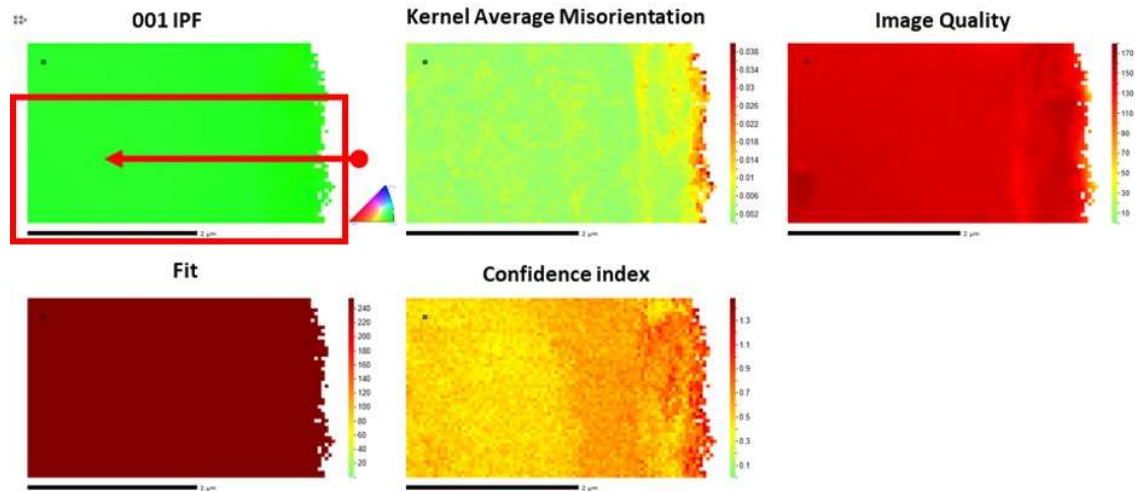
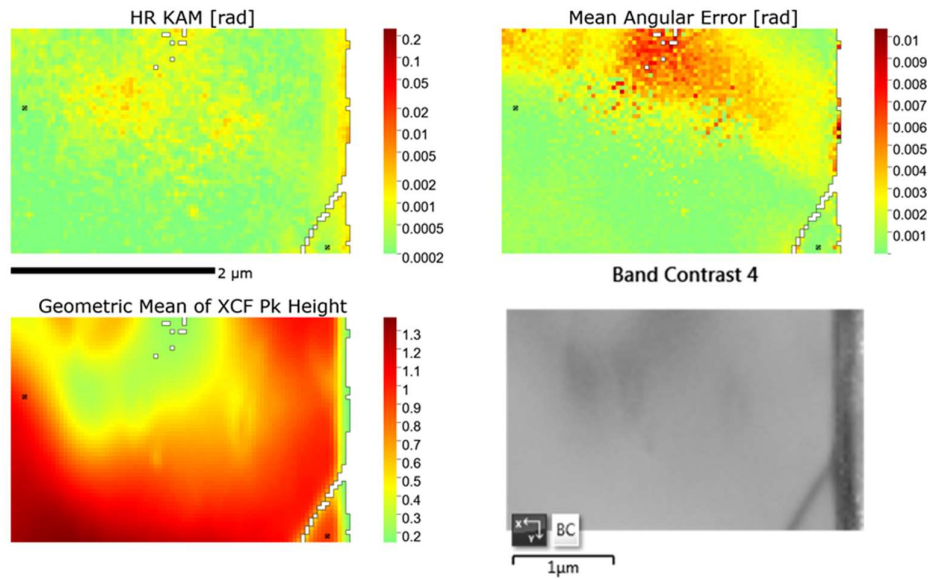


Figure 113 Pre-analysis summary of gold ion irradiated face cross section, HR-EBSD.

In **Figure 113**, the gold ion implanted EBSD images show the crystallographic damage caused by the gold ions. The band contrast and slope (image quality and fit) show a change in the lattice up to 1.20 μm. These results fit well with the backscatter imaging and TEM analysis.

XCF Quality maps V ZrN



XCF Quality maps I ZrN

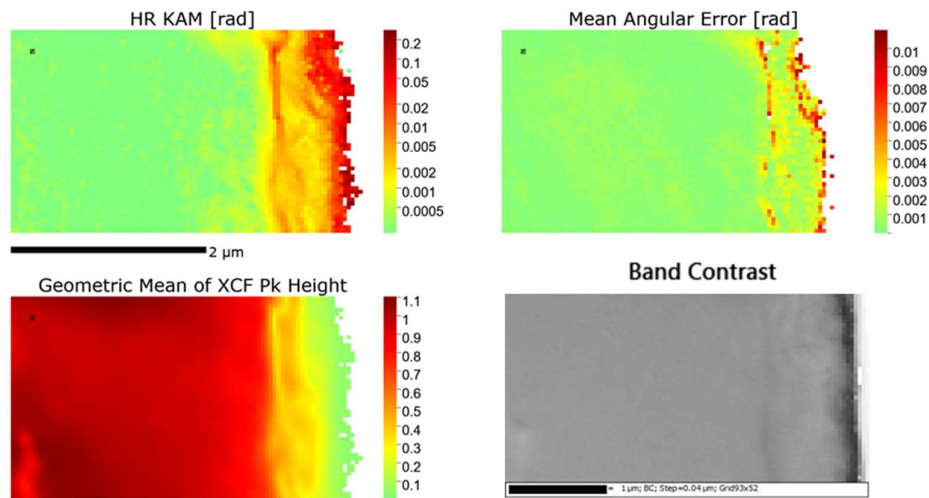


Figure 114 Remapped quality maps from the polished and gold ion implanted face.

The geometric mean of the cross-correlation function (XCF) peak height maps are shown. Each region of interest (ROI) has its peak height normalised by setting the value of the cross-correlation peak height to a ratio of the reference ROI.

The geometric mean of the cross-correlation height shows the lack of certainty produced by the patterns from the surface of the implanted and polished materials; values greater than 0.3 are considered valid. As such, stress values from the first 0.2 μm of the polished sample

should be interpreted with some caution, while the first 0.5 μm of the ion irradiated surface should also be interpreted with care. The lack of certainty at the surfaces is expected to arise from two factors; the effects of surface damage, and dislocations from polishing causing a reduction in pattern quality. Focus ion beam milling was attempted for sample preparation but did not yield significantly better data and presented a number of alternative problems. The second factor identified is the effect of the electron beam probe size. Further attempts could have been made to reduce the accelerating voltage to limit the depth of the EBSP signal. An alternative option is transmission Kikuchi diffraction (TKD). TKD uses a TEM lamellar rather than a bulk sample this offers increased spatial resolution due to the decreased interaction volume. TKD was attempted as a solution to the issues of gathering high quality patterns from the implanted surface. Initial attempts from these scans can be seen in the appendix (page 235). TKD was found to have a low / variable hit rate dependent on lamellar thickness. The literature suggests other potential errors from TKD, such as lamellar relaxation, which can reduce the measurable stress in the sample.

The mean angular error map takes the calculated distortion tensor and back-calculates what the shifts 'should be' for each ROI. The difference between these back-calculated shifts and the actual shifts are then found and converted into a value in radians. These calculations showed that the polished sample had a very low mean angular error across the base of the sample with a maximum error of 0.001 rad (0.06°). The bulk of the ion implanted ZrN had a low angular error while the top surface had an error reaching up to 0.009 rad (0.5°).

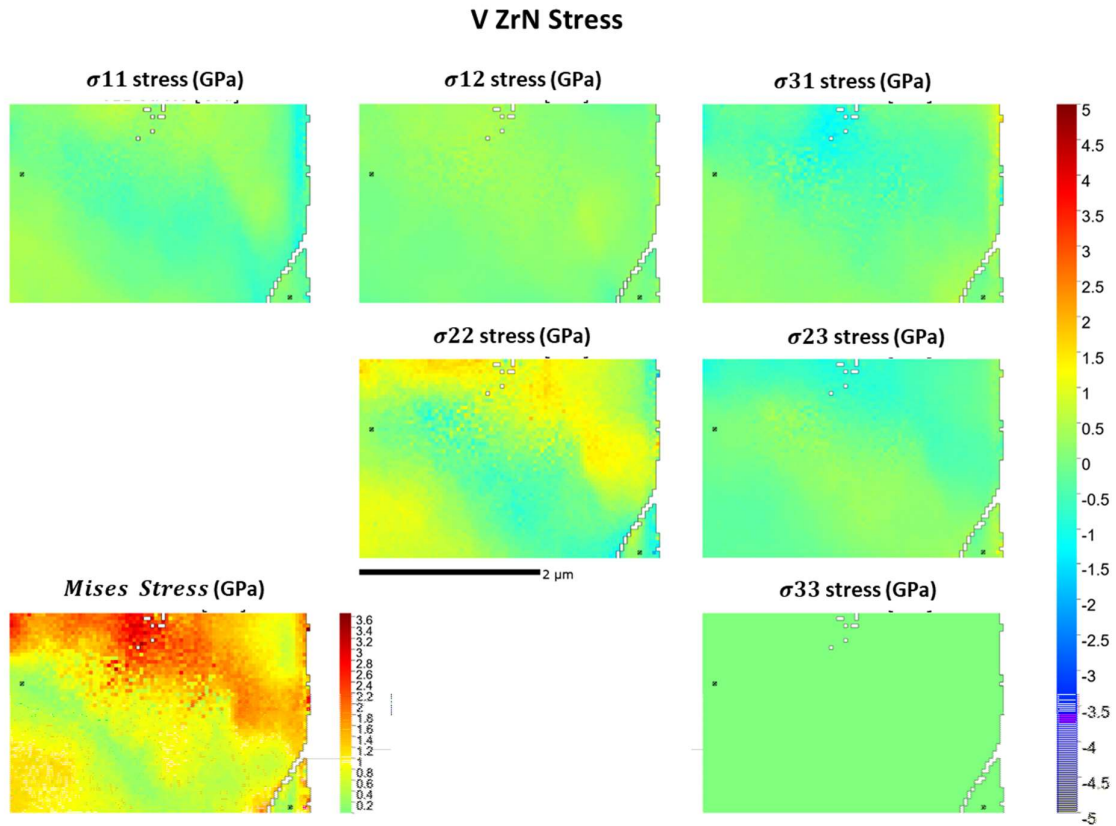


Figure 115 Elastic stress maps of a cross-section of section $1\mu\text{m}$ polished ZrN.

From the stress maps of the polished sample in Figure 115, it is clear that some residual compressive stress was introduced in the sample surface. Polishing is known to introduce plastic deformation and residual compressive stress at the surface of ceramics. Some other modest stress variations are visible in the grain surrounding an area of unindexable points. It is likely that second phase particles below the surface of the sample could have introduced this variation in stress.

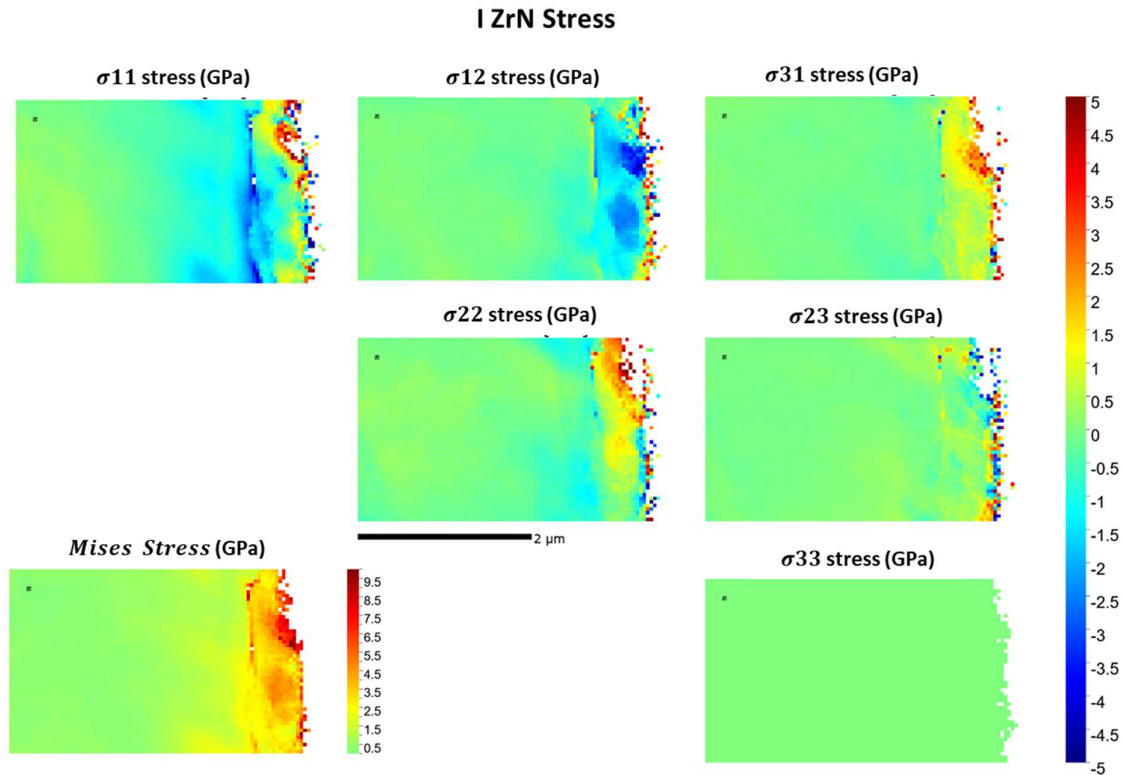
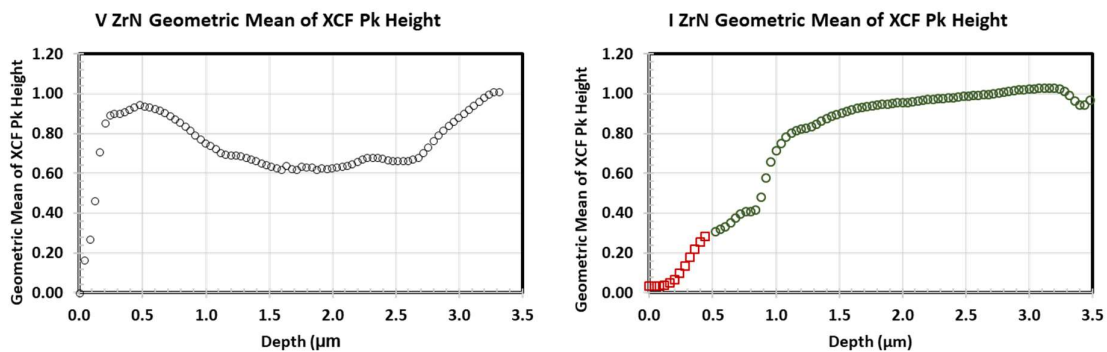
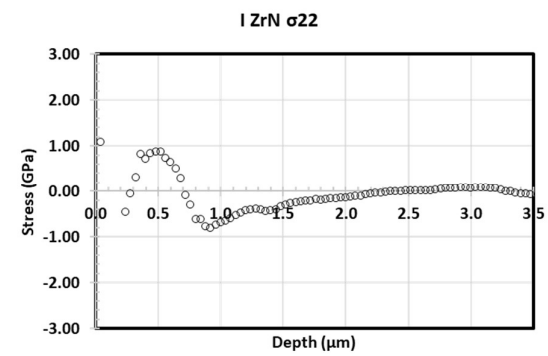
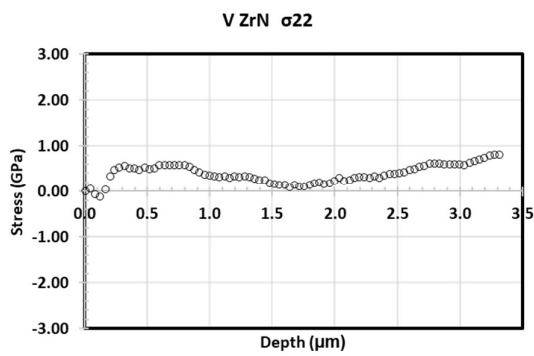
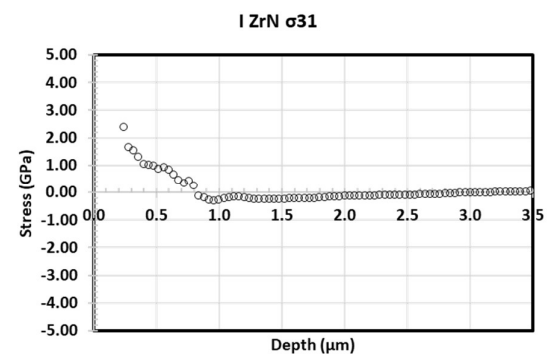
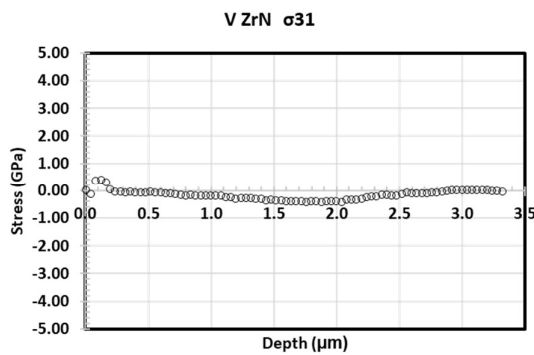
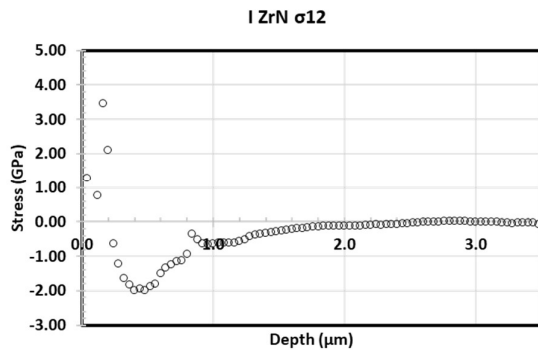
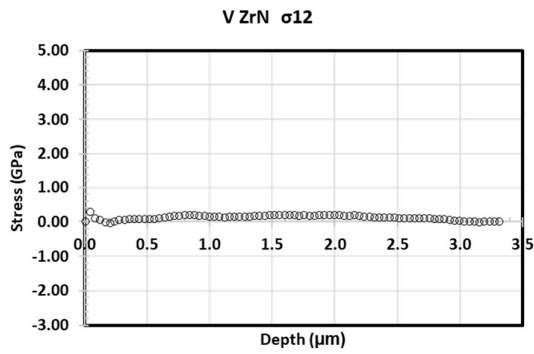
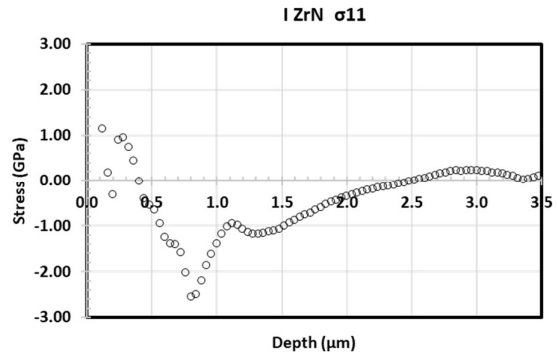
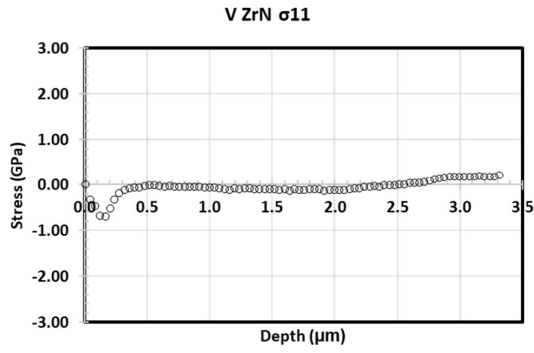


Figure 116 Elastic stress plots from the gold ion irradiated face of the ZrN sample.

In Figure 116, the stress maps show the location of the high dislocation zone at 1.20 μm aligning with an area of residual compressive stress. The top right of the map showed a slight scratch on the implanted face, leading to stress variation in the cross section. For ease of analysis, this area will be excluded from the line scan plots. Elastic stress maps from both the polished and gold irradiated samples are shown above. These maps (Figure 115Figure 116) were averaged column by column to produce line scans of the stress (Figure 117) from the surface to the bulk. The σ_{33} line scans are omitted, as HR-EBSD does not provide sensitivity in this plane.





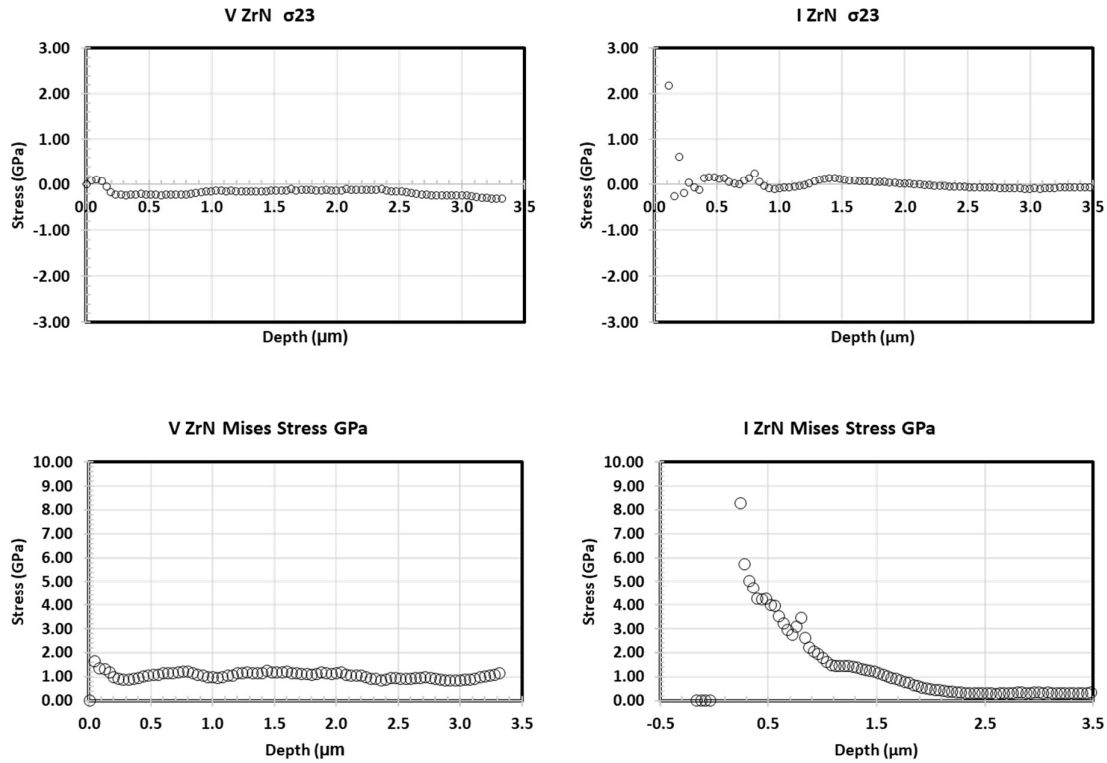


Figure 117 Average line scans from each stress map in the x-direction from the surface to the bulk of the ZrN. Plots of the geometric mean of the cross-correlation height are shown to provide context as to the accuracy of the data. The plots are started from the surface of the material.

The virgin ZrN polished face exhibited a localised compressive stress in the σ_{11} direction. The magnitude of this stress was 0.90 GPa. Plots from σ_{31} , σ_{12} , σ_{23} showed slight tensile stress at the surface, the magnitude of which was small, and, due to the lack of confidence in the data from the surface, this result was not deemed conclusive. The σ_{22} line scan shows tensile stress increasing from the surface, peaking at 1 μm and decreasing at 2 μm where it increases again into the bulk. Based on the maps, the σ_{22} results are interpreted as a result of the small second phase particles at the top of the scan. These particles seemed to have caused a strain gradient in the grain. Mis-matches in the coefficient of thermal expansion (CTE) between bulk and secondary phase particles is a well-known effect that is capable of causing residual stress in grains [111], [199]. Future work could use HR-EBSD to quantify the residual strain effect caused by secondary phases with differing CTE.

The results recorded for the unirradiated ZrN sample match well with those of other polished ceramics in the literature. Wu *et al.* conducted an extensive polishing study on alumina

silicon carbide nanocomposite, concluding that polishing with media $< 3 \mu\text{m}$ produces 1.5 GPa compressive stress in the surface of the material [200]. Ling *et al.* reported on residual tensile stresses of 0.29 GPa introduced into silicon nitride ceramics following grinding, as measured by XRD [201]. Both authors suggest that variation in grinding media size results in different residual stress distributions, magnitude and polarity (compressive or tensile) [200], [201]. Direct values for residual stress in ZrN following polishing could not be identified in the literature.

During testing gold ion implantation was observed to have a significant effect on the residual stress below the ZrN surface. All but the σ_{31} and σ_{33} stress plots show the effects of the gold ions, which caused residual tensile stress at the surface leading to a compressive stress layer around $1 \mu\text{m}$ (see Figure 117). The residual stress beyond the $1.20 \mu\text{m}$ range then tended to zero. The magnitude of these tensile surface stress was 1-2.8 GPa, while the maximum residual compressive stress was 2-2.8 GPa. Surface tensile stress was observed in the σ_{31} stress line plot. These results match well with the literature, namely Hargue *et al.* who conducted a range of nanoindentation tests on chromium ion implanted sapphire. Hargue *et al.* used nanoindentation to assess the residual stress levels in the sample post-implantation [33]. They concluded that 1.1 GPa residual compressive stress was induced with a similar distribution to the ion implantation profile [33]. However, inferring distribution of the stress from nanoindentation is not a robust experimental approach when compared to crystallographic mapping techniques. Perry *et al.* reported on yttria ion implantation of titanium nitride analysed with XRD/ grazing incidence angle XRD [202]. They identified compressive residual stress in a distribution similar to the ion distribution. The stress distribution presented matched well with the HR-EBSD results from the irradiated ZrN where a slight tensile surface stress matched was accompanied by a 4.5 GPa compressive residual stress around $0.5 \mu\text{m}$ from the surface [202]. The corroboration between these results and the HR-EBSD data is particularly important, as titanium nitride is analogous to ZrN due to their similar properties and crystallographic structure. Before analysing the von Mises stress results, it is worth considering the von Mises stress formula [203]:

$$\sigma_{\text{Von Mises}} = \sqrt{\frac{1}{2} [(\sigma_{11} - \sigma_{22})^2 + (\sigma_{22} - \sigma_{33})^2 + (\sigma_{33} + \sigma_{11})^2 + 6(\sigma_{12}^2 + \sigma_{23}^2 + \sigma_{31}^2)]}$$

(38) [203]

Equation (38) shows how von Mises stress is calculated. When the principal stresses are opposed (large compressive or tensile stress) high von Mises stresses are resultant. As such, from the von Mises stress plots we can conclude that the polished surface is in a low-stress state, while the ion implanted surface has high residual stress. The magnitude of the surface stress is approaching 10 GPa at the surface.

4.2.4. X-ray diffraction (XRD) of ZrN and ion implanted ZrN

X-ray diffraction was undertaken on the bulk sample (see Figure 118) and the gold ion irradiated ZrN sample (see Figure 119). In both samples, two sets of diffraction patterns were identified. The first high-intensity peaks were indexed as ZrN (JCPDS Card (35-0753)), while the lower intensity peaks were suggested to be Zr_2ON_2 . As will be discussed, ZrO_2 particles may also have contributed to the intensity of these peaks due to the similar peak positions. This matches well with the EBSD and EDS data collected. It is worth noting that the Zr_2ON_2 phase was not an intentional constituent in the microstructure, but was rather a product of oxygen contamination in the raw product or during hot pressing.

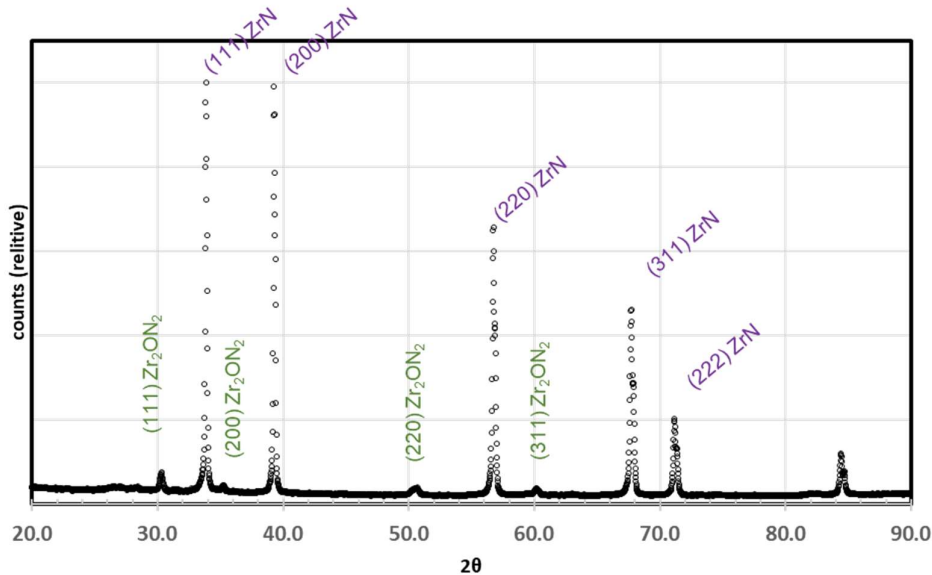


Figure 118 Virgin ZrN XRD plot showing indexed ZrN and Zr_2ON_2 peaks.

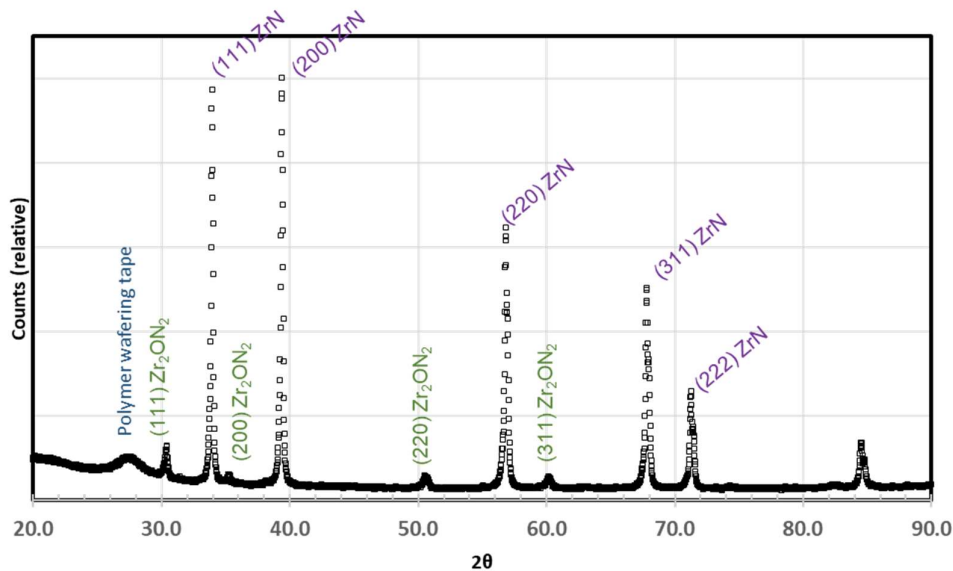


Figure 119 Gold ion irradiated ZrN XRD plot showing indexed ZrN and Zr₂ON₂ peaks.

The peak positions of each of the XRD peaks were located along with their FWHM (see Table 23). The change in shift between the peaks and FWHM was within experimental error between the ion irradiated and unirradiated sample. TEM did show some local lattice expansion; however, the resolution available from the Brooker D3 XRD was not sufficient to resolve this change.

Table 23 ZrN XRD results including indexed peak positions and FWHM.

	Amorphous layer	Zr ₂ ON ₂ (111)	ZrN (111)	Zr ₂ ON ₂ (200)	ZrN (200)	Zr ₂ ON ₂ (220)	ZrN (220)	Zr ₂ ON ₂ (311)	ZrN (311)	ZrN (222)	ZrN (400)
ZrN centre		30.34	33.89	35.27	39.33	50.59	56.80	60.21	67.78	71.24	84.51
ZrN I centre	26.90	30.39	33.97	35.27	39.40	50.63	56.88	60.21	67.87	71.33	84.62
Shift		-0.05	-0.08	0.00	-0.08	-0.05	-0.09	0.00	-0.09	-0.09	-0.10
ZrN FWHM		0.31	0.17	0.29	0.18	0.41	0.26	0.32	0.32	0.35	0.46
ZrN I FWHM	4.80	0.36	0.19	0.16	0.21	0.27	0.28	0.29	0.32	0.33	0.49
Δ FWHM		-0.05	-0.01	0.12	-0.03	0.14	-0.02	0.03	0.00	0.02	-0.03

One fundamental difference was the amorphous peak at the 28 ° angle collected from the ion irradiated sample. The source of this peak was likely the polymer wafering tape on the ion irradiated surface (see Figure 119). The peak positions and intensities for ZrO₂ are very close to those of Zr₂ON₂; as such, some contribution from the peaks may be ZrO₂. This area of

uncertainty is expanded upon in the TEM analysis section. It is worth recognising that XRD could have been used to estimate grain size and quantify residual stress in the surface of the ZrN sample. The equipment available and resolution available from XRD was deemed inferior to SEM based characterisation equivalents.

4.2.5. TEM analysis of ZrN and ion implanted ZrN

Cross-section TEM samples were prepared from both the irradiated and virgin ZrN surfaces (see Figure 120). Conventional transmission electron microscopy (TEM) and scanning transmission electron microscopy (STEM) were conducted. The two virgin ZrN samples lifted out contained multiple grains and exhibited a surface dislocation layer thickness of 0.06 μm . Surface dislocations of this nature are typical of 1 μm polished surfaces lifted out using FIB. This result matches well to the HR-EBSD data where stress was observed on the surface of the samples.

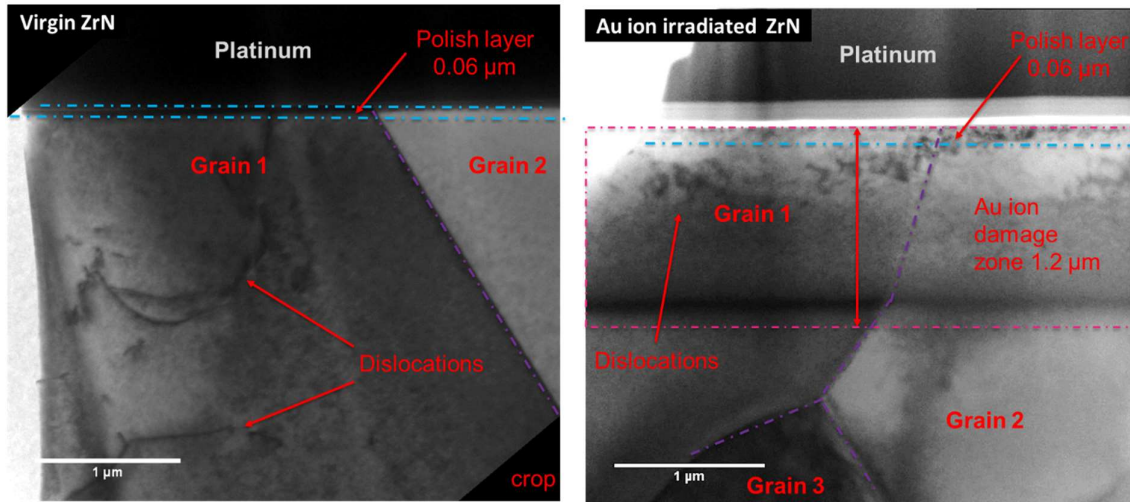


Figure 120 TEM lift outs from virgin and gold ion irradiated ZrN. The Irradiated sample shows a dislocation band and gold contrast band.

The ion irradiated sample exhibited a multilayer structure (see Figure 121) that will be analysed in greater detail. The bulk dislocation density in the virgin sample away from the polished surface was as low as $1 \text{ E}+11 \text{ m}^{-2}$. Site-specific selective area diffraction (SAD) was used to assess residual strain caused by the implantation of the gold ions. No significant changes were observed in the diffraction patterns collected from each of the regions. As previously discussed, selective area diffraction for the determination of strain

relies on limited lamellar relaxation, as, anecdotally, the lamellar were prone to twisting during cleaning. This lamellar warping may be related to a release of stress in the material.

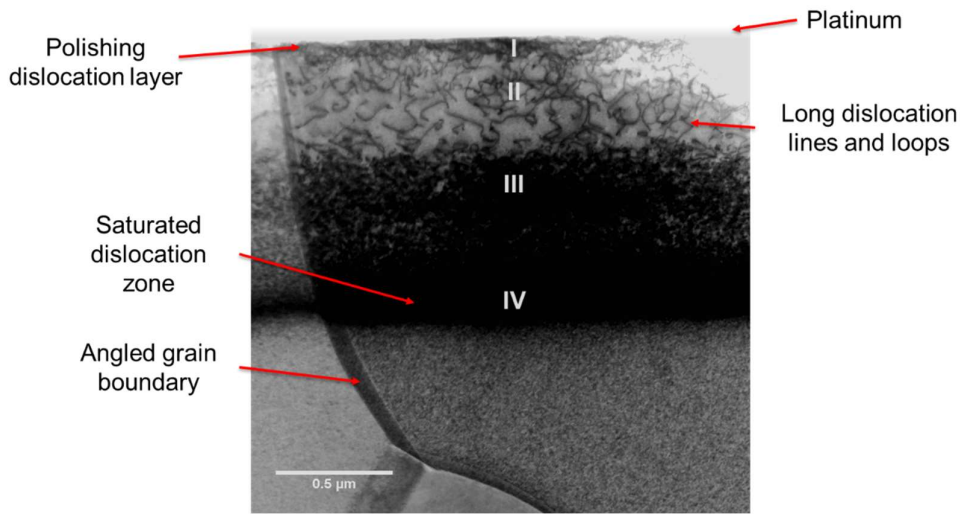


Figure 121 STEM image showing ZrN layered structure following gold ion irradiation with the four-layered structure.

The features in each layer are highlighted as (shown in **Figure 121**):

Layer-I: the thickness of this layer is 35 ± 1.1 nm, where the dislocations are highly crowded and difficult to resolve, the resolvable dislocation lines are fairly long (on the order of 250 nm). The estimated dislocation density is 5×10^{14} 1/m².

Layer-II: the thickness of this layer is about 500 nm, where almost all dislocations can be clearly resolved and have much longer length. The estimated dislocation density is 3×10^{14} 1/m².

Layer-III: the thickness of this layer is about 500 nm, where dislocations are hardly resolved. However, near the boundary between Layer-II and Layer-III, there are dislocation loops with a diameter of 50 nm that can be resolved, and sparsely distributed bright regions can be seen in this region.

Layer-IV: the thickness of this layer is about 200 nm, where no single dislocation can be resolved and the whole region is in dark contrast. However, near the boundary between Layer-IV and the non-irradiated region, dislocation loops are resolved with a diameter of 15 nm.

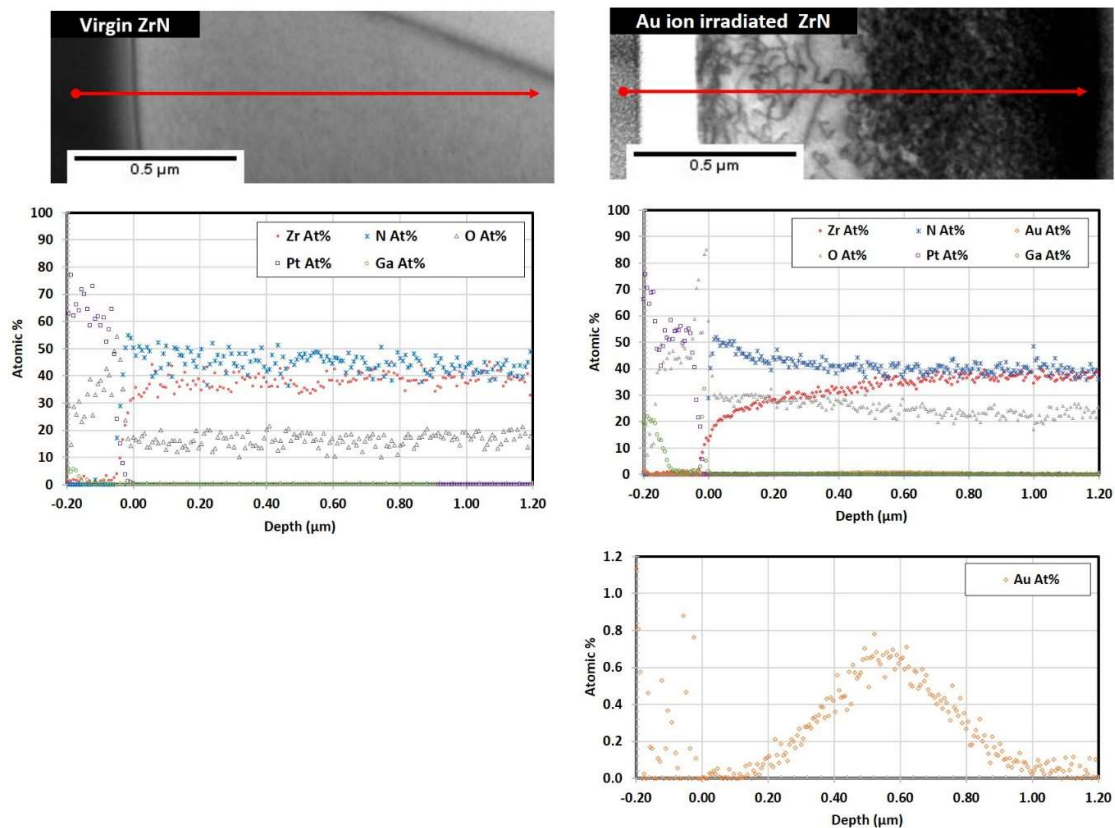


Figure 122 STEM-EDS of virgin and gold ion implanted ZrN.

Energy dispersive spectroscopy (EDS) line scans from the surface to the bulk of both gold ion irradiated ZrN and virgin ZrN exhibited compositions close to stoichiometry once away from the surface of the material (see Figure 122). At the surface of the ion irradiated material zirconium was depleted; this depletion was likely due to the sputtering effects of the gold ions at the surface. Oxygen and nitrogen were enriched at the surface. The enrichment of gaseous elements at the surface was unexpected: atomic percent reporting of elements in TEM line scans assume a consistent sample density; however, in the case of a sputtered surface this is not always accurate. For this reason, the STEM-EDS count line profiles were also assessed to assure that the enrichment of nitrogen and oxygen were not a function of the data processing. The STEM-EDS count data also suggested that nitrogen and oxygen were enriched at the surface of the sample, and it is suggested, that a poor vacuum in the implantation chamber could have assisted in the implantation of oxygen and nitrogen to the surface of the sample, resulting in this increased oxygen and nitrogen in the surface.

The averaged ratio of Zr/N is 0.88 ± 0.10 for along the examined depth of 1.2 μm . When observing the Zr to N ratio over the complete scan depth, it is apparent that the ratio of Zr: N is lower, up to 500 nm in depth into the irradiated sample (see Figure 123).

XPS was attempted to determine if the STEM-EDS line data was repeatable over a larger area, and to determine the bonding state of the nitrogen at the surface. Milling of the ZrN was found to be challenging and a stable etch rate was not achievable, resulting in inconsistent results. XPS was used to confirm the starting composition of the sample.

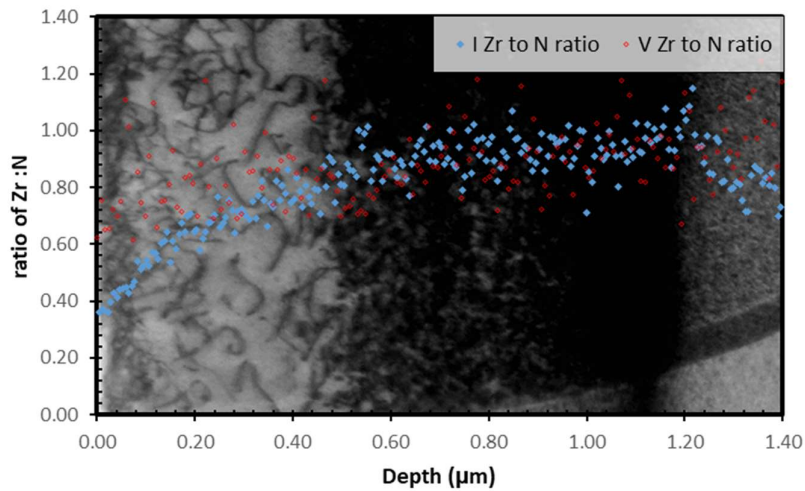


Figure 123 Plot of Zr to N ratio on a graph showing the ion irradiated microstructure.

Gold was found to be implanted from 0.2-1.0 μm centred around 0.56 μm . The average atomic percentage deposited was 0.66 % at the implantation centre. This distribution of gold ions fitted well with the stopping range of ions in matter (SRIM) simulations of 4 MeV gold ions, (as shown in Figure 128).

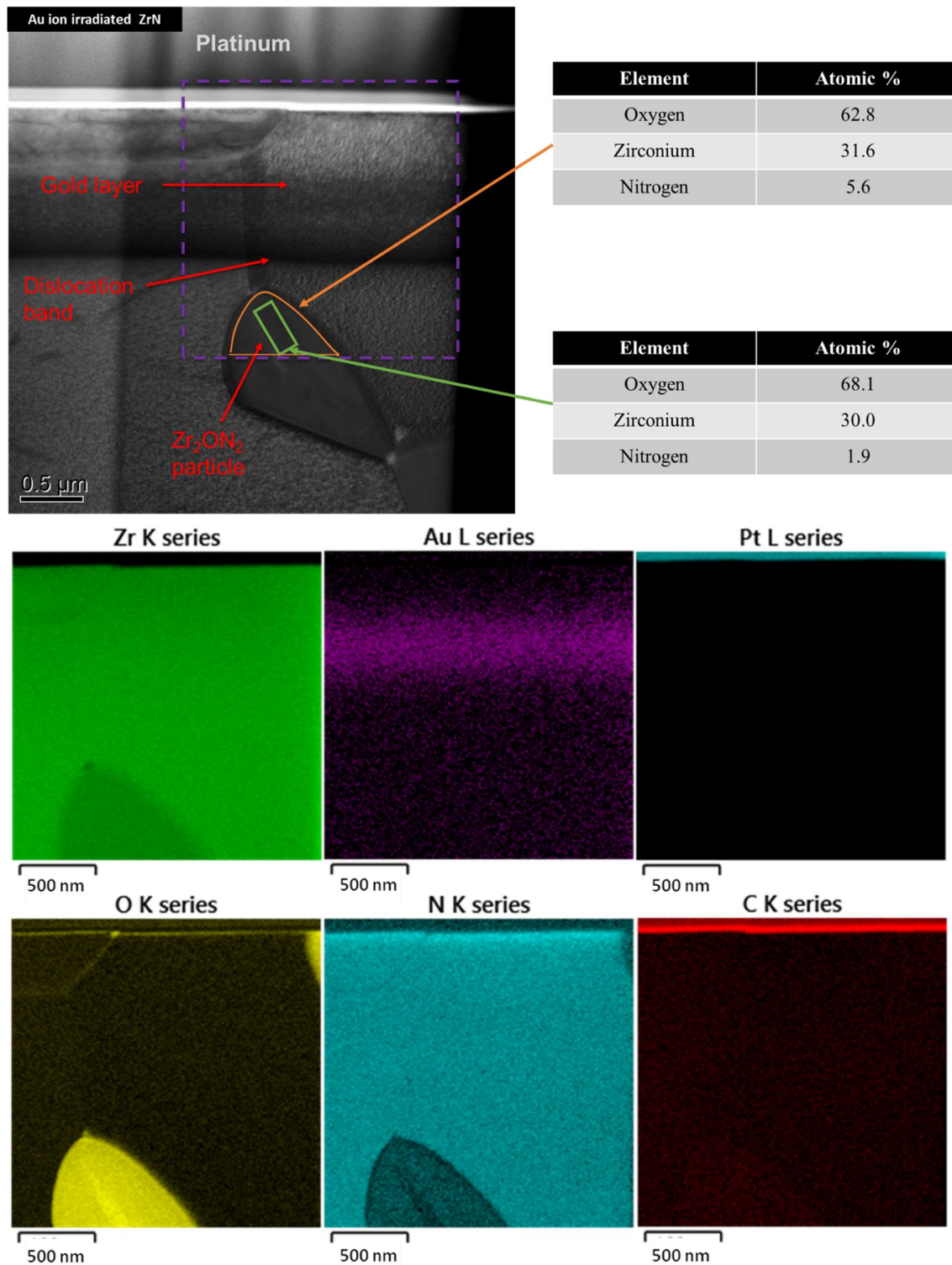


Figure 124 STEM-EDS map data from the ZrN gold ion damaged layer and a zirconium oxynitride particles.

The STEM-EDS map (Figure 124) shows the uniformity of the gold implanted layer. Interestingly, the maps also show an increase in oxygen and nitrogen at the surface of the

ZrN sample, as had been observed in the STEM-EDS line scans. Many of the SEM images of the zirconium-oxy-nitride particles showed a core shell-like structure; these structures were not resolvable in the SEM with EDS (due to the electron beam interaction volume). However, in this STEM-EDS map (Figure 124), it is apparent that the particle has an enrichment of oxygen at its centre. The particle composition was calculated to be closer to ZrO_2 at the centre. While the majority of the grain contained nitrogen (5.6 %), care was taken to exclude the boundary of the grain which could have nitrogen from the surrounding ZrN grains.

There is not a clear consensus in the literature as to the microstructural features of hot pressed ZrN. Many researchers have identified oxide particles and characterised them solely as monoclinic ZrO_2 [167], [178], while some researchers have suggested that Zr_2ON_2 particles are also present specifically at the sample surface [174]. The STEM-EDS data presented in Figure 124 suggests that under the manufacture conditions, used Zr_2ON_2 particles with a ZrO_2 inner core structure are present. This matches well with the SEM / EBSD, TEM and XRD data collected from these samples.

HR-TEM was conducted on the ion irradiated surface of the ZrN sample by our collaborators at Donghua University/Shanghai Institute of Ceramics. Using argon ion milling, thinner samples were prepared allowing images to be formed in the HR-TEM condition.

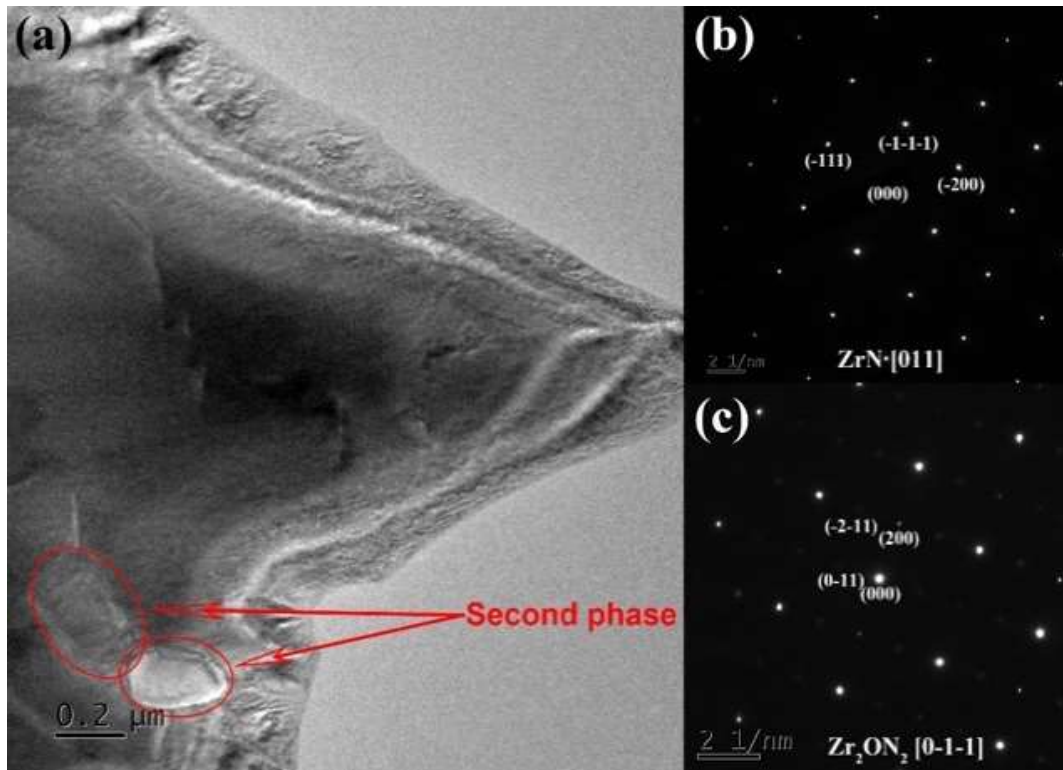


Figure 125 A TEM BF image of as-manufactured ZrN and microdiffraction patterns – (b) taken from ZrN grain and (c) from secondary Zr₂ON₂ particles embedded inside a ZrN crystal as circled. [Credit Weichao Bao]

Figure 125 shows the TEM microstructure of the as-manufactured polycrystalline ZrN. It is noted that inside the ZrN crystallite, there are a few dislocations. The dislocations present were likely formed during hot pressing or TEM sample preparation. The electron diffraction pattern along [011] zone axis of ZrN grain is presented in the inset of Figure 125. This diffraction pattern shows the standard cubic structure of ZrN with an estimated lattice parameter of 4.58 Å. Inside the grain, two smaller particles with a dimension of ~200 nm were resolved, as indicated by the two red ovals. The selected area electron diffraction pattern along a zone axis of $[0\bar{1}\bar{1}]$ of one of the particles is shown in the inset of Figure 125 b, giving a lattice parameter of 10.19 Å. This value is close to the theoretical value for Zr₂ON₂ 10.1394 Å [204]. The structure of the secondary particle has a larger lattice parameter than ZrN, giving a theoretical density of 5.77 g/cm³. Following examination of the un-irradiated surface, further TEM analysis was undertaken on the irradiated ZrN surface.

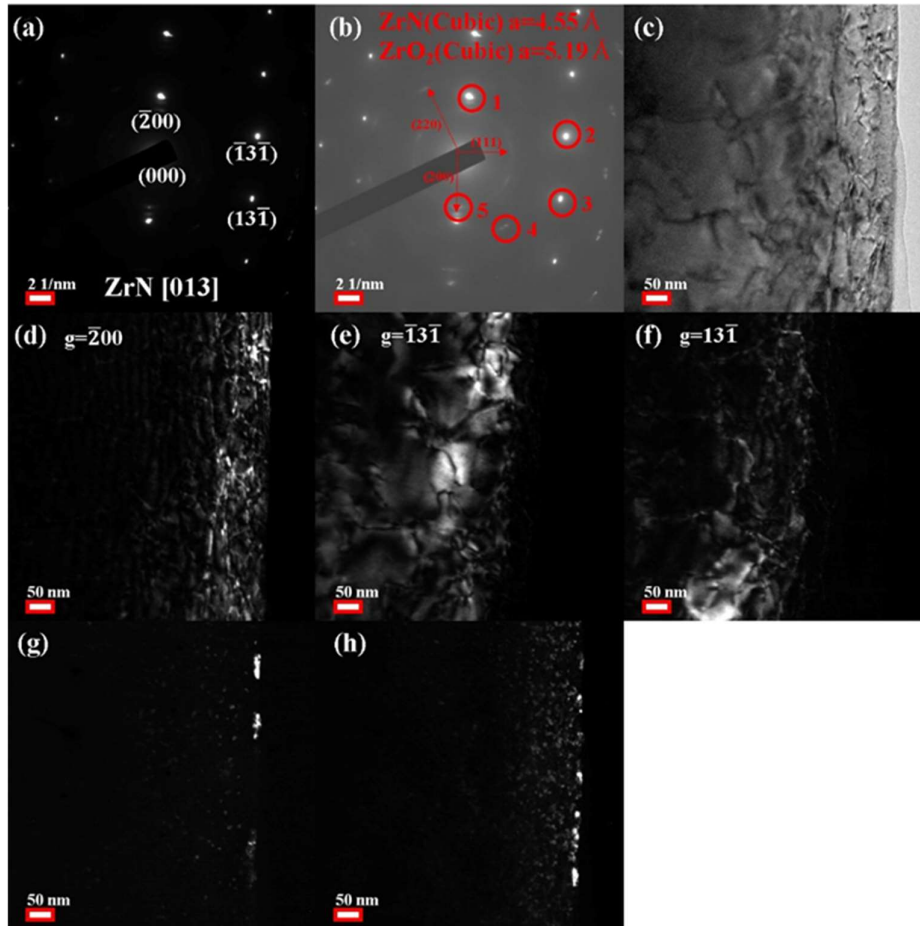


Figure 126 Diffraction contrast images for characterising lattice defects and small precipitates inside ion irradiated region of ZrN. (a-b) The SAD patterns of irradiated ZrN; (c) BF image; (d-h) DF images with different diffraction spots in sequence. [Credit Weichao Bao]

Figure 126 shows a region near the irradiated surface with a bright field (BF) (Figure 126 (c)) and a range of dark field (DF) images (Figure 126 d-h). Figure 126 a shows the SAD patterns acquired from this region with a zone axis of [013], and three (DF) images were recorded with a g of $\bar{2}00$, $\bar{1}3\bar{1}$, $13\bar{1}$ and other extra diffraction spots, as indicated by the red circles in (Figure 126 b). The contrast of all defects follows $g \cdot \mathbf{l} > 0$, where \mathbf{l} is the B-W contrast vector, running from the black lobe to that of the white. The defects are very clear in the irradiated ZrN from the variation of contrast (Figure 126 c-h), and defects are different with different observation points. The dislocation lines and loops can be observed clearly with $g = \bar{1}3\bar{1}$ (Figure 126 e), but it is difficult to identify dislocation lines and loops with $g = \bar{2}00$ (Figure 126 d). This illustrates that the dislocations follow the Bragg vector ($\mathbf{b} = \pm[01\bar{1}]_b/2$) according to the $g \cdot \mathbf{b} = 0$ invisibility criterion following the irradiation of ZrN; this is related to the configurational energy [205]. Precipitate-type defects also can be found at a depth of ~ 150

nm (Figure 126 g-h), in the particles of ~5 nm in size at a depth of ~10 nm and smaller ones in the deeper depth. Moreover, the nanocrystalline particles were identified as ZrO₂, the lattice parameters of which give a set of diffraction rings matched well by those shown in (Figure 126 b). As such, it is likely that nanocrystalline ZrO₂ particles precipitated inside the irradiated region.

Figure 127 shows the HR-TEM image of irradiated ZrN at near surface. A ~30 nm polycrystalline layer was identified. There are a significant number of nanocrystalline (~10 nm) particles in co-existence with the crystal:

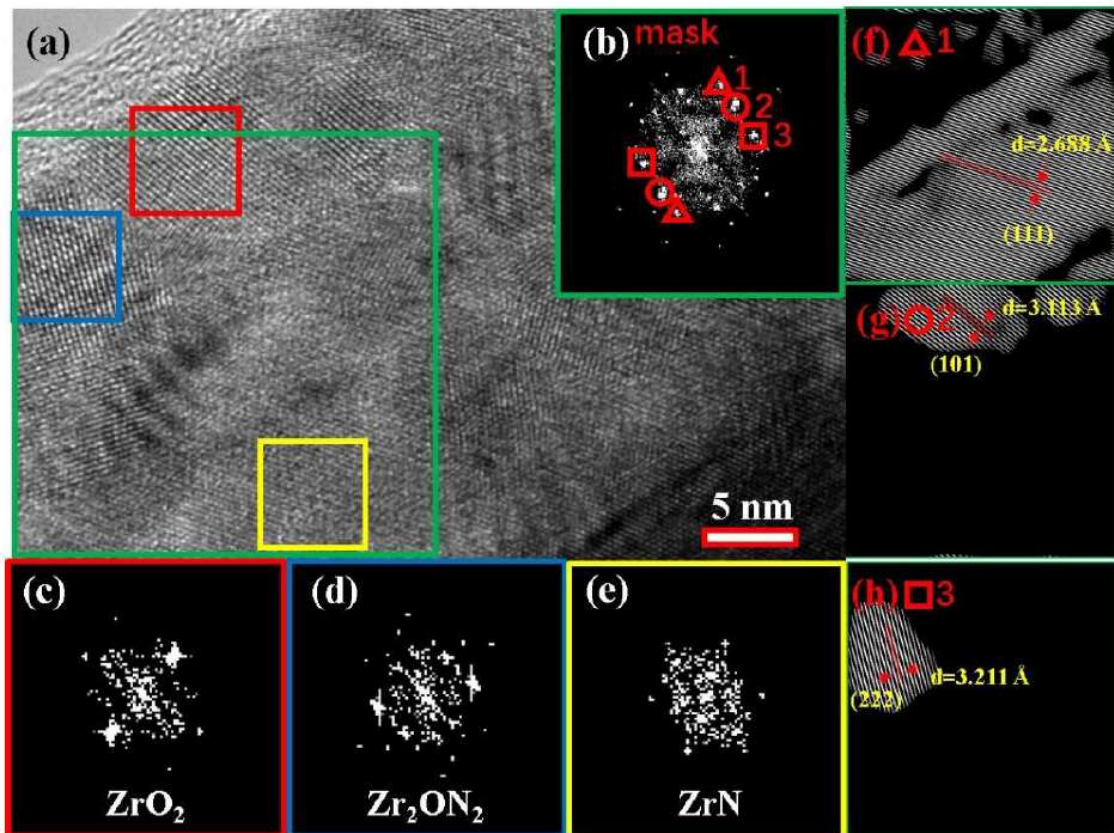


Figure 127 Processed HRTEM images (a) HRTEM image of irradiated ZrN; (b), (c), (d) and (e) are the FFT patterns of the green, red, blue and yellow squared regions respectively shown in (a); (f), (g) and (h) are the inverse FFT patterns of the green area in (a), and twin mask filtering with the red triangle, circle and square in (b) respectively. [Credit Weichao Bao]

Fast Fourier transform (FFT) image processing was used to isolate each phase. FFT processing of HRTEM images give a diffraction pattern of the selected field of view; (b) shows the pattern for the whole area including each phase. FFT patterns were produced from each phase individually; these were then used to assist in indexing and reprocessing the overall FFT pattern to create FFT dark field type images (f-h). From these inverse FFT

patterns, the orientation and lattice spacing of the phases were calculated. Processing the HR-TEM images in this manner provides additional evidence as to the phases within the ion damaged surface of the ZrN sample. The ion damaged surface comprises of ZrO₂ and Zr₂ON₂ nanoparticles. We postulate that while the Au ions impacted the ZrN sample a high speed and energy, the O (oxygen) in the chamber would also become implanted by the impacting Au ions. The oxygen impacting the ZrN sample could contribute to the oxygen contamination in the surface layer of the sample.

FFT processing was taken a step further using geometric phase analysis (GPA). GPA processing uses the differences in lattice spacing to determine the residual stress in an area of a HRTEM image. GPA analysis suggested that residual elastic strains up to 18% were introduced into the microstructure of the material. When a particle (neutron, proton or ion) is moving through the lattice at high velocity, it will slow as a result of momentum transfer, Coulomb interaction and electron interaction forces. Thus the structure of lattice is modified, resulting in a high level of lattice disorder. Nano-crystallinity is easily generated by the torsional effects of the impinging fast heavy ions (or neutrons/protons). It is this phenomenon which likely formed the ZrO₂ nanocrystalline domains at the surface of the ZrN sample. These phase transformations at the surface are evidence of ion tracks.

The results show that 4 MeV Au ions with a fluence up to $5 \times 10^{16}/\text{cm}^2$ did not destroy the crystal lattice framework of ZrN, or the primary microstructure of its polycrystalline structure either. This observation has further confirmed the excellent resilience of ZrN to ion irradiation without amorphisation, as has been reported by previous researchers. This proves to be the case even after irradiation with significantly higher fluences than those used in previous studies [25], [178], [206]. The integrity of its polycrystalline structure, manufactured through a traditional ceramic processing route, is of particular importance in developing inert matrix fuel (IMF) for transmuting transuranium elements [207]. Apart from the merits of polycrystalline ZrN, the following structural and chemical features were identified inside the irradiated layer, as shown in Figure 120 - Figure 127:

- i. Most of Au ions were deposited beyond the long dislocation layer, and ZrN lattice is heavily distorted by dislocation loops and elastic strains.
- ii. ZrO₂ or Zr₂ON₂ crystallites with a diameter of ~5 nm were developed inside the top layer of the irradiated regime.

- iii. The nitrogen/oxygen content increased and zirconium reduced in the top layer of the irradiated regime.
- iv. Inside the top layer of the irradiated regime, long dislocations with a density of $3.2 \times 10^{14} \text{ 1/m}^2$ were developed.
- v. Beyond the Au ion enriched layer, the ZrN lattice was also heavily distorted by dislocation loops and elastic strains.

The details of these changes can assist in the understanding of the irradiation process.

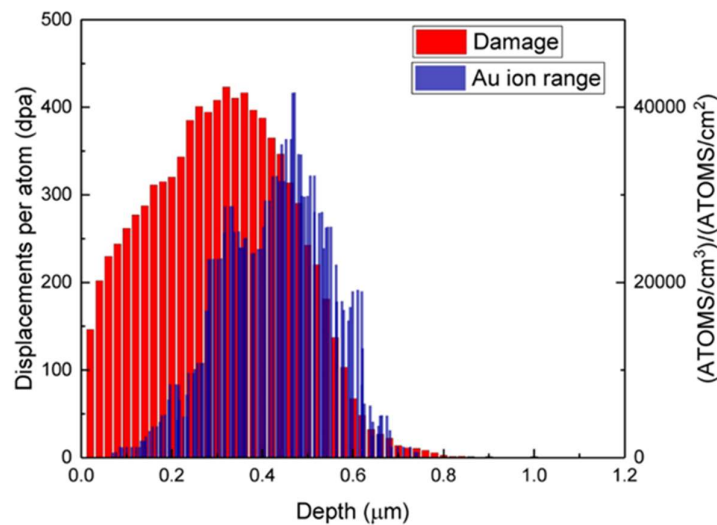


Figure 128 Lattice damage and Au ion deposition profile estimated with SRIM in ZrN, irradiated with 4 MeV Au ions with an accumulated fluence of $5 \times 10^{16} \text{ cm}^{-2}$

For the implantation of Au ions, we can estimate its deposition profile using the classic SRIM with an average threshold displacement energy (E_d) of 40 eV for both zirconium (Zr) and nitrogen (N) atoms [25], [208], [209]. Note that the values of E_d for Zr is based on estimated values of ZrC, while the E_d for N is unknown, hence assumed to be the same as Zr based on the sublattice structure [210]. The results are shown in Figure 128, where blue bars describe the histogram profile of deposited Au underneath the surface. The profile is close to a Gaussian distribution, and fitting shows the central position is at a depth of 0.5 μm , and FWHM of 0.31 μm . The central position of the Gaussian distribution is close to the distribution identified in the TEM (0.58 μm) and estimated by SRIM. However, the estimated FWHM is about 22 % smaller than the experimentally measured value. Such inconsistency could be associated with the assumed E_d value, but, as a first approximation,

this assumption should be sufficient to estimate the Au deposition inside ZrN. In addition, the contamination of oxygen may have had an impact on the SRIM estimations.

Without considering thermal effect, the predicted damage region should be inside about 0.5 μm . This investigation shows that inside this region, only long dislocations are observed in Layer-I and Layer-II, with the crystal structure of ZrN well maintained and free from amorphous phase. It could be concluded that thermal-induced recovery is responsible for the observed microstructure. With thermal effects considered, we may be able to explain other structural features seen inside the irradiated layer, as detailed in **Figure 129**:

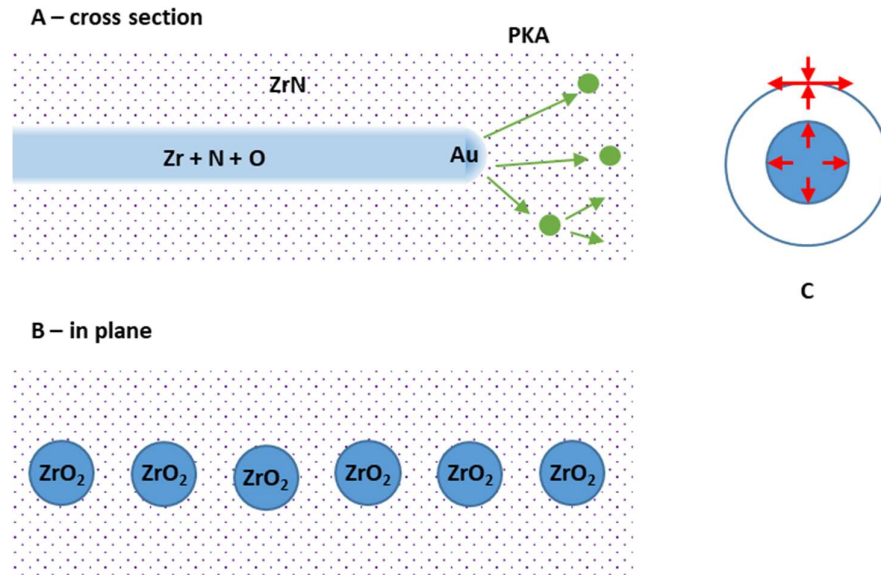


Figure 129 Schematics showing a ion trajectory composed of a mixture of Zr, N and O that are excited by the thermal spike and Coulomb explosion, as shown in (a), followed by crystallisation or recrystallization leading to the formation of spherical ZrO₂ particles and epitaxial ZrN crystal formed inside the track, as shown in (b). When the ion track is formed, the transient volume expansion leaves the track itself under hydrostatic pressure and surroundings under shock stress wave with shear stress developed by the tension along the hoop directions and compression along the radial directions, as shown in (c).

In general, an energetic heavy ion passing through a solid material is expected to lose its energy via two independent mechanisms: electronic excitation/ ionisation (also called Coulomb explosion), and elastic collisions with the nuclei of the target atoms [208]. High energy-heavy ion irradiation can lead to high density of electronic excitation in materials along its pathway, and this is a primary mechanism for a passing ion to lose its energy. On the other hand, energy loss by the elastic collisions with the nuclei of the target atoms

is so small that it is normally ignored in discussion. Hence, the energy loss along a trajectory of a heavy ion leads to a very local and high excitation of atoms in the lattice through ionisation, making atoms around the heavy ion pathway very different in structure, and possibly in chemistry, from the parent solid. In this manner, a column of material is formed with a composition/phase different from that of the parental solid. The thermal spike and Coulomb explosion models are frequently used to describe what happens within a heavy ion track. It is generally agreed that the following can occur inside the trajectory: the density of atoms is reduced in the core, and a surrounding region is densified. Such an unstable system is likely rebalanced by recrystallisation, amorphisation or even phase transformation, depending on the physical and chemical properties of the target material. Hence, after irradiation, the ion trajectory may not be marked by an amorphous phase, but could be a recrystallised region, or a region with different phases.

Based on the aforementioned physical process of energetic heavy ion irradiation, the detected chemical composition and crystal structure inside the irradiated regime, we assume that ion trajectory has a chemical composition of Zr, N and O. During irradiation these atoms are likely to be excited to a highly disordered structure, or even to a molten state. Upon cooling, recrystallisation or precipitation occurs when enough thermal energy is provided for the kinetics to proceed; otherwise an amorphous track would have been seen. The speculated ion trajectory and its change are schematically shown in Figure 129. Following this hypothesis, if there are enough oxygen atoms inside the ion trajectory, the size of the zirconia crystallites or diameter of ZrN should be the same as the diameter of the ion trajectory cylinder. As ZrN could precipitate through an epitaxy process to minimise interface energy, we may not be able to differentiate the precipitated ZrN from the parental ZrN, which is true as shown in Figure 129. However, we could differentiate the ZrO₂ crystallites from the ZrN matrix with less ambiguity. The measured average diameter of ZrO₂ crystallites was ~5 nm, a size very close to the measured ion trajectory channel by Khalil *et al.* who measured a diameter of ~5 nm for Au ion trajectory in indium phosphide (InP) [31].

Based on this theoretical model, (shown in Figure 129) the expansion of the trajectory applies a shock stress wave through its fast expansion. The stress wave applied to the surrounding ZrN crystals leads to compression along radial directions and tension along hoop directions, together resulting in a maximum shear stress along 45° deviated from the radial direction.

It may be that it is this shear stress that drives the initiation and gliding of dislocations. Inside the inelastic impact region, the region near the ion trajectory gives highest possible temperature, as shown in Figure 129 (a), which leads to a lowest possible critical shear stress for a dislocation to glide. At the same time, this is the region where the highest possible shear stress can appear, as both the tensile along hoop direction and compression along radial direction decline at positions away from the trajectory boundaries. Altogether, dislocations in a region around a trajectory can glide easily, giving very long dislocation lines and lower dislocation density as the density is governed by critical shear stress. When the position goes deeper than the peak position of deposited Au ions ($>0.58 \mu\text{m}$), there are no long length dislocation lines, apart from dislocation loops. It is proposed that this is a consequence of the absence of additional inelastic collision between Au ions and atoms in this region, and hence much lower transient temperature and shear stress exist, making dislocation loops difficult to glide for long length dislocation development. Because of the higher gliding resistance, it is therefore expected to see much higher dislocation density in this region, as shown in **Figure 121**, where the density of dislocation loops is too high to be resolved in the TEM image. In the near top surface region, the pre-existing dislocation on the polished surface may have provide extra resistance for dislocation glide, hence higher density dislocation with relatively shorter length is observed.

4.2.6. Nanoindentation of ZrN

To assess the consequences of the microstructural and chemical changes to the ZrN material following ion irradiation, continuous stiffness measurement (CSM) nanoindentation testing was employed along with SEM/EDS analysis. The load displacement nanoindentation plots were found to be bimodal, with two average hardnesses, moduli and load indentation depth curve shapes. Before further analysis of the mechanical properties, SEM analysis (see **Figure 130**) was used to link this bimodal nature to the microstructure:

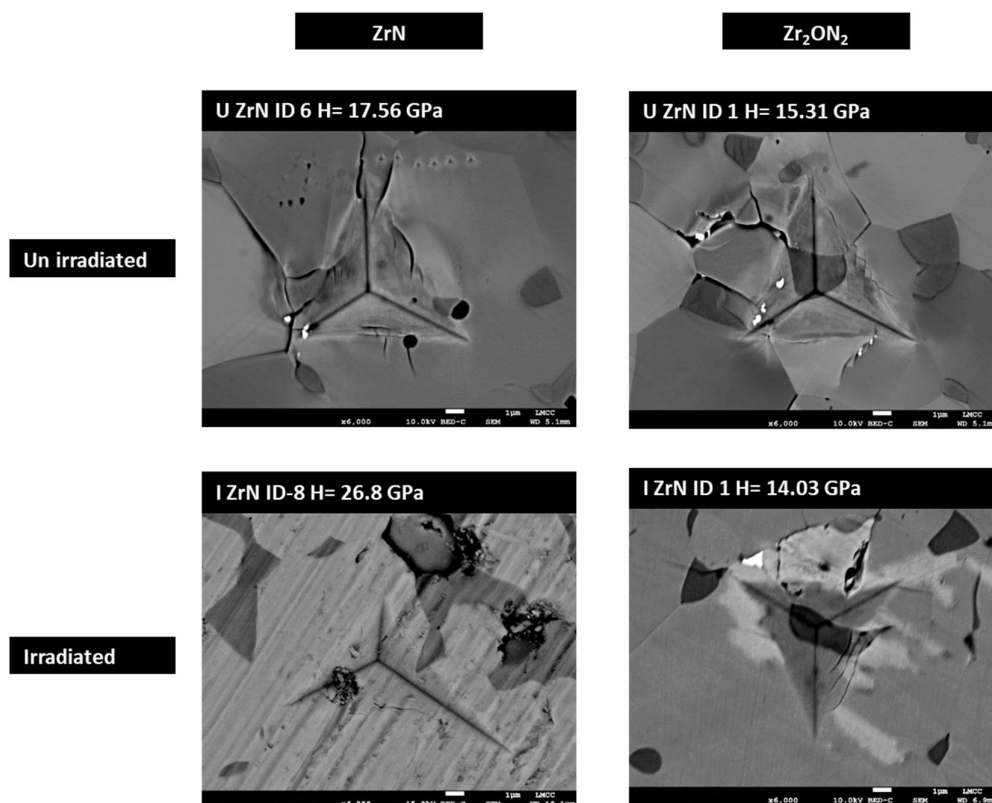


Figure 130 Backscatter SEM images of 1500 nm indents on the unirradiated face of the ZrN sample, peak hardness as calculated by the nanoindenter and hardness calculated from the indent areas imaged in the SEM shown.

SEM analysis previously revealed the dual phase nature of the microstructure, which comprised of ZrN and Zr₂ON₂. EDS was used to identify the two phases, as shown in Figure 131, and identify which phase was predominantly indented. The phases are identifiable in the back-scatter SEM due to atomic mass contrast, (the dark grains are Zr₂ON₂); however EDS highlights this with more certainty. Each indent was identified, EDS mapped, and characterised as ZrN or Zr₂ON₂ dominant (as shown in Figure 131). First, we will consider the unirradiated sample:

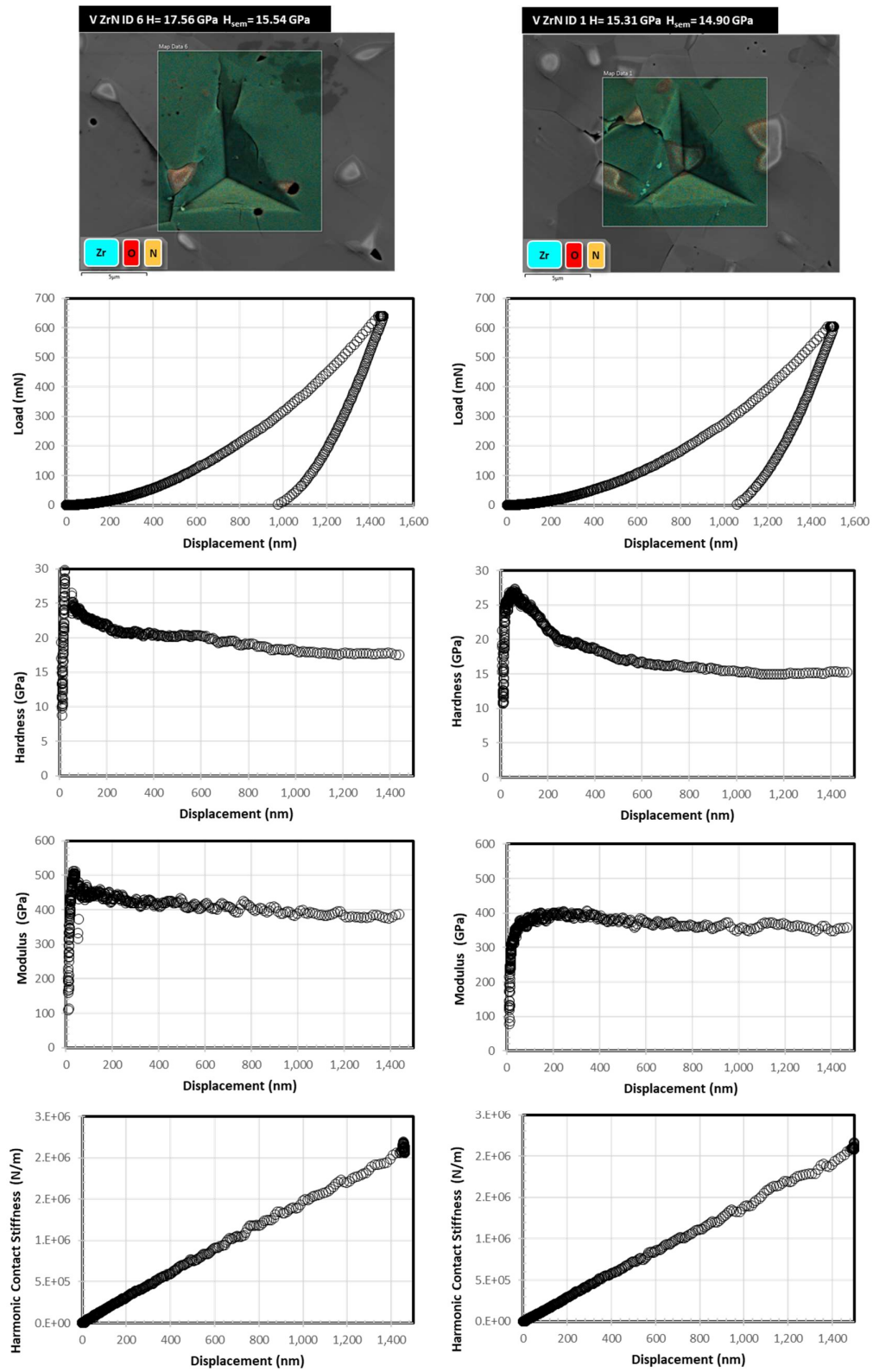


Figure 131 EDS maps and related nanoindentation hardness displacement profiles for unirradiated ZrN. ID 6 shows an indentation made up predominantly of ZrN. ID 1 shows an indentation into Zr_2ON_2 and the ZrN matrix.

Based on the STEM-EDS and XRD conducted in previous sections, the red/pink areas in the EDS maps in Figure 131 are Zr_2ON_2 . Qualitatively, the fracture patterns from indentations containing Zr_2ON_2 failed preferentially at the Zr_2ON_2 oxide particles and not in the bulk material; examples of this can be seen in Figure 130. The indentations into the bulk ZrN material showed classic corner cracking, as was observed in the Berkovich nanoindentation conducted on the SiC sample. This indentation crack pattern did not match with other nanoindentation in the literature due to differences in grain size [179]. The lack of defined corner cracks made the calculation of fracture toughness impractical: the model proposed by Lawn *et al.* is best suited to halfpenny type median cracks [87].

The hardness and modulus displacement data presented in Figure 131 shows the reduction in overall hardness and modulus due to the presence of the Zr_2ON_2 particle. With only four indentations into a mix of the Zr_2ON_2 and ZrN, the properties of the Zr_2ON_2 cannot be isolated other than suggesting that its hardness is less than that of the ZrN. A distinct size effect was identified in both phases (see Figure 133). The ZrN phase showed an increase in modulus and hardness at the surface. The $Zr_2ON_2 + ZrN$ had a low initial contact hardness and modulus; the hardness then increased in a manner similar to the ZrN phase, while the modulus raised to a consistent level around 400 GPa.

The indentations of the irradiated zirconium nitride (ZrN) (see Figure 132) sample was imaged using the same experimental set up as was used to image the un-irradiated ZrN:

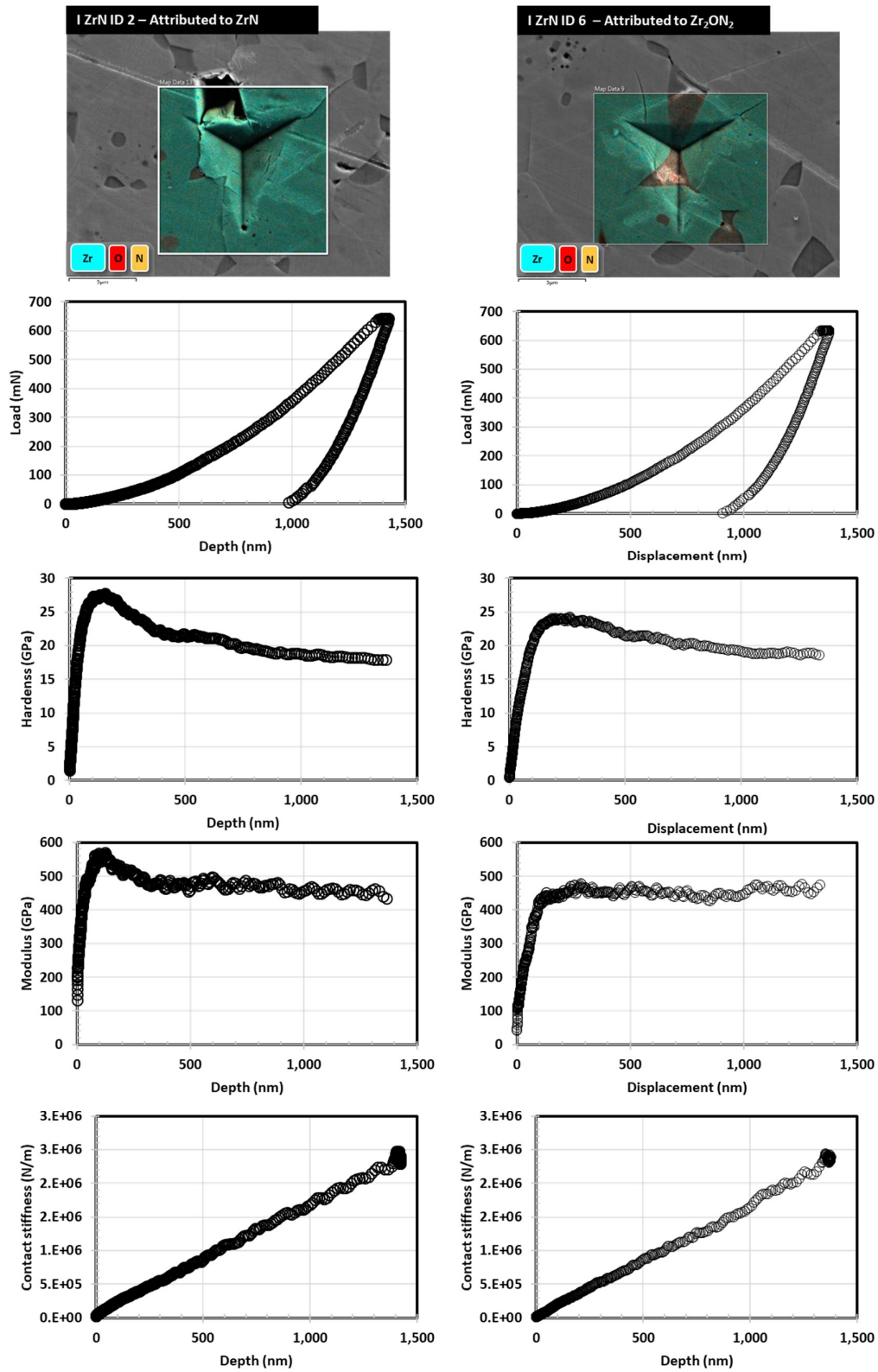
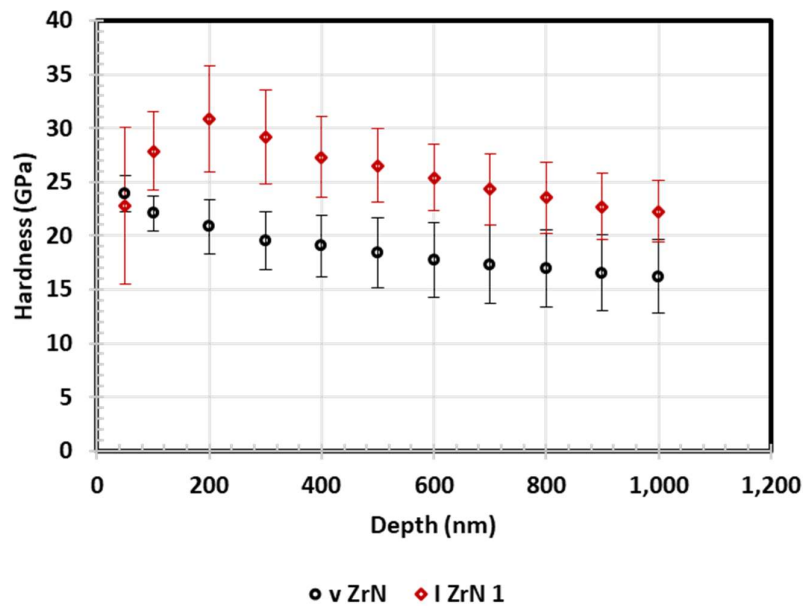


Figure 132 EDS maps and related nanoindentation hardness displacement profiles for unirradiated ZrN. ID 2 shows an indentation made up predominantly of ZrN. ID 6 shows an indentation into Zr₂ON₂ and the ZrN matrix.

Both the SEM and EDS images showed similar fracture mode trends, with oxide particles frequently being the initiation point for cracking (see Figure 131, Figure 132). Mechanical property plots for the two materials are, however, significantly different. As seen in Figure 132, the example curves show a reduction in all mechanical properties. Most notably, the hardness and modulus are reduced during the initial contact point up to 200 nm depth in the ZrN indentations. During the TEM analysis, a reduction in signal at the surface of the cross-section STEM-EDS scans was identified. This was linked to a reduction in density at the surface of the I ZrN (see Figure 122). The nanoindentation data fits well with this analysis, as the hardness and modulus are reduced at the surface. Further to this, HR-EBSD showed residual tensile stress at the surface and compressive stress as a layer in the bulk. These stress fields match well with the observed mechanical properties. To comment further on the mechanical property changes, the results were averaged and plotted, as seen in Figure 133 and Figure 134. The data was separated by phase where indentations including a Zr_2ON_2 particle at their centre were categorised as such.



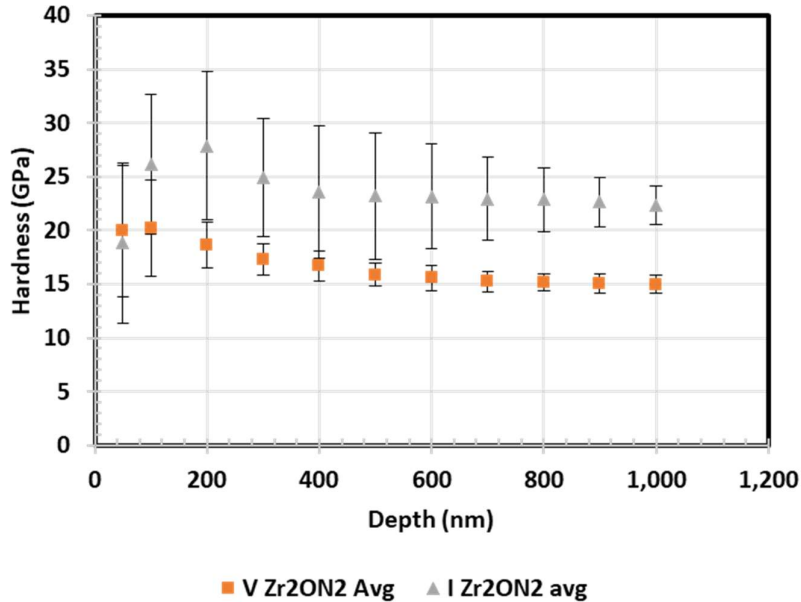


Figure 133 Mean hardness data from irradiated and unirradiated ZrN and Zr₂ON₂ nano indents, separated by phase and irradiation state.

The hardness of the unirradiated ZrN followed a typical size effect profile, with the initial contact being harder than the bulk material. The hardness of the irradiated ZrN was significantly reduced at the surface. Once the indentation depth exceeded 200 nm, any hardness changes were within error. After 200nm, the I ZrN showed a size effect with a similar gradient as that observed in the V ZrN sample. As ZrN is a ceramic comprising of two phases and porosity, estimation of the probe size of the indenter is very complicated. Literature estimates suggest that the probe size of the indenter can be 2 to 5 times the depth of the indentation [94]. Given this information, it is reasonable to assume that beyond 200-400 nm the mechanical properties measured by the CSM indentation are that of the bulk, as the ion damage layer as previously discussed is around 1.2 μm in thickness. The initial reduction in hardness may be based on the reduction in density, as identified during the STEM-EDS analysis. A hardening effect was expected due to the dislocation structure below the gold implanted layer from 0.6 μm to 1.2 μm . Despite this, the effects of the zirconium depletion of the top face seem to have been more detrimental. The HR-EBSD analysis conducted supports the hardness data for the ion-implanted ZrN. The HR-EBSD shows tensile stress at the surface leading to a band of residual compressive stress. The hardness data shows a similar trend, with a softened surface due to the increased tensile stress followed by a high hardness point around the 200 nm zone: due to the probe size effect expected by nanoindentation, these results compare well. Based on the strength estimation equation discussed in the literature

review, Equation (16) ($H_v \approx 3\sigma_{ys}$), a fracture strength value from 8-6 GPa could be expected from the micro bend test results. For ceramics, this equation can only be used to offer an estimate to inform experimental design.

The hardness of the unirradiated Zr_2ON_2 containing indentations exhibited similar trends to ZrN areas, with a distinct size effect and low hardness at the surface. The bulk hardness of the Zr_2ON_2 containing areas were reduced when compared to the ZrN indentations; based on a law of mixtures methodology this result could be expected.

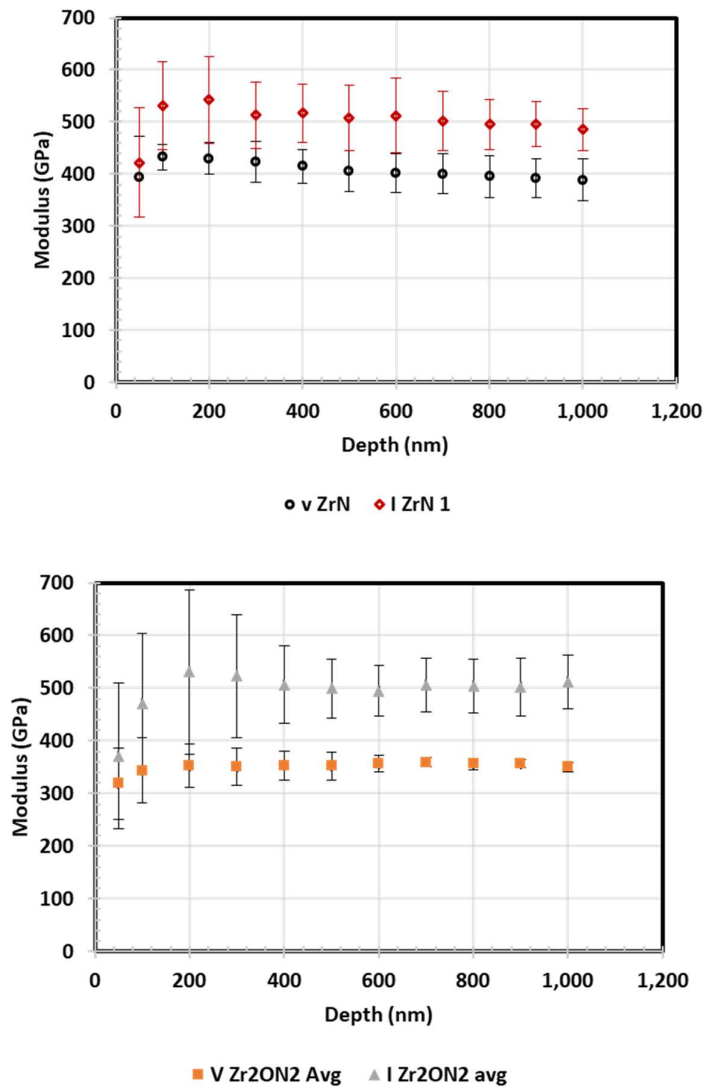


Figure 134 Mean modulus data from irradiated and unirradiated ZrN nano indents, separated by phase and irradiation.

The Young's modulus for the irradiated and unirradiated ZrN was within error throughout the indentation depth. The irradiated ZrN sample had a higher average modulus compared to the unirradiated sample. The surface modulus of both samples was lower than the rest of the data. A chemical change in the surface composition could have contributed to the reduced surface modulus, but isolating these changes is challenging. A more likely factor is the effects of indenter instability caused by sample roughness and touch-on instability. No change in modulus was expected based on the literature. However, the modulus for the oxide phase had a high standard deviation, and the irradiated particles showed an increased modulus.

There was a change in the trends from hardness to modulus for the ZrN phase. Most notably, the modulus of the ZrN at the surface of the virgin sample (50 nm) was the same as that of the irradiated ZrN. For the remainder of the indentation depths, there was a 100 GPa offset between the modulus of the two samples.

Table 24 Meyer's law and PSR model results for irradiated and un-irradiated ZrN.

	Meyer's law			PSR		
	n	A	R ²	a ₁	a ₂	R ²
V ZrN	1.74 ± 0.11	4.20 ± 0.38	0.9986	13.25 ± 3.00	80064 ± 14848	0.9941
I ZrN	1.74 ± 0.05	4.37 ± 0.18	0.9990	31.50 ± 5.53	104139 ± 12651	0.9959
V Zr₂ON₂	1.78 ± 0.06	4.31 ± 0.18	0.9990	13.12 ± 4.32	76434 ± 6044	0.9985
I Zr₂ON₂	1.83 ± 0.08	4.62 ± 0.20	0.9989	23.69 ± 5.94	107353 ± 5452	0.9868

Meyer's law with an N value of (1.74-1.83) served to show that there was a size effect for both constituents of the ZrN sample (see Table 24). The averages with standard deviation of the n values overlap with the irradiated and unirradiated samples, suggesting that the size effect was not significantly affected by ion irradiation (see Table 24).

The PSR model values for a₁ are a determinant of energy absorption from cracking; ion irradiation caused a significant increase in a₁ for both ZrN and Zr₂ON₂. Increased cracking can be attributed to the increased dislocation density in the surface of the material leading to increased hardness and premature fracture. The a₂ values for ZrN and Zr₂ON₂ also increased following ion implantation.

As discussed in the literature review, a modest amount of research has been undertaken on the nanoindentation of ZrN and irradiated ZrN. The general trends from the literature show

that hardness is typically increased from 21 GPa up to around 27 GPa following 80 dpa 300 keV Xe⁺ ion irradiation [25], while Young's modulus has been reported to be essentially unchanged by ion irradiation at the same levels. Further to this, Knoop hardness measurements have been shown to increase following 2.6 MeV proton irradiation [178]. Our findings match relatively well with these findings; variation in the magnitude of hardness value are likely related to sample porosity grain size and test set up. Two factors are thought to have modified the hardness of the sample and its constituents. Firstly, the introduction of a high-density dislocation region on the surface is thought to have contributed to the increase in hardness. Secondly, the introduction of residual compressive stress from gold ions and dislocations will also have had the effect of increasing hardness. The limited (within error) changes in modulus were consistent with the lack of change in crystal structure of the irradiated ZrN sample.

The hardness and Young's modulus of the Zr₂ON₂ phases was affected more significantly by the gold ion beam damage than the ZrN phase. For this reason, it is suggested that future research attempts to reduce the Zr₂ON₂ phase volume fraction. Further to this, additional indentation should be conducted to gain a more representative data set including low load indentations.

4.2.7. Micro mechanical testing ZrN and ion implanted ZrN

Before undertaking micro mechanical testing, a basic understating of the effects of gallium ion damage on ZrN was sought.

4.2.7.1. Gallium ion damage in ZrN

Although ion beam cleaning was not explored during the micro bend testing of the zirconium nitride, an understanding of the effects of gallium ion damage was sought through experimentation. As discussed in the experimental section, a selected area of the ZrN sample was exposed at 90° to the gallium ion beam at 30 keV and a current of 3 nA, followed by 0.3 nA to simulate a cutting/cleaning procedure, and a TEM cross-section lift out was conducted on the area Ga⁺ area, the results from which can be seen in Figure 135, STEM-EDS plots are presented in Figure 136:

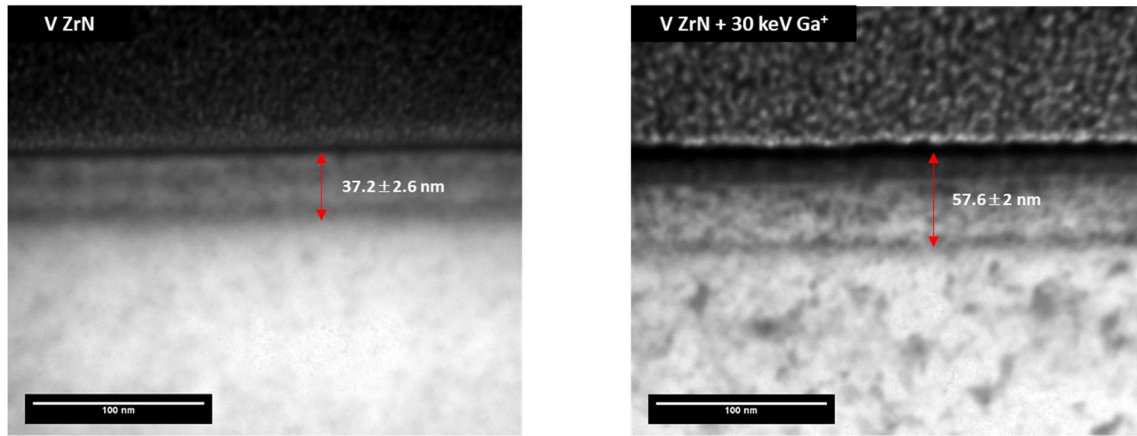


Figure 135 bright field TEM images of the unmodified and Ga^+ ion implanted ZrN surface.

There was an increase in the damage on the surface of the material with a 57.6 ± 2 nm contrast band being formed on the gallium ion irradiated surface. Selective area diffraction showed this layer to have remained crystalline.

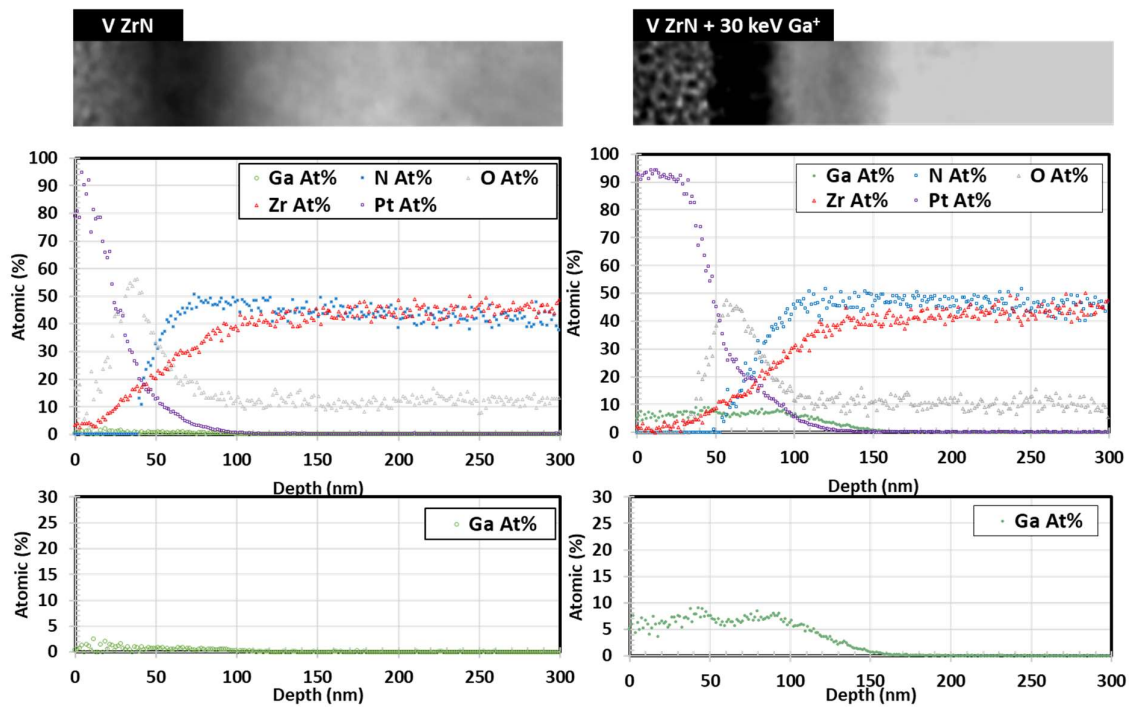


Figure 136 STEM-EDS plots and images from the surface of ZrN and ZrN exposed to gallium ions.

The gallium ions were implanted into the ZrN surface to a depth of 100 nm. This implantation was associated with a contrast band. The stoichiometry of the zirconium in proportion to nitrogen was maintained into the bulk of the material (see Figure 136). Similar to the gold ion implanted samples, there was an observed enrichment of oxygen and nitrogen

at the sample surface. Based on these findings it is expected that gallium ion damage would have had a far less detrimental effect on the mechanical property data obtained through micro bend testing when compared to the SiC test results. Further work could include effects of gallium ion implantation on gold ion irradiated ZrN. It is expected that the effects of gallium ion milling may be more pronounced in the pre-implanted material. Further work could study the effects of combined gold and gallium ion implantation.

4.2.8. Micro bend testing of ZrN and ion implanted ZrN

As a polycrystalline material, micro bend testing ZrN introduced a range of issues not previously encountered while testing the single crystal SiC. Due to the added complexity and the cost of equipment time, tests were performed without EBSD or BSC imaging making the location of grain boundaries challenging. It was identified that ion beam milling caused a slight preferential etching of grain boundaries (see Figure 137). Experimentally, the aim was to test both the bulk and grain boundary properties; however, it was often found that micro bend beams would preferentially fail at the grain boundary.

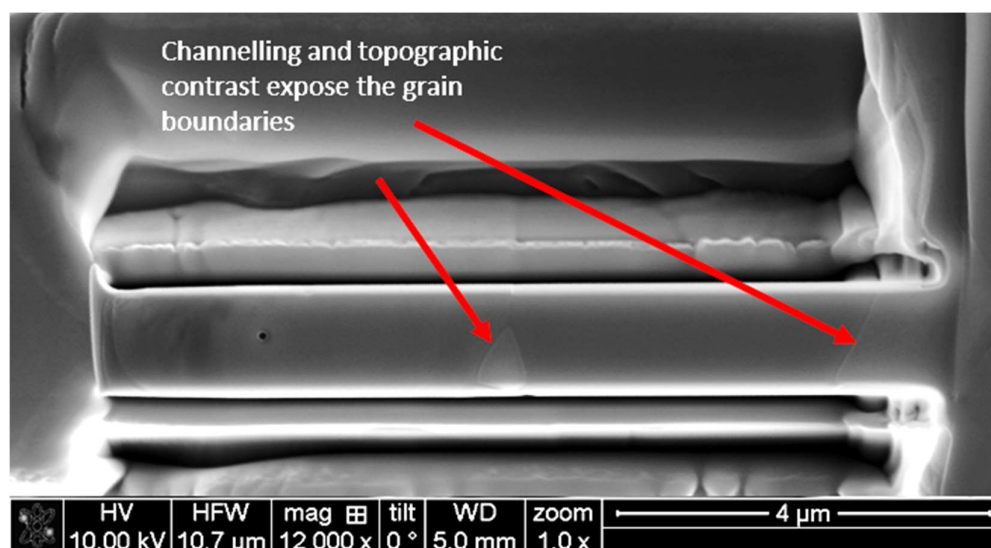


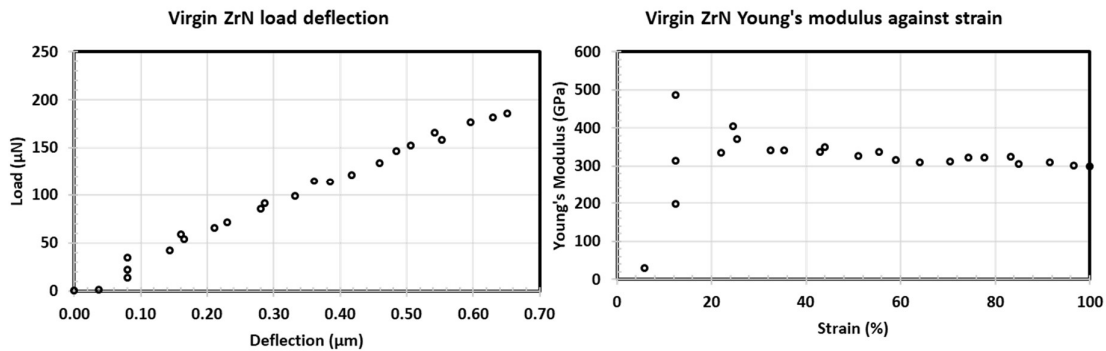
Figure 137 SEM image showing the channelling and topographic contrast of the ion milled ZrN microbeam.

Another experimental challenge faced was in attempting to locate the ion damaged layer within the microbeams. Unlike the SiC microbeams, the ZrN beams top faces were lightly cleaned to ensure that the gold implanted layer and dislocation layer was within the microbeam. This light cleaning had the effect of the beam not being positioned below the surface of the sample. As this set up was similar for each beam, no adjustments were made to the microbeam calculations.

Table 25 ZrN micro bend test parameters. (Each specimen was milled with a gallium ion beam at 30 keV and 0.3 nA). Beams ZrN 3 and I ZrN 4 were excluded as they included significant porosity at their roots.

Sample	Height (μm)	Breadth (μm)	Initial length (μm)	Length at failure (um) "LO"	Fracture angle (°)	Area (μm ²)	Volume (μm ³)	Load at failure (uN)	Deflection at failure (um)
ZrN V 01	1.02	1.01	8.33	8.08	40	1.03	8.61	117	0.71
ZrN V 02	1.05	1.03	9.26	9.08	76	1.08	10.03	220	1.05
ZrN V 03	1.01	0.97	7.75	7.53	67	0.98	7.59	23	0.78
ZrN V 04	0.94	1.03	7.45	7.14	113	0.97	7.21	108	0.80
ZrN V 05	1.12	1.11	7.68	7.41	132	1.24	9.54	190	0.65
ZrN V 06	1.09	1.06	7.50	7.28	102	1.16	8.67	239	
ZrN I 01	1.08	1.29	8.23	7.52	54	1.40	11.53	259	1.29
ZrN I 02	0.99	1.25	8.04	7.95	75	1.23	9.87	77	0.55
ZrN I 03	0.84	1.06	7.73	7.77	96	0.89	6.85	71	1.01
ZrN I 04	0.99	1.13	8.13	8.43	77	1.12	9.10	8	0.30
ZrN I 05	0.81	1.36	6.73	6.25	44	1.10	7.41	220	1.03
ZrN I 06	1.13	1.26	7.80	7.57	102	1.42	11.09	160	0.53

As can be seen in Table 25, the dimensions of the beams were consistently around $1 \times 1 \mu\text{m}$. The unirradiated beams were a height of $1.04 \pm 0.07 \mu\text{m}$, width of $1.04 \pm 0.04 \mu\text{m}$, length of $7.75 \pm 0.69 \mu\text{m}$, and area of $1.08 \pm 0.10 \mu\text{m}^2$. The irradiated beams were milled to a height of $0.97 \pm 0.12 \mu\text{m}$, width of $1.22 \pm 0.11 \mu\text{m}$, length of $7.78 \pm 0.55 \mu\text{m}$, and area of $1.19 \pm 0.20 \mu\text{m}^2$.



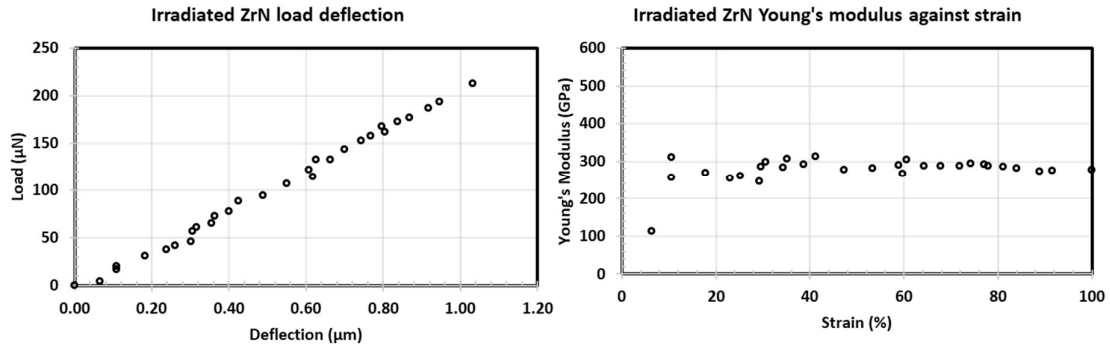


Figure 138 Example of load deflection and Young's modulus against strain micro bend tests plots from bulk ZrN and Au ion irradiated ZrN.

The load-deflection curves and modulus-strain plots are comparable to those collected while testing silicon carbide, in that the deformation of the beams was predominantly elastic, with some noise during the initial loading. The modulus change during testing is less pronounced than in the silicon carbide test. This difference is likely due to the reduced deflection from the ZrN when compared to SiC. No significant differences were identified between the irradiated and unirradiated load-deflection plots or the modulus strain plots.

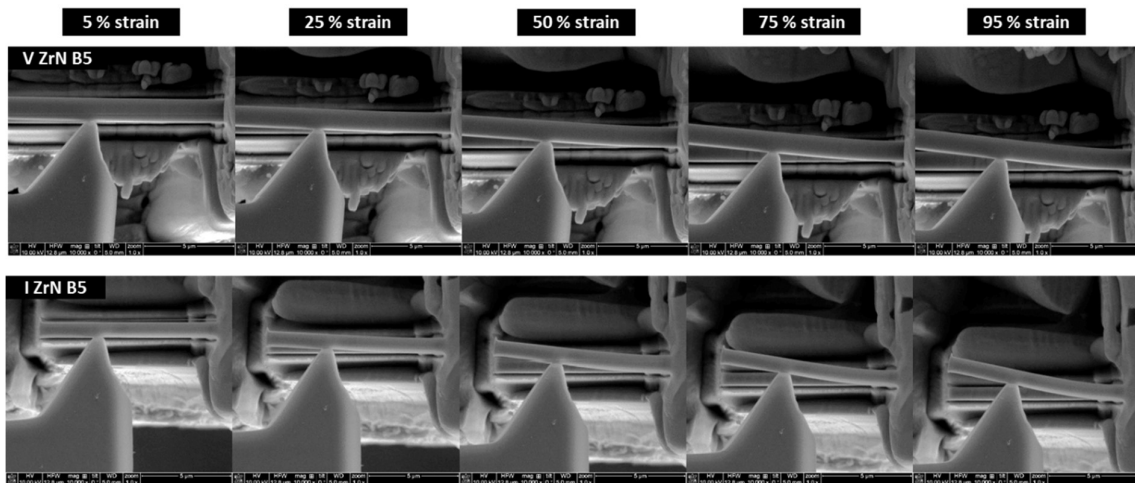


Figure 139 Example images from the various stages of the example micro bend tests; images shown are from the 5th test beam in both the virgin and gold ion irradiated tests.

The SEM images of the microbeam testing in progress illustrate the similarity between the bulk and ion irradiated samples (see Figure 139). The ZrN sample deformation (strain) before failure is less than that of the silicon carbide. As previously discussed the equations used are better suited to small deflections.

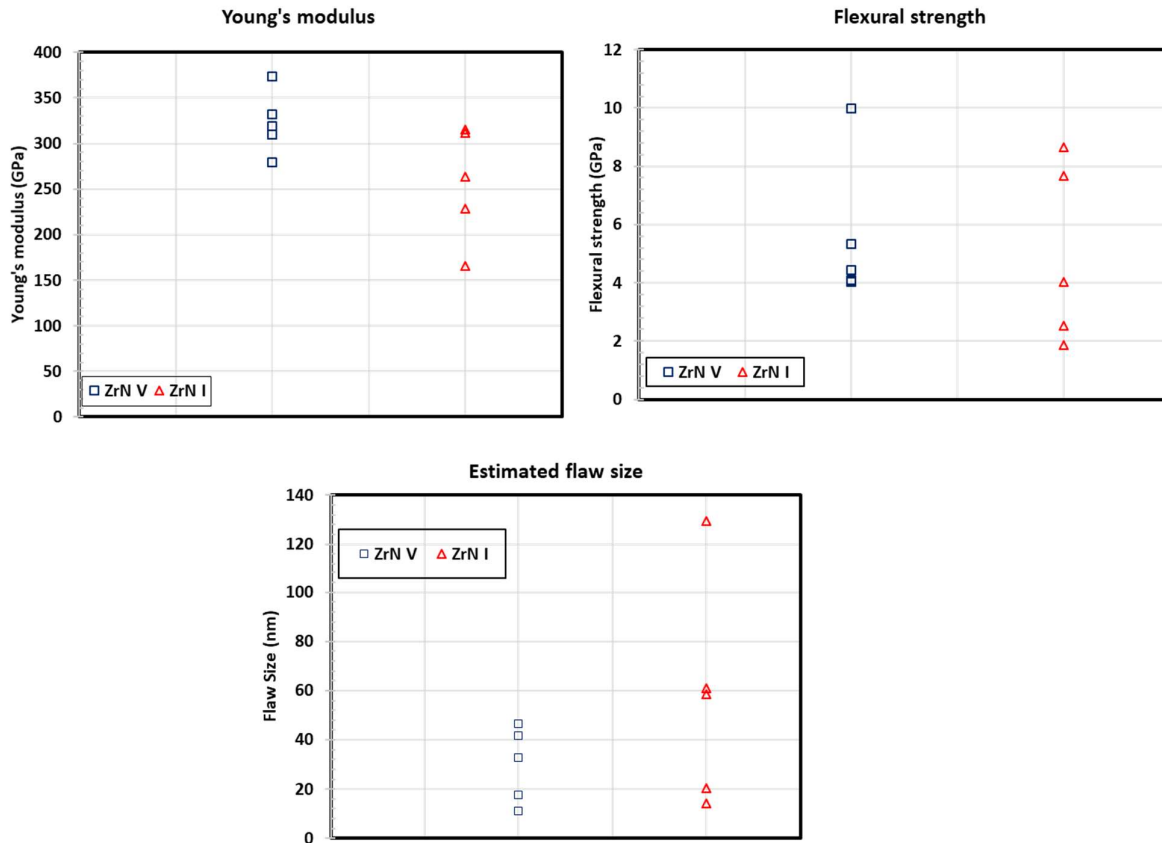


Figure 140 Young's modulus, flexural strength and flaw size results of the unirradiated and irradiated zirconium nitride microbeams.

Table 26 Summary table of results from ion-irradiated and unirradiated ZrN samples.

	Average Young's modulus (GPa)	Standard deviation (GPa)	Average flexural strength (GPa)	Standard deviation (GPa)	Average flaw size (m)	Standard deviation (GPa)
V ZrN	323	34	5.5	3	30	15
I ZrN	257	63	4.9	3	56	45

From the Young's modulus results (Figure 140 and Table 26) it is apparent that ion irradiation has caused a significant change in Young's modulus and some change to the flexural strength. The variation between data points is considerable: this is due to the inhomogeneity of poly-crystalline samples and the dual phase nature of the sample. Based on the SEM images of the samples before and after testing, microstructural features can be linked back to mechanical properties (see Figure 141 and Figure 142):

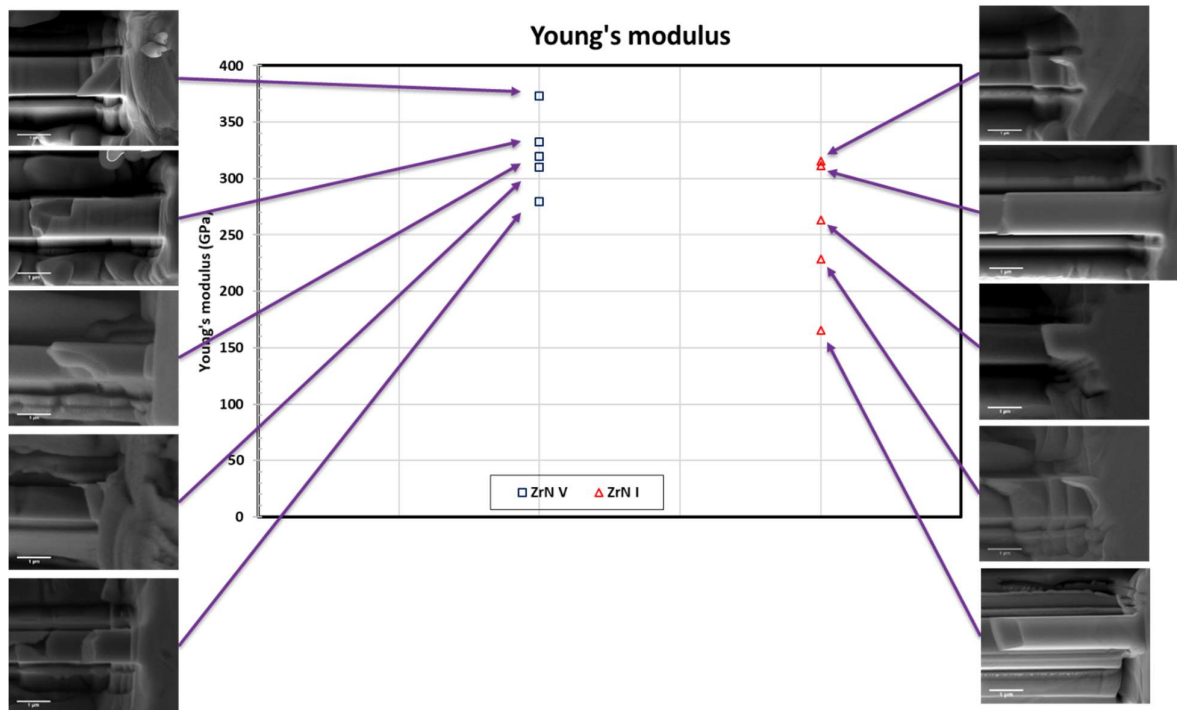


Figure 141 Young's modulus data from micro bend tests with fracture face images for each point.

Compared to flexural strength, Young's modulus measurements were less sensitive to the presence of the second phase or grain boundaries. This is expected as the modulus is calculated from the initial portion of the elastic deformation of the beam. Disparity in modulus values may have arisen due to crystallographic orientation variation in the grains tested, or experimental error.

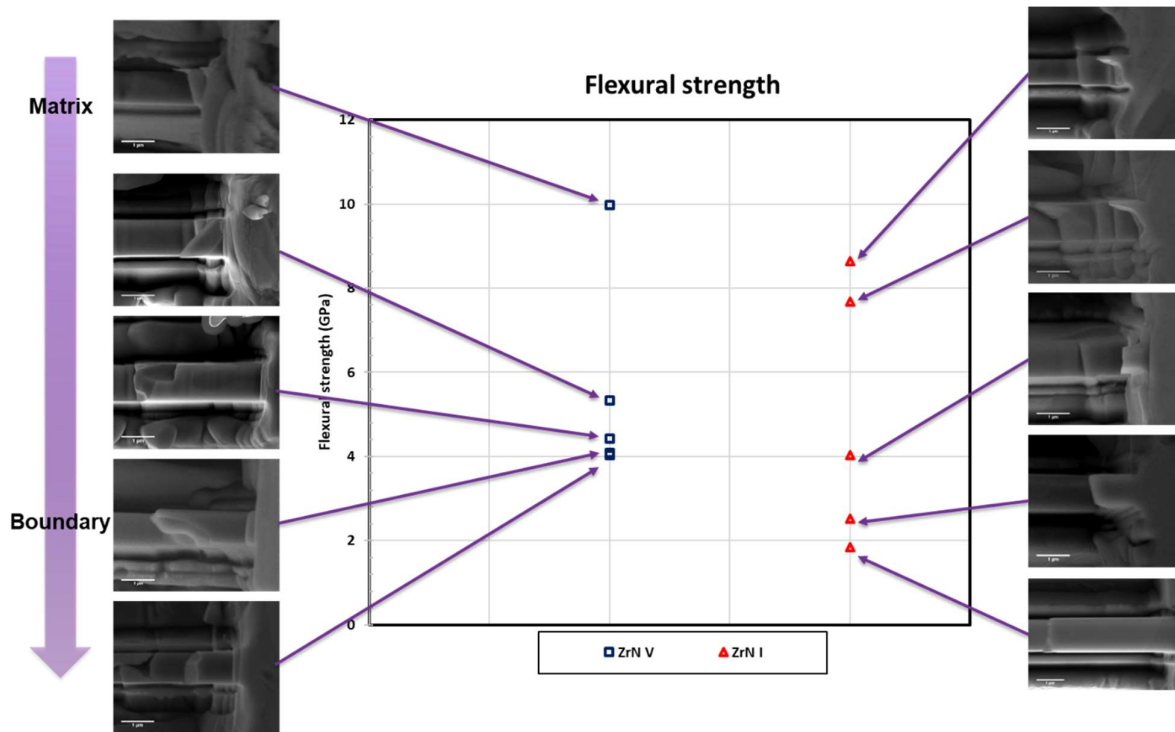


Figure 142 Flexural strength data from micro bend tests with fracture face images for each point.

The location of the microbeam fracture had a significant effect on bend strength. Beams which fractured at the root typically were composed of the ZrN matrix. Beams failing at their mid-point frequently had secondary phase particles or grain boundaries. Unsurprisingly, the second phase/grain boundary containing beams failed at a lower flexural strength. There was a general trend that implanted beams had a reduced grain boundary and matrix strength. Due to the small number of samples, the variation in crystallographic orientation and grain boundary location, it is difficult to draw a numerical conclusion; however, there is some certainty that strength and modulus of the matrix and boundaries were reduced by ion irradiation.

Based on the stress field identified during HR-EBSD, an ideal experimental set up would have orientated the beam such that the implanted face would have been on indenter side of the beam. With the indenter on the implanted face, the stress variation caused by the gold ions would have produced a more marked change in mechanical properties. These results would also have been better suited for comparison to the nano indentation data.

5. Conclusions

Due to growing energy demands, nuclear power is becoming an ever more appealing energy source. The next generation and future reactors are set to burn more fuel, resulting in higher efficiency and lower quantities of persistent radioactive waste. To move to the next generation of reactor designs, the effects of radiation damage on ceramics will have to be better understood; ion damage studies and microscale mechanical property characterisation will be key to this process. Fuel cladding materials such as SiC and ZrN will be required to resist higher temperatures and fluences, resulting in high thermal stress and stress developed from evolved gases within the fuel pellets. As such, in this work a micro bend test technique was developed in a model material, single crystal silicon carbide, and a range of ion cleaning parameters were explored along with the effects of microbeam size. Following the development of the micro bend technique in SiC, the technique was applied to ZrN implanted with gold ions at 4 MeV to 400 dpa. The results of the micro bend tests were compared to continuous stiffness nanoindentation measurements.

One of the critical issues with micromechanical testing of ceramics is in preparing a sufficient number of samples to gain a data set of statistical significance. The approach used in this research was particularly time-consuming because of the need to measure each image to track displacement and to cut large areas of material for bend testing. Making two beams typically took 4-5 hours to cut and test. Nanoindentation was considerably quicker to conduct and allowed the preparation of much more statistically significant data sets. Despite the number of results available, the ambiguity as to the link between the indentation depth and ion damage makes robust interpretation of the data difficult. It was found that imaging of the indents after indentation was key to developing reliable results, as the phase indented had significant effect on materials properties.

The orientation of both microbeams and nanoindentations was unknown during testing. As discussed in the introductory section, depending on crystallographic orientation variations in mechanical properties are observable. These variations can be overlooked in the majority of macro-scale testing due to the large number of grains being tested, however, in micromechanical testing and nanoindentation, single grains are being tested, and variations in modulus grain to grain can cause significant variation in results. As a consequence, the unknown orientations of the beams and small number of tests, these orientation variations make up part of the experimental error. Future work could include in-situ EBSD analysis to

identify the trends in mechanical property changes based on orientation, or at least to reduce the mechanical property variation.

Practical recommendations

- For successful mechanical characterisation of ion implanted surfaces, the micro structure of the bulk and implanted layer must first be understood. This information can then inform the size of micro beam/ load of nano indent required.
- Characterisation / understanding of the damage introduced through FIB milling of micro bend samples is required for the collection of robust data sets.
- Without the characterisation of a materials size effect, micro beams of a similar cross section and length should only be compared to beams of a similar cross section and length.
- In dual phase materials, post indentation characterisation of nano idents is required to link the microstructure to the mechanical performance of the phase in question.

5.1. Silicon carbide

Before micromechanical testing, the SiC wafers were characterised to identify their suitability as model materials. The wafers were found to be suitable due to their consistent chemical composition, oxide-free surface, single crystal nature and low roughness.

From the nanoindentation tests, Young's modulus 349-473 GPa, hardness 36-60 GPa and fracture toughness 1.43-1.76 MPa.m^{-1/2} values for the studied 6H crystal were determined. The Young's modulus results from nanoindentation 349-473 GPa, correlates well with the average Young's modulus values 320–469 GPa recorded for the micro bend tests.

Nanoindentation followed the classic size effect, where smaller is harder. Fracture toughness was found to be size independent as is reported in the literature.

Ion beam machining was examined in-depth as a method for the manufacture of microbeams. It was found that SiC was particularly sensitive to ion beam amorphisation. The reduction in modulus measured during nanoindentation to micro bending is attributed to amorphisation. Ion beam cleaning at lower accelerating voltages did not significantly reduce the amorphous layer on the material surface. Low accelerating voltage cleaning induced additional sources of error such as beam rounding, reducing the effective area of the microbeams. As such, it

was concluded that no cleaning steps beyond 30 keV, 0.3 nA were necessary. Microbeams of $\approx 1 \times 1 \times 8 \mu\text{m}$ were found to perform consistently and to operate in an appropriate range for the load cell while being relatively quick to manufacture. The bend test results were found to be less size-dependent than nano indentation, with other factors such as ion damage being more clearly linked to size effect.

5.2. Zirconium nitride resistance to gold ion irradiation

The microstructure of hot press ZrN was characterised. The samples were found to consist of ZrN and $\text{Zr}_2\text{ON}_2/\text{ZrO}_2$ particles. The Zr_2ON_2 was observed to have a core shell-like structure with a Zr_2ON_2 exterior and ZrO_2 interior. This core-shell structure had not previously been identified in the literature. EBSD combined with EDS was used to confirm the grain size and distribution in the material. Despite the potential for ion channelling to result in specific crystallographic orientations gathering deeper damage, no such effect was observed during TEM or SEM analysis.

Ion beam damage was identified as a factor in micro bend testing of 6H SiC. The surface damage layer in the SiC was characterised as a 20-30 nm amorphous layer. This layer was removed from the microbeam calculations, resulting in higher Young's modulus and flexural strength. In the ZrN micro bend test study, the ion damage layer was not removed from the calculations, as the data is intended to be used as a comparative study between the irradiated and unirradiated microbeams. Further to this, a gallium ion beam damage study was conducted on the ZrN sample. This study concluded that ZrN was significantly more resilient to gallium ion damage when compared to SiC.

The micro bend tests showed a reduction in modulus and strength following irradiation. Nano indentation showed surface property reduction, followed by a modest increase in modulus and significant increase in hardness following ion irradiation.

Based on these findings, it is suggested that ZrN should be studied further as a candidate nuclear material. However what has not been addressed is the suitability of ZrN for the manufacture of ceramic fuel coatings and rod assembly components. The samples tested were hot pressed; hot pressing is limited to relatively simple shapes and would not be suitable for producing long rod structures. Lack of scalability is an issue for all ceramic, and the ability to

produce sizeable structural engineering ceramic components and bond them to form larger assemblies is a challenge that materials scientist are working on [185].

5.3. Recommendations for future work

5.3.1. Recommendations for future SiC analysis

On the basis of the experimentation conducted and reported here, the following recommendations are made:

- Orientation based micro bend testing is recommended to identify modulus and strength dependency relative to crystallographic orientation. Plastic deformation is highly dependent on the slip planes available. By orientating the microbeams in alternative directions, the properties of different slip planes could be assessed; a comparison to nanoindentation studies of this nature could be of interest.
- Additional larger-scale micro bend $+1.50\ \mu\text{m}$ cross sections to identify the range of the microbeam size effect. Producing additional microbeams at a larger scale would allow regression fitting of the data, making scaling of the results to a wider range of length scales possible.
- Further analysis of the residual strain caused by ion damage using geometric phase analysis (GPA) and HR-EBSD (spatial resolution dependent). This could be used to explain strength variations in micro bend tests with different ion milled surface finishes.
- Characterisation of the mechanical properties of the amorphous SiC layer, and the development of a layered microbeam model to account for the damage layer. Low load continuous stiffness nanoindentation could be an approach to determining the modulus of the amorphized SiC.

5.3.2. Recommendations for future testing of ZrN

Based on the experimentation conducted and reported here, the following recommendations for future testing of ion implanted ZrN are made:

- Additional micro bend testing to gather a data set with a higher statistical significance could be conducted.
- Loading of the microbeams perpendicular to the implanted surface may have elicited greater variation in strength: additional tests in this orientation would be insightful. Beams perpendicular to the implanted layer would also produce results which match better with the EBSD and nanoindentation data.
- Future tests should include complementary EBSD and EDS data to assess the phase tested and orientation of the grain/grains tested during micro bending.
- Future work could consider the effects of surface finish on ion penetration, comparing low-stress surface finishes such as-sintered surfaces and high-stress ground surfaces. It is unlikely that every aspect of a component could be polished to a 1 μm surface finish before being placed in service; as such, samples with an as manufactured-finished should be investigated.
- Further exploration into the effects of ZrN stoichiometry should be conducted. As discussed in the literature, a range of stichometryies of ZrN are possible, and the effects and control of these factors would have to be considered before ZrN could be used as an actinide fuel.
- Characterisation of ZrN self-implanted with nitrogen in a helium atmosphere should be explored before neutron validation experiments. Various authors have identified changes in deformation characteristics in metals following ion implantation in the presence of helium. The consensus in the literature is that self-implantation better simulates neutron damage.

References

- [1] W. Nuclear, “Operational nuclear power plants a global summary.” [Online]. Available: <http://www.world-nuclear.org/information-library/current-and-future-generation/nuclear-power-in-the-world-today.aspx>. [Accessed: 04-Feb-2017].
- [2] “Pressurised water reactor schematic,” *World nuclear association*. [Online]. Available: <http://www.world-nuclear.org/information-library/nuclear-fuel-cycle/nuclear-power-reactors/nuclear-power-reactors.aspx>. [Accessed: 04-Feb-2017].
- [3] L. Chaffron, C. Sauder, C. Lorrette, L. Briottet, and A. Michaux, “Innovative SiC/SiC Composite for Nuclear Applications,” in *Materials innovation for nuclear optimized systems*, 2012.
- [4] “Fuel rod assembly,” *World nuclear association*. [Online]. Available: <http://www.world-nuclear.org/information-library/nuclear-fuel-cycle/conversion-enrichment-and-fabrication/fuel-fabrication.aspx>. [Accessed: 01-Feb-2018].
- [5] M. S. T. Price, “The dragon project origins, achievements and legacies,” *Nucl. Eng. Des.*, vol. 251, pp. 60–68, 2012.
- [6] M. K. Meyer, R. Fielding, and J. Gan, “Fuel development for gas-cooled fast reactors,” *J. Nucl. Mater.*, vol. 371, no. 1–3, pp. 281–287, 2007.
- [7] X. Zhao, R. M. Langford, J. Tan, and P. Xiao, “Mechanical properties of SiC coatings on spherical particles measured using the micro-beam method,” *Scr. Mater.*, vol. 59, pp. 39–42, 2008.
- [8] Y. Katoh, L. L. Snead, I. Szlufarska, and W. J. Weber, “Radiation effects in SiC for nuclear structural applications,” *Curr. Opin. Solid State Mater. Sci.*, vol. 16, no. 3, pp. 143–152, 2012.
- [9] T. Allen, J. Busby, M. Meyer, and D. Petti, “Materials challenges for nuclear systems,” *Mater. Today*, vol. 13, no. 12, pp. 14–23, 2010.
- [10] “Generation 4 reactor designs,” *World nuclear association*. [Online]. Available: <http://www.world-nuclear.org/information-library/nuclear-fuel-cycle/nuclear-power-reactors/generation-iv-nuclear-reactors.aspx>. [Accessed: 01-Feb-2018].
- [11] G. S. Was *et al.*, “Emulation of reactor irradiation damage using ion beams,” *Scr. Mater.*, vol. 88, pp. 33–36, 2014.
- [12] W. Van Renterghem *et al.*, “Transmission electron microscopy investigation of neutron irradiated Si and ZrN coated UMo particles prepared using FIB,” *J. Nucl. Mater.*, vol. 498, pp. 60–70, 2018.
- [13] Y. Lee, C. Y. Joung, S. H. Kim, and S. Lee, “Inert Matrix Fuel - A New Challenge for Material Technology in the Nuclear Fuel Cycle,” *Met. Mater. Int.*, vol. 7, no. 2, 2001.
- [14] H. Kleykamp, “Selection of materials as diluents for burning of plutonium fuels in nuclear reactors,” *J. Nucl. Mater.*, vol. 275, pp. 1–11, 1999.
- [15] D. T. Hoelzer *et al.*, “Development of High-Strength ODS Steels for Nuclear Energy Applications,” in *ODS 2019 materials workshop*, 2010.
- [16] D. Kopeliovich, “Imperfections of crystal structure.” [Online]. Available: http://www.substech.com/dokuwiki/doku.php?id=imperfections_of_crystal_structure. [Accessed: 03-Feb-2019].
- [17] S. J. Zinkle and J. T. Busby, “Structural materials for fission & fusion,” Elsevier, 2009.

- [18] P. Rodriguez, R. Krishnan, and C. V. Sundaram, "Radiation effects in nuclear reactor materials-correlation with structure," *Bull. Mater. Sci.*, vol. 6, no. 2, pp. 339–367, 1984.
- [19] E. Woolley, "Surface Hardening by Ion Implantation," *Materials world*, pp. 3–5, Sep-1997.
- [20] W. R. Grove, "VII . On the electro-chemical polarity of gases," *Philos. Trans.*, no. January, pp. 87–101, 1852.
- [21] G. Dearnaley, "Historical perspective of metal implantation," *Surf. Coat. Technol.*, vol. 65, pp. 1–6, 1994.
- [22] N. Angert, "Ion sources," *International atomic energy agency*. Darmstadt, Germany, pp. 619–642, 1994.
- [23] M. Goorsky, "Ion implantation," in *Ion implantation*, M. Goorsky, Ed. Croatia: InTech, 2012.
- [24] G. M. McCracken, "The behaviour of surfaces under ion bombardment," *Reports Prog. physics*, 1975.
- [25] G. W. Egeland, J. A. Valdez, S. A. Maloy, K. J. McClellan, K. E. Sickafus, and G. M. Bond, "Heavy-ion irradiation defect accumulation in ZrN characterized by TEM, GIXRD, nanoindentation, and helium desorption," *J. Nucl. Mater.*, vol. 435, no. 1–3, pp. 77–87, 2013.
- [26] J. Lindhard, M. Scharff, and H. Schiott, "Range concepts and heavy ion ranges (notes on atomic collisions,II)," vol. 14, no. 14, 1963.
- [27] H. Townes, C, "Theory of cathode sputtering in low voltage gaseous discharges," *Phys. Rev.*, vol. 65, 1944.
- [28] A. Y. Didyk and A. S. Khalil, "Properties of Indium Phosphite and Selected Compounds under Irradiation with Swift Heavy Ions 1," vol. 41, no. 2, pp. 230–284, 2010.
- [29] E. M. Bringa and R. E. Johnson, "Coulomb explosion and thermal spikes," *Phys. Rev. Lett.*, vol. 88, no. 16, pp. 1–4, 2002.
- [30] M. Lang, R. Devanathan, M. Toulemonde, and C. Trautmann, "Advances in understanding of swift heavy-ion tracks in complex ceramics," *Curr. Opin. Solid State Mater. Sci.*, vol. 19, no. 1, pp. 39–48, 2015.
- [31] A. S. Khalil, L. T. Chadderton, A. M. Stewart, M. C. Ridgway, D. J. Llewellyn, and A. P. Byrne, "Track formation and surface evolution in indium phosphide irradiated by swift heavy ions," *Radiat. Meas.*, vol. 40, pp. 770–774, 2005.
- [32] M. L. Crespillo, F. Agulló-lópez, and A. Zucchiatti, "Cumulative approaches to track formation under swift heavy ion (SHI) irradiation : Phenomenological correlation with formation energies of Frenkel pairs," *Nucl. Inst. Methods Phys. Res. B*, vol. 394, pp. 20–27, 2017.
- [33] C. J. Mc Hargue, M. E. O'Hern, C. W. White, and M. B. Lewis, "Ion implantation in ceramics-residual stress and properties," *Mater. Sci. Eng. A*, vol. 115, no. C, pp. 361–367, 1989.
- [34] Q. Wang, K. Ozaki, H. Ishikawa, S. Nakano, and H. Ogiso, "Indentation method to measure the residual stress induced by ion implantation," *Nucl. Instruments Methods Phys. Res. Sect. B Beam Interact. with Mater. Atoms*, vol. 242, no. 1–2, pp. 88–92, 2006.
- [35] K. W. Weng, Y. C. Chen, S. Han, C. S. Hsu, Y. L. Chen, and D. Y. Wang, "Effects of ion implantation on the microstructure and residual stress of filter arc CrN films," *Thin Solid Films*, vol. 516, no. 16, pp. 5330–5333, 2008.
- [36] B. J. P. and L. U. Ziegler J F, "The Stopping and Range of Ions in Solids (New York:

- Pergamon).” 1985.
- [37] K. Nordlund *et al.*, *Primary Radiation Damage in Materials*. 2015, p. NEA/NSC/DOC(2015)9.
- [38] S. V. Kutsaev *et al.*, “Heavy ion linear accelerator for radiation damage studies of materials,” *Rev. Sci. Instrum.*, vol. 88, no. 3, 2017.
- [39] “Standard Practice for Neutron Radiation Damage Simulation by Charged-Particle irradiation,” 2003.
- [40] S. J. Zinkle and L. L. Snead, “Opportunities and limitations for ion beams in radiation effects studies: Bridging critical gaps between charged particle and neutron irradiations,” *Scr. Mater.*, vol. 143, pp. 154–160, 2018.
- [41] M. F. Pantano, H. D. Espinosa, and L. Pagnotta, “Mechanical characterization of materials at small length scales,” *J. Mech. Sci. Technol.*, vol. 26, no. 2, pp. 545–561, 2012.
- [42] B.S.I Standards, “Semiconductor devices — devices Part 10 : Micro-pillar compression test for MEMS materials,” 2011.
- [43] C. Shin, H. H. Jin, H. Sung, D. J. Kim, Y. S. Choi, and K. Oh, “Evaluation of Irradiation Effects on Fracture Strength of Silicon Carbide using Micropillar Compression Tests,” *Exp. Mech.*, vol. 53, no. 2013, pp. 687–697, 2013.
- [44] P. Hosemann, “Small-scale mechanical testing on nuclear materials : bridging the experimental length-scale gap,” *Scr. Mater.*, vol. 143, pp. 161–168, 2018.
- [45] Z. F. Shi *et al.*, “Determination of the microscale stress-strain curve and strain gradient effect from the micro-bend of ultra-thin beams,” *Int. J. Plast.*, vol. 24, no. 9, pp. 1606–1624, 2008.
- [46] J. R. Greer, W. C. Oliver, and W. D. Nix, “Size dependence of mechanical properties of gold at the micron scale in the absence of strain gradients,” *Acta Mater.*, vol. 53, no. 6, pp. 1821–1830, 2005.
- [47] W. D. Nix, J. R. Greer, G. Feng, and E. T. Lilleodden, “Deformation at the nanometer and micrometer length scales: Effects of strain gradients and dislocation starvation,” *Thin Solid Films*, vol. 515, no. 6, pp. 3152–3157, 2007.
- [48] D. Kiener, C. Motz, and G. Dehm, “Micro-compression testing: A critical discussion of experimental constraints,” *Mater. Sci. Eng. A*, vol. 505, no. 1–2, pp. 79–87, 2009.
- [49] H. Liu, Z. Huang, M. Fang, Y. Liu, and X. Wu, “Preparation and growth mechanism of β -SiC nanowires by using a simplified thermal evaporation method,” *J. Cryst. Growth*, vol. 419, pp. 20–24, 2015.
- [50] Y. S. Jang, C. Zollfrank, M. Jank, and P. Greil, “Fabrication of silicon carbide micropillar arrays from polycarbosilanes,” *J. Am. Ceram. Soc.*, vol. 93, no. 11, pp. 3929–3934, 2010.
- [51] S. Shim, H. Bei, M. K. Miller, G. M. Pharr, and E. P. George, “Effects of focused ion beam milling on the compressive behavior of directionally solidified micropillars and the nanoindentation response of an electropolished surface,” *Acta Mater.*, vol. 57, no. 2, pp. 503–510, 2009.
- [52] M. J. Burek and J. R. Greer, “Fabrication and microstructure control of nanoscale mechanical testing specimens via electron beam lithography and electroplating,” *Nano Lett.*, vol. 10, pp. 69–76, 2010.
- [53] C. Shin, H. H. Jin, W. J. Kim, and J. Y. Park, “Mechanical properties and deformation of cubic silicon carbide micropillars in compression at room temperature,” *J. Am. Ceram. Soc.*, vol. 95, pp. 2944–2950, 2012.

- [54] R. Maaß, S. Van Petegem, C. N. Borca, and H. Van Swygenhoven, “In situ Laue diffraction of metallic micropillars,” *Mater. Sci. Eng. A*, vol. 524, no. 1–2, pp. 40–45, 2009.
- [55] G. E. Ice and J. W. L. Pang, “Tutorial on x-ray microLaue diffraction,” *Mater. Charact.*, vol. 60, no. 11, pp. 1191–1201, 2009.
- [56] K. Y. Xie, Y. Wang, S. Ni, X. Liao, J. M. Cairney, and S. P. Ringer, “Insight into the deformation mechanisms of alpha-Fe at the nanoscale,” *Scr. Mater.*, vol. 65, no. 12, pp. 1037–1040, 2011.
- [57] S. Kiani, K. W. K. Leung, V. Radmilovic, A. M. Minor, and J. Yang, “Dislocation glide-controlled room-temperature plasticity in 6H-SiC single crystals,” *Acta Mater.*, vol. 80, pp. 400–406, 2014.
- [58] H. Bei, S. Shim, M. K. Miller, G. M. Pharr, and E. P. George, “Effects of focused ion beam milling on the nanomechanical behavior of a molybdenum-alloy single crystal,” *Appl. Phys. Lett.*, vol. 91, no. 11, pp. 1–3, 2007.
- [59] A. M. Korsunsky *et al.*, “Quantifying eigenstrain distributions induced by focused ion beam damage in silicon,” *Mater. Lett.*, vol. 185, pp. 47–49, 2016.
- [60] A. Tseng, “Recent developments in nanofabrication using focused ion beams,” *Small*, vol. 1, no. 10, pp. 924–939, 2005.
- [61] S. Rubanov and P. R. Munroe, “FIB-induced damage in silicon,” *J. Microsc.*, vol. 214, no. 3, pp. 213–221, 2004.
- [62] R. Kelley, K. Song, B. Van Leer, D. Wall, and L. Kwakman, “Xe⁺ FIB Milling and Measurement of Amorphous Silicon Damage,” *Microsc. Microanal.*, vol. 19, no. Suppl 2, pp. 862–863, 2013.
- [63] B. D. Kiener, C. Motz, T. Schöberl, M. Jenko, and G. Dehm, “Determination of Mechanical Properties of Copper at the Micron Scale **,” *Adv. Eng. Mater.*, no. 11, pp. 1119–1125, 2006.
- [64] D. Di Maio and S. G. Roberts, “Measuring fracture toughness of coatings using focused-ion-beam-machined microbeams,” *J. Mater. Res.*, vol. 20, no. 02, pp. 299–302, 2005.
- [65] D. E. J. Armstrong, A. J. Wilkinson, and S. G. Roberts, “Measuring anisotropy in Young’s modulus of copper using microcantilever testing,” *J. Mater. Res.*, vol. 24, no. 11, pp. 3268–3276, 2009.
- [66] P. Hosemann, C. Shin, and D. Kiener, “Small scale mechanical testing of irradiated materials,” *J. Mater. Res.*, pp. 1–15, 2015.
- [67] D. Liu, P. J. Heard, S. Nakhodchi, and P. E. J. Flewitt, “Small-Scale Approaches to Evaluate the Mechanical Properties of Quasi-Brittle Reactor Core Graphite,” *ASTM Int.*, pp. 84–104, 2014.
- [68] C. Howard, C. D. Judge, D. Poff, S. Parker, M. Grif, and P. Hosemann, “A novel in-situ, lift-out, three-point bend technique to quantify the mechanical properties of an ex-service neutron irradiated inconel X-750 component,” *J. Nucl. Mater.*, vol. 498, 2018.
- [69] B. Moser, K. Wasmer, L. Barbieri, and J. Michler, “Strength and fracture of Si micropillars: A new scanning electron microscopy-based micro-compression test,” *J. Mater. Res.*, vol. 22, no. 04, pp. 1004–1011, 2007.
- [70] K. S. Ng and a. H. W. Ngan, “Breakdown of Schmid’s law in micropillars,” *Scr. Mater.*, vol. 59, no. 7, pp. 796–799, 2008.
- [71] M. F. Ashby, *Useful solutions to standard problems*, CES Edupack. 2006.

- [72] N. Hansen, "Hall-petch relation and boundary strengthening," *Scr. Mater.*, vol. 51, no. 8 SPEC. ISS., pp. 801–806, 2004.
- [73] "Hall Petch - why nano composite." [Online]. Available: <http://www.ramaseshan.com/WHYNANOCOMPOSITE.PHP>. [Accessed: 05-Feb-2018].
- [74] W. W. Gerberich *et al.*, "Scale effects for strength, ductility, and toughness in 'brittle' materials," *J. Mater. Res.*, vol. 24, no. 3, pp. 898–906, 2009.
- [75] F. Östlund *et al.*, "Brittle-to-ductile transition in uniaxial compression of silicon pillars at room temperature," *Adv. Funct. Mater.*, vol. 19, no. 15, pp. 2439–2444, 2009.
- [76] F. Östlund *et al.*, "Ductile-brittle transition in micropillar compression of GaAs at room temperature," *Philos. Mag.*, vol. 91, no. 7–9, pp. 1190–1199, 2011.
- [77] P. Haasen, U. Messerschmidt, and W. Skrotzki, "Low energy dislocation structures in ionic crystals and semiconductors," *Mater. Sci. Eng.*, vol. 81, no. C, pp. 493–507, 1986.
- [78] "Vickers indenter schematic." [Online]. Available: https://www.hera.org.nz/Category?Action=View&Category_id=516. [Accessed: 02-Feb-2017].
- [79] J. Wade, S. Ghosh, P. Claydon, and H. Wu, "Contact damage of silicon carbide ceramics with different grain structures measured by Hertzian and Vickers indentation," *J. or Eur. Ceram. Soc.*, vol. 35, no. 6, pp. 1–25, 2015.
- [80] J. Wade, "Contact damage of ceramics and ceramic nanocomposites," Loughborough, 2017.
- [81] W. D. Nix and H. Gao, "Indentation size effects in crystalline materials: a law for strain gradient plasticity," *J. Mech. Phys. Solids*, vol. 46, no. 3, 1998.
- [82] Q. Ma and D. R. Clarke, "Size dependent hardness of silver single crystals," vol. 5050, no. December 1994, pp. 853–863, 2017.
- [83] H. Li and R. Bradt, "The indentation load / size effect and the measurement of the hardness of vitreous silica," *Non Cryst. Solids*, vol. 146, pp. 197–212, 1992.
- [84] J. Wade and H. Wu, "Hardness of alumina/silicon carbide nanocomposites at various silicon carbide volume percentages," 2014.
- [85] P. Zhang, S. X. Li, and Z. F. Zhang, "General relationship between strength and hardness," *Mater. Sci. Eng. A*, vol. 529, no. 1, pp. 62–73, 2011.
- [86] ASTM, "Standard Test Methods for Determination of Fracture Toughness of Advanced Ceramics." pp. 1–33, 2007.
- [87] B. R. Lawn, A. G. Evans, and D. B. Marshall, "Elastic / Plastic Indentation Damage in Ceramics : The MediadRadial Crack System," *J. Am. Ceram. Soc.*, pp. 574–582, 1980.
- [88] R. G. Anstis, P. Chantikul, B. R. Lawn, and D. B. Marshall, "A critical evaluation of indentation techniques for measuring fracture toughness, I, direct crack measurements," *J. Am. Ceram. Soc.*, vol. 46, no. September, pp. 533–538, 1981.
- [89] D. B. Marshall *et al.*, "The Compelling Case for Indentation as a Functional Exploratory and Characterization Tool," *J. Am. Ceram. Soc.*, vol. 10, no. 2015, p. n/a-n/a, 2015.
- [90] W. C. Oliver and G. M. Pharr, "Measurement of hardness and elastic modulus by instrumented indentation: Advances in understanding and refinements to methodology," *J. Mater. Res.*, vol. 19, no. 01, pp. 3–20, Mar. 2011.
- [91] W. C. Oliver and G. M. Pharr, "An improved technique for determining hardness and elastic modulus using load and displacement sensing indentation experiments," *Journal of Materials*

Research, vol. 7. pp. 1564–1583, 1992.

- [92] X. Li and B. Bhushan, “A review of nanoindentation continuous stiffness measurement technique and its applications,” *Mater. Charact.*, vol. 48, pp. 11–36, 2002.
- [93] C. a. Schuh, “Nanoindentation studies of materials,” *Mater. Today*, vol. 9, no. 5, pp. 32–40, 2006.
- [94] A. Kareer, A. Prasitthipayong, D. Krumwiede, D. M. Collins, P. Hosemann, and S. G. Roberts, “An analytical method to extract irradiation hardening from nanoindentation hardness-depth curves,” *J. Nucl. Mater.*, vol. 498, pp. 274–281, 2018.
- [95] G. M. Pharr, J. . Strader, and W. C. Oliver, “Critical issues in making small-depth mechanical property measurements by nanoindentation with continuous stiffness measurement,” *J. Mater. Res.*, 2017.
- [96] a. C. Fischer-Cripps, “Critical review of analysis and interpretation of nanoindentation test data,” *Surf. Coatings Technol.*, vol. 200, no. 14–15, pp. 4153–4165, 2006.
- [97] A. C. Fischer-Cripps, “Nanoindentation,” pp. 21–38, 2011.
- [98] C. D. Hardie, S. G. Roberts, and A. J. Bushby, “Understanding the effects of ion irradiation using nanoindentation techniques,” *J. Nucl. Mater.*, vol. 462, pp. 391–401, 2015.
- [99] J. Gong, J. Wang, and Z. Guan, “A comparison between Knoop and Vickers hardness of silicon nitride ceramics,” *Mater. Lett.*, vol. 56, no. 6, pp. 941–944, 2002.
- [100] K. Niihara, “Slip systems and plastic deformation of silicon carbide single crystals at high temperatures,” *J. Less-Common Met.*, vol. 65, pp. 155–166, 1979.
- [101] Y. Yang, C. Zhang, Z. Ding, C. Su, and T. Yan, “A correlation between micro- and nano-indentation on materials irradiated by high-energy heavy ions,” *J. Nucl. Mater.*, vol. 498, pp. 129–136, 2018.
- [102] D. Tabor, “The physical meaning of indentation and scratch hardness,” *Br. J. Appl. Phys.*, 1956.
- [103] P. Hosemann, D. Kiener, Y. Wang, and S. a. Maloy, “Issues to consider using nano indentation on shallow ion beam irradiated materials,” *J. Nucl. Mater.*, vol. 425, no. 1–3, pp. 136–139, 2012.
- [104] D. Dingley, “Strain measurement using EBSD : An introduction without the math . By Dr . David Dingley.”
- [105] E. y Tsybal, “Section 4 : Elastic Properties,” in *Physics 927*, no. i, pp. 1–7.
- [106] “BLG. Vantage ‘Our stroy.’” [Online]. Available: <http://www.hrebsd.com/wp/about-us/#1473091049327-80c0bdbc-b0f5>. [Accessed: 24-May-2018].
- [107] A. J. G. Lunt *et al.*, “A state-of-the-art review of micron- scale spatially resolved residual stress analysis by FIB-DIC ring-core milling and other techniques,” 2015.
- [108] M. E. Kartal, R. Kiwanuka, and F. P. E. Dunne, “Determination of sub-surface stresses at inclusions in single crystal superalloy using HR-EBSD, crystal plasticity and inverse eigenstrain analysis,” *Int. J. Solids Struct.*, vol. 67–68, pp. 27–39, 2015.
- [109] H. Abdolvand and A. J. Wilkinson, “Assessment of residual stress fields at deformation twin tips and the surrounding environments,” *Acta Mater.*, vol. 105, pp. 219–231, 2016.
- [110] N. Zaafarani, D. Raabe, R. N. Singh, F. Roters, and S. Zaefferer, “Three-dimensional investigation of the texture and microstructure below a nanoindent in a Cu single crystal using 3D EBSD and crystal plasticity finite element simulations,” *Acta Mater.*, vol. 54, no. 7, pp.

1863–1876, 2006.

- [111] B. Britton, J. Jiang, P. S. Karamched, A. J. Wilkinson, and A. J. W. T. Ben Britton, Jun Jiang, Phani S. Karamched, “Probing deformation and revealing microstructural mechanisms with cross-correlation-based, high-resolution electron backscatter diffraction,” *Jom J. Miner. Met. Mater. Soc.*, vol. 65, no. 9, pp. 1245–1253, 2013.
- [112] D. Cooper, T. Denneulin, N. Bernier, A. Béch , and J. Rouvi re, “Strain mapping of semiconductor specimens with nm-scale resolution in a transmission electron microscope,” *Micron*, vol. 80, pp. 145–165, 2016.
- [113] M. J. Hytch, E. Snoeck, and R. Kilaas, “Quantitative measurement of displacement and strain fields from HREM micrographs,” *Ultramicroscopy*, vol. 74, pp. 131–146, 1998.
- [114] A. Beche, J. L. Rouviere, J. P. Barnes, and D. Cooper, “Ultramicroscopy Dark field electron holography for strain measurement,” *Ultramicroscopy*, vol. 111, pp. 227–238, 2011.
- [115] M. H tch, C. Gatel, F. Houdellier, E. Snoeck, K. Ishizuka, and U. De Toulouse, “Darkfield electron holography for strain mapping at the nanoscale,” no. November, pp. 6–10, 2012.
- [116] “Studying silicon carbide for nuclear fuel cladding,” *Nuclear engineering international*, 2013.
- [117] H. Sadeghian, C. K. Yang, J. F. L. Goosen, E. Van Der Drift, and A. Bossche, “Characterizing size-dependent effective elastic modulus of silicon nanocantilevers using electrostatic pull-in instability Characterizing size-dependent effective elastic modulus of silicon nanocantilevers using electrostatic pull-in instability,” *Appl. Phys. Lett.*, vol. 221903, pp. 1–4, 2009.
- [118] L. Jiang and R. Cheung, “A review of silicon carbide development in MEMS applications,” *Int. J. Comput. Mater. Sci. Surf. Eng.*, vol. 2, pp. 225–240, 2009.
- [119] L. L. Snead, T. Nozawa, Y. Katoh, and T. Byun, “Handbook of SiC properties for fuel performance modeling,” *J. Nucl. Mater.*, vol. 371, no. 2007, pp. 329–377, 2008.
- [120] N. W. Jepps and T. F. Page, “Polytypic transformations in silicon carbide,” *Prog. Cryst. Growth Charact.*, vol. 7, no. 1–4, pp. 259–307, 1983.
- [121] J. . She and K. Ueno, “Effect of additive content on liquid-phase sintering on silicon carbide ceramics,” *Mater. Res. Bull.*, vol. 34, no. 99, pp. 1629–1636, 2000.
- [122] J. Binner and B. Vaidhyanathan, “Processing of bulk nanostructured ceramics,” *J. Eur. Ceram. Soc.*, vol. 28, pp. 1329–1339, 2008.
- [123] Z. H. Huang, D. C. Jia, Y. Zhou, and Y. G. Liu, “A new sintering additive for silicon carbide ceramic,” *Ceram. Int.*, vol. 29, no. 3, pp. 13–17, 2003.
- [124] C. J. Shih, V. F. Nesterenko, and M. Meyers, “High-strain-rate deformation and comminution of silicon carbide,” *J. Appl. Phys.*, vol. 83, no. May 1998, pp. 4660–4671, 1998.
- [125] M. Flinders, “Microstructural control of silicon carbide for ballistic applications,” The University of Utah.
- [126] G. H. Wroblewska and R. Hamminger, “Microanalytical Investigations of the Intermediate Sintering State of Silicon Carbide,” *Ceram. Int.*, vol. 17, pp. 199–203, 1991.
- [127] D. Ritchardson, *Modern Ceramic Engineering*, 3rd ed. London: Taylor & Francis Ltd, 2006.
- [128] M. a. Mulla and V. D. Krstic, “Mechanical properties of β -SiC pressureless sintered with Al₂O₃ additions,” *Acta Metall. Mater.*, vol. 42, no. 1, pp. 303–308, 1994.
- [129] G. Magnani, G. Sico, A. Brentari, and P. Fabbri, “Solid-state pressureless sintering of silicon carbide below 2000°C,” *J. Eur. Ceram. Soc.*, vol. 34, no. 15, pp. 4095–4098, 2014.

- [130] J. H. She and K. Ueno, "Densification behavior and mechanical properties of pressureless-sintered silicon carbide ceramics with alumina and yttria additions," *Mater. Chem. Phys.*, vol. 59, pp. 139–142, 1999.
- [131] J. David, L. Farbaniec, T. Sano, M. Shaeffer, and K. T. Ramesh, "The effects of defects on the uniaxial compressive strength and failure of an advanced ceramic," *Acta Mater.*, vol. 102, pp. 263–272, 2016.
- [132] A. R. Powell and C. Calvin, "Growth of SiC substrates," *Int. J. High speed Electron. Syst.*, no. May 2015, 2006.
- [133] D. Hofmann and J. Volkl, "SiC-bulk growth by physical-vapor transport and its global modelling," *J. Cryst. Growth*, vol. 174, pp. 669–674, 1997.
- [134] M. Dudley *et al.*, "Contribution of x-ray topography and high-resolution diffraction to the study of defects in SiC," *J. Phys. D Appl. Phys.*, vol. 36, pp. A30-36, 2002.
- [135] S. G. Mu *et al.*, "The status of SiC bulk growth from an industrial point of view," *J. Cryst. Growth*, vol. 211, pp. 325–332, 2000.
- [136] K. Kakimoto, B. Gao, and S. Nishizawa, "Thermodynamic analysis of SiC polytype growth by physical vapor transport method," *J. Cryst. Growth*, vol. 324, no. 1, pp. 78–81, 2011.
- [137] A. Fissel, "Thermodynamic considerations of the epitaxial growth of SiC polytypes," *J. Cryst. Growth*, vol. 212, pp. 438–450, 2000.
- [138] I. Chowdhury, M. V. S. Chandrasekhar, P. B. Klein, J. D. Caldwell, and T. Sudarshan, "High growth rate 4H-SiC epitaxial growth using dichlorosilane in a hot-wall CVD reactor," *J. Cryst. Growth*, vol. 316, no. 1, pp. 60–66, 2011.
- [139] Accuratus, "accuratus SiC data sheet," 2013. [Online]. Available: <https://www accuratus.com/silicar.html>. [Accessed: 01-Feb-2019].
- [140] Saint-Gobain, "Hexoloy SA Silicon Carbide," *Saint-Gobain technical data sheet*. Saint-Gobain, p. 4, 2012.
- [141] S. Shim, J. Jang, and G. M. Pharr, "Extraction of flow properties of single-crystal silicon carbide by nanoindentation and finite-element simulation," *Acta Mater.*, vol. 56, no. 15, pp. 3824–3832, Sep. 2008.
- [142] L. Yin, E. Y. J. Vancoille, K. Ramesh, and H. Huang, "Surface characterization of 6H-SiC (0001) substrates in indentation and abrasive machining," *Int. J. Mach. Tools Manuf.*, vol. 44, no. 6, pp. 607–615, 2004.
- [143] B. Hähnlein, J. Kovac, and J. Pezoldt, "Size effect of the silicon carbide Young's modulus," *Phys. Status Solidi Appl. Mater. Sci.*, vol. 214, no. 4, pp. 1–9, 2017.
- [144] J. Reddy, A. Volinsky, C. Frewin, C. Locke, and S. Sadow, "Mechanical Properties of 3C-SiC Films for MEMS Applications," in *materials research society*, 2008, vol. 1049.
- [145] Z. Li and R. C. Bradt, "The Single Crystal Elastic Constants of Hexagonal SiC to 1000°C," *Int. J. High Technol. Ceram.*, vol. 4, pp. 1–10, 1988.
- [146] K. Kamitani *et al.*, "The elastic constants of silicon carbide : A Brillouin-scattering study of 4H and 6H SiC single crystals," *J. Appl. Phys.*, vol. 3152, no. 1997, pp. 13–16, 2010.
- [147] M. Iwami, "Silicon carbide : fundamentals," *Nucl. Inst. Methods Phys. Res. A*, vol. 466, pp. 406–411, 2001.
- [148] T. L. D. Aulton, T. J. B. Ernatowicz, R. S. L. Ewis, S. M. Essenger, F. J. S. Tadermann, and S. A. Mari, "Polytype distribution of circumstellar silicon carbide : Microstructural

- characterization by transmission electron microscopy,” *Geochim. Cosmochim. Acta*, vol. 67, no. 24, pp. 4743–4767, 2003.
- [149] P. Reviewed, “University of California In Situ TEM Nanomechanical Testing of Ceramics : Room-Temperature Plastic Deformation Mechanisms,” 2014.
- [150] T. Mayama, K. Aizawa, Y. Tadano, and M. Kuroda, “Influence of twinning deformation and lattice rotation on strength differential effect in polycrystalline pure magnesium with rolling texture Pyramidal-1,” *Comput. Mater. Sci.*, vol. 47, no. 2, pp. 448–455, 2009.
- [151] J. Yan, X. Gai, and H. Harada, “Subsurface damage of single crystalline silicon carbide in nanoindentation tests.,” *J. Nanosci. Nanotechnol.*, vol. 10, pp. 7808–7811, 2010.
- [152] L. . Snead, S. J. Zinkle, J. . Hay, and M. . Osborne, “Amorphization of SiC under ion and neutron irradiation,” *Nucl. Instruments Methods Phys. Res. Sect. B Beam Interact. with Mater. Atoms*, vol. 141, no. 1–4, pp. 123–132, 1998.
- [153] A. Debelle and L. Thom, “Characterization and modelling of the ion-irradiation induced disorder in 6H-SiC and 3C-SiC single crystals,” *J. Phys. D Appl. Phys.*, 2010.
- [154] J. Costantini, X. Kerbiriou, M. Sauzay, and L. Thom, “Ion-beam modifications of mechanical and dimensional properties of silicon carbide,” *J. Appl. Phys.*, vol. 45, 2012.
- [155] G. Kwon, H. J. Sangyeob, and L. Chansun, “Room-temperature yield and fracture strength of single-crystalline 6H silicon carbide,” *J. Mater. Sci.*, vol. 50, no. 24, pp. 8104–8110, 2015.
- [156] R. Sarkar, C. Rentenberger, and J. Rajagopalan, “Electron Beam Induced Artifacts During in situ TEM Deformation of Nanostructured Metals,” *Nat. Sci. reports*, pp. 1–11, 2015.
- [157] D. Frazer *et al.*, “Localized mechanical property assessment of SiC / SiC composite materials,” *Compos. Part A*, vol. 70, pp. 93–101, 2015.
- [158] J. Qian, L. L. Daemen, and Y. Zhao, “Hardness and fracture toughness of moissanite,” *Diam. Relat. Mater.*, vol. 14, pp. 1669–1672, 2005.
- [159] T. F. Page, W. C. Oliver, and C. J. McHargue, “The deformation behavior of ceramic crystals subjected to very low load (nano)indentations,” *J. Mater. Res.*, vol. 7, pp. 450–473, 1992.
- [160] I. Szlufarska, R. K. Kalia, A. Nakano, and P. Vashishta, “Nanoindentation-induced amorphization in silicon carbide,” *Appl. Phys. Lett.*, vol. 85, no. 3, p. 378, 2004.
- [161] G. Newsome, L. L. Snead, T. Hinoki, Y. Katoh, and D. Peters, “Evaluation of neutron irradiated silicon carbide and silicon carbide composites,” *J. Nucl. Mater.*, vol. 371, pp. 76–89, 2007.
- [162] Y. Katoh, T. Nozawa, L. L. Snead, K. Ozawa, and H. Tanigawa, “Stability of SiC and its composites at high neutron fluence,” *J. Nucl. Mater.*, vol. 417, no. 1–3, pp. 400–405, 2011.
- [163] G. W. Egeland *et al.*, “Plastic deformation in zirconium nitride observed by nanoindentation and TEM,” *J. Nucl. Mater.*, vol. 416, no. 3, pp. 253–261, 2011.
- [164] D. Pilloud, A. S. Dehlinger, J. F. Pierson, A. Roman, and L. Pichon, “Reactively sputtered zirconium nitride coatings : structural , mechanical , optical and electrical characteristics,” *Surf. Coat. Technol.*, vol. 175, pp. 338–344, 2003.
- [165] M. Burghartz, G. Ledergerber, R. R. van der Lann, H. Hein, and R. J. M. Konings, “Some Aspects of the Use of ZrN as an Inert Matrix for Actinide Fuels fuels,” *J. Nucl. Mater.*, no. February 2014, 2001.
- [166] A. J. Van Vuuren, J. H. Neethling, V. A. Skuratov, V. V Uglov, and S. Petrovich, “The effect of He and swift heavy ions on nanocrystalline zirconium nitride,” *Nucl. Inst. Methods Phys.*

Res. B, vol. 326, pp. 19–22, 2014.

- [167] Y. Tang, G. Zhang, J. Xue, X. Wang, C. Xu, and X. Huang, “Densification and mechanical properties of hot-pressed ZrN ceramics doped with Zr or Ti,” *J. Eur. Ceram. Soc.*, vol. 33, no. 7, pp. 1363–1371, 2013.
- [168] K. Wheeler, P. Peralta, M. Parra, K. McClellan, J. Dunwoody, and G. Egeland, “Effect of sintering conditions on the microstructure and mechanical properties of ZrN as a surrogate for actinide nitride fuels,” *J. Nucl. Mater.*, no. July, 2007.
- [169] A. Ermoline, M. Schoenitz, and E. L. Dreizin, “High-temperature phase equilibria in the system Zr – O – N,” *Mater. Res. Soc.*, 2006.
- [170] R. W. Harrison and W. E. Lee, “Processing and properties of ZrC, ZrN and ZrCN ceramics : a review,” *Adv. Appl. Ceram.*, vol. 6753, 2016.
- [171] L. Gribaudo and J. Abriata, “The N-Zr (Nitrogen-Zirconium) System,” *Phase Diagr. Eval.*, vol. 15, no. 4, pp. 441–442, 1994.
- [172] P. Carvalho, “Introduction - The Decorative thin films.”
- [173] C. Marsden, “Zirconia - Physical and Mechanical Property Comparison of the Different Types of Zirconias,” *AZO materilas*, 2014. [Online]. Available: <https://www.azom.com/article.aspx?ArticleID=940>. [Accessed: 02-Jan-2018].
- [174] P. Peralta and G. W. Egeland, “A nano-indentation study of surface plasticity in zirconium nitride,” *J. Nucl. Mater.*, vol. 416, no. 3, pp. 253–261, 2008.
- [175] N. J. Ashley, Æ. R. W. Grimes, and K. J. McClellan, “Accommodation of non-stoichiometry in TiN 1- x and ZrN 1- x,” *J. Mater. Sci.*, pp. 1884–1889, 2007.
- [176] J. Gan, Y. Yang, C. Dickson, and T. Allen, “Proton irradiation study of GFR candidate ceramics,” *J. Nucl. Mater.*, vol. 389, no. 2, pp. 317–325, 2009.
- [177] L. Jiao *et al.*, “Radiation tolerant nanocrystalline ZrN films under high dose heavy-ion irradiations,” *J. Appl. Phys.*, vol. 145901, 2015.
- [178] Y. Yang, C. A. Dickerson, and T. R. Allen, “Radiation stability of ZrN under 2.6 MeV proton irradiation,” *J. Nucl. Mater.*, vol. 392, no. 2, pp. 200–205, 2009.
- [179] Z. T. Wu, Z. B. Qi, D. F. Zhang, and Z. C. Wang, “Nanoindentation induced plastic deformation in nanocrystalline ZrN coating,” *Mater. Lett.*, vol. 164, pp. 120–123, 2016.
- [180] W. Periodicals, “CASINO V2 . 42 — A Fast and Easy-to-use Modeling Tool for Scanning Electron Microscopy and Microanalysis Users,” vol. 29, pp. 92–101, 2007.
- [181] A. J. Wilkinson and T. Ben Britton, “Strains, planes, and EBSD in materials science,” *Mater. Today*, vol. 15, no. 9, pp. 366–376, 2012.
- [182] T. Maitland and S. Sitzman, “(EBSD) Technique and Materials Characterization Examples,” in *Scanning microscopy for nanotechnology techniques and applications*, 2007, pp. 41–76.
- [183] A. J. Wilkinson and D. J. Dingley, “Quantitative deformation studies using electron back scatter patterns,” *Acta Metall. Mater.*, vol. 39, no. 12, pp. 3047–3055, 1991.
- [184] V. Tong, J. Jiang, A. J. Wilkinson, and T. Ben Britton, “The effect of pattern overlap on the accuracy of high resolution electron backscatter diffraction measurements,” *Ultramicroscopy*, vol. 155, pp. 62–73, 2015.
- [185] T. Butler, “On the determination of dislocation densities,” Annapolis, Maryland, 1969.
- [186] “Kleindiek Nanotechnik.” [Online]. Available: <https://www.nanotechnik.com/fms-em.html>.

- [187] A. Leatherbarrow and H. Wu, "Mechanical behaviour of the constituents inside carbon-fibre/carbon-silicon carbide composites characterised by nano-indentation," *J. Eur. Ceram. Soc.*, vol. 32, no. 3, pp. 579–588, Mar. 2012.
- [188] J. B. Malherbe *et al.*, "Scanning electron microscopy of the surfaces of ion implanted SiC," *Nucl. Inst. Methods Phys. Res. B*, vol. 354, pp. 23–27, 2015.
- [189] A. A. Suvorova and S. Samarin, "Secondary electron imaging of SiC-based structures in secondary electron microscope," *Surf. Sci.*, vol. 601, no. 18, pp. 4428–4432, 2007.
- [190] K. H. Pang, E. Tymicki, and A. Roy, "Indentation in single-crystal 6H silicon carbide: Experimental investigations and finite element analysis," *International Journal of Mechanical Sciences*, vol. 144, pp. 858–864, 2018.
- [191] E. Demir, D. Raabe, N. Zaafarani, and S. Zaefferer, "Investigation of the indentation size effect through the measurement of the geometrically necessary dislocations beneath small indents of different depths using EBSD tomography," *Acta Mater.*, vol. 57, no. 2, pp. 559–569, 2009.
- [192] D. Hallam, A. Heaton, B. James, P. Smith, and J. Yeomans, "The correlation of indentation behaviour with ballistic performance for spark plasma sintered armour ceramics," *J. Eur. Ceram. Soc.*, vol. 35, no. 8, pp. 2243–2252, 2015.
- [193] J. Herring, "Small Scale Mechanics Applied to Nuclear Materials," Oxford, 2015.
- [194] K. L. Johnson, "The correlation of indentation experiments," *J. Mech. Phys. Solids*, vol. 18, no. 2, pp. 115–126, 1970.
- [195] J. E. Darnbrough, D. Lui, and P. Flewitt, "Micro-scale testing of ductile and brittle cantilever beam specimens in situ with a dual beam workstation," *Meas. Sci. Technol.*, p. 9, 2013.
- [196] J. Li *et al.*, "Evolution of amorphization and nanohardness in SiC under Xe ion irradiation," *J. Nucl. Mater.*, vol. 454, no. 1–3, pp. 173–177, 2014.
- [197] S. Zaefferer and N. Elhami, "Theory and application of electron channelling contrast imaging under controlled diffraction conditions," *Acta Mater.*, vol. 75, no. 154, pp. 20–50, 2014.
- [198] F. Guiberteau, N. P. Padture, and B. R. Lawn, "Effect of Grain Size on Hertzian Contact Damage in Alumina," *J. Am. Ceram. Soc.*, vol. 77, no. 7, pp. 1825–1831, Jul. 1994.
- [199] R. J. Arsenault and N. Shi, "Dislocation generation due to differences between the coefficients of thermal expansion," *Mater. Sci. Eng.*, vol. 81, no. C, pp. 175–187, 1986.
- [200] H. Wu, S. G. Roberts, and B. Derby, "Residual Stress and Subsurface Damage in Machined Alumina and Alumina / Silicon Carbide Nanocomposite Ceramics," vol. 49, pp. 507–517, 2001.
- [201] G. Ling, Y. Haitao, Z. Shikun, L. Huaping, and Y. Runzhang, "Effect of Grinding and Polishing on the Residual Stress and Bending Strength of a Silicon Nitride Ceramic *," *J. Wuhan Univ. Technol. -Mater. Sci. Ed*, vol. 20, no. 1, 2005.
- [202] A. J. Perry and D. E. Geist, "On the residual stress profile developed implantation in titanium nitride by ion implantation," *Nucl. Inst. Methods Phys. Res. B*, vol. 128, pp. 967–971, 1997.
- [203] R. V Mises, "Hauptaufatza mechanik der plastischen formänderung von kristallen," *Zeitschrift Angew. Math. und Mech.*, vol. 1, no. 1925, 1928.
- [204] S. J. Clarke, C. W. Michie, and M. J. Rosseinsky, "Structure of Zr₂ON₂ by Neutron Powder Diffraction : The Absence of Nitride-Oxide Ordering," *J. Solid State Chem.*, vol. 405, pp. 399–405, 1999.

- [205] P. Li and J. M. Howe, "Dislocation reactions in ZrN," *Acta Mater.*, vol. 50, pp. 4231–4239, 2002.
- [206] K. B. Kuznetsov *et al.*, "Stability of the structure of compact zirconium nitride ceramics to irradiation with high-energy xenon ions," *Inorg. Mater.*, vol. 52, no. 12, pp. 1235–1239, 2016.
- [207] Y. W. Lee *et al.*, "Preparation of simulated inert matrix fuel with different powders by dry milling method," *J. Nucl. Mater.*, vol. 274, no. 1, pp. 7–14, 1999.
- [208] J. Z. and J. Biersack, "Stopping range of ions in matter." 2003.
- [209] G. S. Randhawa and H. S. Virk, "Stopping power and range of heavy ions in solids: A comparative study," *Radiat. Meas.*, vol. 26, no. 4, pp. 541–560, 1996.
- [210] S. Pellegrino, L. Thomé, A. Debelle, S. Miro, and P. Trocellier, "Radiation effects in carbides: TiC and ZrC versus SiC," *Nucl. Instruments Methods Phys. Res. Sect. B Beam Interact. with Mater. Atoms*, vol. 327, no. 1, pp. 103–107, 2014.
- [211] S. Nakashima and H. Harima, "Raman investigation of SiC polytypes," *Phys. Status Solidi Appl. Res.*, vol. 162, no. 1, pp. 39–64, 1997.
- [212] J. Huguet-garcia *et al.*, "Characterization of the ion-amorphization process and thermal annealing effects on third generation SiC fibers and 6H-SiC," *Nucl. Sci. Technol.*, vol. 8, pp. 1–9, 2015.
- [213] X. Chen *et al.*, "Irradiation effects in 6H e SiC induced by neutron and heavy ions : Raman spectroscopy and high-resolution XRD analysis," *J. Nucl. Mater.*, vol. 478, pp. 215–221, 2016.
- [214] W. Wu, Z. Xu, F. Fang, and H. Liu, "Decrease of FIB-induced lateral damage for diamond tool used in nano cutting," *Nucl. Inst. Methods Phys. Res. B beam Interact. with Mater. atoms*, no. October, pp. 91–98, 2014.
- [215] A. Tiberj and J. Camassel, "Raman Imaging," in *Raman Imaging, Series in Optical Sciences 168*, vol. 168, Berlin: Springer-Verlag, 2012.
- [216] W. Liu, L. Cheng, Y. Wang, and H. Ma, "Investigation of the residual stress in reaction-bonded SiC under irradiation," *J. Eur. Ceram. Soc.*, vol. 36, no. 16, pp. 3901–3907, 2016.
- [217] X. Wang, Y. Zhang, S. Liu, and Z. Zhao, "Depth profiling by Raman spectroscopy of high-energy ion irradiated silicon carbide," *Nucl. Instruments Methods Phys. Res. Sect. B Beam Interact. with Mater. Atoms*, vol. 319, pp. 55–61, 2014.
- [218] I. Ahmad, M. Holtz, N. N. Faleev, and H. Temkin, "Dependence of the stress-temperature coefficient on dislocation density in epitaxial GaN grown on α -Al₂O₃ and 6H-SiC substrates," *J. Appl. Phys.*, vol. 95, no. 4, pp. 1692–1697, 2004.
- [219] J. A. Creighton and R. Withnall, "The Raman spectrum of gallium metal," *Chem. Phys. Lett.*, no. August, pp. 311–313, 2000.
- [220] X. Chen *et al.*, "Mechanical properties of 6H-SiC irradiated by neutron and MeV heavy ions: A nanoindentation and finite element method study," *J. Appl. Phys.*, vol. 123, no. 2, 2018.
- [221] G. C. Sneddon, P. W. Trimby, and J. M. Cairney, "Transmission Kikuchi diffraction in a scanning electron microscope: A review," *Mater. Sci. Eng. R Reports*, vol. 110, pp. 1–12, 2016.

7. Appendix

7.1 X-ray photoelectric spectroscopy (XPS) of SiC experimental

XPS is one of the most widely used and accessible surface characterisation methods. XPS can identify all elements except helium and hydrogen, elements can be detected at concentrations >0.1 atomic % to a depth of 3-10 nm. When coupled with an argon ion beam depth-resolved chemical analysis can be performed up to depths of 1.5 μm (dependent on the sample).

The samples required for XPS analysis were mounted on a copper test plate with copper clips or carbon putty. Once mounted each sample was analysed with a K-Alpha xps system, (Thermo Scientific, Massachusetts, USA). The analysis parameters selected were as follows; 400 μm spot size, 200 eV Pass Energy, 1 eV step size, 10 ms dwell time, 10 scans. To produce depth resolved elemental plots argon ion milling was used to mill through the SiC surface. Ion milling was conducted at 200 keV at low current with a 1mm raster size and 5 s etch per level this provided a 0.11 nm/s etch rate when compared to tantalum pentoxide (Ta_2O_5). The compucentric zalar depth profile technique was used to ensure even milling of the substrate. To mitigate any time dependency of oxide layer growth the SiC samples were colloidal silica polished on the day of analysis. Peak fitting and analysis of the XPS data was undertaken with the Fisher Scientific software (Thermo Scientific, Massachusetts, USA).

7.2 SiC surface chemistry XPS

To asses if surface oxide layers were present on the SiC wafer depth-resolved XPS was used these results are presented below;

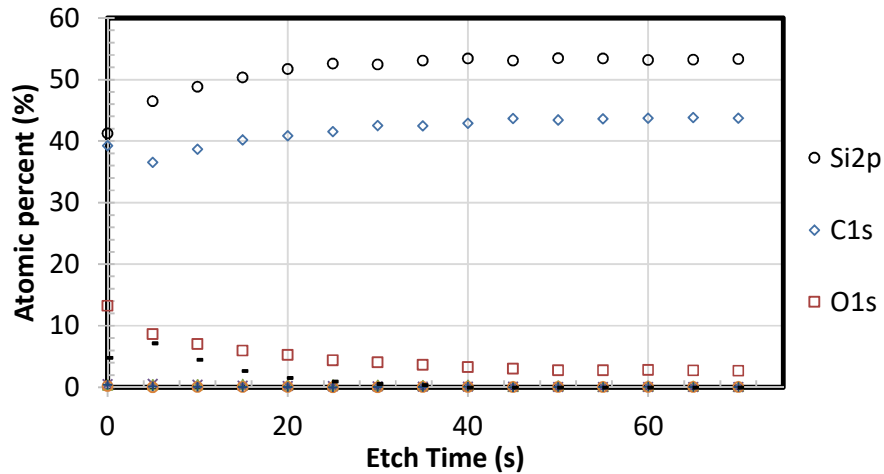


Figure 143 XPS depth profile data of the 6H 0001 SiC sample.

The plot Figure 143 shows a slight enrichment of oxygen at the surface along with some magnesium and Zinc.

Table 27 XPS atomic % composition analysis before and argon ion milling.

Sample	Milling	Ar	C	Cu	Fe	Mg	N	Na	O	Si	Zn
6h 0001 sic	Before	-	41.95	0.9	0.97	4.86	0.72	0.43	14.01	35.91	0.24
6h 0001 sic	After	-	43.1	-	-	-	-	-	4.25	52.65	-

The bulk composition (following etching) is very close to that recorded during the SEM-EDS analysis. To quantify the potential oxide layer first the etch time must be converted to an estimated depth. The tantalum etch rate can be scaled to give an estimated etch rate of silicon carbide. The etch rate of tantalum is shown below.

$$\text{Ta etch rate} = \frac{\text{mass of Ta} \times \text{sputter yield of Ta}}{\rho \text{ of Ta}}$$

Using a molar mass of SiC = 40.0962 g/mol, density of SiC = 3.21 g/cm³ a scaling factor for the etch rate of SiC can be calculated

$$\text{SiC etch rate} = \frac{40.0962 \times 0.5}{3.21}$$

Scaling factor for SiC = 1.69736, Etch rate of Ta = 0.11 nm/s

$$\frac{0.11}{1.69736} = 0.0648 \text{ nm/s}$$

Based on the XPS plots a 5s step is required to reduce oxygen layer thus oxide layer approximate depth.

$$5 \times 0.0648 = \mathbf{0.324 \text{ nm}}$$

It was found that the surface of the silicon carbide samples tested have an estimated oxide layer thickness of 0.324 nm this is comparable to a few atom layers. The 6H 0001 sample exhibited additional elements to SiC, oxygen and carbon. Many of the elements found at the surface of the 6H sample were not present in the bulk material, these elements may have been surface contamination or could be part of the doping scheme used in the material. Typical interaction volumes for XPS are 0-10 nm thus the measurement of layer composition below this depth are estimates. The Sp2 peak was observed to shift from the surface scan to the second scan (at 5s).

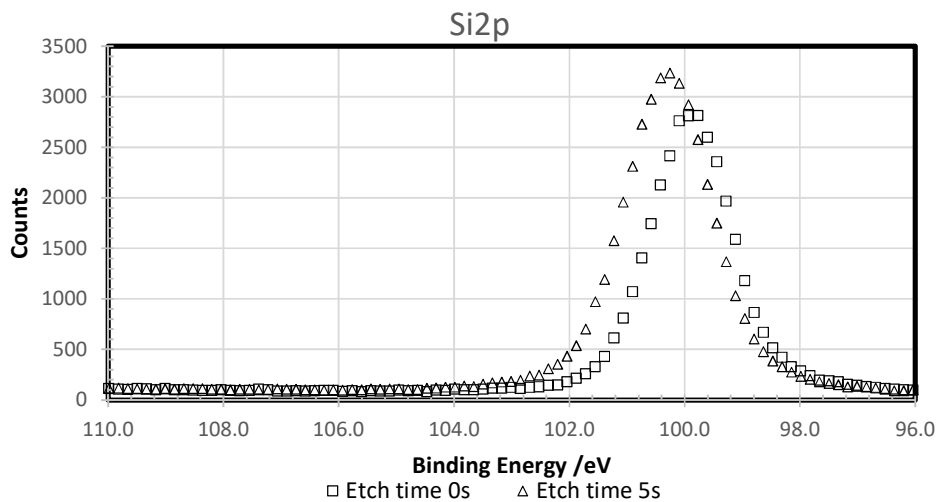


Figure 144 Si2p peak from 6h sic single crystal XPS at 0s and 5s.

A small shift + 0.406 Binding energy / eV was identified in the Si2p peak from the surface at 0 seconds to 5s into the etch. Along with a broadening and intensity increase from the surface to the 5s etch (from FWHM 1.439 to 1.547). This change from the surface to the bulk is attributed to a surface oxide layer. due to the negligible thickness of the oxide layer the samples wre deemed suitable for nanoindentation and microbend testing.

5.3.3. Raman and fluorescence microscopy

Raman microscopy was performed using a true confocal Raman microscope (Horiba, Japan) equipped with a 633 nm red line He-Ne laser. A 50× objective lens was used in conjunction with a true confocal setup. For the analysis of gallium ion damage in silicon carbide a grating of 1800 with a slit size of 150 and a hole size of 400. To produce a silicon carbide Raman spectra 750-1050 Raman shift (cm^{-1}) range was scanned. For gallium 130-630 (cm^{-1}) was scanned. Before testing the spectrometer was calibrated to a silicon (520 cm^{-1}) calibration sample as directed by Horiba operational procedures.

To produce Gallium ion damaged areas comparable to those produced under typical milling conditions, three boxes $50 \times 20 \times 0.02 \mu\text{m}$ were milled at 30 keV, 3 nA. The first box was then cleaned with 30 keV, 0.3 nA for (5 minutes), box two was then cleaned at 10 keV, 0.72 nA for 23 minutes and the third box was cleaned at 5 keV, 0.52 nA for 35 minutes.

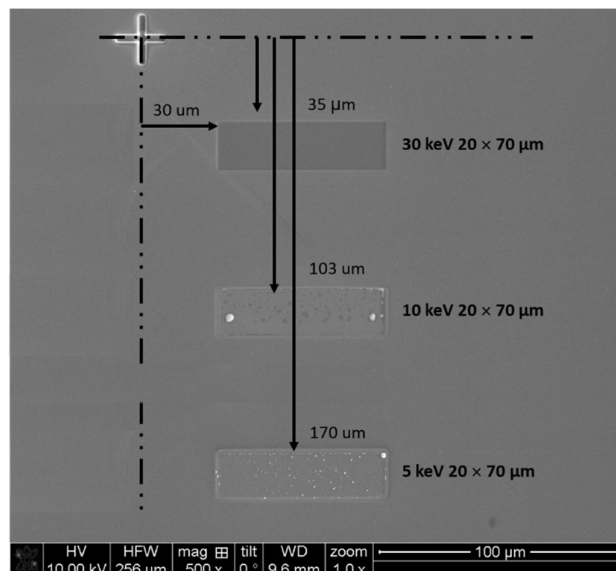


Figure 145 Large area gallium ion damage schematic layout.

PeakFit (Systat Software Inc, California, USA) was used to characterise the peak position and FWHM of each Raman peak for the SiC samples.

7.3 Raman analysis of SiC

To assess the amorphisation of the SiC further Raman spectroscopy was employed. The Raman spectra peaks were indexed based on the literature [211]. The Raman-active modes in 6H SiC (wurtzite structure) are the A_1 , E_1 and E_2 mode these are the Si-C bonds [212]. The A_1 and E_1 photon modes are split into longitudinal (LO) and transverse (TO) optical modes [212], [213].

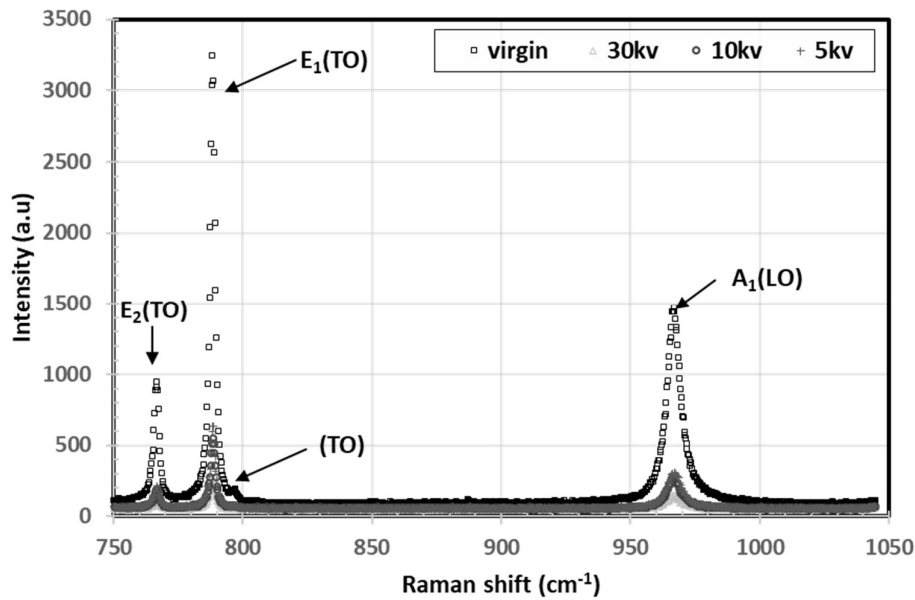


Figure 146 Raman spectrum of SiC exposed to 30 keV, 10 keV and 5 keV Raman shift from 750 to 1050 cm⁻¹.

Table 28 table of peak position and full width half maximum (fwhm) of the $e_1(to)$.

	E_1 (TO) Peak position (cm ⁻¹)	Standard deviation	FWHM	Standard deviation
Bulk	788.50	0.01	2.97	0.01
5	788.44	0.02	3.62	0.14
10	788.44	0.02	3.53	0.59
30	788.35	0.02	2.76	0.08

The spectra showed a reduction in intensity and slight broadening following gallium ion implantation. The E_1 TO peak exhibited a slight shift and FWHM variation over the 10 spectra recorded for each of the implanting keV. While increasing keV / ion dose resulted in a reduction in Raman spectra intensity. In Figure 146, the reduction in intensity between the

unirradiated and irradiated areas is clear, further to this the TO peak is removed following ion beam exposure. These results match well with those published by Wu *et al.* in their paper on FIB cleaning of Dimond tools [214]. Along with Chen *et al.*'s paper on Irradiation effects in 6H SiC induced by neutron and heavy ions [213]. Chen attributes the reduction in spectral intensity to the increase in defects resulting in an increase in optical absorption, this conclusion matches well with our TEM analysis [213].

Raman spectroscopy is frequently used in the semiconductor industry for the mapping of residual stress [215]. Several researchers have used Raman to characterise residual stress in cubic SiC [216]. J.Liu presented a model for strain mapping in SiC, in this paper, SiC was compressed between Dimond anvils and the Raman spectra of the material measured (514 nm laser). A plot of LO-TO splitting was plotted against stress. As an empirical rather than physical model its validity for the analysis of residual stress is questionable. Additionally, the undefined probe size of the laser in the SiC damage layer makes resolving the residual stress caused by the ion damage problematic. Wang *et al.* measured the residual stress in 6H SiC irradiated with higher energy carbon ions using a formula previously presented by Ahmad *et al.* in this original paper the residual stress of SiC on GaN [217], [218]. The paper provided evidence for the relationship between stress and phonon shift in GaN not SiC, extrapolating to SiC is not appropriate [218].

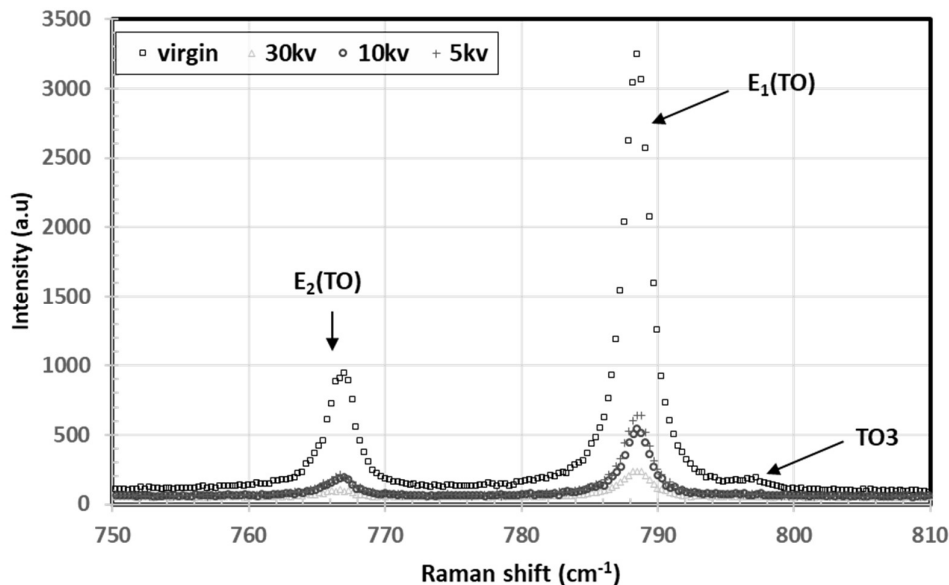


Figure 147 Raman spectrum of SiC exposed to 30 keV, 10 keV and 5 keV from Raman shift from 13- to 630 cm⁻¹.

The literature suggests that new broader bands near 180-200 and 535-540 cm^{-1} are typically observed when the TO and LO peaks are reduced under irradiation conditions [213]. The bands which emerge at 180-200 and 535-540 cm^{-1} are related to crystalline silicon which forms following irradiation. The emergence of these areas of the spectrum did not occur during analysis following ion irradiation. Rather the Si-Si bond peak was higher in intensity and width before ion irradiation.

Further to the assessment of the SiC damage, information on the gallium implanted in the material was also sought. It is typical that due to their single atom primitive unit cell metals do not exhibit first-order Raman spectra. Gallium has 4 atoms in its primitive unit cell and as such can be identified with Raman spectroscopy [219]. The gallium band has been reported as $246 \pm 1 \text{ cm}^{-1}$ at room temperature when excited with a 633 nm red laser [219]. No gallium metal was identified in the Raman spectra recorded, this could be due to the low levels of gallium present or the bonding state of the implanted gallium. Gallium metal spectra are reported to be low intensity this may have also contributed to an inability to locate the spectra.

Raman did not provide much additional information as to the effects of the gallium ion damage on the residual stress in the sample. due the small damage layer thickness and large probe size of the laser in the single crystal, cross sectional mapping was not suitable. Thus in plane analysis was conducted, Raman intensity was linked to disorder. Due to the addition of gallium ions it was decided that the uses of the standard method to determine disorder based on the normalised integral areas of the Raman peaks was not scientifically appropriate [220].

7.4 TKD HR-EBSD of ZrN

Transmission kikuchi diffraction offers improved spatial resolution (5-10 nm) when compared to traditional EBSD at the cost of strain resolution due to lamellar relaxation [221]. A proof of concept experiment was conducted on an I ZrN TEM lamellar to asses the quality of patterns from the top surface of the irradiated sample. A tilt angle of 20° was used with an accelerating voltage of 20 keV and 26 nA as suggested in the literature [221].

Forward scatter mixed image of the I ZrN lamellar

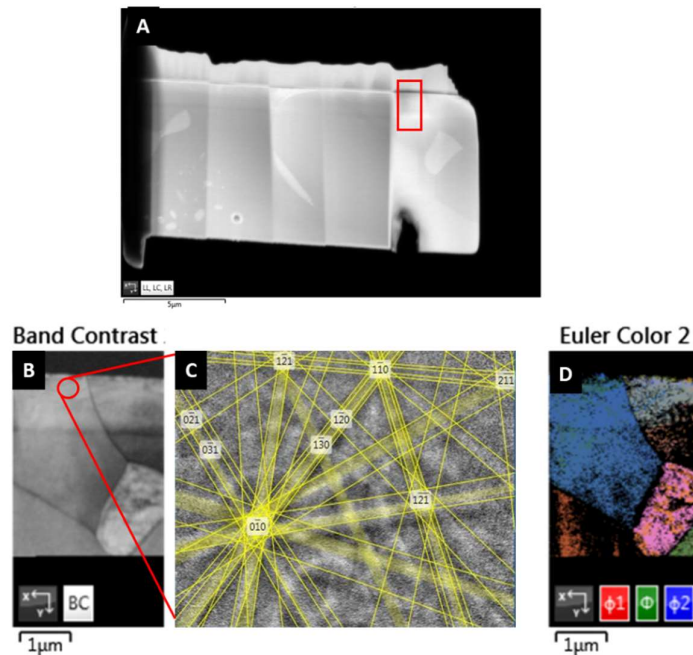


Figure 148 (A) forward scatter image of I ZrN lamellar, (B) band contrast image of the ion irradiated layer with indexed pattern location, (C) indexed EBSP, (D) Euler colour map where back signifies unindexable points.

Patterns of sufficient quality to index were achieved from the irradiated layer. Despite this initial success pattern quality was found to be highly dependent on the beam location and lamellar thickness relative to the beam. As shown on part D of Figure 148, a low hit rate was achieved, increasing the keV and re-cleaning the lamellar may have improved the hit rate. Due to the low hit rate HR-EBSD mapping was not completed, however, the concept has been demonstrated and with refinement could be utilised in future work.

To summarise HR-EBSD was used to map and quantify the residual stress induced by gold ion irradiation in ZrN and polished ZrN. Mechanical polishing resulted in a small level of residual compressive stress at the surface of the sample, as supported by the literature. Ion implantation resulted in residual compressive stress centred about the dislocation zone 1.20 μm from the surface of the sample. The magnitude and distribution of the compressive stress identified matches well with the literature.

